

分类号：  
密 级：

单位代码：10422  
学 号：201111364



山东大学  
SHANDONG UNIVERSITY

# 博士学位论文

Dissertation for Doctoral Degree

论文题目：**RHIC-STAR 实验上  $W^\pm$  玻色子纵向单自旋不对称的测量**  
**Measurement of Longitudinal Single Spin Asymmetry of  $W^\pm$  Boson Production at RHIC-STAR**

作者姓名	张金龙
培养单位	物理学院
专业名称	粒子物理原子核物理
指导教师	徐庆华 教授
合作导师	

2016 年 5 月 9 日



## 原创性声明

本人郑重声明：所呈交的学位论文，是本人在导师的指导下，独立进行研究所取得的成果。除文中已经注明引用的内容外，本论文不包含任何其他个人或集体已经发表或撰写过的科研成果。对本文的研究作出重要贡献的个人和集体，均已在文中以明确方式标明。本声明的法律责任由本人承担。

论文作者签名：\_\_\_\_\_ 日期：\_\_\_\_\_

## 关于学位论文使用授权的声明

本人同意学校保留或向国家有关部门或机构送交论文的印刷件和电子版，允许论文被查阅和借阅；本人授权山东大学可以将本学位论文的全部或部分内容编入有关数据库进行检索，可以采用影印、缩印或其他复制手段保存论文和汇编本学位论文。

(保密论文在解密后应遵守此规定)

论文作者签名：\_\_\_\_\_ 导师签名：\_\_\_\_\_ 日期：\_\_\_\_\_



# Abstract

It has been a fundamental and longstanding challenge in particle and nuclear physics to understand the spin structure of nucleon. In polarized deep inelastic scattering (DIS) experiments, the nucleon spin structure can be accessed through the spin-dependent structure function from the polarized cross section. The total contribution of quark spin has been measured to be about  $\sim 25\%$  of the proton spin. The first flavor separated contributions of quark and anti-quark spin have been obtained in semi-inclusive DIS experiments with involvement of the fragmentation functions. Subject to uncertainties of fragmentation functions, the polarized parton distribution functions (PDFs) of sea quark are still not well constrained compared to the valence quark.

RHIC, the relativistic heavy ion collider, located at Brookhaven National Laboratory in United States, is the first polarized proton-proton collider in the world. Taking the advantage of polarized proton-proton collision, RHIC can provide new insights into the nucleon spin structure, in particular the gluon and sea quark polarizations. At RHIC, the production of  $W^\pm$  boson in longitudinally polarized proton-proton collisions is a powerful tool to study the flavor separation of nucleon spin. The coupling of  $W^\pm$  bosons to left-handed quarks and right-handed anti-quarks naturally determines the helicity of the incident quarks. This provides direct sensitivity to the polarized PDFs of sea quarks through the parity-violating longitudinal single-spin asymmetry,  $A_L$ , which is defined as  $A_L \equiv (\sigma_+ - \sigma_-)/(\sigma_+ + \sigma_-)$ , where  $\sigma_{+(-)}$  is the cross section when the polarized beam has positive (negative) helicity. At leading order, the  $A_L$  of  $W^\pm$  can be directly associated to  $\Delta\bar{u}$  and  $\Delta\bar{d}$ , the helicity dependent PDFs of  $\bar{u}$  and  $\bar{d}$  quarks.

At STAR, one of the two main experiments at RHIC, the  $W$  production is measured via its leptonic decay based on the topological and kinematic features of  $W \rightarrow e\nu$  signal with the Time Projection Chamber, Barrel and Endcap Electromagnetic Calorimeters. The  $W \rightarrow e\nu$  event is characterized as an isolated high  $p_T$  track pointing to an isolated large energy deposited in the electromagnetic calorimeter. It is expected that there is a large  $p_T$  imbalance caused by the undetected neutrino. Based on these features, the  $W$  leptonic decay candidates whose  $E_T$  spectrum is expected to peak at  $\sim 40\text{GeV}$  (Jacobian peak) can be selected out from the large amount of QCD background.

The longitudinal single spin asymmetry as function of the lepton pseudorapidity is extracted from the spin-sorted and charge-separated  $W^\pm$  yields. From 2011 (9.4 pb<sup>-1</sup>) and 2012 (77.4 pb<sup>-1</sup>) data, STAR measured  $A_L^{W^\pm}$  as a function of the decay lepton pseudorapidity for the first time. While  $A_L^{W^+}$  is consistent with the theoretical predictions based on polarized PDFs mainly determined from DIS experiments,  $A_L^{W^-}$  for the negative lepton pseudorapidity is systematically larger than the theoretical predictions which indicates that these data provide new constraints for  $\Delta\bar{u}$  than previous data from semi-inclusive DIS experiments. The results have been included into global analysis, and the impact confirms the conclusion with a more positive  $\Delta\bar{u}$  in the range of  $0.05 < x < 0.2$ . The uncertainties for  $\Delta\bar{u}$  and  $\Delta\bar{d}$  are significantly reduced with the new constraints from STAR  $A_L^{W^\pm}$  data. The 2013 data sample is much larger than previous years. The measured  $A_L^{W^\pm}$  results from 2013 data are in general consistent with these of 2011 and 2012, and the statistical uncertainties is further reduced by 40%. The quantitative impact will be manifested after being included in global analysis. The  $A_L^{W^\pm}$  measurements at STAR provide unique constraints on the polarized PDFs of the light sea quarks.

**Keywords:**  $W$  boson, proton spin structure, spin asymmetry, RHIC-STAR.

# Contents

<b>Abstract</b>	<b>i</b>
<b>1 Introduction</b>	<b>1</b>
1.1 Proton Spin Structure . . . . .	1
1.1.1 DIS Experiments and Parton Distribution Functions . . . . .	2
1.1.2 Polarized Parton Distributions . . . . .	7
1.2 Probing Sea Quark Polarization via $W^\pm$ Production . . . . .	11
1.3 Thesis Organization . . . . .	16
<b>2 Experiment Setup</b>	<b>19</b>
2.1 The Relativistic Heavy Ion Collider . . . . .	19
2.1.1 Overview . . . . .	19
2.1.2 Polarized Proton Acceleration . . . . .	20
2.1.3 Polarimeter . . . . .	22
2.2 STAR – the Solenoidal Tracker at RHIC . . . . .	23
2.2.1 TPC – the Time Projection Chamber . . . . .	25
2.2.2 BEMC – the Barrel Electromagnetic Calorimeter . . . . .	27
2.2.3 EEMC – the Endcap Electromagnetic Calorimeter . . . . .	29
<b>3 Data Sample and MC Embedding</b>	<b>33</b>
3.1 Data Sample . . . . .	33
3.1.1 $W$ Stream . . . . .	33
3.1.2 Datasets of 2011, 2012, and 2013 . . . . .	34
3.1.3 Beam Polarization . . . . .	36
3.1.4 Spin Sorting at STAR . . . . .	36
3.2 Embedding MC Simulation . . . . .	39
3.2.1 MC Simulation Based on PYTHIA . . . . .	40
3.2.2 Embedding . . . . .	40

<b>4</b>	<b><i>W/Z</i> Boson Reconstruction</b>	<b>43</b>
4.1	<i>W</i> Selection . . . . .	43
4.1.1	Vertex Finding and Track Selection . . . . .	44
4.1.2	Isolation Cut . . . . .	46
4.1.3	Signed $p_T$ -balance Cut . . . . .	50
4.1.4	Jacobian Peak of <i>W</i> Events . . . . .	52
4.1.5	Charge Separation . . . . .	54
4.2	$Z \rightarrow e^+e^-$ Reconstruction . . . . .	57
4.3	Definition of $\eta$ -bins . . . . .	58
4.4	Background Study . . . . .	59
4.4.1	Electroweak Backgrounds . . . . .	60
4.4.2	Second Endcap Background for Barrel <i>W</i> . . . . .	61
4.4.3	Data-driven QCD Background for Barrel <i>W</i> . . . . .	64
4.4.4	Background Study for Endcap <i>W</i> . . . . .	69
4.4.5	Background Summary and Systematic Uncertainty . . . . .	69
<b>5</b>	<b>Single-Spin Asymmetry Extraction</b>	<b>77</b>
5.1	Formulas of Single-Spin Asymmetry . . . . .	77
5.2	Background correction . . . . .	79
5.3	Relative Luminosity . . . . .	80
5.4	Spin Sorted <i>W</i> Yields . . . . .	82
5.5	Profile Likelihood Method . . . . .	84
5.6	Results and Discussions . . . . .	85
5.6.1	$A_L^{W^\pm}$ Results from 2011 and 2012 Data . . . . .	85
5.6.2	$A_L^{W^\pm}$ Results from 2013 Data . . . . .	88
5.6.3	$A_L^{Z/\gamma^*}$ and $A_{LL}^{W^\pm}$ . . . . .	89
<b>6</b>	<b>Conclusions and Outlook</b>	<b>93</b>
	<b>Appendix A Profile Likelihood Method</b>	<b>97</b>
	<b>Appendix B Parameters in Jet Reconstruction</b>	<b>115</b>
	<b>Bibliography</b>	<b>117</b>
	<b>Acknowledgements</b>	<b>129</b>

**Publications and Talks**



# List of Figures

1.1	Development of “elementary” particle. . . . .	1
1.2	Quark Model: Ground-state baryons: $(8,2) + (10, 4)$ . . . . .	2
1.3	Schematic of the Deep Inelastic Scattering process: $e + p \rightarrow e + X$	3
1.4	The proton structure function $F_x(x, Q^2)$ measurements from various DIS experiments. . . . .	5
1.5	MSTW 2008 NLO PDFs at $Q^2 = 10$ and $Q^2 = 10^4$ GeV <sup>2</sup> , where the bands indicate the uncertainty of 68% confidence level. . . . .	6
1.6	Schematic of the polarized Deep Inelastic Scattering process: $\vec{e} + \vec{p} \rightarrow e + X$ . . . . .	7
1.7	Evolution of our knowledge about proton spin structure. . . . .	8
1.8	Polarized PDFs from DSSV08 global analysis. . . . .	10
1.9	STAR 2009 Jet $A_{LL}$ results and the latest DSSV fit results. . . . .	11
1.10	Feynman diagrams for $W^+$ boson production in $\vec{p}p$ collisions, where the subscript and superscript on the quark indicate the helicity of proton and quark respectively. Combine (a) and (b) to probe $\Delta u(x)$ , while combine (c) and (d) to probe $\Delta \bar{d}(x)$ . Same logic for $W^-$ production by swapping the flavor u and d. . . . .	12
1.11	Helicity conservation in $W$ production and decay, see text for detail description. . . . .	13
1.12	Average momentum fractions $x_{1,2}$ as functions of the charged leptons’ rapidity $\eta_l$ for $W^-$ (left) and $W^+$ (right) production at RHIC. . . . .	14
1.13	Theoretical predications for $W^\pm$ longitudinal single-spin asymmetry as function of decay lepton pseudo-rapidity based on PDFs sets DSSV08 and LSS10. . . . .	15
1.14	Longitudinal single-spin asymmetry measurement from RHIC run 2009 by STAR (left) and PHENIX (right) . . . . .	16
2.1	RHIC complex. . . . .	20

2.2	Schematic geometry layout of proton-Carbon polarimeter. . . . .	22
2.3	Schematic geometry layout of H-Jet polarimeter. . . . .	23
2.4	STAR detector overview. . . . .	24
2.5	STAR detector cut view with the subsystems. . . . .	25
2.6	Structure of STAR Time Projection Chamber . . . . .	26
2.7	The anode pad plane with one full sector. . . . .	27
2.8	Overview of STAR Barrel Electromagnetic Calorimeter. . . . .	28
2.9	Schematic view of one module of Barrel Electromagnetic Calorimeter. . . . .	29
2.10	Tower structure of Endcap Electromagnetic Calorimeter. The left side shows the half view of the tower grids, and the right side shows the cut view of the tower layer structure. . . . .	30
2.11	Layout of one 30° sector of the Shower Maximum Detector of EEMC. . . . .	31
3.1	2011: Beam Polarization for blue and yellow beams respectively, the line in each plots are the luminosity weighted average value. . . . .	37
3.2	2012: Beam Polarization for blue and yellow beams respectively, the line in each plots are the luminosity weighted average value. . . . .	38
3.3	2013: Beam Polarization for blue and yellow beams respectively, the line in each plots are the luminosity weighted average value. . . . .	38
3.4	Schematic diagram for spin patterns of RHIC beam around STAR interaction region. . . . .	39
3.5	ZDC coincidence rate and $z_{vertex}$ distributions for 2013 data and the corresponding embedding sample. . . . .	42
4.1	$W \rightarrow e\nu$ event versus QCD di-jet event. . . . .	43
4.2	(a) Rank of all vertices, pile-up vertices have negative rank, middle and right peaks for single and multi track vertex. (b) Vertex rank of the event passing all W selection cuts. . . . .	45
4.3	Barrel: (a) Number of hit on the track. (b) Ratio of number of hits for fitting and number of possible hits. (c) Radius from beam-line of the track's first hit. (d) Radius from beam-line of the track's last hit. . . . .	47
4.4	Endcap: (a) Number of hits on the track. (b) Ratio of number of hits for fitting and number of possible hits. (c) Radius from beam-line of the track's first hit. (d) Radius from beam-line of the track's last hit. . . . .	48

4.5	The upper row is for Barrel region and the lower row is for Endcap region. (a)(d) distance between track and cluster vs cluster $E_T$ for Data. (b)(e) distance between track and cluster vs cluster $E_T$ for MC $W \rightarrow e\nu$ . (c)(f) comparison of data and MC (blue). . . . .	49
4.6	Barrel: (a) Tower grids for $2 \times 2$ cluster isolation in $4 \times 4$ cluster, (b) Near Cone with Radius $\Delta R < 0.7$ , $\Delta R = \sqrt{\Delta\eta^2 + \Delta\phi^2}$ . . . . .	50
4.7	Barrel: (a) Distribution $E_T^{2 \times 2} / E_T^{4 \times 4}$ with comparison between data and MC (b) Distributions of $E_T^{2 \times 2} / E_T^{\Delta R < 0.7}$ . . . . .	50
4.8	Endcap: (a) Distribution $E_T^{2 \times 2} / E_T^{4 \times 4}$ with comparison between data and MC (b) Distributions of $E_T^{2 \times 2} / E_T^{\Delta R < 0.7}$ . . . . .	51
4.9	(a) Distribution of $R_{ESMD}$ , (b)(c) correlation between $R_{ESMD}$ and signed $p_T$ -balance for data(b) and MC(c). . . . .	51
4.10	Signed $p_T$ -balance vs $E_T^e$ for run13 data on the left and $W \rightarrow e\nu$ MC on the right. The red dash lines indicate the cut value. . . . .	52
4.11	Leading Order and Next-to-Leading Order cross section at RHIC for $l_+$ and $l_-$ decaying from $W^\pm$ bosons. . . . .	53
4.12	$E_T^e$ spectrum of candidate electrons from cluster construction to final selection, different color histograms indicate different selection stages, (a)(c) for Barrel region, (b)(d) for Endcap region, for 2011+2012 and 2013 respectively. . . . .	54
4.13	Charge separation based on TPC track bending . . . . .	55
4.14	Barrel: Ratio of $E_T$ and $p_T$ with reconstructed charge sign $Q$ as function of $E_T^e$ (a) and the projection of $25 < E_T < 50\text{GeV}$ range which is used to estimate the charge contamination via fitting . . . .	55
4.15	Endcap: (a) Ratio of $E_T$ and $p_T$ with reconstructed charge sign $Q$ as function of $E_T^e$ (b) projection on $Q * E_T / p_T$ axis of (a) in $E_T^e$ signal window, with fitting based on curve from (c) and (d). (c) $W^+$ and (d) $W^-$ embedding with Gaussian fitting. . . . .	56
4.16	$Z \rightarrow e^+e^-$ event . . . . .	57
4.17	Invariant mass distribution of $Z/\gamma^*$ with comparison between data and MC, for 2011+2012 and 2013 separately. . . . .	58
4.18	$\eta$ bin index definition in STAR detector and in physics referring to the polarized beam. . . . .	58

4.19	$Z/\gamma^* \rightarrow e^+e^-$ background contribution in $W \rightarrow e\nu$ raw signal $E_T$ spectrum for both $W^+$ and $W^-$ and both periods of 2013 (P1 and P2 in the sub-captions).	62
4.20	Estimate the second Endcap background for one $\eta$ range from its mirror $\eta$ -range, considering the forward-forward and forward-backward di-jet background events.	63
4.21	Second Endcap background contribution in $W \rightarrow e\nu$ raw signal $E_T$ spectrum for both charge signs and both periods of run13.	64
4.22	Data-driven QCD background: Red histograms are the raw signal spectrum with all other backgrounds subtracted, blue solid histograms are the QCD spectrum for data-driven, blue dash histograms are normalized the data-driven QCD background results. The black boxes indicate the normalization window. Run periods and charge signs are put on the plots.	66
4.23	Electron $E_T$ spectrum of Barrel $W^+$ and $W^-$ production with all background contributions in 2011+2012 data at STAR.	67
4.24	Electron $E_T$ spectrum of Barrel $W^+$ and $W^-$ production with all background contributions in 2013 data at STAR.	68
4.25	Signed $p_T$ -balance distribution of Endcap $W^\pm$ productions with all background contributions in 2011+2012 data at STAR.	70
4.26	Signed $p_T$ -balance distribution of Endcap $W^\pm$ productions with all background contributions in 2013 data at STAR.	71
4.27	Data-driven QCD: 729 different shapes from 9 normalization windows and 81 QCD samples. This example shows for Barrel $W^+$ candidates from run13 period I. The other parts are similar.	72
4.28	Barrel: $\beta$ distributions in systematic uncertainty study. In every rows, from left to right, they are for eta bin from 1 to 4. The blue line indicates the default $\beta$ value used in Section 4.4.3.	73
4.29	Endcap: $\beta$ distributions in systematic uncertainty analysis. The blue line indicates the $\beta$ value get in Section 4.4.3.	74
4.30	$\beta$ with uncertainties, both statistical and systematic, for all the eta bins. Eta bin = 8 is for the full Barrel.	75
5.1	Normalized relative luminosity for the four spin states, for 2011, 2012, 2013 period I and period II.	81

5.2	Longitudinal single-spin asymmetry $A_L$ for $W^\pm$ productions as a function of lepton pseudorapidity from STAR 2011+2012 data set in comparison to theory predictions . . . . .	85
5.3	NNPDFpol1.1 $x$ dependent $\Delta\bar{u}$ and $\Delta\bar{d}$ including the impact of STAR 2011+2012 $A_L^{W^\pm}$ results, and the absolute PDF uncertainty. . . . .	86
5.4	DSSV++: $\chi^2$ profiles for $\Delta\bar{u}$ (left) and $\Delta\bar{d}$ (right) with the impact of the preliminary 2012 STAR $A_L^{W^\pm}$ result and the projection $W$ data . . . . .	87
5.5	Longitudinal single-spin asymmetry $A_L$ for $W^\pm$ productions as a function of lepton pseudorapidity of STAR 2013 in comparison to 2011+2012 results and theory predictions. . . . .	89
5.6	Longitudinal single-spin asymmetry $A_L$ for $Z/\gamma^*$ productions as a function of Bjorken scaling, $x_1$ . . . . .	90
5.7	Longitudinal double spin asymmetry $A_{LL}$ for $W^\pm$ productions as a function of lepton pseudorapidity of STAR 2011+2012 in comparison to theory predictions. . . . .	91
5.8	Positivity bounds $A_{LL}^{W^\pm(y_W)} - \left  A_L^{W^\pm(y_W)} \pm A_L^{W^\pm(-y_W)} \right $ as a function of $W$ rapidity, from NNPDFpol1.1 and DSSV08 polarized PDFs. . . . .	92
5.9	Longitudinal double spin asymmetry $A_{LL}$ for $W^\pm$ productions as a function of lepton pseudorapidity of STAR 2013 in comparison to 2011+2012 results and theory predictions. . . . .	92
6.1	Regions in $x$ , $Q^2$ covered by previous spin experiments and anticipated to be accessible at an EIC. . . . .	95
A.1	Definition of confidence interval for the case w/o constrain on support (a) and with additional constrain (b). . . . .	104
A.2	Definition of beam direction and signs of the angles in the detector with respect to polarized beam needed to define dependence of polarized yields on SSA & DSA in eqs. A.25. . . . .	106
A.3	Illustration of applying the physics constrain, $L_{PHY}$ , on the support of the total likelihood for Eqn. A.16 . a) no constrains, b) after constrains are applied the support has been reduced. . . . .	108



# List of Tables

3.1	Number of runs and integral luminosities for final datasets of 2011 and 2012 used for $W$ candidates selection. . . . .	35
3.2	Number of runs and integral luminosities for final datasets of 2013 used for $W$ candidates selection. . . . .	35
3.3	Average of the beam polarization for 2011, 2012, and 2013 at RHIC. . . . .	36
3.4	STAR spin bits. . . . .	39
3.5	Numbers of MC events for each channel generated for 2011, 2012, 2013 respectively. The cross sections are from PYTHIA. . . . .	40
4.1	Track selection cuts for Barrel and Endcap regions. . . . .	46
4.2	$W^+$ boson primary decay modes. . . . .	60
4.3	$\tau^-$ semi-leptonic decay modes. . . . .	60
4.4	Some of $Z$ boson decay modes. . . . .	61
4.5	$\beta$ values for all the eta bins, both $W^+$ and $W^-$ , corresponding to the data points in Figure 4.30. . . . .	74
5.1	Normalized relative luminosities for the four spin states corresponding to Figure 5.1. . . . .	80
5.2	Asymmetries measured for high $p_T$ QCD background events (charge separated). . . . .	81
5.3	$W$ yields of STAR 2011 dataset. . . . .	82
5.4	$W$ yields of STAR 2012 dataset. . . . .	82
5.5	$W$ yields of STAR 2013 Period I dataset. . . . .	83
5.6	$W$ yields of STAR 2013 Period II dataset. . . . .	83
5.7	Spin sorted $Z/\gamma^*$ yields for STAR 2011, 2012, and 2013. . . . .	90

A.1	$A_1^W, A_2^W$ from RooStats and a comparison with the Gaussian method for 16-yields, input discussed in Sec. A.3.4. *Gaussian method: calculate $A^W$ for each detector eta bin of each year dataset and then average them with error weight defined by Gaussian error propagation.	110
A.2	$A_1^W, A_2^W$ from RooStats and comparison with the Gaussian method for 8-yields, input discussed in Sec. A.3.4. . . . .	111

# Chapter 1

## Introduction

### 1.1 Proton Spin Structure

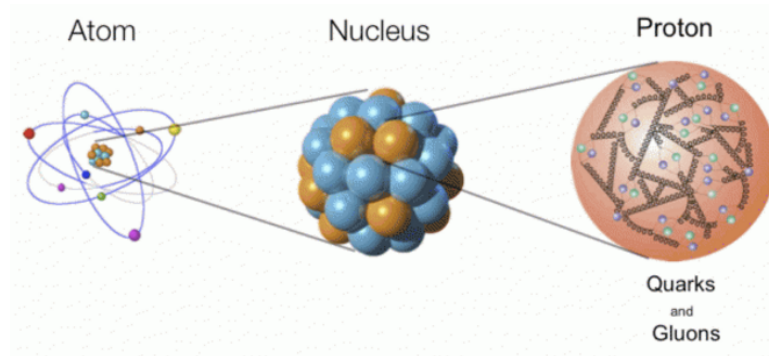


Figure 1.1: Development of “elementary” particle.

During the course of civilization, it has been one of the most ambitious curiosities to understand what the world is made of. The idea that the world is made of elementary particles was brought up by ancient philosophers as early as thousands years ago. For a very long time, atom had been thought to be the elementary and indivisible unit to build the world. As the first evidence in modern science, John Dalton found the law of multiple proportions which could be explained by the atomic theory. In the cathode ray experiment, J. J. Thomson found out the cathode ray is made of particles which have the mass much lighter than the atom mass. This was the first time people saw the subatomic structure. In 1909, the famous Rutherford scattering experiment was directed by one of Thomson’s students, Ernest Rutherford. By scattering the alpha particles ( $\alpha$ ) at layers of gold foil, the results indicated that the atom is composed by the nucleus with very small size and the electrons surrounding it. Subsequently, a series of important discoveries were made. It was found that the nucleus is composed of protons and neutrons.

From 1950s, the high energy accelerators were constructed and opened a new era of particle physics. From the experiments based on accelerators, various particles were produced and measured in 1950s and 1960s. It was recognized that proton and neutron were still not the elementary particle but only parts of hadrons. In 1964, the constituent quark model was independently proposed by Gell-Mann [1] and Zweig [2], where the smaller particle “quark” was introduced as the component of hadron based on the flavor-SU(3) symmetry. The naive quark model successfully categorized hadrons and well estimated their mass and magnetic moment. According to the quark model, proton was thought to be the bound state of  $uud$  quarks as shown in Figure 1.2.

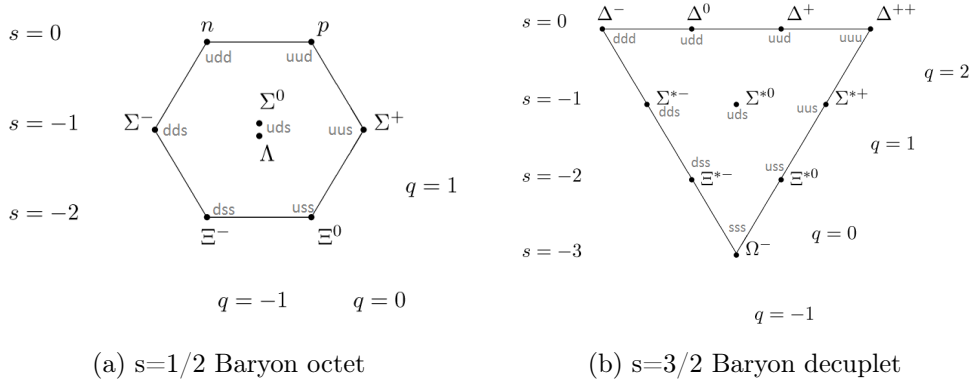


Figure 1.2: Quark Model: Ground-state baryons:  $(8,2) + (10, 4)$  [3].

### 1.1.1 DIS Experiments and Parton Distribution Functions

Experimentally, the internal structure of proton can be detected via Deep Inelastic Scattering (DIS) processes by scattering high energy leptons (e.g. electron, muon) on hadrons (e.g. proton, neutron) as an extension of Rutherford experiment to high energy. Detailed discussions of the DIS can be found in many particle physics text books e.g. Ref. [4]. A thorough review can be found in Ref. [5], [6], and [7]. As shown in Figure 1.3, electron scatters with proton via virtual photon with momentum transfer  $Q^2$  ( $= -q^2$ ). The cross section can be written as

$$\frac{d^2\sigma}{dE'd\Omega}|_{lab} = \frac{4\alpha^2 E'^2}{Q^4} \left[ W_2(\nu, Q^2) \cos^2 \frac{\theta}{2} + 2W_1(\nu, Q^2) \sin^2 \frac{\theta}{2} \right], \quad (1.1)$$

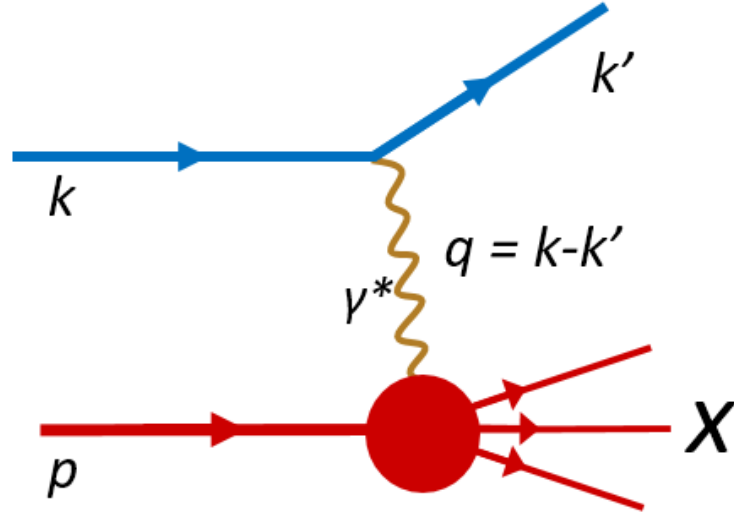


Figure 1.3: Schematic of the Deep Inelastic Scattering process:  $e + p \rightarrow e + X$

where  $\Omega$  is a phase space term,  $\alpha$  is the fine structure constant,  $E(E')$  is the energy of the incident (scattered) lepton,  $\theta$  is the lepton scattering angle,  $\nu \equiv E - E'$  is the energy loss of the scattered lepton, and  $W_{1,2}(\nu, Q^2)$  are the proton inelastic structure functions which depend on both  $\nu$  and  $Q^2$ . Proposed by Bjorken [8], the inelastic structure functions only depend on one variable,  $x \equiv Q^2/2M\nu$ , which is referred as Bjorken- $x$ , at the limitation of  $Q^2 \rightarrow \infty$  and  $\nu \rightarrow \infty$ . This is known as Bjorken scaling. Thus, the structure functions can be written as

$$F_1(x) = MW_1(\nu, Q^2), \quad (1.2)$$

$$F_2(x) = \nu W_2(\nu, Q^2). \quad (1.3)$$

This behavior was experimentally confirmed in DIS measurements [9][10], indicating the point-like constituents inside the proton.

In the quark-parton model [11][12][13], it is proposed that the proton is composed of three kinds of partons, including three valence quarks which carry a large fraction of proton's momentum, a collection of quark-antiquark pairs (called "sea" quarks), and gluon which carries the neutral force between quarks. The model represents the DIS cross section as the incoherent sum of elastic lepton scattering with

the effectively free partons. The inelastic structure functions can be expressed as

$$F_1(x) = \frac{1}{2} \sum_i e_i^2 f_i(x), \quad (1.4)$$

$$F_2(x) = x \sum_i e_i^2 f_i(x), \quad (1.5)$$

where  $e_i$  is the electric charge of parton with flavor  $i$ ,  $f_i(x)$  is introduced as the parton distribution function (PDF) which represents the probabilities of finding a parton of flavor  $i$  carrying a fraction  $x$  of the proton's momentum. There is relation  $F_2(x) = 2xF_1(x)$  which is referred to as Gallan-Gross relation [14] holding for the spin-1/2 of the partons. Based on quark-parton model, the QCD is developed as the theory which describes the Strong Force mediating the interaction between quarks and gluons.

The structure functions have been measured by many experiments, e.g. as shown in Figure 1.4. The PDFs cannot be calculated only in theoretical way [15], but need to be extracted from experimental data accumulated by DIS experiments together with the collider experiments which is known as global analysis. Several groups, e.g. CTEQ [16], MSTW [17], and NNPDF [18], have reported their results of global analysis. Figure 1.5 shows the next-to-leading order (NLO) PDFs results from MSTW 2008 at  $Q^2 = 10$  and  $10^4$  GeV<sup>2</sup>.

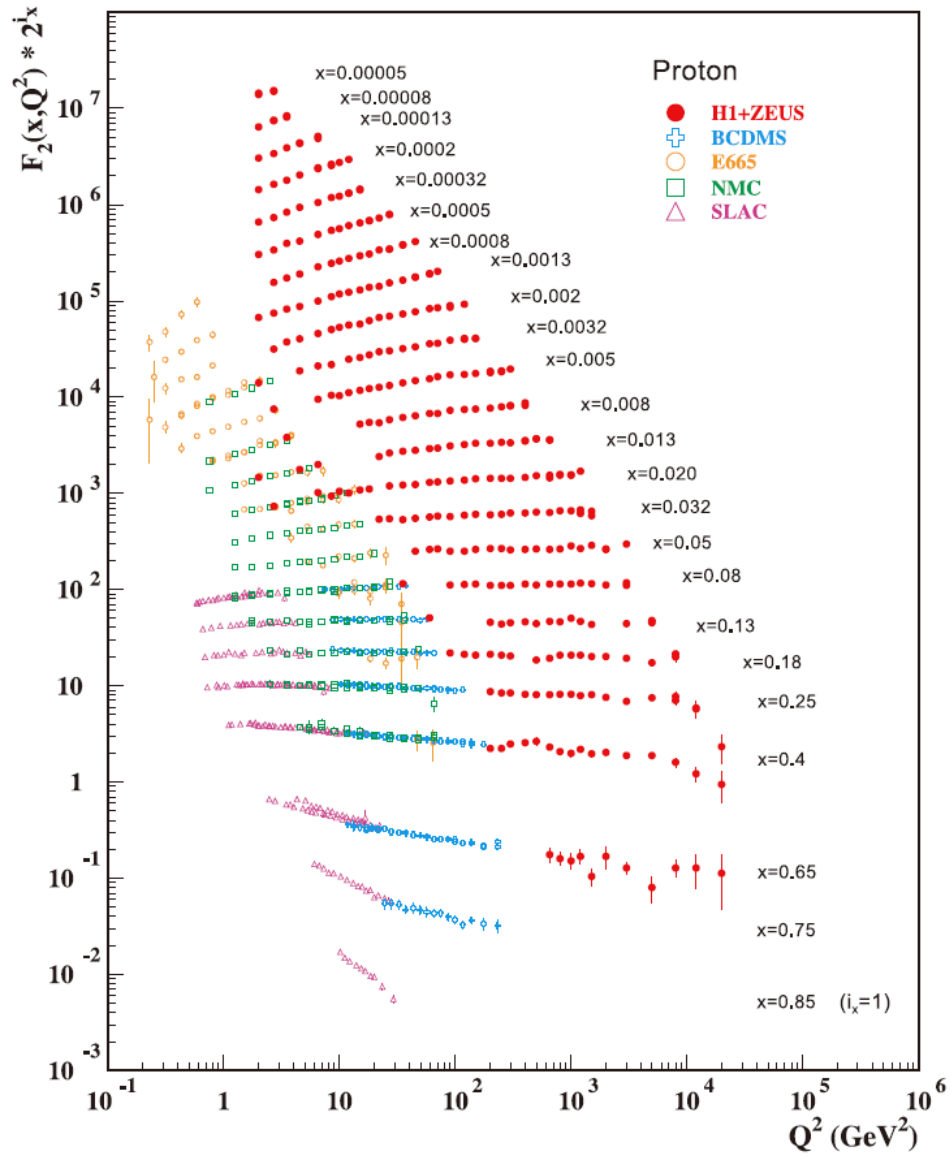


Figure 1.4: The proton structure function  $F_2(x, Q^2)$  measurements from various DIS experiments [3].

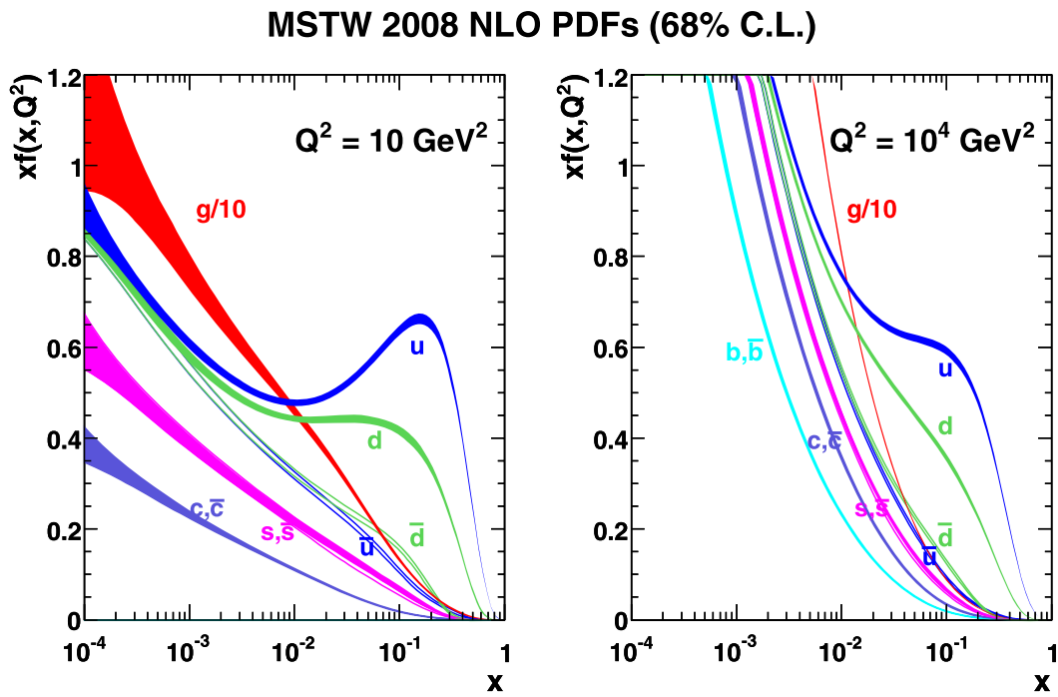


Figure 1.5: MSTW 2008 NLO PDFs at  $Q^2 = 10$  and  $Q^2 = 10^4 \text{ GeV}^2$ , where the bands indicate the uncertainty of 68% confidence level [3].

### 1.1.2 Polarized Parton Distributions

Spin, an intrinsic form of angular momentum in Quantum Mechanism, is a fancy dimension of modern physics. The spin structure of proton is definitely attractive for physicists in both theoretical and experimental areas. Similar with the unpolarized case, the polarized DIS experiments have also provided plentiful discoveries. Reviews of polarized DIS experiments can be found in Refs. [19], [20].

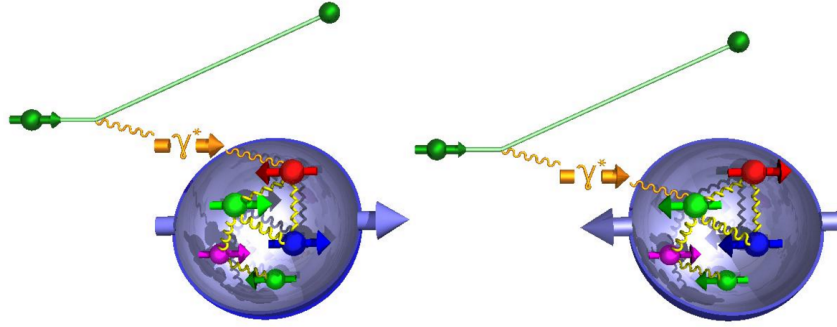


Figure 1.6: Schematic of the polarized Deep Inelastic Scattering process:  $\vec{e} + \vec{p} \rightarrow e + X$

For polarized DIS experiments (see Figure 1.6), polarized lepton scattering on polarized proton, the spin dependent cross section can be discriminated by  $\uparrow\uparrow$  and  $\uparrow\downarrow$ , where the single arrow denotes the lepton beam polarization and the double arrow denotes the proton polarization. The cross section difference between cases that lepton spin and proton spin are parallel and anti-parallel can be written as

$$\frac{d^2\sigma^{\uparrow\uparrow}}{d\Omega dE'} - \frac{d^2\sigma^{\uparrow\downarrow}}{d\Omega dE'} = \frac{4\alpha^2 E'}{Q^2 E} [(E + E' \cos\theta)mG_1(\nu, Q^2) - Q^2 G_2(\nu, Q^2)]. \quad (1.6)$$

Similar to the unpolarized structure functions  $W_{1,2}(\nu, Q^2)$  to  $F_{1,2}(x)$ , the polarized structure functions  $G_{1,2}(\nu, Q^2)$  can be deduced to  $g_{1,2}(x)$  at the Bjorken limitation where  $g_1(x)$  can be expressed in term of the polarized PDFs,

$$g_1(x) = \frac{1}{2} \sum_i e_i^2 [\Delta f_i(x) + \Delta \bar{f}_i(x)]. \quad (1.7)$$

The polarized PDFs are defined as

$$\Delta f(x) \equiv q^+(x) - q^-(x), \quad (1.8)$$

where  $q^{+(-)}$  represents the parton density for parton with spin parallel (anti-parallel) to the proton spin.

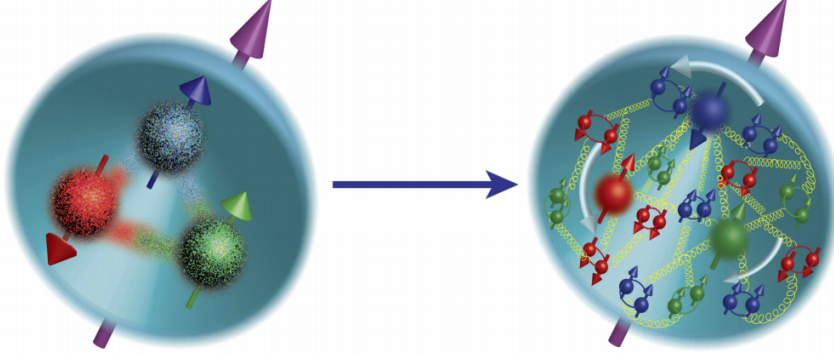


Figure 1.7: Evolution of our knowledge about proton spin structure.

The results measured from the polarized DIS experiments initiated by European Muon Collaboration (EMC) gave us a big surprise that the total contributions from quarks and antiquarks spin are very small [21][22]. This is referred to as “proton spin crisis”. In 1990, Jaffe and Monahar [23] proposed that the proton spin can be decomposed into four parts as,

$$\langle S_p \rangle = \frac{1}{2} = \frac{1}{2} \Delta \Sigma + L_q + \Delta G + L_g, \quad (1.9)$$

where  $L_q$  and  $L_g$  donate orbital angular momentum of quarks and gluons respectively and

$$\Delta \Sigma = \int dx (\Delta u(x) + \Delta \bar{u}(x) + \Delta d(x) + \Delta \bar{d}(x) + \Delta s(x) + \Delta \bar{s}(x)), \quad (1.10)$$

$$\Delta G = \int dx \Delta g(x), \quad (1.11)$$

where  $\Delta \Sigma$  is the total contribution from quark and antiquark spin,  $\Delta G$  is the gluon polarization.

In the past couple of decades, a lot of data have been accumulated.  $\Delta \Sigma$  has been well constrained by the inclusive polarized DIS data to be  $\sim 25\%$ . In addition, the semi-inclusive DIS experiments have been developed to decompose the flavor of the quark spin [24], which detect not only the scattered leptons but also one (or more) hadron(s) additionally. The relevant spin-dependent structure function can

be written as

$$g_1^h(x, Q^2, z) = \frac{1}{2} \sum_i e_i^2 \left[ \Delta f_i(x) D_f^h(z, Q^2) + \Delta \bar{f}_i(x) D_{\bar{f}}^h(z, Q^2) \right], \quad (1.12)$$

where  $D_{f,\bar{f}}^h(z, Q^2)$  represent the fragmentation functions which are used to characterize the processes from the scattered partons to the hadronic final states and  $z$  is the momentum fraction that is transferred from the outgoing parton to the observed hadron. The non-perturbative fragmentation functions are determined primarily from precision data on hadron production in  $e^+e^-$  annihilation through perturbative QCD analysis [25] [26]. As expressed in Equation (1.12), the flavor separated contributions of quark and antiquark polarization can be accessed from the weights determined by the fragmentation functions.

Similar to the unpolarized case, the polarized PDFs can be determined via global analysis. The idea is to extract the universal polarized PDFs entering factorized cross sections by optimizing the agreement between the measured asymmetries from spin experiments (polarized DIS, SIDIS, and  $pp$  scattering) and the theoretical calculations. Several groups performed their global analysis, such as DSSV [28][29], LSS [30], NNPDF [31][32]. For instance, Figure 1.8 shows the results from DSSV08 global analysis based on data from the polarized DIS, semi-inclusive DIS experiments and some preliminary results from RHIC. The uncertainties for each polarized PDFs is estimated using an approach of Lagrange multipliers to investigate how  $\chi^2$  varies around the minimum as a function of the variable of interest. In Figure 1.8, it is noted that the total contribution of  $up$  and  $down$  quarks spin has been well constrained. However, the flavor separated contributions of the sea quarks, e.g.  $\Delta \bar{u}(x)$ ,  $\Delta \bar{d}(x)$ , still have quite large uncertainties due to the dependence on the fragmentation functions with limited precision in the semi-inclusive DIS experiments. The gluon polarization,  $\Delta g(x)$ , also shows large uncertainty band, and the contribution is quite small which is based on the early  $\pi^0$  and jet data from RHIC.

RHIC, as the first polarized proton-proton collider (see Section 2.1), provides complementary and powerful ways to advance our understanding of the spin and flavor structure of the proton. Using the longitudinally polarized proton beams, one can probe the helicity preferences of gluons and flavor separated quarks and antiquarks. RHIC has completed very successful polarized  $pp$  runs both at  $\sqrt{s} = 200$  GeV and 500(510) GeV. The recent RHIC results on the inclusive jet double

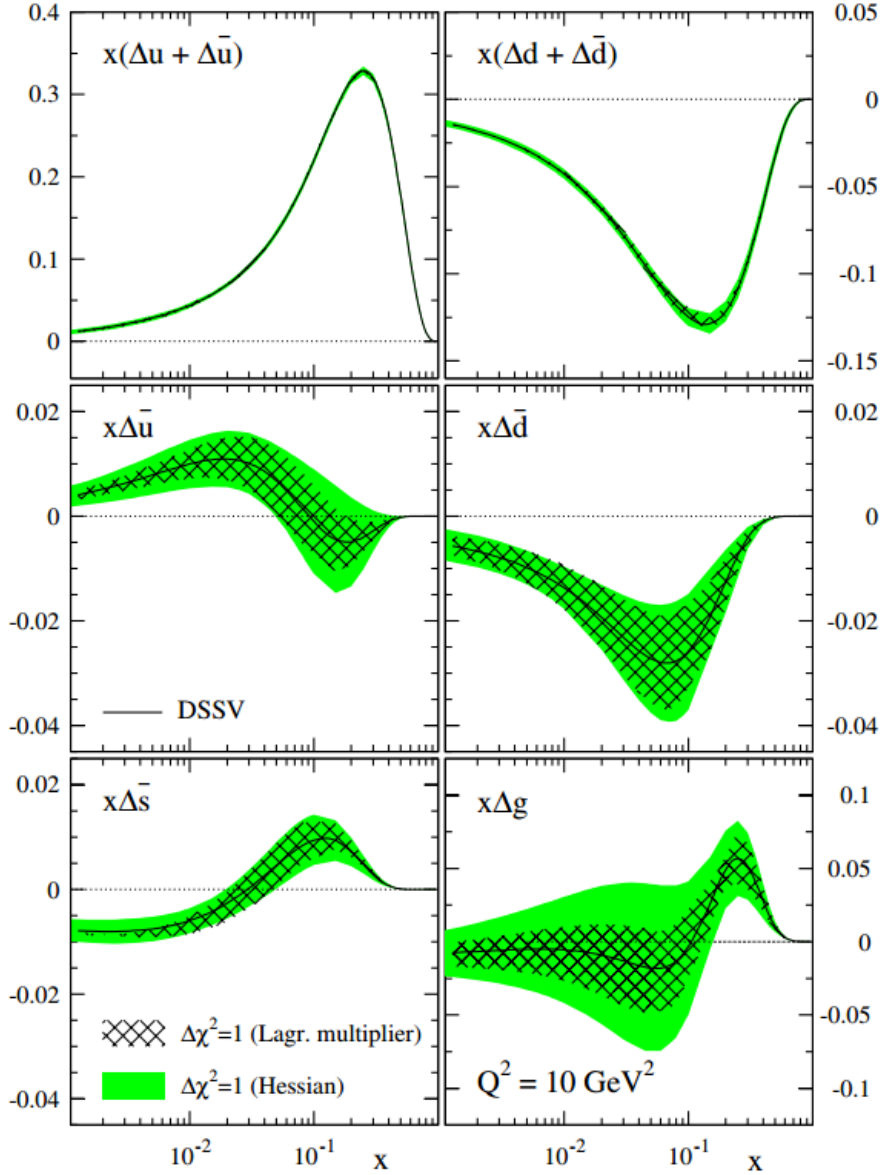
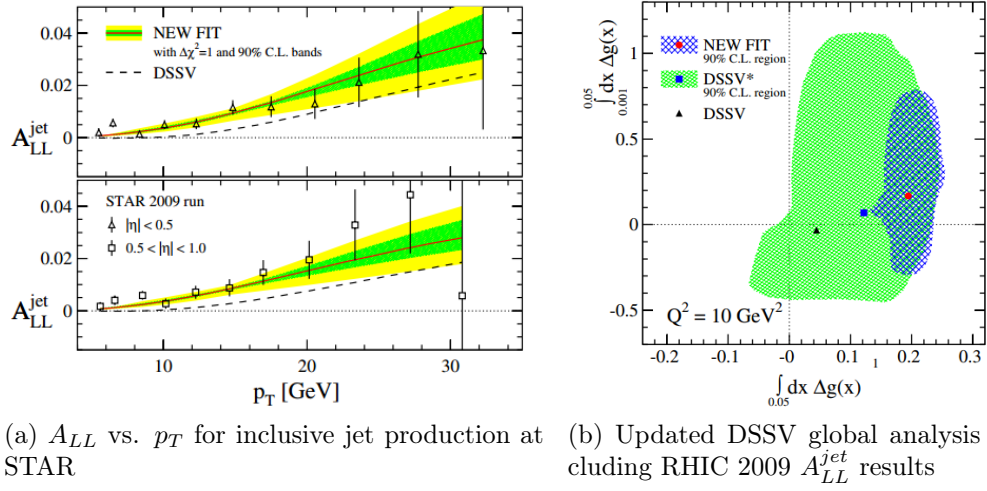


Figure 1.8: Polarized PDFs from DSSV08 global analysis [27].

spin asymmetry (shown in left-hand side of Figure 1.9) have provided the first evidence of a non-zero gluon polarization [33]. With RHIC results, the global fit for  $\Delta g(x)$  has been updated which is shown in the right-hand side plot of Figure 1.9. The contribution of gluon polarization shows significant positive value with comparable magnitude to the quark contribution in the Bjorken- $x$  range  $x > 0.05$ . The  $W$  bosons production in polarized proton-proton collisions can access the flavor decomposition of valance and sea quark spin contributions to proton spin at high scale ( $Q^2 \sim M_W^2$ ), without the need of fragmentation functions as in semi-inclusive



(a)  $A_{LL}$  vs.  $p_T$  for inclusive jet production at STAR (b) Updated DSSV global analysis including RHIC 2009  $A_{LL}^{jet}$  results

Figure 1.9: STAR 2009 Jet  $A_{LL}$  results and the latest DSSV fit results [29].

DIS. Taking the advantage of the  $V - A$  feature of weak interactions, the  $W$  boson only couples to left-handed particles and right-handed anti-particles. The helicity information of interaction quarks and antiquarks are naturally known combining with the charge of  $W$  bosons. This makes  $W$  production an unique probe to the sea quark polarization.

## 1.2 Probing Sea Quark Polarization via $W^\pm$ Production

As mentioned, the production of  $W^\pm$  boson in polarized proton-proton collisions at RHIC is a powerful and unique tool to study the spin-flavor structure of the proton. In  $pp$  collision, the  $W$  boson is produced via scattering of a quark and an antiquark from the two scattering protons respectively. Neglecting the contribution from the quark flavor mixing,  $W^+$  is mainly produced via  $\bar{d} + u \rightarrow W^+$  and  $W^-$  is mainly produced via  $\bar{u} + d \rightarrow W^-$ .

$W$  boson only couples to left-handed quarks and right-handed antiquarks due to the  $V - A$  structure of the weak interaction. In Figure 1.10 [34], let us take Feynman diagrams of the  $W^+$  production for example to illustrate how the  $W$  production probes the quark and antiquark polarization. The observable  $A_L$ , the

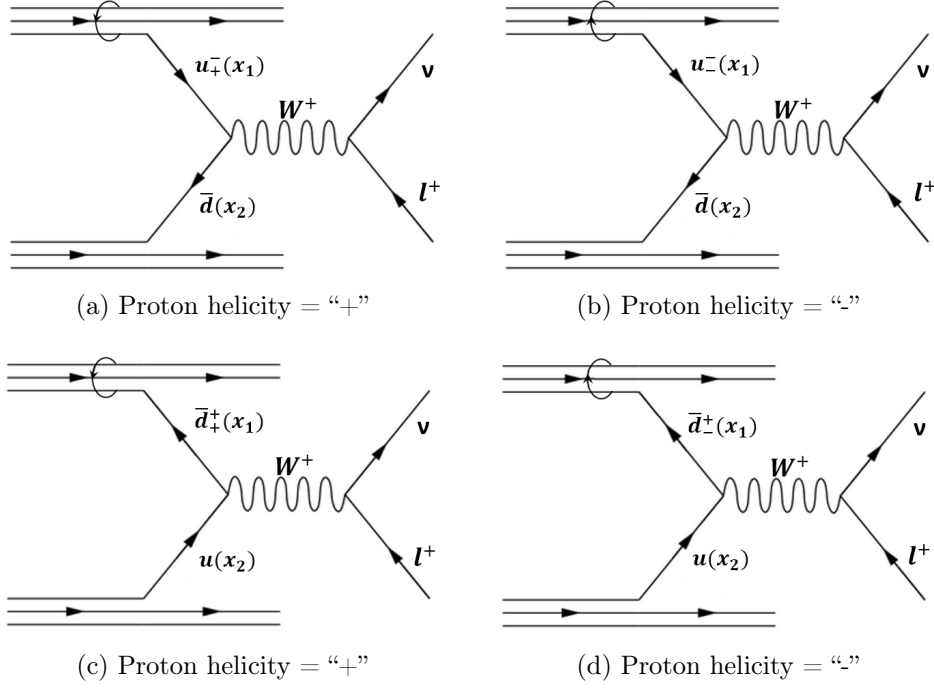


Figure 1.10: Feynman diagrams for  $W^+$  boson production in  $\vec{p}p$  collisions, where the subscript and superscript on the quark indicate the helicity of proton and quark respectively. Combine (a) and (b) to probe  $\Delta u(x)$ , while combine (c) and (d) to probe  $\Delta \bar{d}(x)$ . Same logic for  $W^-$  production by swapping the flavor  $u$  and  $d$  [34].

longitudinal single-spin asymmetry, is defined as

$$A_L = \frac{\sigma^+ - \sigma^-}{\sigma^+ + \sigma^-}, \quad (1.13)$$

where  $\sigma^+$  ( $\sigma^-$ ) is the cross section of the  $W$  production in  $pp$  collisions with one proton beam helicity positive (negative). In Figure 1.10a and 1.10b,  $W^+$  is produced from the  $u$  quark provided by the polarized beam and the  $\bar{d}$  quark provided by the unpolarized beam.  $A_L^{W^+}$  can be extracted from the asymmetry of 1.10a and 1.10b as,

$$A_L^{W^+} = \frac{u_+^-(x_1)\bar{d}(x_2) - u_-^-(x_1)\bar{d}(x_2)}{u_+^-(x_1)\bar{d}(x_2) + u_-^-(x_1)\bar{d}(x_2)} = -\frac{\Delta u(x_1)}{u(x_1)}, \quad (1.14)$$

where  $\Delta u(x_1)$  is the polarized PDF of  $u$  quark as defined in Equation(1.8). For another case when the polarized beam provides the  $\bar{d}$  quark and the unpolarized one provides the  $u$  quark as shown in Figure 1.10c and 1.10d. Similarly,  $A_L^{W^+}$  can

be written as

$$A_L^{W^+} = \frac{\bar{d}_+^+(x_1)u(x_2) - \bar{d}_+^-(x_1)u(x_2)}{\bar{d}_+^+(x_1)u(x_2) + \bar{d}_+^-(x_1)u(x_2)} = \frac{\Delta\bar{d}(x_1)}{\bar{d}(x_1)}. \quad (1.15)$$

In practice, the  $A_L^{W^+}$  should be the superposition of these two cases

$$A_L^{W^+} = \frac{-\Delta u(x_1)\bar{d}(x_2) + \Delta\bar{d}(x_1)u(x_2)}{u(x_1)\bar{d}(x_2) + \bar{d}(x_1)u(x_2)}. \quad (1.16)$$

The  $W^-$  production is very similar by just exchanging flavor  $u$  and  $d$ . Thus, it is easy to get the  $A_L^{W^-}$  expression from Equation(1.16) as,

$$A_L^{W^-} = \frac{-\Delta d(x_1)\bar{u}(x_2) + \Delta\bar{u}(x_1)d(x_2)}{d(x_1)\bar{u}(x_2) + \bar{u}(x_1)d(x_2)}. \quad (1.17)$$

With respect to the polarized beam, the forward  $W^+$ s ( $y_{W^+} \gg 0$ ) are expected predominantly from the  $u$  quark provided by the polarized protons and  $\bar{d}$  quark provided by the unpolarized protons. In this case,  $A_L^{W^+}$  becomes  $-\Delta u(x)/u(x)$  in the limitation of  $y_{W^+} \gg 0$ . Similarly for backward  $W^+$ s,  $A_L^{W^+}$  reduces to  $\Delta\bar{d}(x)/\bar{d}(x)$  at limitation of  $y_{W^+} \ll 0$ . It is just analogous for  $W^-$ .  $A_L^{W^-}$  would become  $-\Delta d(x)/d(x)$  and  $\Delta\bar{u}(x)/\bar{u}(x)$  in the cases  $y_{W^-} \gg 0$  and  $y_{W^-} \ll 0$  respectively.

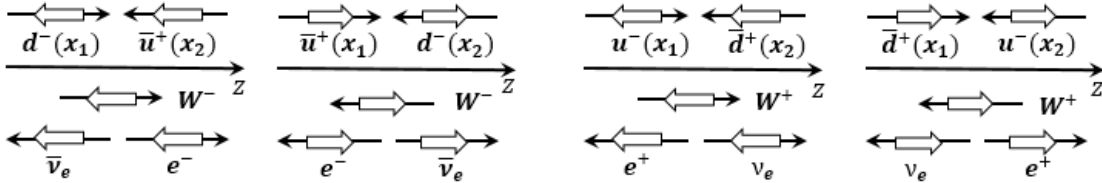


Figure 1.11: Helicity conservation in  $W$  production and decay, see text for detail description.

For experimental detection of  $W$  production at RHIC, only the leptonic decay is considered because the hadronic decay is indistinguishably contaminated by the QCD events. With the non-hermetic detector, the charged leptons are the only final state which can be detected. It is required to relate the lepton rapidity to the  $W$  rapidity. As mentioned above,  $W$  boson only couples to left-handed quarks and right-handed antiquarks. Thus the polarization of the incident quark and antiquark are in the same direction. Then the polarization direction of the produced  $W$  boson is perfectly determined to be same with the antiquark momentum direction. For

the decay, the neutrino (anti-neutrino) from  $W^+$  ( $W^-$ ) must be left-handed (right-handed). So, the charged lepton prefers to be emitted to the antiquark incoming direction for  $W^+$  and to the quark incoming direction for  $W^-$ . In  $pp$  collision, the produced  $W$  bosons tend to be emitted in the direction of the incoming valance quark. Thus the direction of lepton from  $W^+$  decay tends to be opposite to the boost of  $W^+$ , and the direction of lepton from  $W^-$  decay tends to be along with the boost of  $W^-$ . The helicity configurations of the production decay processes are illustrated in Figure 1.11.

Figure 1.12 shows the average parton momentum fractions  $x_{1,2}$  as functions of the charged leptons' pseudorapidity  $\eta_l$  for  $W^-$  (left) and  $W^+$  (right) production at RHIC [35]. There one can find strong correlation between the average  $x_{1,2}$  and  $\eta_l$  for both cases, consistent with above discussion. The relation can be approximately parameterized by simple formula:

$$\langle x_1 \rangle \sim \frac{M_W}{\sqrt{s}} e^{y_l/2}, \quad \langle x_2 \rangle \sim \frac{M_W}{\sqrt{s}} e^{-y_l/2}. \quad (1.18)$$

Considering that pseudorapidity coverage at RHIC (see Chapter 2),  $|\eta| < \sim 2$ , one can expect sensitivity to the polarized quark and antiquark distributions in the region  $0.05 \lesssim x \lesssim 0.4$ .

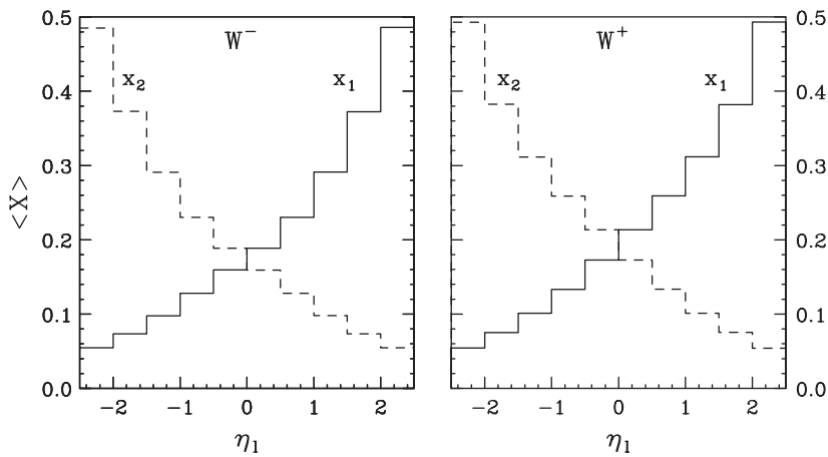


Figure 1.12: Averages of the momentum fractions  $x_{1,2}$  as functions of the charged leptons' rapidity  $\eta_l$  for  $W^-$  (left) and  $W^+$  (right) production at RHIC [35].

The theoretical frame work has been developed to describe the inclusive leptonic decay of  $W$  production at RHIC, where the expected  $A_L$  values are given as a function of the lepton pseudorapidity. The measurements of  $A_L$  versus the lepton

pseudorapidity can be directly compared with theoretical predictions [36]. Figure 1.13 shows several theoretical predications which are from a fully resummation calculation framework known as RHICBOS [37] and a next-to-leading order calculation known as CHE [35]. The unpolarized and polarized cross sections can be computed for a given set of input helicity-dependent PDFs. The input PDFs used in Figure 1.13 are DSSV08 [28] and LSS10 [30]. The  $\Delta\chi^2/\chi^2 = 2\%$  uncertainty band, provided by M. Stratmann of the DSSV group, is determined using a Lagrange multiplier method to map out the  $\chi^2$  profile of the global fit [28].

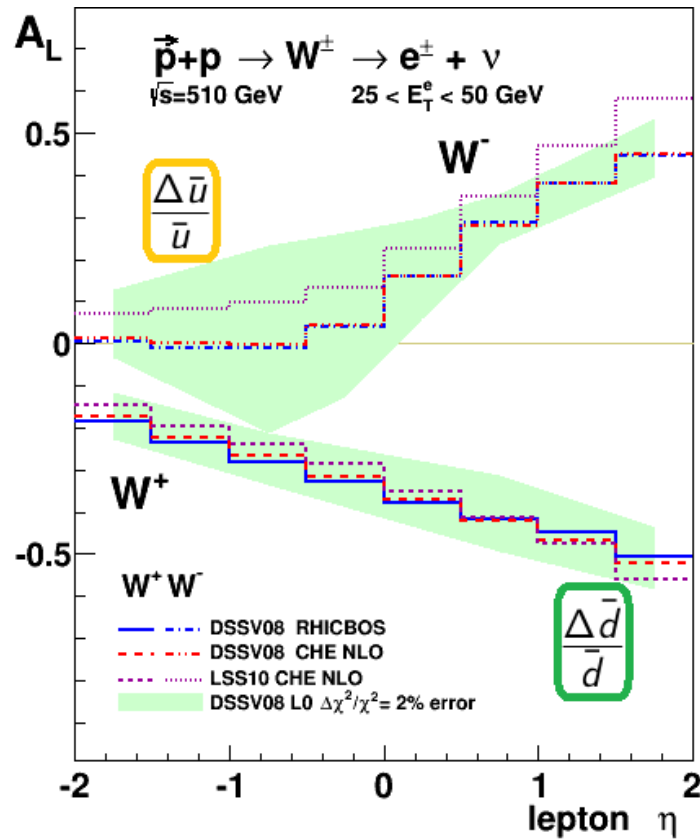


Figure 1.13: Theoretical predications for  $W^\pm$  longitudinal single-spin asymmetry as function of decay lepton pseudo-rapidity based on PDFs sets DSSV08 [28] and LSS10 [30].

From relations shown in Figure 1.11 and the  $A_L^{W^\pm}$  expressions (Equation(1.16) and (1.17)), it is easy to find that,

- for  $A_L^{W^-}$ , negative  $\eta_l$  region provides sensitivity to  $\Delta\bar{u}/\bar{u}$ ,
- for  $A_L^{W^+}$ , positive  $\eta_l$  region provides sensitivity to  $\Delta d/d$ ,

- for  $A_L^{W^+}$ , negative  $\eta_l$  region provides sensitivity to  $\Delta u/u$ ,
- for  $A_L^{W^+}$ , positive  $\eta_l$  region provides sensitivity to  $\Delta \bar{d}/\bar{d}$ .

This is also reflected in the theoretical predictions. The large uncertainty appears in the lepton  $\eta$  regions sensitive to the antiquark helicity which is poorly constrained. As highlighted in Figure 1.13, probing the polarizations of  $\bar{u}$  and  $\bar{d}$  is the main motivation of  $W$  longitudinal single-spin asymmetry measurement at RHIC.

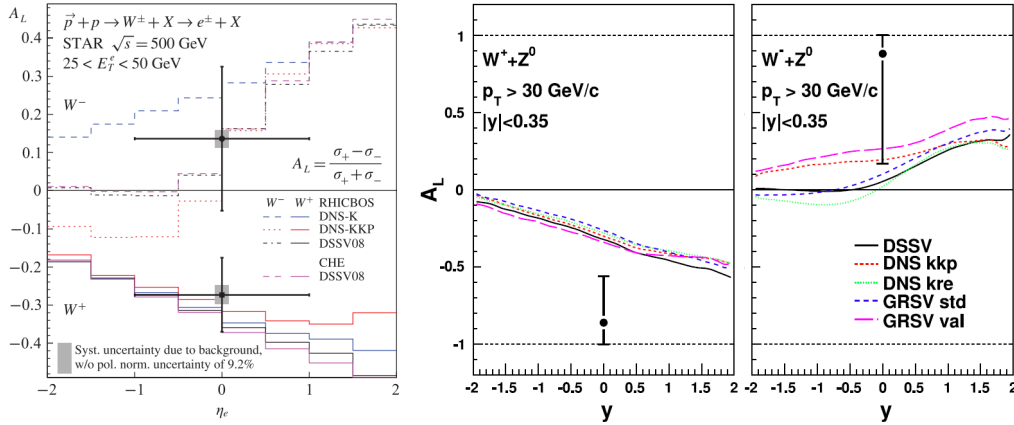


Figure 1.14: Longitudinal single-spin asymmetry measurement from RHIC run 2009 by STAR [38] (left) and PHENIX [39] (right).

In 2009, the first 500 GeV longitudinally polarized proton-proton run at RHIC, both STAR [38] and PHENIX [39] successfully performed the first measurement of longitudinal single-spin asymmetry of  $W^\pm$  boson production. Figure 1.14 shows the results of STAR (left) and PHENIX (right). Although only one data point for  $W^+$  and  $W^-$  respectively limited by the statistics, the measurements established a new and direct way to explore the spin structure of the proton using the parity-violating weak interactions in polarized  $pp$  collisions. With the much larger statistics, the measurements reported in this thesis will provide new insight into the proton spin structure.

### 1.3 Thesis Organization

In the previous sections of this chapter, a brief introduction to the nucleon spin structure is given. Taking the advantage of the weak interaction in polarized hadron-hadron collisions the  $W$  program at RHIC provides unique tool to probe

---

the flavor separated spin structure of light quarks. This thesis focuses on the most important parts of RHIC  $W$  program, the measurement of the helicity distribution of  $\bar{u}$  and  $\bar{d}$  quarks via the longitudinal single-spin asymmetry,  $A_L$ . The measurements are based on data collected in 2011, 2012, and 2013  $\sqrt{s} = 500(510)$  GeV longitudinally polarized  $pp$  runs by STAR detector. The organization of this thesis is as follows. Chapter 2 briefly introduces the experiment setup of the RHIC accelerator and the STAR detector, with some detailed descriptions of the sub-systems relevant to  $W$  analysis. The description of the data sample and the MC simulation sample is provided in Chapter 3. In Chapter 4, the analysis procedure including the  $W$  reconstruction and background study are discussed. Chapter 5 gives the measured  $A_L$  results with comparison between different datasets and between data and theoretical predications. Constraints on the polarized PDFs of  $\bar{u}$  and  $\bar{d}$  from the published 2011 and 2012 results are also shown in Chapter 5. Chapter 6 provides a conclusion of this analysis.



# Chapter 2

## Experiment Setup

The data used for this analysis are taken by STAR, the Solenoidal Tracker at RHIC, which is one of the two main ongoing experiments at RHIC. In this chapter, a general introduction to RHIC and STAR is provided, and subsystems related with this analysis will be described in detail.

### 2.1 The Relativistic Heavy Ion Collider

#### 2.1.1 Overview

The Relativistic Heavy Ion Collider (RHIC) is the only polarized proton-proton collider so far, as the one of the heavy ion colliders in the world [40]. Located at Brookhaven National Laboratory, in Long Island, New York, in United States, RHIC was designed to collide heavy ions with relativistic speed to investigate the quark matter thought exist in the very beginning of the universe after the Big Bang, and also collide the polarized protons to study the spin structure of the proton.

RHIC consists of two 3.8 km quasi-circular accelerator/storage rings on a common horizontal plane, one (Blue Ring) for clockwise and the other (Yellow Ring) for counter-clockwise beams. It can accelerate and store various beams in bunches, including polarized proton with collision energy  $\sqrt{s}$  up to 510 GeV, and different heavy ions with wide collision energy from few GeV to 200 GeV. As shown in Figure 2.1, the RHIC complex is composed of a long “chain” of particle accelerators [41], the linear accelerator (LINAC), the Booster Synchrotron, the Alternating Gradient Synchrotron (AGS), the AGS to RHIC (AtR) transfer line, and two RHIC rings. There are four interaction region located at 2, 6, 8, and 10 O’clock respectively. Among them, only the two main experiments, STAR at 6 O’clock and PHENIX at 8 O’clock, are now running.

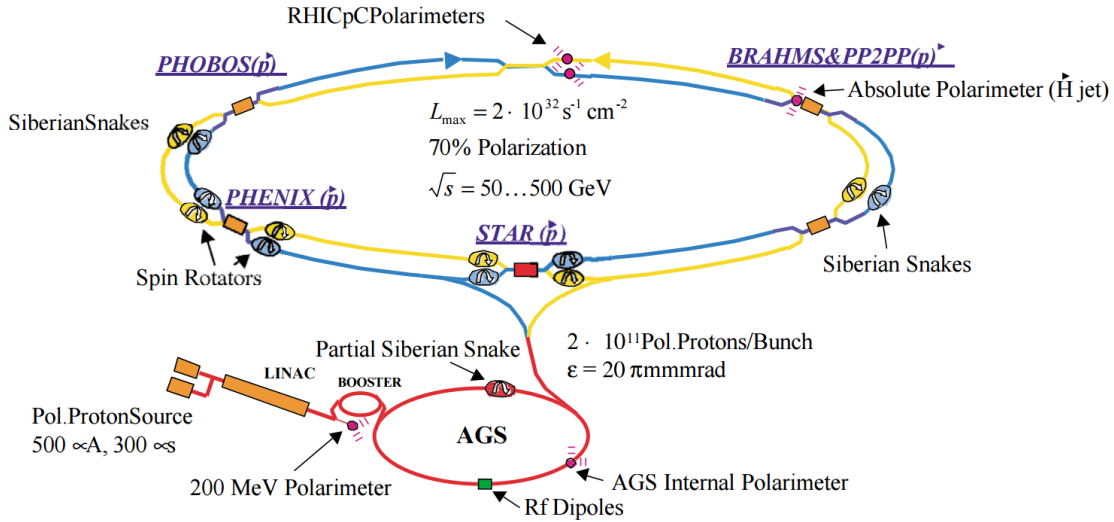


Figure 2.1: RHIC complex.

## 2.1.2 Polarized Proton Acceleration

For polarized protons, RHIC uses an optically pumped polarized  $H^-$  source (OPPIS) constructed at TRIUMF from KEK OPPIS source [42]. Polarized  $H^-$  source produces  $9 \times 10^{11}$  polarized  $H^-$  in  $300 \mu\text{s}$  pulse with a current of  $500 \mu\text{A}$  with 80% polarization. Leaving from the source, these  $H^-$  ions are accelerated to 200 MeV with an RFQ (radio-frequency quadrupole) and the 200 MHz LINC. Then the pulses are strip-injected into the Booster Synchrotron where the  $H^-$  ions are stripped off to polarized protons in bunches with  $4 \times 10^{11}$  in each one. Then, the proton bunches are transferred to AGS and accelerated to  $\sim 25$  GeV. Out from AGS, the polarized proton bunches are filled into RHIC rings via the AtR. At RHIC, the bunches are finally accelerated to the work energy, e.g. 100 GeV or 255 GeV, and stored for collision. For each RHIC ring, there are 360 RF buckets. For every three buckets, only one of them is filled with a bunch and the others are kept empty for spacing requirement between bunches. Each ring can store 120 bunches in total although experimentally only  $\sim 111$  of them are filled while  $\sim 9$  of them are left for the so-called abort gaps. It is denoted as a “fill” for each time that the bunches are injected, accelerated, stored and collided. “Fill” is a basic “unit” for the data taking, usually lasting for about 10 hours at the full energy, e.g. 500 GeV.

It is known that charged particles can be accelerated by electronic field in longitudinal direction and kept in a circular orbit by magnetic field in transverse direction. However, it will be a big challenge if the accelerated particles are polarized

and need to maintain a stable polarization direction while being accelerated to high energy. The spin vector evolution of polarized proton beams in magnetic fields such as RHIC circular accelerator can be described by the Thomas-BMT equation [43],

$$\frac{d\vec{P}}{dt} = \frac{e}{\gamma m} \vec{P} \times \left[ G\gamma \vec{B}_\perp + (1 + G)\vec{B}_\parallel \right], \quad (2.1)$$

where  $\vec{P}$  is the polarization vector,  $G = 1.7928$  is the anomalous magnetic moment of proton, and  $\vec{B}_{\perp(\parallel)}$  is the magnetic field component perpendicular (parallel) to the particle momentum. In principal, the transversely polarized proton should not lose its polarization if its spin direction aligns with the vertical magnetic field in circular accelerator where  $\vec{B}_\parallel = 0$  and  $\vec{B}_\perp \times \vec{P} = 0$ . But in practice, the possible misalignment can lead to the precession of number  $G\gamma$  in each orbital revolution, and there is imperfection which can cause a horizontal magnetic field component and perturb the polarization direction. This kind of perturbations are expected to be random and can be canceled out by themselves. However, the polarization points to same direction when it arrives same perturbing position. Then, the so called depolarizing resonance occurs. To fix this problem of depolarization, a powerful device named ‘‘Siberian Snake’’ was designed by former Soviet Union scientists and installed at RHIC [44]. The Siberian Snakes is composed of a string of helical dipole magnets and can rotate the proton spin direction by  $180^\circ$ , from up to down or from down to up. A pair of such devices are installed on each ring on opposite sides as indicated in Figure 2.1. In this way, the periodic perturbations can be canceled out and the polarization direction are maintained. In addition this is energy independent.

With 4 sets of the Siberian Snakes, the transversely polarized proton beams can be accelerated and stored in RHIC rings. But for physics goal in many scenarios (e.g. the  $W A_L$  measurement in this analysis), longitudinal polarization is needed for the colliding beams. Another device, spin rotator [45], is implemented before the beams going into the collision region. The spin rotator is similar with the Siberian Snake, consisting of a series of helical dipole magnets. It can rotate the polarization direction by  $90^\circ$  from transverse to longitudinal or from longitudinal to transverse. For both STAR and PHENIX experiments, and for both blue and yellow rings, 4 pairs of spin rotators are installed just at the locations before and after the interaction regions. With all of them on, the beams will collide with longitudinal

polarization and back to transverse in storage rings.

### 2.1.3 Polarimeter

For physical measurements, the beam polarization value is usually a very important parameter. At RHIC, the measurement of beam polarization is performed by two different types of polarimeters, the proton-Carbon (pC) polarimeter [46] and the hydrogen gas jet (H-Jet) polarimeter [47]. Both of them are based on the principle of transverse spin asymmetry measurement,

$$\varepsilon_N = PA_N = \frac{N_L - N_R}{N_L + N_R}, \quad (2.2)$$

where  $A_N$  and  $\varepsilon_N$  is the transverse spin asymmetry and the raw asymmetry respectively,  $P$  is the polarization of the beam or the target,  $N_{L(R)}$  is the number of events detected at the left (right)-side detector with respect to the beam direction.

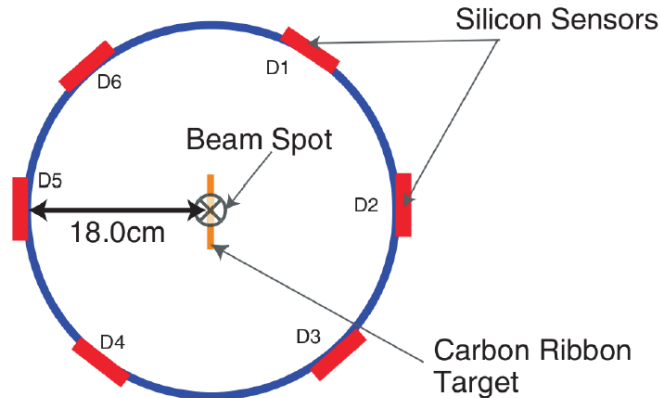


Figure 2.2: Schematic geometry layout of proton-Carbon polarimeter.

The proton-Carbon polarimeter is based on the elastic proton-Carbon scattering in Coulomb-Nuclear Interference (CNI) region by inserting a very thin Carbon fixed target into the beams, and measuring the left-right asymmetry of the recoil carbon nuclei. Figure 2.2 shows a schematic of the pC polarimeter. There are six silicon strip detectors surrounding the scattering region. It is placed at 12 O'clock of RHIC also indicated in Figure 2.1. With the large cross section, it is a fast polarimeter which can take enough statistic for one measurement in one minute. Usually, the pC polarimeter is inserted into the proton beams at the beginning/end

of each fill, and every 3 hours during the data-taking. The transverse spin asymmetry  $A_N$  for the proton-Carbon elastic scattering is not well known. The results from pC polarimeter only give the relative values of the beam polarization and the time dependence (reducing as time) for each fill.

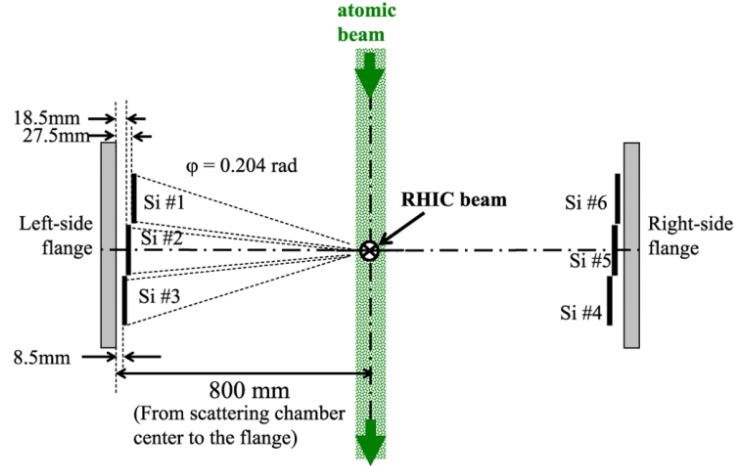


Figure 2.3: Schematic geometry layout of H-Jet polarimeter.

The absolute polarization values are measured by the hydrogen gas jet polarimeter which is based on the elastic proton-proton scattering in the CNI region. Figure 2.3 shows the schematic layout of H-Jet polarimeter. Since the beam and target are identified, the polarization of proton beam can be directly described by the target polarization which can be measured by the Breit-Rabi polarimeter. As complementary to the pC polarimeter, the analyzing power of  $pp$  elastic scattering in CNI region can be well measured by the H-Jet polarimeter. Combining these two polarimeters by normalizing the results from pC by the H-Jet results, the fill by fill beam polarization results can be obtained. The results for run by run are reported at Reference [48]. On average, the beam polarization is about 55% for 500 GeV and 60% for 200 GeV proton-proton runs at RHIC.

## 2.2 STAR – the Solenoidal Tracker at RHIC

STAR, the Solenoidal Tracker at RHIC [49], is one of the two main detectors (another one is PHINEX [50]) at RHIC. As indicated in Figure 2.1, STAR is located at 6 O'clock position of RHIC ring with a large acceptance covering the full azimuthal ( $2\pi$ ) within a wide pseudo-rapidity range ( $-1 < \eta < 1$ ) at barrel

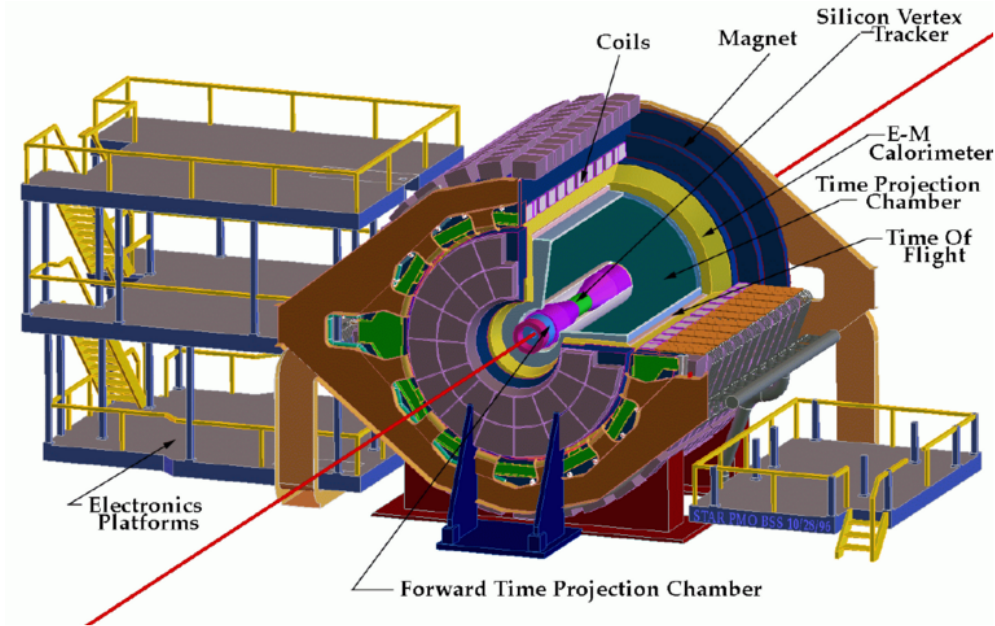


Figure 2.4: STAR detector overview.

region, and effectively extended by the forward subsystems. STAR can measure many observables simultaneously to study the signatures of a possible quark-gluon plasma (QGP) in heavy ion collisions and the nucleon spin structure in the polarized proton-proton collisions. The large acceptance makes it well suited for correlation measurements. Figure 2.4 is the schematic view of STAR detector and Figure 2.5 shows its cut view. STAR is a large system with many subsystems. The main parts are listed below.

- TPC, the Time Projection Chamber, covering pseudorapidity rang  $|\eta| < 1.3$
- BEMC, the Barrel EM Calorimeter, covering range  $|\eta| < 1.0$
- EEMC, the Endcap EM Calorimeter, covering range  $1.086 < |\eta| < 2.0$
- TOF, the Time Of Flight detector
- MTD, the Muon Telescope Detector
- HFT, the Heavy Flavor Tracker
- FMS, the Forward Meson Spectrometer
- BBC, the Beam Beam Counter

- ZDC, the Zero Degree Calorimeter

Among them, the core of STAR is the TPC which is the main reason of STAR named as the solenoidal tracker. Some of the subsystems, e.g. TOF, MTC, and HFT are mostly designed for heavy ion physics. In this section, detailed descriptions will be given only for the detectors used in this analysis, TPC, BEMC and EEMC.

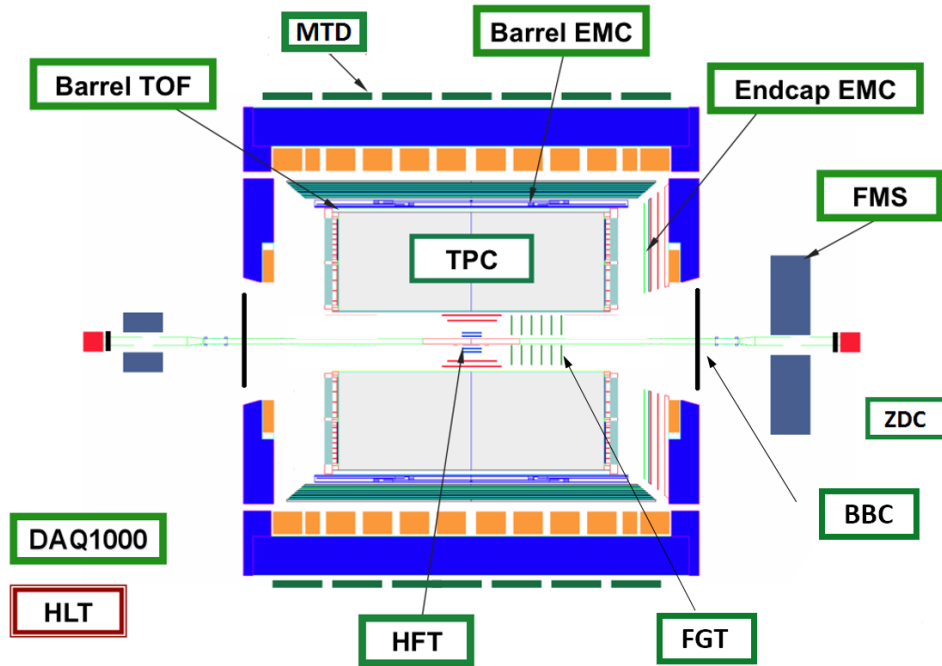


Figure 2.5: STAR detector cut view with the subsystems.

### 2.2.1 TPC – the Time Projection Chamber

Shown in Figure 2.6, the Time Projection Chamber (TPC) [51] is the most important subsystem and the primary tracking device of STAR detector. The TPC records the trajectories of charged particles, and provides the momentum and charge sign information based on the trajectories, and provides the particle identification based on their energy loss in the gas.

The TPC consists of a 4.2 m long drift volume filled with gas, with an inner radius of 50 cm and an outer radius of 200 cm which covers pseudorapidity range  $|\eta| < 1.3$  and the full azimuthal angle around the beam-line. The magnetic field is 0.5 T (full) and parallel to the beam pipe supplied by the solenoidal magnet surrounding the TPC [52]. The charged particles pass through the working gas, P10

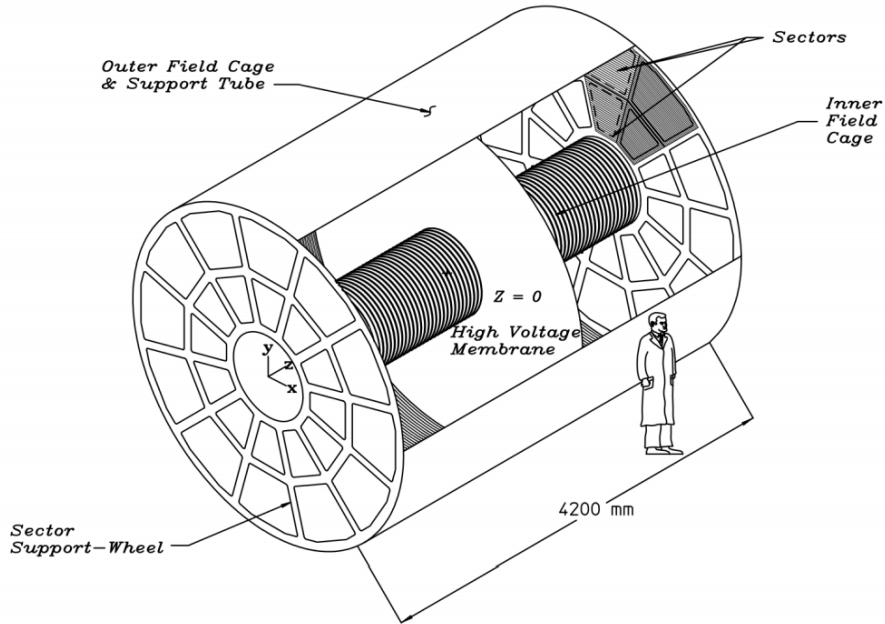


Figure 2.6: Structure of STAR Time Projection Chamber [51].

(90% argon and 10% methane) which is introduced in detail in Reference [53], and ionize with secondary electrons on its path. With the electric field on, the ionization electrons drift to the end caps to be collected by the readout system. The readout system used by TPC is based on the Multi-Wire Proportional Chambers (MWPC) with the readout pads [54]. In Figure 2.6, it can be seen that the readout system is segmented into 12 sectors in each end, and further into inner and outer parts for each sector. The readout pads are elaborately segmented and can provide high precision transverse position, in  $x - y$  plane ( $x, y, z$  are indicated in Figure 2.6). Figure 2.7 shows a full sector of the anode pad plane. Compared with the full pad rows in outer sector, there are space between pad rows in inner sector. A program is ongoing to upgrade the pad planes of inner sectors to the same row density as outer sectors [55]. The  $z$  position is measured from the drift time of the ionization electrons where the drift velocity can be well calibrated by a laser system [56].

The tracks are reconstructed from the hits with 3-D positions and subsequently the momentum information can be extracted from the track parameters. The vertex finding is based on the tracks provided by TPC. The tracks are extrapolated to the beam-line and the points pointed by multi-tracks are accepted as vertex with some algorithms. The vertex position along the beam-line is expected to distribute

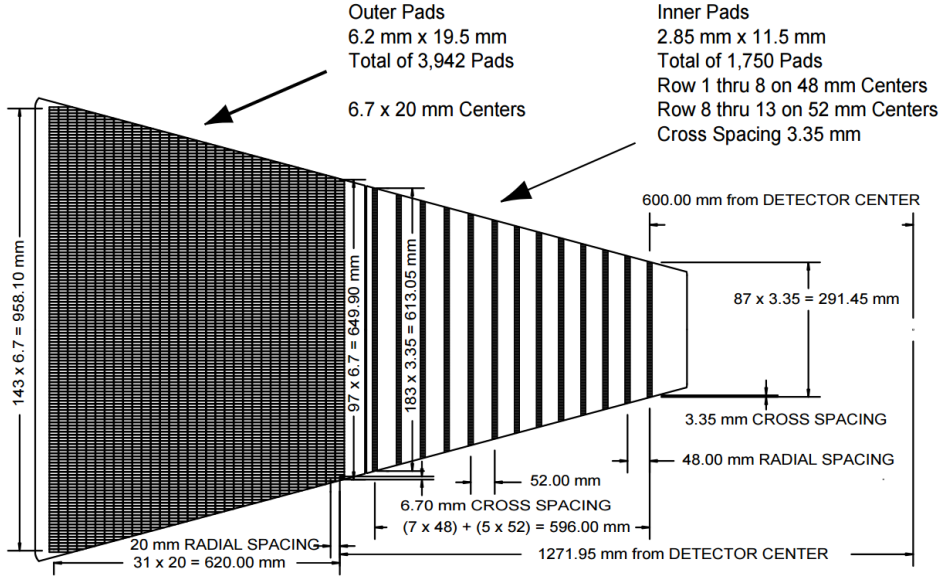


Figure 2.7: The anode pad plane with one full sector [51].

normally around the center of STAR with a sigma of about 45cm. The TPC was designed primarily for low and medium momentum tracks reconstruction. For high momentum tracks like electrons from  $W$  decay, they become very straight due to the limitation of magnetic field and the momentum resolution thus gets worse. For this analysis, the momentum information will not be used for the signal candidates, but it is needed in suppressing the backgrounds. The high precision spatial reconstruction makes the charge separation working well even at the high momentum region of our interest. According to the bending direction of the tracks, the charge signs which is very important for this analysis can be reconstructed. More details will be discussed in Section 4.1.5

The energy loss,  $dE/dx$ , which is reconstructed from how many electrons are collected for each hits, is also a valuable variable. Since different particles have different  $dE/dx$  functions of momentum, TPC can provide particle identification which is very important for most of STAR physics programs.

## 2.2.2 BEMC – the Barrel Electromagnetic Calorimeter

The Barrel Electromagnetic Calorimeter, BEMC [57], is located outside TPC and inside the solenoidal magnet covering full azimuthal angle in pseudorapidity range  $|\eta| \leq 1.0$ . An overview of BEMC structure is shown in Figure 2.8. The BEMC consists of 120 modules, with 60 in  $\phi$  ( $\Delta\phi = 6^\circ, \sim 0.1rad$ ) and 2 in  $\eta$

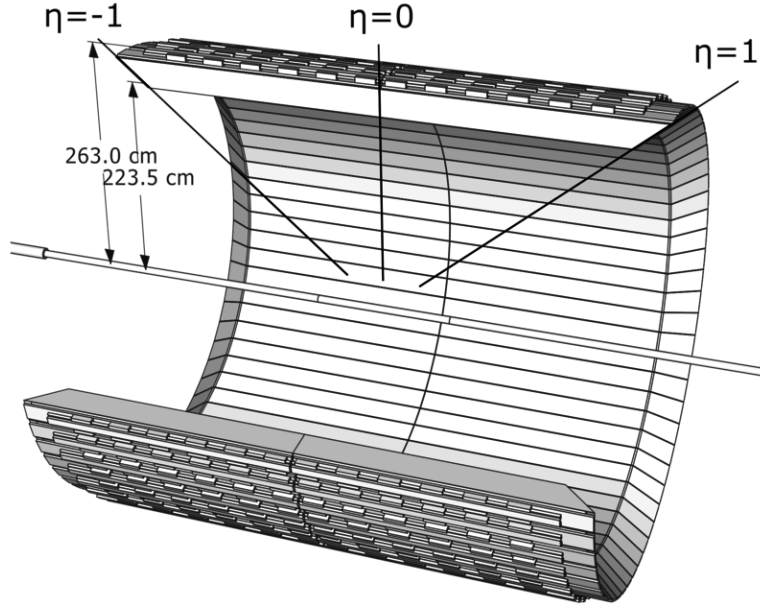


Figure 2.8: Overview of STAR Barrel Electromagnetic Calorimeter.

( $\Delta\eta = 1.0$ ). The grids in the inner wall shown in Figure 2.8 indicate the gaps between the modules. Each module is segmented into 40 towers with 2 in  $\phi$  and 20 in  $\eta$  ( $0.05 \times 0.05$  for each tower in  $\eta - \phi$  frame), and with every tower pointing to the center of STAR.

As a sampling calorimeter, the BEMC modules are composed of 20 layers of 5 mm thick lead and 21 layers of thick scintillator, 19 of 5 mm and 2 of 6 mm, interleaving with each other. With such a structure, BEMC has a total depth of  $\sim 20$  radiation lengths at  $\eta = 0$ , and can satisfy the performance requirement even at high  $E_T$  region like  $W$  events. Located at depth of  $\sim 5.6$  radiation lengths, a Shower Maximum Detector (SMD) is employed to measure the shower position. A schematic view of BEMC module is shown in Figure 2.9. The signal from each scintillating tile is transported through a wavelength shifting (WLS) fiber embedded in a  $\sigma$ -groove that is machined in the tile. Then, the signal exits the WLS fiber and goes into fibers of the multi-fiber optical cables through the multi-fiber optical connector at the backplate of the module. The multi-fiber optical cables are connected to the photomultiplier tubes (PMT) inside the detector boxes which are mounted on the out of the magnet.

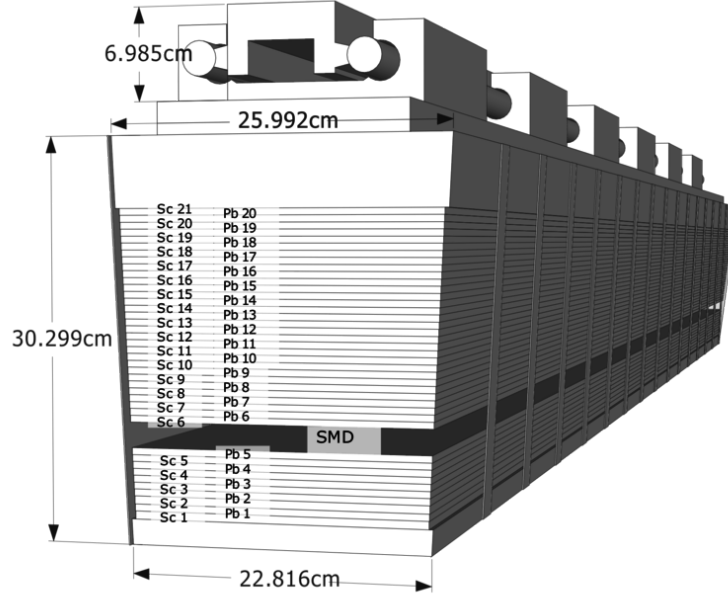


Figure 2.9: Schematic view of one module of Barrel Electromagnetic Calorimeter [57].

While the resolution of TPC getting worse for high momentum track, the resolution of energy measured from BEMC gets improved for high energy. From the cosmic rays and test beams, the energy resolution is estimated to be  $\sim 14\%/\sqrt{E} \oplus 1.5\%$ . In the  $W$  analysis, the BEMC plays a key role in reconstructing the electron candidates. In addition, the BEMC is a fast detector which is an important part of STAR trigger system [58] to efficiently select out the high- $p_T$  physical events on-line.

### 2.2.3 EEMC – the Endcap Electromagnetic Calorimeter

The Endcap Electromagnetic Calorimeter (EEMC) [59] which is located at the west end of TPC covers pseudorapidity range  $1.086 \leq \eta \leq 2.00$  over the full azimuthal angle. It significantly extends the acceptance in forward region. Similar to the BEMC, EEMC is also a sampling calorimeter stacked by the alternating layers of lead and scintillator, and with a Shower Maximum Detector (ESMD) at the depth of 5 radiation lengths. A cut view of the tower structure can be seen in right side of Figure 2.10. The EEMC is segmented into 720 towers in total as shown in Figure 2.10 (only half view). The coverage of each tower is  $\Delta\phi = 0.1$  and  $\Delta\eta$  from 0.057 to 0.099 with increasing  $\eta$ . The tower segmentation is produced

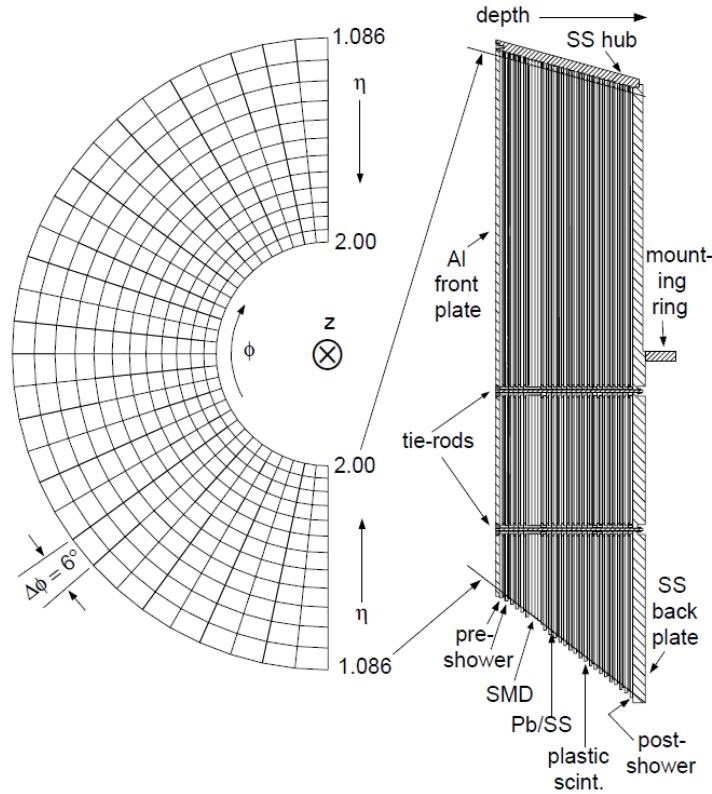


Figure 2.10: Tower structure of Endcap Electromagnetic Calorimeter. The left side shows the half view of the tower grids, and the right side shows the cut view of the tower layer structure [59].

using megatile construction. Wavelength-shifting (WLS) optical fibers, inserted into  $\sigma$ -grooves machined in the face of each tile, run through channels in a white plastic fiber-routing layer (FRL) out to the edge of each megatile. Using the optical connectors, the WLS fibers bundling from the 24 scintillator layers are connected to 12 photomultiplier tubes (PMT) for each sector. Light from the 24 layers within each tower is combined via an optical mixer in a single PMT, to produce a signal proportional to the total energy deposited in that tower.

The shower maximum detector ESMD is made of extruded polystyrene-based scintillator strips of triangular cross-section with  $u$  and  $v$  planes orthogonal with each other. The layout of the ESMD sector is shown in Figure 2.11. The ESMD can help to distinguish the single electron or photon from the photon pairs from  $\pi^0$  or  $\eta^0$  based on their shower profiles.

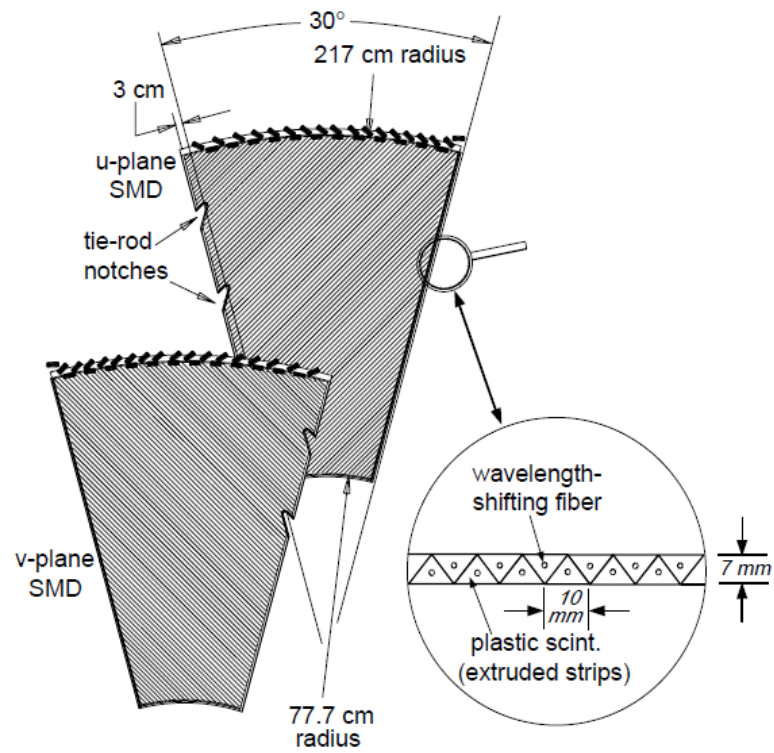


Figure 2.11: Layout of one 30° sector of the Shower Maximum Detector of EEMC [59].



# Chapter 3

## Data Sample and MC Embedding

This chapter will describe the data sample and the MC embedding sample used for  $W$  longitudinal single-spin asymmetry analyses.

### 3.1 Data Sample

#### 3.1.1 $W$ Stream

The  $W$  longitudinal single-spin asymmetry analyses at STAR is based on the data samples taken in longitudinally polarized proton-proton collisions at  $\sqrt{s} = 500$  (510) GeV at RHIC. In 2009, RHIC successfully finished the 500GeV commissioning run. For the first time,  $W$  signals were successfully reconstructed. The single-spin asymmetry and cross section were measured using 2009 data by both STAR [38][60] and PHENIX [39]. In 2011 and 2012, STAR collected more data on longitudinally polarized proton-proton collisions at  $\sqrt{s} = 500$  (510) GeV which provide opportunity to measure the lepton pseudorapidity dependence of  $W$  single-spin asymmetry. In 2013, STAR collected a much larger data sample of longitudinally polarized proton-proton run at 510 GeV.

During data taking, STAR uses a trigger system [58] which is designed to efficiently record the collision events of interest with the necessary detector subsystems. The STAR trigger is based on the signals from the fast detectors response for each bunch crossing at a  $\sim 10$ MHz rate to pick out events at a rate of  $\sim 100$ Hz where the slow detectors (e.g. TPC) can operate. The trigger system consists of several levels which are described in detail in Ref. [58]. Different trigger configurations are designed for different physical goals. Two triggers, L2BW and L2EW which aim to select high  $E_T$  electrons based on the BEMC and EEMC responses respectively,

have been specially designed for the data taking for  $W$  physics. The L2BW trigger contains two levels of requirements for the energy signal measured from BEMC towers:

- Firstly, one event needs to pass the high tower trigger BHT3 which requires that at least one BEMC tower with  $E_T$  passing the BHT3 threshold 7.3 GeV.
- Then, the higher level trigger algorithm searches for a seed tower with  $E_T > 5$  GeV and sums the  $E_T$  deposited in the  $2 \times 2$  cluster. The maximum of the  $E_T$  in the 4 possible clusters including the seed tower is required to pass the threshold 12 GeV.

The L2EW trigger also contains two stages of requirements for the energy deposited in EEMC towers:

- Firstly, one event is required to pass the high tower trigger EHT1 which requires that at least one EEMC tower with  $E_T$  passing threshold 7.3 GeV.
- Furthermore, the higher level trigger requires at least one tower with  $E_T > 10$  GeV.

### 3.1.2 Datasets of 2011, 2012, and 2013

The work of this thesis is based on the STAR data taken in 2011, 2012, and 2013 at  $\sqrt{s} = 500$  (510) GeV longitudinally polarized proton-proton collisions at RHIC.

In high energy experimental physics, the particle scattering processes are usually characterized using the instantaneous luminosity which is defined as the number of particles detected in unit area and unit time. For interaction in region of collider like RHIC, the instantaneous luminosity can be written as,

$$\mathcal{L} = \frac{f_{rev}K}{2\pi\sigma_x\sigma_y}, \quad (3.1)$$

under the assumption that the beams have Gaussian transverse profiles, where  $f_{rev}$  is the revolution frequency,  $K \equiv \sum_i N_i^a N_i^b$  is the product of the bunch intensities ( $N_i$ ) of the two beams ( $a, b$ ) summed over all bunches, and  $\sigma_x, \sigma_y$  are the transverse widths of the beam overlap region. At RHIC, the intensity of each bunch is determined during a scan by the Wall Current Monitors [61]. The transverse

	Number of runs after QA	Effective Integral Luminosity
2011	143	9.4 pb <sup>-1</sup>
2012	638	77.4 pb <sup>-1</sup>

Table 3.1: Number of runs and integral luminosities for final datasets of 2011 and 2012 used for  $W$  candidates selection.

	Number of runs after QA	Effective Integral Luminosity
Period I L2BW	916	125.1 pb <sup>-1</sup>
Period I L2EW	874	118.3 pb <sup>-1</sup>
Period II L2BW	716	121.1 pb <sup>-1</sup>
Period II L2EW	596	101.0 pb <sup>-1</sup>

Table 3.2: Number of runs and integral luminosities for final datasets of 2013 used for  $W$  candidates selection.

widths of the beam overlap region are obtained from the Vernier scan runs [62] [63]. Integrating the instantaneous luminosity with respect to time, the integrated luminosity  $L \equiv \int \mathcal{L} dt$  is obtained and is used to quantitatively describe the size of a data sample.

It has been mentioned in Section 2.1.2 that one RHIC “fill” usually lasts about 10 hours for 500 GeV  $pp$  running. During each RHIC “fill”, STAR takes data in unit of “run” which is about 30 minutes in order to maximize the utilization of the beams and minimize the risk of effect from the possible detector problems. From the runs recorded by STAR, a manual QA (Quality Assurance) is performed via checking the run logs and the online plots generated during the data taking to remove the runs with problems. Then, another QA is done by plotting the mean values of the basic variable from the main detectors, TPC track ( $\eta, \phi, p_T, DCA, \chi^2$ , and  $dE/dx$ ), BEMC and EEMC towers ( $\eta, \phi$ , and  $E_T$ ), and the ESMD strips. The runs with outliers are then excluded from the analysis.

In 2011, RHIC delivered 500 GeV longitudinally polarized proton-proton collisions for only one week. It is a relatively small dataset comparing with following two years. After the QA procedures, 143 runs are accepted for the physics analysis. In 2012, 510 GeV longitudinally polarized proton beams are delivered for about 5 weeks with increased beam polarizations. After the QA, there are 638 runs accepted. The numbers of runs and effective integral luminosities for 2011 and 2012 data are listed in Table 3.1.

Year	Blue beam	Yellow beam
2011	0.49	0.49
2012	0.55	0.57
2013	0.56	0.56

Table 3.3: Average of the beam polarization for 2011, 2012, and 2013 at RHIC.

Run 2013 at STAR is a long run for  $W$  program which is divided into two periods due to the HFT installation in the middle of run. As HFT was installed inside the TPC inner volume, STAR geometry was unavoidably changed. So, separate TPC calibrations are needed for the two periods, and subsequently, the data production, data QA, and analysis are also done separately. For run 2013 datasets, 1010 runs of period I and 822 runs of period II are produced. In Table 3.2, the numbers of runs and the integral luminosities after the QA procedures are listed for both L2BW and L2EW streams.

### 3.1.3 Beam Polarization

The beam polarization is measured by using the polarimeters which have been introduced in Section 2.1.3. The fill by fill results are provided by the RHIC Polarimetry Group [48] with the average value, begin value and the polarization decay slopes for both beams. Based on these fill-by-fill information, the polarization for each run are calculated and plotted as function of the run index as shown in Figures 3.1, 3.2, and 3.3 for 2011, 2012, and 2013 respectively. The beam polarization values for blue and yellow beams for all these three datasets are listed in Table 3.3.

### 3.1.4 Spin Sorting at STAR

As introduced in Section 1.2, the measured single-spin asymmetry  $A_L$  is defined as the cross section difference for different beam polarization direction. Experimentally, the  $W$  yields for each spin state normalized by luminosity are required. At RHIC, the beams contain 120 bunches including a abort gap with 9(11) of them empty. The polarization directions for the bunches are not the same but altering in periodic patterns. A schematic diagram is shown in Figure 3.4 where we can see the blue beam and yellow beam in a same fill have the different spin patterns,  $++--$  and  $+ - + -$ . In this way, all four possible collision spin states,  $++$ ,  $+-$ ,  $-+$ ,  $--$ ,

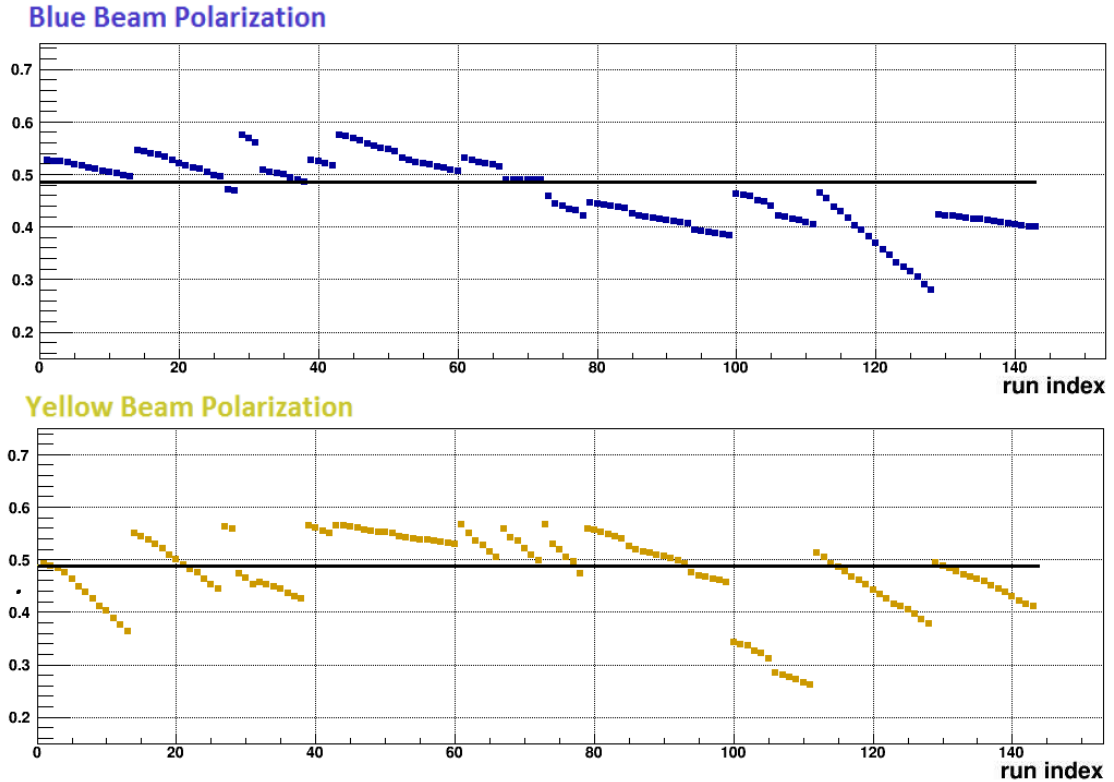


Figure 3.1: 2011: Beam Polarization for blue and yellow beams respectively, the line in each plots are the luminosity weighted average value.

are recorded. The bunch-by-bunch spin patterns in consecutive fills are varied in order to reduce potential systematic effects. The spin patterns are different from year to year but the logic is same. In 2011 and 2012, the spin directions repeat with period of 4 bunches. In run 2013, the spin direction altering is by unit of two bunches and the repeating period became 8 bunches. The spin state of each bunch is provided by the CAD (Collider Accelerator Department) and recorded by STAR into an offline database. The spin state for each bunch crossing at STAR can be obtained by matching bunch crossing distribution with the RHIC bunch ID and the abort gaps.

The spin information is recorded as a series of binary numbers. As shown in Table 3.4, the numbers in the first column are what the collision spin states are recorded in database. The first 4 bits and second 4 bits are for the blue beam and yellow beam respectively. For each 4 bits, the first bit indicates the polarization status, 0 for polarized and 1 for unpolarized. The last one is for the fill status, 0 for intended filled and 1 for intended unfilled. The middle two bits are for polarization

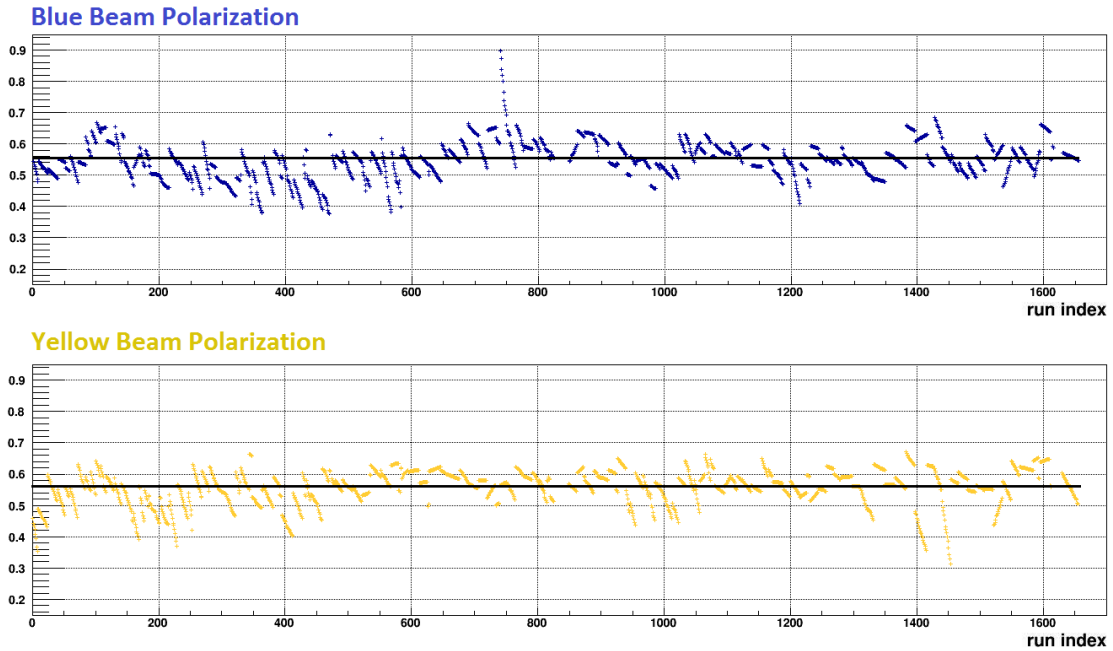


Figure 3.2: 2012: Beam Polarization for blue and yellow beams respectively, the line in each plots are the luminosity weighted average value.

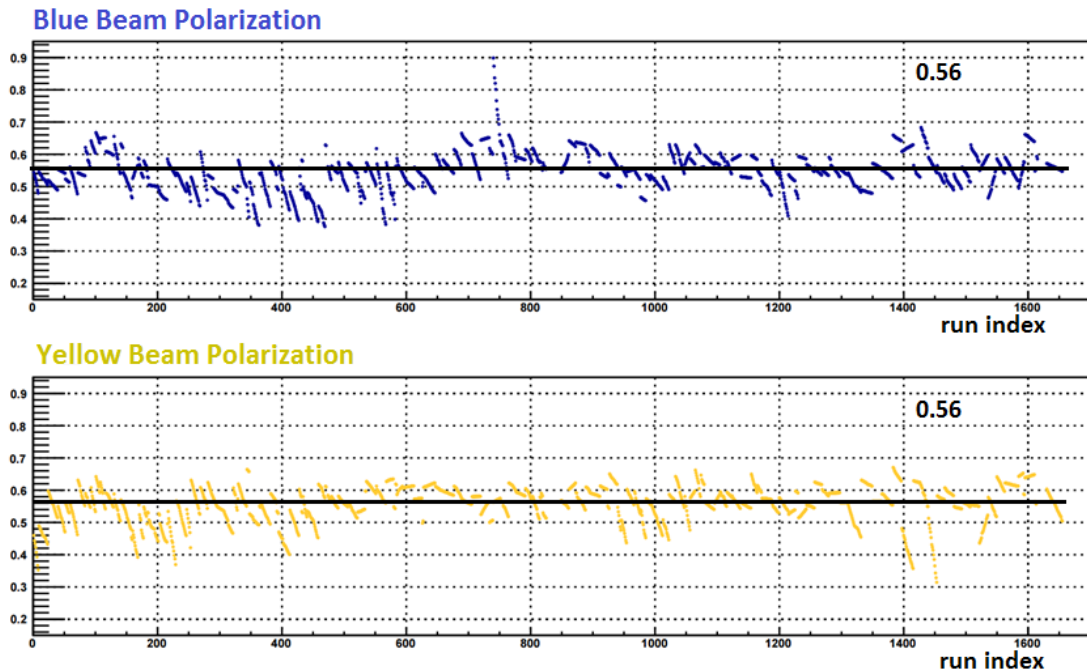


Figure 3.3: 2013: Beam Polarization for blue and yellow beams respectively, the line in each plots are the luminosity weighted average value.

direction, 10 for positive polarization and 01 for negative polarization. For the

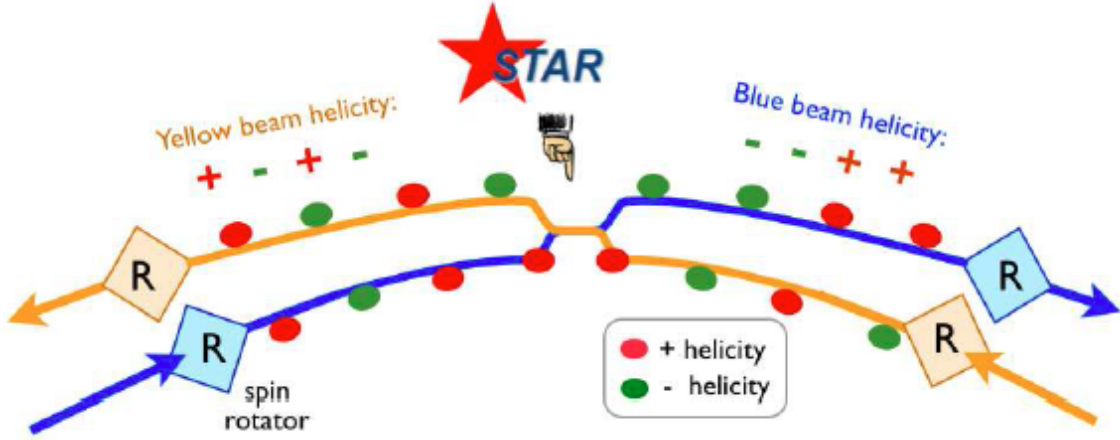


Figure 3.4: Schematic diagram for spin patterns of RHIC beam around STAR interaction region.

spin 8 bits	Blue beam polarization	Yellow beam polarization	spin4 index
00110011	—	—	5
00110101	—	+	6
01010011	+	—	9
01010101	+	+	10

Table 3.4: STAR spin bits.

analysis, the only information needed is the “spin4” information for each event, which is just the two middle bits for each beam. Namely, “—” is indicated by “0101” which corresponds to the decimal number “5”. Similarly, “6, 9, 10” stand for the rest three spin states respectively.

## 3.2 Embedding MC Simulation

In high energy physics experiments, Monte-Carlo (MC) simulation usually plays a very important role. In this analysis, the simulation sample is produced by embedding the MC events generated from PYTHIA event generator [64] into the STAR “zero bias” events which are triggered only by the coincidence of east and west ZDC responses. The embedding procedure in particular the “zero bias” events describes the possible event pile-up situation in the data, compared to pure pythia events.

Event Channel	X-section	2011	2012	2013 Period I	2013 Period II
$W^+ \rightarrow e^+\nu$	98.5 pb	11.9 K	109.1 K	136.4 K	148.9 K
$W^- \rightarrow e^-\nu$	31.3 pb	3.8 K	34.9 K	43.7 K	47.6 K
$W^+ \rightarrow \tau^+\nu$	98.5 pb	11.9 K	109.1 K	136.4 K	148.9 K
$W^- \rightarrow \tau^-\nu$	31.3 pb	3.8 K	34.9 K	43.7 K	47.6 K
$Z/\gamma^* \rightarrow e^+e^-$	23.9 pb	2.7 K	25.1 K	31.4 K	34.2 K

Table 3.5: Numbers of MC events for each channel generated for 2011, 2012, 2013 respectively. The cross sections are from PYTHIA.

### 3.2.1 MC Simulation Based on PYTHIA

PYTHIA version 6.4.22 [64] with Perugia 0 tune [65] is used to produce the MC events for 2011, 2012, and 2013 data sample independently. The MC events are generated for the  $pp \rightarrow W^\pm + X$  process with  $W^\pm \rightarrow e\nu$  signal decay channels, and  $W^\pm \rightarrow \tau\nu$  background decay channels, and the  $pp \rightarrow Z/\gamma^* \rightarrow e^+e^-$  process. For  $W^\pm \rightarrow \tau\nu$  events generation, the TAUOLA [66] package is additionally used because  $\tau$  from  $W$  decay is treated as unpolarized and not decay in PYTHIA. The event size of each channel is listed in Table 3.5. In order to reduce the statistical uncertainty from embedding sample, the event sizes are determined to be roughly larger than the data by one order of magnitude for the integral luminosity.

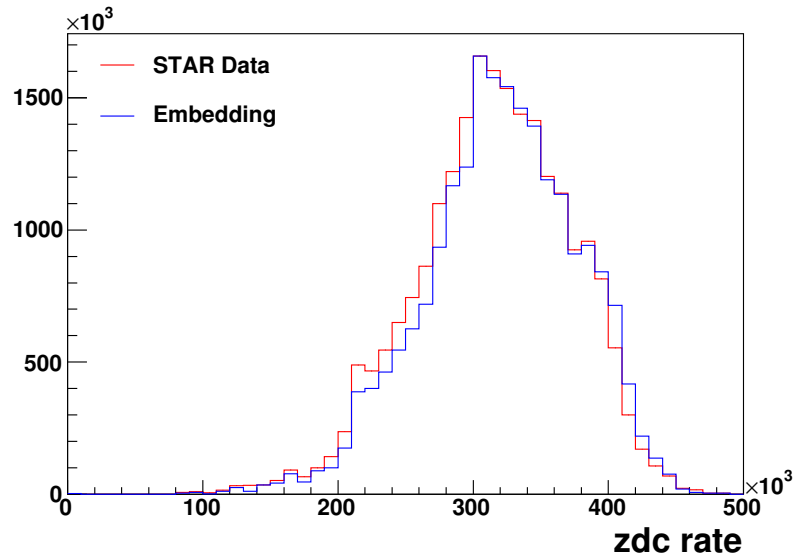
### 3.2.2 Embedding

As mentioned above, the MC events will be embedded into the real events triggered by the “zerobias” trigger. Before that, the MC events are put into STAR detector simulation system GSTAR which is based on GEANT [67]. In 500 GeV  $pp$  collisions, the rate is very high to be several hundred kHz, and in 2013 the luminosity is further increased. However, the drift velocity of the ionized electrons in TPC is only  $\sim 5$  cm/ $\mu$ s, which leads to quite a lot of pile-up events belonging to the collisions occurring during the drift time before and after the triggered events. With so many pile-up TPC clusters recoded into one event, the efficiency of track and vertex reconstruction and the subsequent  $W$  reconstruction will be significantly impacted. Beside the detector resolution effects, the pile-up effect is the key factor included in the embedding sample. The pile-up effect is expected to be well reflected in the zero bias events which are recorded simultaneously with the physics trigger events and contain the real performance of the TPC and other subsystems. The

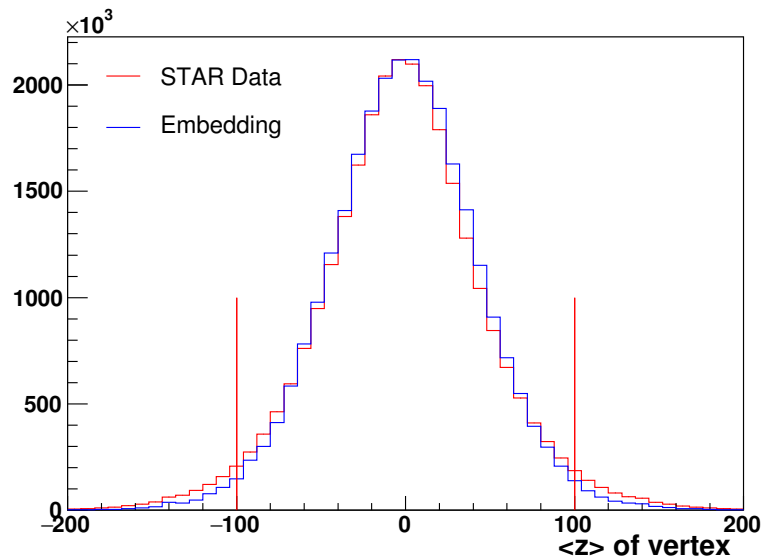
density of pile-up tracks is proportional to the instantaneous luminosity, which can be characterized by the ZDC coincidence rate. The zero bias events are chosen run by run corresponding to the  $W$  stream data, based on the following formula:

$$N_i^{zerobias} = \frac{L_i}{L_{total}} \cdot N_{total}, \quad (3.2)$$

where  $N_i^{zerobias}$  is the number of events for run  $i$ ,  $N_{total}$  is the total number of events to embed the MC events for each data sample which is listed in Table 3.5,  $L_i$  is the integral luminosity of run  $i$  and  $L_{total}$  is the integral luminosity of all the runs of each data sample. Figure 3.5a shows the ZDC coincidence rate distributions for data and embedding comparison. As expected, the luminosity weights in data have been reasonably included by the sampled zero-bias events. There is no vertex information in the zero-bias event. The generated PYTHIA events are assigned vertex positions with Gaussian distributions for  $x$ ,  $y$ , and  $z$  components with widths determined from real data. The distributions of  $z_{vertex}$  for embedding sample and data sample are shown in Figure 3.5b. It can be observed that the assigned vertex distribution is consistent with data.



(a) Normalized distributions of ZDC coincidence rate.

(b) Normalized distributions of vertex  $z$  rateFigure 3.5: ZDC coincidence rate and  $z_{vertex}$  distributions for 2013 data and the corresponding embedding sample.

## Chapter 4

# $W/Z$ Boson Reconstruction

This chapter provides the details about the  $W/Z$  bosons reconstruction at STAR.  $W/Z$  bosons are reconstructed via the leptonic decay, by selecting out the high  $E_T$  isolated electrons from the QCD backgrounds. The background studies will be also discussed in this chapter.

### 4.1 $W$ Selection

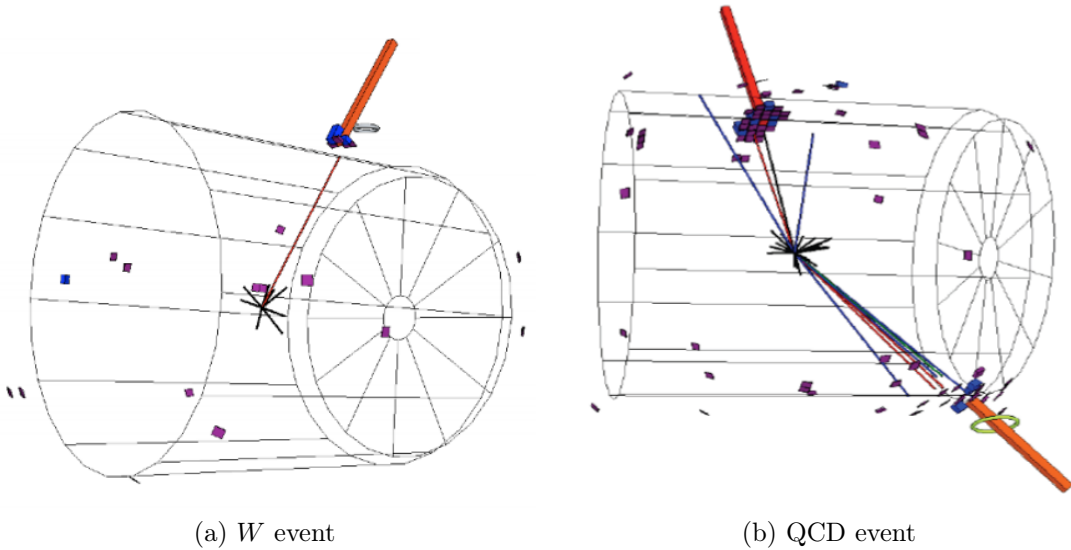


Figure 4.1:  $W \rightarrow e\nu$  event versus QCD di-jet event.

As mentioned earlier, the  $W$  candidates are determined through its leptonic decay. At STAR,  $W$  is reconstructed from the electron final state, namely from the  $W^\pm \rightarrow e^\pm\nu$  channel. The electron from  $W$  decay should leave an almost straight track in the TPC, and then deposit its energy in the towers of the BEMC or EEMC.

The neutrino is undetected and carries away energy of similar amount of the electron in the azimuthally opposite direction. In contrast, the predominated QCD events (e.g. partonic  $2 \rightarrow 2$  processes) are usually characterized by a pair of azimuthally back-to-back jets from the parton fragmentations. Compared the isolated electron from  $W$  leptonic decay, a jet usually consist of a set of tracks pointing to a patch of energy deposition in the BEMC or EEMC. The  $W$  selection algorithm is developed based on these kinematic and topological differences between the  $W$  leptonic decay event and the QCD event as shown in Figure 4.1. It is expected that the  $E_T$  spectrum of the electron candidates has a shape of Jacobian peak around 40 GeV (half of  $W$  mass) plus a smoothly and exponentially varying residual background shape.

Note, the  $W$  reconstructions are separately processed based on BEMC and EEMC because the reconstructions strongly rely on the EM calorimeters. The  $W$  reconstructions in BEMC coverage and EEMC coverage are denoted as “Barrel” and “Endcap” respectively in this thesis. For Barrel and Endcap regions, they are similar but not exactly same due to the TPC coverage limitation and the difference performance of BEMC and EEMC. In this section, we mainly use the plots from 2013 dataset to demonstrate the method of  $W$  leptonic decay event reconstruction. The corresponding plots of 2011 and 2012 are very similar.

### 4.1.1 Vertex Finding and Track Selection

With all the collision events recoded, and ready for analysis, the first task is to reconstruct the vertex for every event. In 500 GeV  $pp$  runs, the collision rate is usually a few hundred kHz. Considering the relatively slow response of TPC, there are always a lot of pile-up collisions. So, it becomes very important to correctly pick out the collision vertex belonging to the trigger fired event, which is also known as the primary vertex, from the pile-up collisions. The Pile-up Proof Vertex Finder (PPV) [68] was developed for this purpose to determine the vertex location along the  $z$ -axis from low multiplicity events embedded in 2 orders of magnitude larger pile-up events. All tracks reconstructed in the TPC are denoted as global tracks in the STAR framework. From all the global tracks, PPV selects high quality tracks which match to the fired towers in BEMC, EEMC, or tracks use hits from both sides of TPC central membrane, or tracks with very high  $p_T$  ( $> 10$  GeV/c. Also, a small closest distance (referred to as DCA) within 3 cm between global tracks and

beam-line is required. Tracks associated with the primary vertices ( $DCA < 3$  cm) are known as primary tracks. A “rank” is assigned to each vertex based on factors described above. Figure 4.2a shows the PPV vertex rank distribution for all events, where the rank has been transformed to easy view values. We can see there are clearly three peaks. The left peak has negative rank, where the vertices have no valid primary track belonging to. The middle peak is for vertices which have one primary track. The right peak corresponds to the vertices which have two or more tracks originated from them. After all the  $W$  selection cuts which will be described in following sections, the rank distribution for most possible  $W$  candidate events is shown in Figure 4.2b. We will start the  $W$  analysis with vertices with rank  $> 0$  and  $|V_z| < 100$  cm.

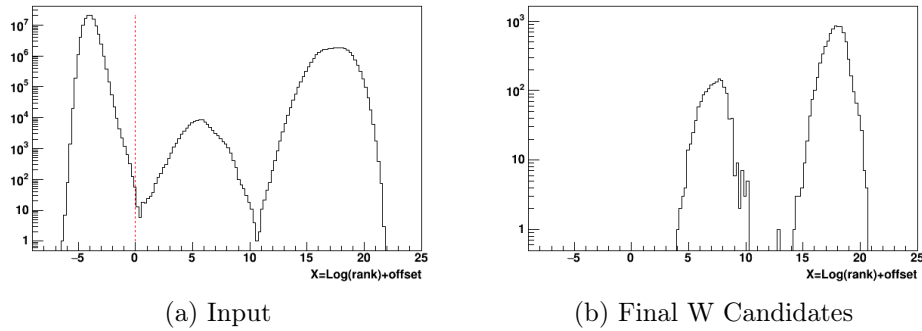


Figure 4.2: (a) Rank of all vertices, pile-up vertices have negative rank, middle and right peaks for single and multi track vertex. (b) Vertex rank of the event passing all  $W$  selection cuts.

The candidate electrons are expected to produce high  $p_T$  TPC tracks originated from primary vertex. In order to ensure the track and its charge sign are well reconstructed, it is required that the qualified tracks should have more than 15 TPC hits ( $nFitPoints > 15$ ) and the fraction of fitting hits over possible hits ( $nHitFit/nHitPoss$ ) should be greater than 51%. A candidate electron track should be a long one which has hits in both inner sectors and outer sectors of the TPC. In this analysis, it is required that the radius of the first hits from beam-line ( $RxyIn$ ) should be smaller than 90cm and of the last hits ( $RxyOut$ ) should be larger than 160cm. These requirements also can help to reduce the effect from the pile-up tracks. Tracks with  $p_T > 10$ GeV are accepted as candidates for further selection. Here, the 10 GeV cut is relatively relax to avoid efficiency loss, since TPC momentum resolution would significantly decrease at high momentum. For

candidate electron spectrum, the transverse energy measured from EMC will be used instead of the track  $p_T$  measured from TPC.

Considering the EMC tower size and the  $\sim 20$  radiation lengths, the electron is expected to deposit almost all its energy and be well limited in as large as  $2 \times 2$  tower range. Tracks passed above cuts will be extrapolated to the BEMC, EEMC towers. With the pointed tower as a seed, a  $2 \times 2$  cluster is reconstructed by picking out from all four possible clusters based on the energy maximum. The transverse energy of the  $2 \times 2$  cluster,  $E_T^{2 \times 2}$  is assigned to the candidate electron. To avoid the possible trigger effects,  $E_T^{2 \times 2}$  is required to be above 14 GeV which is safely above the trigger threshold (12 GeV). The track is extrapolated to the depth of BSMD, and the distance between the track and the cluster is required to be smaller than 7 cm. This cut aims to reject particles other than the one produced the track, e.g. neutral particles. The distribution of the distance between track and cluster is shown in Figure 4.5c, comparing data with normalized MC sample of  $W \rightarrow e\nu$ .

For Endcap region, candidate tracks have larger pseudorapidity ( $0.7 < \eta < 2.5$ ) than Barrel region ( $-1.1 < \eta < 1.1$ ). They are expected to be shorter since they cannot go through the whole outer sectors of TPC. It is needed to accordingly loose the track selection cuts and tower cluster matching cuts for Endcap. Cuts used for both Barrel and Endcap regions are listed in Table 4.1. The relevant distributions with cuts are shown in Figure 4.3, 4.4, 4.5.

cuts	Barrel	Endcap
$\eta$	(-1.1, 1.1)	(0.7, 2.5)
nFitPoints	> 15	> 5
nHitFit/nHitPoss	> 0.51	> 0.51
RxyIn	< 90 cm	< 120 cm
RxyOut	> 160 cm	> 70 cm
3D distance of track-cluster	< 7 cm	< 10 cm

Table 4.1: Track selection cuts for Barrel and Endcap regions.

### 4.1.2 Isolation Cut

As discussed above, the electron from  $W$  decay is expected to be well isolated from other particles. In the calorimeters (BEMC or EEMC), the reconstructed  $2 \times 2$  should contain mostly of the electron energy and there should not be too much energy exceeding the  $2 \times 2$  range. Based on this feature, an isolation cut is

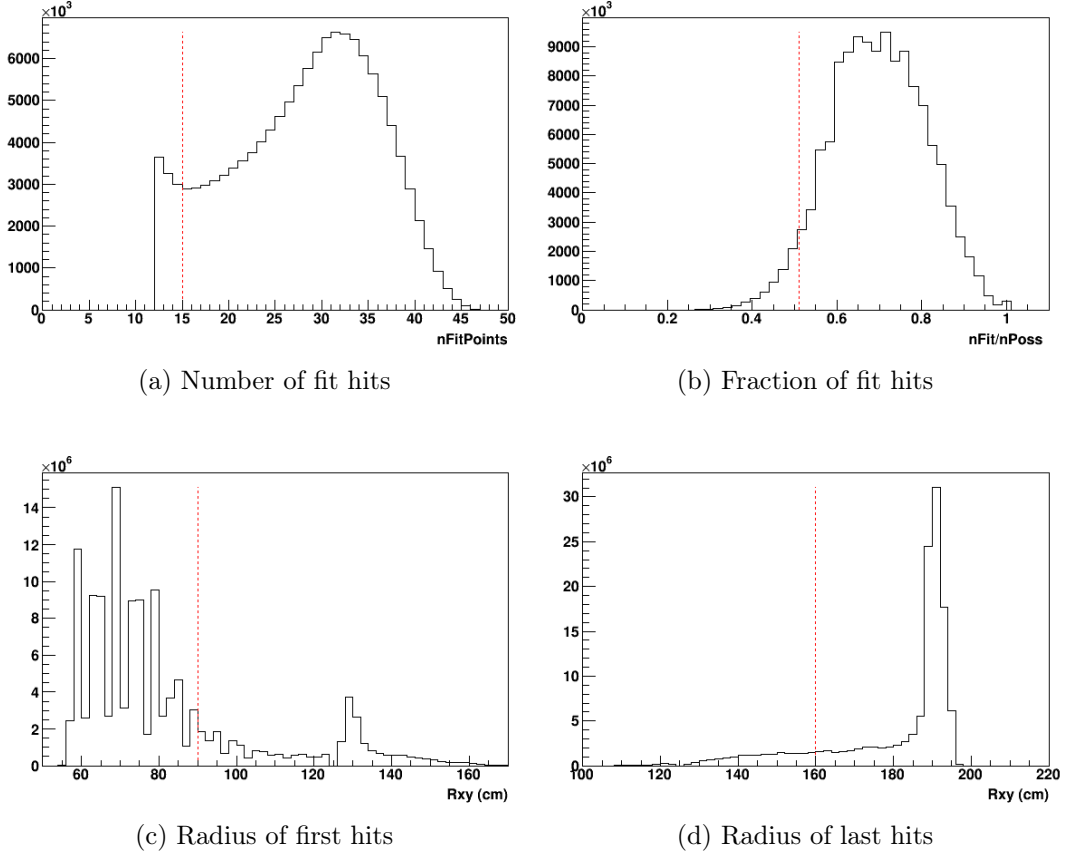


Figure 4.3: Barrel: (a) Number of hit on the track. (b) Ratio of number of hits for fitting and number of possible hits. (c) Radius from beam-line of the track's first hit. (d) Radius from beam-line of the track's last hit.

applied by reconstructing a  $4 \times 4$  cluster surrounding the  $2 \times 2$  cluster, as shown in Figure 4.6a. It is required that the fraction of  $E_T^{2 \times 2}$  over the  $4 \times 4$  cluster  $E_T$  be larger than 95%. The distribution of the ratio  $E_T^{2 \times 2} / E_T^{4 \times 4}$  is shown in Figure 4.7a, with the comparison to  $W \rightarrow e\nu$  embedding MC simulation sample. From the embedding MC simulation events, it can be found that the electron energy is strictly limited in  $2 \times 2$  range.

One of the key tasks of the  $W$  reconstruction is to distinguish the electrons from  $W$  and the electrons belonging to a jet from the parton fragmentation. In order to suppress the jet-like event, another isolation ratio is constructed by summing up all the energy, including BEMC  $E_T$ , EEMC  $E_T$ , TPC track  $p_T$ , inside a near side cone in  $\eta$ - $\phi$  space with radius  $\Delta R = 0.7$ , shown in Figure 4.6b. The electron candidate  $p_T$  has been excluded to avoid the double counting of the electron  $p_T$

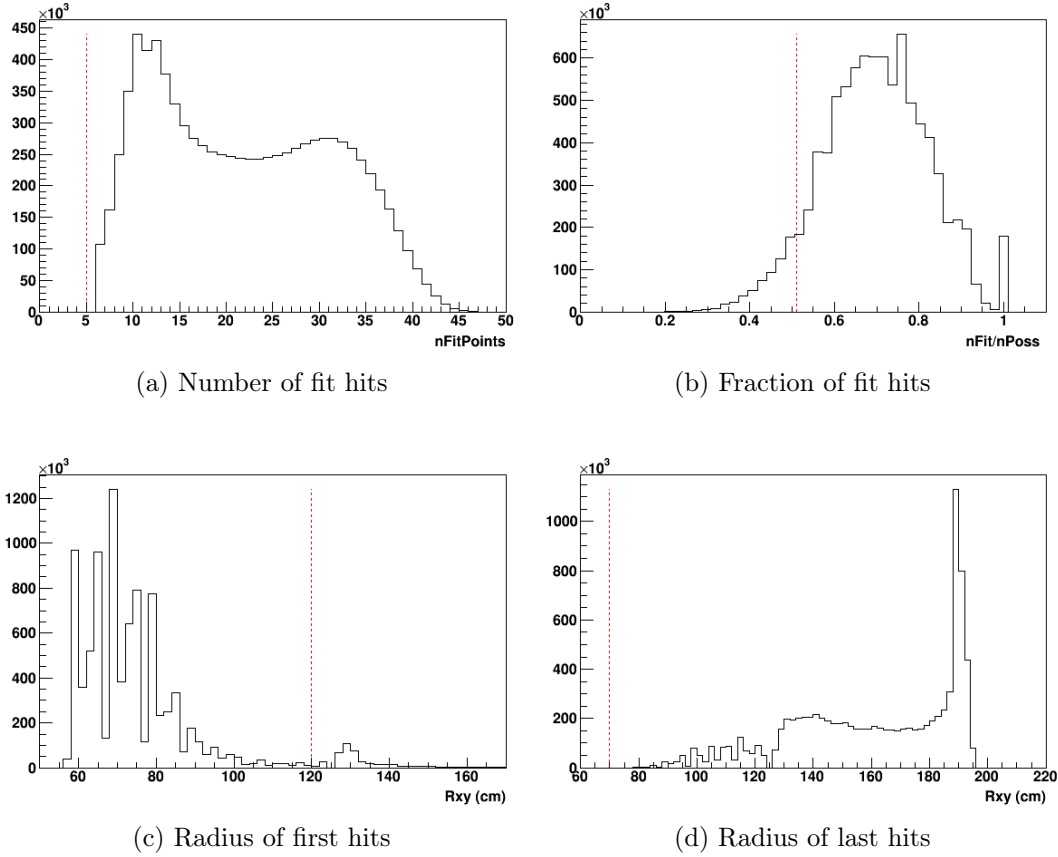


Figure 4.4: Endcap: (a) Number of hits on the track. (b) Ratio of number of hits for fitting and number of possible hits. (c) Radius from beam-line of the track's first hit. (d) Radius from beam-line of the track's last hit.

and  $E_T$ . The fraction of candidate electron  $E_T$  in this near side cone is required to be larger than 88%. The  $E_T^e/E_T^{\Delta R < 0.7}$  distributions of data and MC sample are shown in Figure 4.7b. This is a very important cut since most of the QCD events from parton fragmentation tend to have lots of nearby particles. With this cut, the  $E_T^e/E_T^{\Delta R < 0.7}$  peak in the data are effectively cut off.

The isolation cuts discussed above are similarly applied for Endcap  $W$  selection with slightly loosening thresholds as

- $E_T^e/E_T^{4 \times 4} > 90\%$
- $E_T^e/E_T^{\Delta R < 0.7} > 85\%$

The related distributions for Endcap are shown in Figure 4.8 with the red dash lines indicating the cuts.

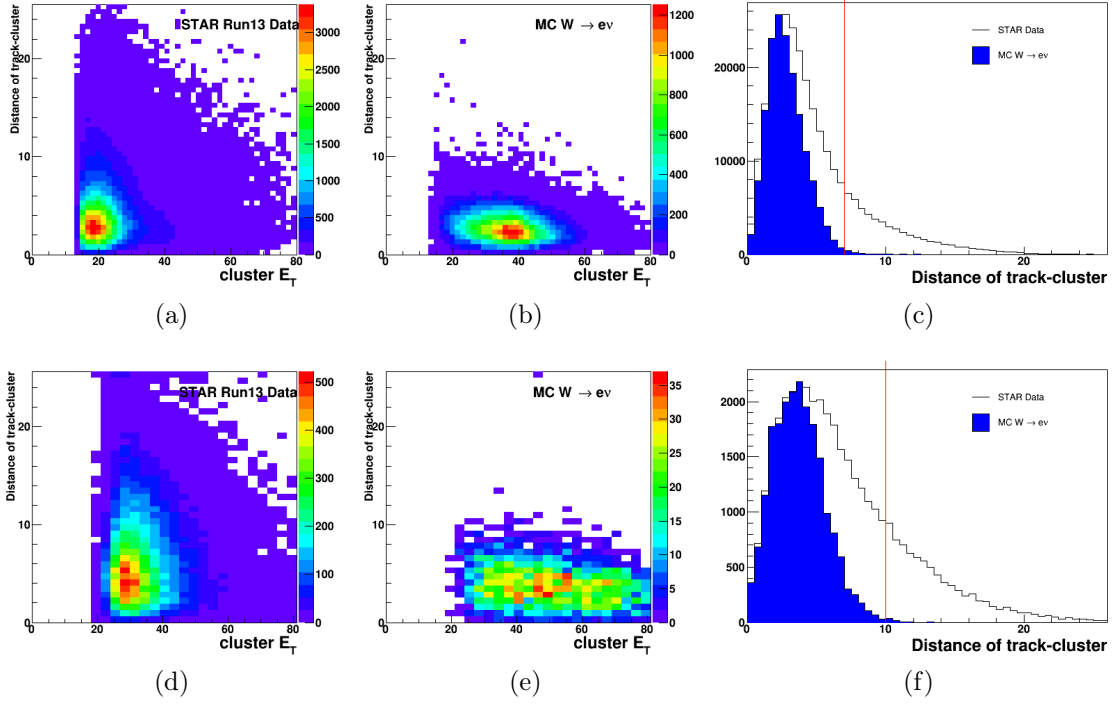


Figure 4.5: The upper row is for Barrel region and the lower row is for Endcap region. (a)(d) distance between track and cluster vs cluster  $E_T$  for Data. (b)(e) distance between track and cluster vs cluster  $E_T$  for MC  $W \rightarrow e\nu$ . (c)(f) comparison of data and MC (blue).

In addition, the EEMC shower maximum detector (ESMD) [59] is used for suppressing QCD background. The ESMD consists of two orthogonal planes (‘U’ plane and ‘V’ plane) of scintillating strips at a depth of  $\sim 5$  radiation lengths as described in Section 2.2.3. It can measure the transverse profile of the electromagnetic shower. As discussed above, electron candidates decayed from  $W$  should be an isolated shower in EMC. Considering the 1.5cm Moliere radius in lead, the isolated electron’s shower would have a narrow transverse profile. In contrast, the possible neutral particle, e.g.  $\pi^0$ , in a QCD event tends to have double showers when one of the photons converts on material. Additionally, electron shower can be well matched by an extrapolated TPC track, while showers from neutral particles are not expected to match to TPC tracks. Based on these characteristics, another isolation ratio from the energy deposited in ESMD strips are constructed. For both ‘U’ and ‘V’, the TPC track is firstly projected to ESMD planes. Then, it is computed that the ratio of energy deposited in strips within 1.5cm,  $\pm 3$  stripes, to the energy deposited in stripes within 10cm,  $\pm 20$  stripes:

$$R_{ESMD} = \frac{\sum_{i=-3}^{+3} E_i^U + E_i^V}{\sum_{i=-20}^{+20} E_i^U + E_i^V}. \quad (4.1)$$

Figure 4.9a shows the ratio  $R_{ESMD}$  with comparison of data and  $W \rightarrow e\nu$  MC sample. In Figure 4.9b and 4.9c, correlation with signed  $p_T$ -balance, which will be introduced in next section, also can well reflect the effectivity of  $R_{ESMD}$  cut.

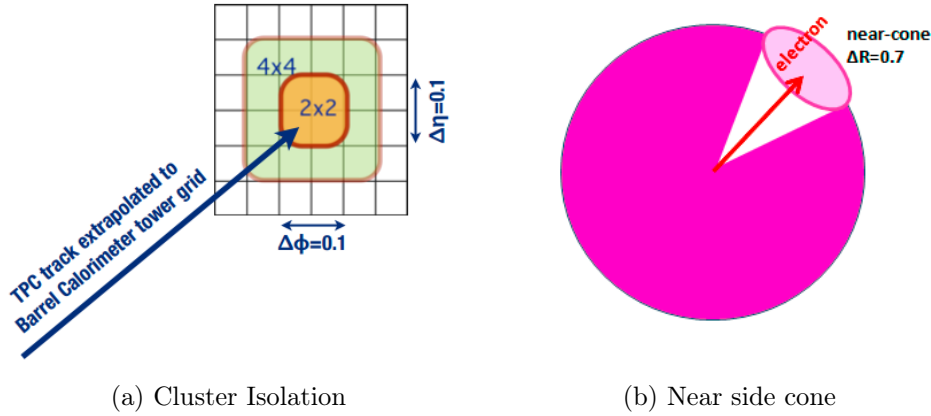


Figure 4.6: Barrel: (a) Tower grids for  $2 \times 2$  cluster isolation in  $4 \times 4$  cluster, (b) Near Cone with Radius  $\Delta R < 0.7$ ,  $\Delta R = \sqrt{\Delta\eta^2 + \Delta\phi^2}$ .

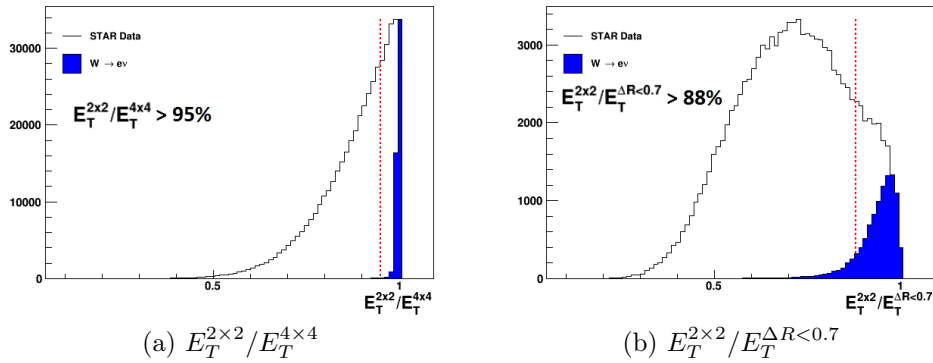


Figure 4.7: Barrel: (a) Distribution  $E_T^{2 \times 2} / E_T^{4 \times 4}$  with comparison between data and MC (b) Distributions of  $E_T^{2 \times 2} / E_T^{\Delta R < 0.7}$

### 4.1.3 Signed $p_T$ -balance Cut

For a candidate  $W$  leptonic decay event, there is an undetected neutrino opposite in  $\phi$  of the produced lepton. It is expected to carry away a large amount

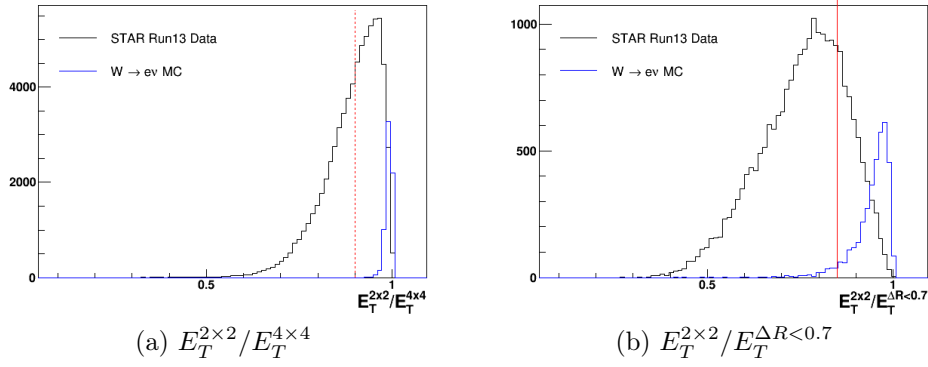


Figure 4.8: Endcap: (a) Distribution  $E_T^{2 \times 2} / E_T^{4 \times 4}$  with comparison between data and MC (b) Distributions of  $E_T^{2 \times 2} / E_T^{\Delta R < 0.7}$

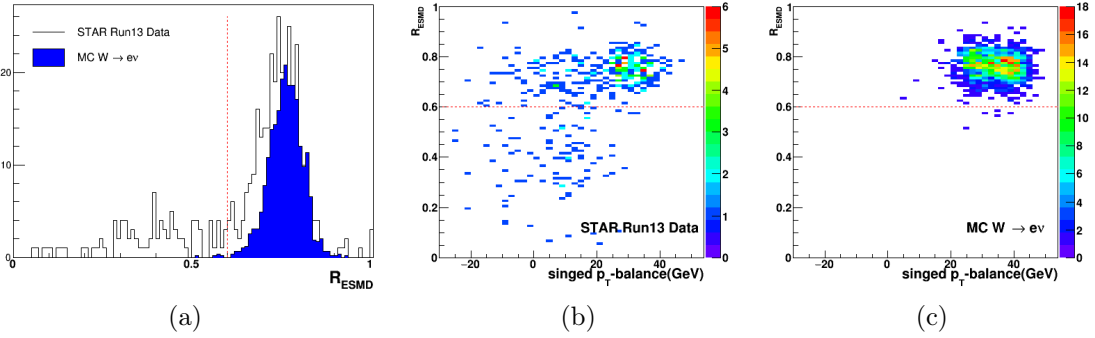


Figure 4.9: (a) Distribution of  $R_{ESMD}$ , (b)(c) correlation between  $R_{ESMD}$  and signed  $p_T$ -balance for data(b) and MC(c).

of transverse energy similar as the candidate electron  $E_T^e$ . Considering this characteristic, there would be a sizable  $p_T$  imbalance effect. In order to quantitatively evaluate this imbalance, jets are reconstructed together with the  $W$  candidate selection. Jets reconstruction in this analysis uses standard anti- $k_T$  algorithm [69], discussed in detail in other STAR jet related measurements e.g. [33], [70]. The parameters used for jet reconstruction are listed in Appendix B. With the reconstructed jets and the candidate electrons, one can construct a  $p_T$ -balance vector,  $\vec{p}_T^{balance}$ , by summing the candidate electron  $p_T^e$  vector which has been assigned to the scalar of  $E_T^e$  and the  $p_T$  vectors of all reconstructed jets with axes outside the near side cone ( $\Delta R < 0.7$ ) as shown in Figure 4.6b,

$$\vec{p}_T^{balance} = \vec{p}_T^e + \sum_{\Delta R > 0.7} \vec{p}_T^{jets}. \quad (4.2)$$

Then, this  $p_T$ -balance vector is projected onto the direction of the candidate electron and get the scalar “signed  $p_T$ -balance” variable as

$$\text{signed } p_T\text{-balance} = \frac{\vec{p}_T^e \cdot \vec{p}_T^{\text{balance}}}{|\vec{p}_T^e|}. \quad (4.3)$$

To produce a  $W$  boson, 80 GeV energy would be needed from the  $\sqrt{s} = 500$  GeV system. Since lots of spectators in very forward/backward cone, there should be not too much transverse energy left accompanying with the  $W$ . It is expected that there is a strong correlation between the signed  $p_T$ -balance and  $E_T^e$ . Figure 4.10 shows the distribution of signed  $p_T$ -balance versus  $E_T^e$ , for data and  $W \rightarrow e\nu$  MC respectively. As expected, there is a clear “ridge” roughly at  $x = y$  in both data and MC sample. The cut of signed  $p_T$ -balance  $> 14$  GeV is applied for Barrel region. Comparing plots for data and MC sample, it was shown how effective of this cut is. For Endcap region, the signed  $p_T$ -balance has been mentioned previously in the end of Section 4.1.2. Due to the limited detector performance and the reduced  $W$  cross section, signed  $p_T$ -balance  $> 20$  GeV combined with  $R_{ESMD} > 0.6$  cuts are used to pick out the  $W$  candidates located in the up-right corner in Figure 4.9b, compared to the  $W \rightarrow e\nu$  MC distribution in Figure 4.9c.

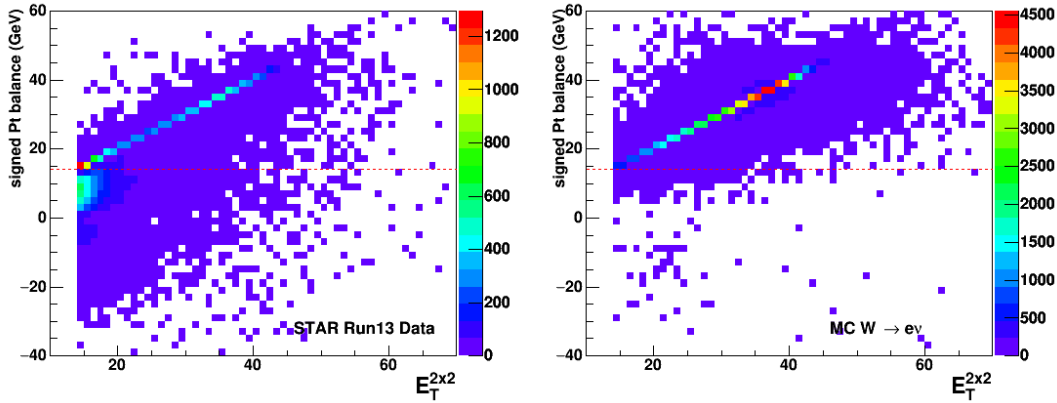


Figure 4.10: Signed  $p_T$ -balance vs  $E_T^e$  for run13 data on the left and  $W \rightarrow e\nu$  MC on the right. The red dash lines indicate the cut value.

#### 4.1.4 Jacobian Peak of $W$ Events

After all the selection cuts discussed above, the lepton  $E_T$  ( $p_T$ ) distribution is expected to peak around 40 GeV (half of the  $W$  mass). In the rest frame of  $W$ ,

there is relation  $p_T = M_W \sin\theta^*/2$ , where  $p_T$  and  $\theta^*$  are the lepton  $p_T$  and scattering angle respectively. Thus,

$$\cos\theta^* = \sqrt{1 - \frac{4p_T^2}{M_W^2}}, \quad (4.4)$$

$$\frac{d\cos\theta^*}{dp_T^2} = \frac{2}{M_W^2 \cos\theta^*}, \quad (4.5)$$

$$\frac{d\sigma}{dp_T^2} = \frac{d\sigma}{d\cos\theta^*} \times \frac{d\cos\theta^*}{dp_T^2} = \frac{d\sigma}{d\cos\theta^*} \times \frac{2}{M_W^2 \sqrt{1 - \frac{4p_T^2}{M_W^2}}} \quad (4.6)$$

where the cross section has a singularity at  $p_T = M_W/2$ . This is the so-called ‘‘Jacobian peak’’ characterizing two body decays. This is under the assumption that  $W$  has no transverse momentum ( $p_T^W = 0$ ) and zero width ( $\Gamma_W = 0$ ) for an ideal case. In practice, the  $p_T$  distribution would be smeared to a peak with finite maximum and width. Figure 4.11 shows the Leading Order (LO) and Next-to-Leading Order (NLO) theoretical predictions for lepton  $p_T$  distributions in  $W$  production.

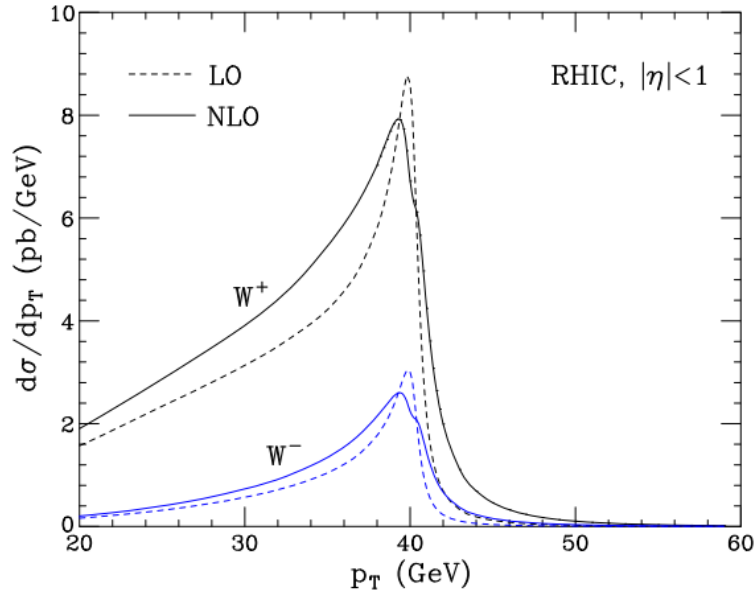


Figure 4.11: Leading Order and Next-to-Leading Order cross section at RHIC for  $l_+$  and  $l_-$  decaying from  $W^\pm$  bosons [71].

The  $E_T$  distributions of the electron candidates are shown in Figure 4.12a-4.12d for 2011+2012 and 2013 for Barrel and Endcap regions respectively. Very visibly,

the Jacobian peaks pronounce more and more as applying the selection cuts step by step. Under the peak, there is still a smooth background which is dominated in low  $E_T$  range but can extend to  $W$  signal region. The background contamination will be discussed in detail later.

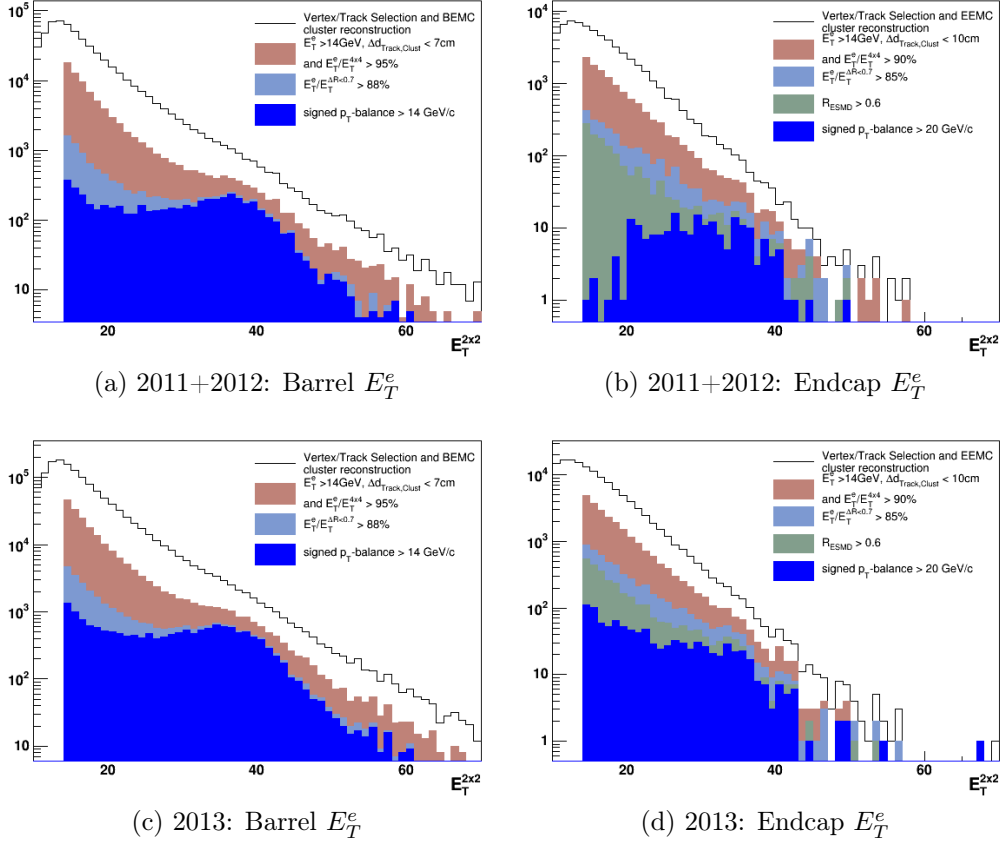


Figure 4.12:  $E_T^e$  spectrum of candidate electrons from cluster construction to final selection, different color histograms indicate different selection stages, (a)(c) for Barrel region, (b)(d) for Endcap region, for 2011+2012 and 2013 respectively.

### 4.1.5 Charge Separation

As described in Section 1.2, the longitudinal single-spin asymmetries for  $W^+$  and  $W^-$  are expected to have opposite signs. Therefore, it is crucial to correctly reconstruct the charge signs of the candidate  $e^\pm$  from  $W^\pm$  decay, and to well estimate the possible wrong sign contamination. The core information that TPC provides is the track momentum and it is very precise for low and medium  $p_T$  tracks. However, the resolution becomes poor for high  $p_T$  region due to the small curvature. For this

analysis, the value of the curvatures of the candidate electron tracks would not be precise enough for such a high  $p_T$  range. But we still can get the reliable charge information from how track bend in the magnetic field, to left or right.

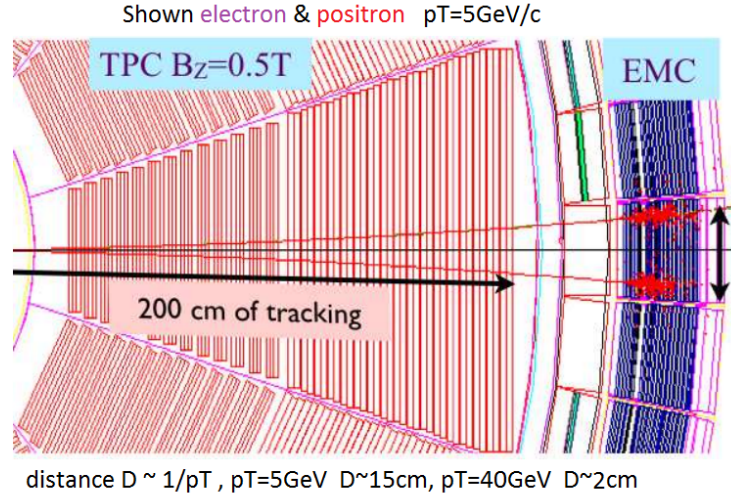


Figure 4.13: Charge separation based on TPC track bending

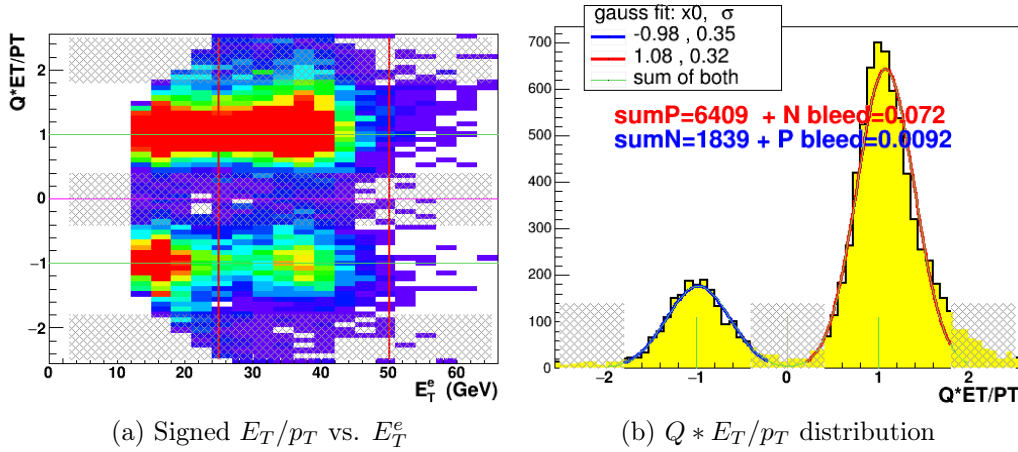


Figure 4.14: Barrel: Ratio of  $E_T$  and  $p_T$  with reconstructed charge sign  $Q$  as function of  $E_T^e$  (a) and the projection of  $25 < E_T < 50$  GeV range which is used to estimate the charge contamination via fitting

Figure 4.13 shows two simulated TPC tracks with opposite signs at  $p_T = 5$  GeV, and they separate from each other by 15 cm when they leave TPC. The displacement between opposite charged tracks should be proportional to  $1/p_T$ . For leptons from  $W$  decay with  $p_T \sim 25$ -50 GeV, the displacement would only be 1-2 cm. In principle, 1-2 cm spatial resolution for TPC is not so hard with the hit

position resolution of mm. However, in 500 GeV pp collisions, there are a lot of pile-up events which left large number of tracks inside the TPC. This would cause significant ionization and nonlinearities. In order to correct the distortion, an offline TPC calibration has been applied. Figure 4.14a shows the distribution of ratio of  $E_T$  and  $p_T$  with reconstructed charge sign  $Q$  as function of  $E_T^e$ , where we can see that the well separated two bands centered at +1 and -1 respectively. The shadowing areas indicate the  $Q * E_T/p_T$  cut which excludes the overlap region  $|Q * E_T/p_T| < 0.4$  and the tails  $|Q * E_T/p_T| > 1.8$ . The red bold lines indicate the signal window, 25-50 GeV. The distribution of  $Q * E_T/p_T$  in the signal  $E_T$  window is shown in Figure 4.14b. There is a clear valley between candidates with opposite charge signs. The curves are from double Gaussian fitting, and the wrong charge sign contamination under each peak is negligible after excluding the shadowing region.

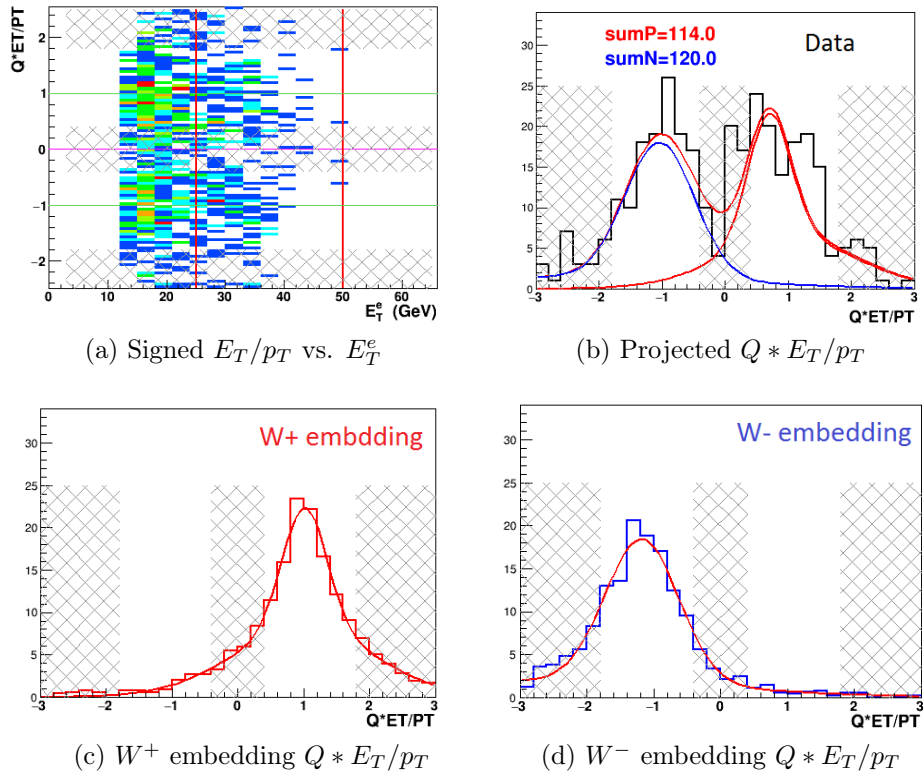


Figure 4.15: Endcap: (a) Ratio of  $E_T$  and  $p_T$  with reconstructed charge sign  $Q$  as function of  $E_T^e$  (b) projection on  $Q * E_T/p_T$  axis of (a) in  $E_T^e$  signal window, with fitting based on curve from (c) and (d). (c)  $W^+$  and (d)  $W^-$  embedding with Gaussian fitting.

For the Endcap region, the TPC capacity reduces due to the TPC hits reduction where the forward tracks don't cross the whole radius. Both  $p_T$  resolution and the

charge reconstruction get worse. In Figure 4.15a, the separation of two bands with opposite charge signs is significantly worse than that in Figure 4.14a for Barrel region. Figure 4.15b shows the projection on  $Q * E_T/p_T$  for  $25 < E_T^e < 50\text{GeV}$ . As expected, both peaks spread widely and overlap with each other. In order to get the fitting function with reasonable parameters, independently fittings on the  $Q * E_T/p_T$  distributions are performed for embedding sample shown in Figure 4.15c and 4.15d for  $W^+$  and  $W^-$  respectively, instead of directly fitting on the data. The double Gaussian curves are used to fit the data as shown in Figure 4.15b. After excluding the shadow region ( $|Q * E_T/p_T| < 0.4$  or  $> 1.8$ ), the wrong charge sign contamination is estimated by extending the double Gaussian into the opposite charge window. For 2013, the contaminations for  $W^+$  and  $W^-$  are 4.1% and 7.2% respectively. For 2011+2012, the contaminations for  $W^+$  and  $W^-$  are both 6.5%.

## 4.2 $Z \rightarrow e^+e^-$ Reconstruction

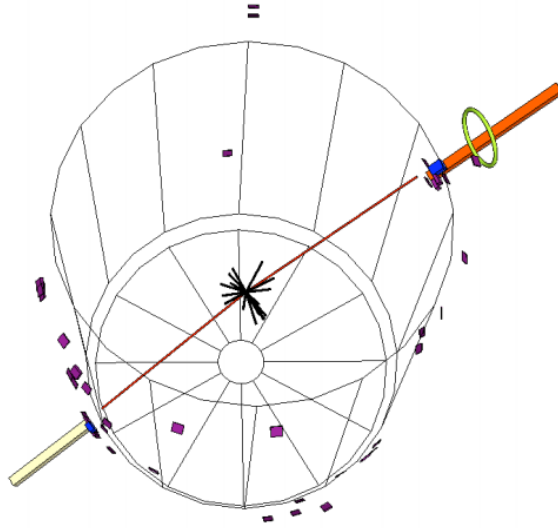


Figure 4.16:  $Z \rightarrow e^+e^-$  event

The  $Z \rightarrow e^+e^-$  events have very similar features with the  $W \rightarrow e\nu$  events. The only difference is the neutrino from  $W$  decay is undetected but the electron-positron pair can be fully reconstructed. Along with the  $W$  reconstruction, the  $Z \rightarrow e^+e^-$  events are reconstructed in the same way except for the signed  $p_T$ -balance cut. As shown in Figure 4.16, a  $Z \rightarrow e^+e^-$  event contains a pair of back to back isolated leptons with opposite charge signs. Except the electron positron pairing, same

vertex, track and isolation cuts as for Barrel  $W$ s are applied. Figure 4.17 shows the reconstructed invariant mass spectrum of  $Z$  candidates with comparison to MC sample. There is a clear peak at  $m_{e^+e^-} \sim M_Z$ . Besides the  $Z$  signal, there is a small smooth peak at lower mass which is likely from the Drell-Yan processes, and the spectrum is consistent with the simulated  $Z/\gamma^* \rightarrow e^+e^-$  sample.

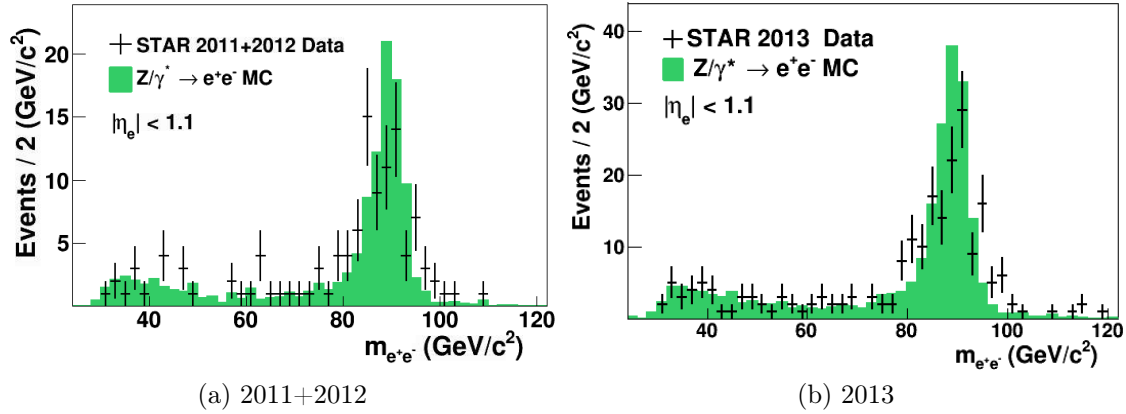


Figure 4.17: Invariant mass distribution of  $Z/\gamma^*$  with comparison between data and MC, for 2011+2012 and 2013 separately.

### 4.3 Definition of $\eta$ -bins

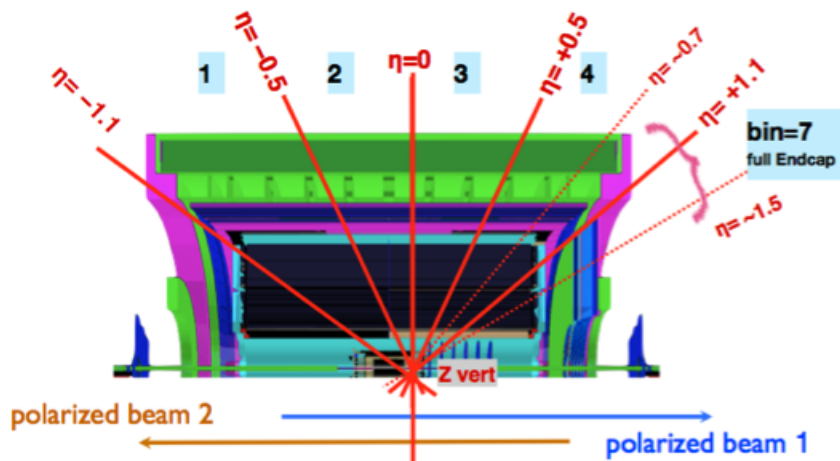


Figure 4.18:  $\eta$  bin index definition in STAR detector and in physics referring to the polarized beam.

Our goal is to measure the parity-violating longitudinal single-spin asymmetry,  $A_L$ , of  $W$  boson production as the function of the lepton pseudorapidity. In order to extract the pseudorapidity dependence, it is natural to sort the final  $W$  candidates into different intervals based on the pseudorapidity of the leptons. The residual background fraction is sensitive to the detector efficiency which significantly depends on the pseudorapidity. The well division of the  $\eta$  bins is necessary for the spin asymmetry extraction and the background estimation. The definition of the  $\eta$  bins with respect to STAR detector coordinates and to the beam polarization is described in the section.

In the coordinate of STAR detector, the Barrel Electromagnetic Calorimeter covers the  $\eta$  range  $-1 < \eta < 1$  where is the region with best TPC performance. It is divided into 4 bins in this analysis. As shown in Figure 4.18, these 4  $\eta$  bins are labeled as 1, 2, 3, 4 with their regions indicated in the figure. For the Endcap region, the  $W$  yields are limited by detector acceptance. It is not further divided and label as bin 7. The detector  $\eta$  coverage is obtained with the assumption that the tracks always originate from the very center of STAR,  $z=0$ . Due to the spread of the vertex distribution in  $z$  direction, the  $\eta$  range of lepton detected in both Barrel and Endcap are actually extended from their default  $\eta$  ranges. Thus, the lepton  $\eta$  ranges of eta bin 1, 4 and 7 are slightly extended to include more candidates in the edge of the Calorimeters.

## 4.4 Background Study

After all selection cuts described previously in Section 4.1, the  $E_T$  distribution of lepton candidates is obtained as shown in Figure 4.12. As expected, it contains a ‘‘Jacobian Peak’’ and a smoothly varying background shape. Since the  $W$  selection is based on its kinematic and topological features instead of relying on any particle identifications or invariant mass, there is possibility to keep some backgrounds which survive from all the selection cuts. The residual backgrounds may contain a couple of well-understood electroweak processes and the QCD events whose jet fragmentation happen to pass the isolation cuts and further have some energy undetected and passed the signed  $p_T$ -balance cut. The electroweak backgrounds can be estimated from embedding MC simulation. The QCD background is the predominated part due to its relatively huge cross section, and it is expected to have

a smooth and exponential shape. The QCD background can be estimated using a data-driven method.

Similar with Section 4.1, the plots from 2013 dataset are taken for example to describe how the background contributions are estimated. Some key plots from 2011+2012 data will be shown in the summary part.

#### 4.4.1 Electroweak Backgrounds

As listed in Table 4.2,  $W$  boson can decay to  $\tau + \nu$  with similar branching ratio as  $e + \nu$  signal. When  $\tau$  further decays to  $e + \nu_e + \nu_\tau$  (see Table 4.3), it would be a fake signal which cannot be distinguished from  $W \rightarrow e + \nu$  events although its  $E_T$  should be relatively lower than lepton  $E_T$  directly from  $W$  decay. The contamination from  $\tau$  is estimated via embedding simulation described in Section 3.2.2.

Decay mode	Fraction
$e^+ + \nu$	$(10.71 \pm 0.16)\%$
$\mu^+ + \nu$	$(10.63 \pm 0.15)\%$
$\tau^+ + \nu$	$(11.38 \pm 0.21)\%$
hadrons	$(67.41 \pm 0.27)\%$
invisible	$(1.4 \pm 2.9)\%$

Table 4.2:  $W^+$  boson primary decay modes [3].

For  $W$  boson, its  $e\nu$  decay and  $\tau\nu$  decay processes are in very similar way and are expected to have exactly the same spin asymmetries,  $A_L$  and  $A_{LL}$ . The only difference is on the measured final states. For  $e\nu$  decay, the rapidity of the final state  $e^\pm$  can be measured directly. However for  $\tau\nu$  decay, what is measured in laboratory is the child electron from  $\tau$  decay. According to the Michel spectrum [3] of the polarized  $\tau$  decay, the  $e^+(e^-)$  tends to be emitted in  $\tau^+(\tau^-)$  momentum direction, which has been discussed in Ref. [72]. Therefore, the contamination from

Decay mode	Fraction
$e^- + \bar{\nu}_e + \nu_\tau$	$(17.83 \pm 0.04)\%$
$\mu^- + \bar{\nu}_\mu + \nu_\tau$	$(17.41 \pm 0.04)\%$
charge hadron	majority

Table 4.3:  $\tau^-$  semi-leptonic decay modes [3].

Decay mode	Fraction
$e^+ + e^-$	$(3.363 \pm 0.004)\%$
$\mu^+ + \mu^-$	$(3.366 \pm 0.004)\%$
$\tau^+ + \tau^-$	$(3.370 \pm 0.004)\%$
invisible	$(20.00 \pm 0.06)\%$
hadrons	$(69.91 \pm 0.06)\%$

Table 4.4: Some of  $Z$  boson decay modes [3].

$\tau\nu$  decay should not impact the results of the spin asymmetry in this analysis, and is simply treated as signal in the single-spin asymmetry extraction.

As discussed in Section 4.2, the  $e^\pm$  from  $Z \rightarrow e^+e^-$  has same isolation behaviors as the  $e^\pm$  from  $W$  decay, expect for its opposite-sign pair production. However, STAR detector are not hermetic. If one of the  $e^\pm$  is undetected, it will be impossible to distinguish such a  $Z$  event from  $W \rightarrow e\nu$  event. In spite of the limited cross section of  $Z$  at RHIC energy and its small branching ratio to  $e^+e^-$  (see Table 4.4), we still need to consider this contribution both to signal and to QCD background. The contamination from  $Z \rightarrow e^+e^-$  is estimated from embedding MC simulation. Applying all the  $W$  selection cuts on the  $Z \rightarrow e^+e^-$  embedding sample as described in Section 4.2, the background contributed from this channel can be estimated from the events passing all  $W$  criteria. Plots in Figure 4.19 are the integral luminosity normalized distributions for  $Z$  background under the raw signal  $E_T$  spectrum, for both run 13 period I and period II and  $W^+$  and  $W^-$  respectively. Here, only Barrel region is shown. For Endcap, the method is same, but with a little difference which will be discussed later in Section 4.4.2.

#### 4.4.2 Second Endcap Background for Barrel $W$

STAR has single Endcap EM calorimeter covering forward pseudo-rapidity range of  $1.09 < \eta < 2$  which has been described in Section 2.2.3. For Barrel  $W$  selection, EEMC can help to reject QCD events, e.g. for a di-jet event that one of the jets is in the range of interest and passes all the isolation cuts and another jet is located at Endcap region. But if another jet is located at the nonexistent Endcap region, for an event as in above example, it would be accepted as a “good”  $W$  event. Let us name this kind of background as “Second Endcap” background (or EEMC background) which is caused by the “absence” of the second EEMC.

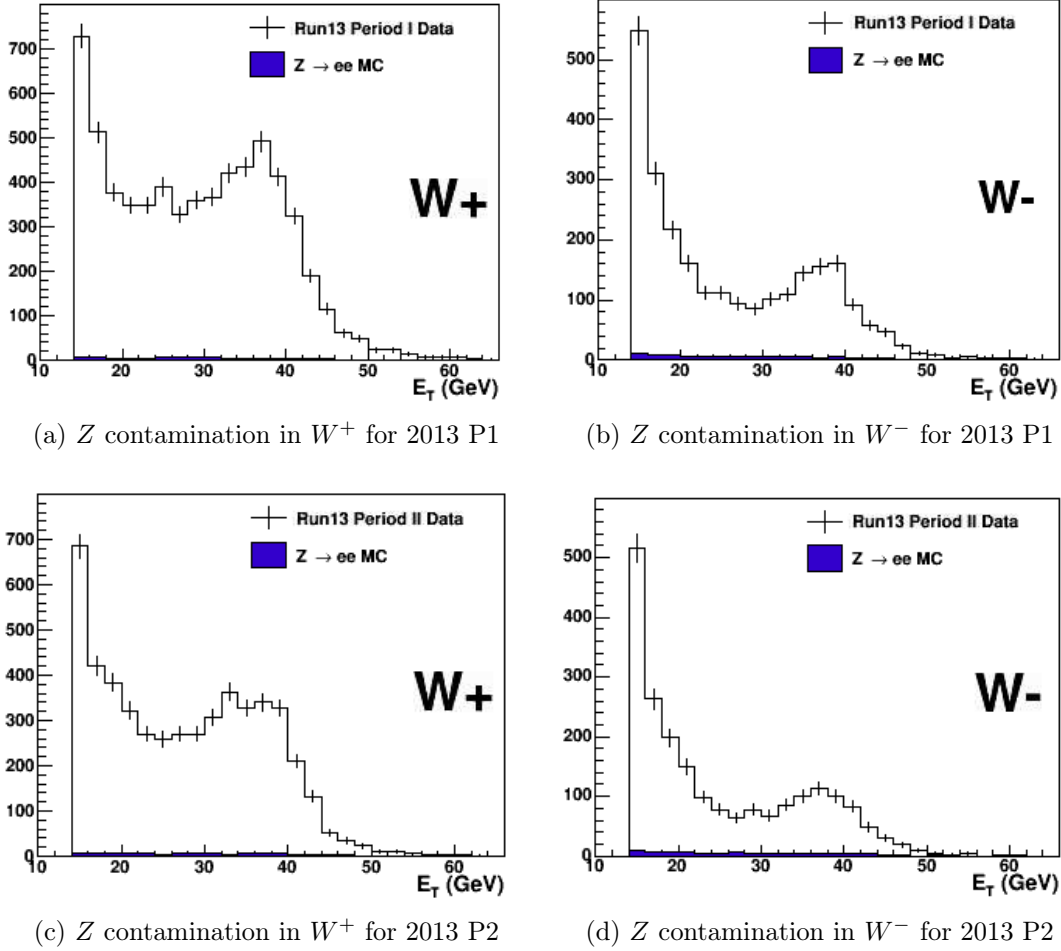


Figure 4.19:  $Z/\gamma^* \rightarrow e^+e^-$  background contribution in  $W \rightarrow e\nu$  raw signal  $E_T$  spectrum for both  $W^+$  and  $W^-$  and both periods of 2013 (P1 and P2 in the sub-captions).

The Second Endcap background can be estimated based on what is learned from the existent real EEMC. In practice, the procedure is made by running the analysis twice, one with the EEMC and the other without the EEMC. From Section 4.1, it is known that EEMC gets involved in the signed  $p_T$ -balance calculation and the isolation ratio in near side cone. There is no doubt that the first time running would reject more background events than the second times. The difference of these two times is just the background that the EEMC help to reject. This is a reasonable estimation of the “second Endcap” background. Considering the possible correlation of the two jets in QCD events, we use an individual  $\eta$ -region to estimate the second Endcap for its mirror  $\eta$ -region in lab frame. In addition, there are some

minor asymmetric dead regions in STAR TPC and BEMC. Such kind of acceptance effects are also corrected.

Cartons in Figure 4.20 demonstrate how the second Endcap background estimation works, where bin=1 and bin=4 referred the division of the  $\eta$ -intervals introduced in Section 4.3. It is worth to note that they are a pair of symmetric  $\eta$  bins on east and west sides of STAR detector. For bin=1, a forward-forward di-jet event has passed previous cuts would be accepted as signal due to the non-coverage of the missing “second Endcap”. This can be estimated in bin=4 using the method described above. Similarly, for bin=4, contribution from forward-backward di-jet event can be estimation in bin=1. Figure 4.21 shows 4 sets of plots for both periods of run13,  $W^+$  and  $W^-$  respectively, with the second Endcap background  $E_T$  distributions under the corresponding raw  $W$  signal  $E_T$  spectrum. There are 4 plots in each set which are for 4  $\eta$ -bins in the full Barrel region. There is significant  $\eta$  dependence for the Second Endcap background, which is an indication of the possible  $\eta$  correlation for the di-jet events. In addition, for the eta bin 1 and 4, the EEMC contributes to suppress the jet like event in the near cone isolation ratio construction.

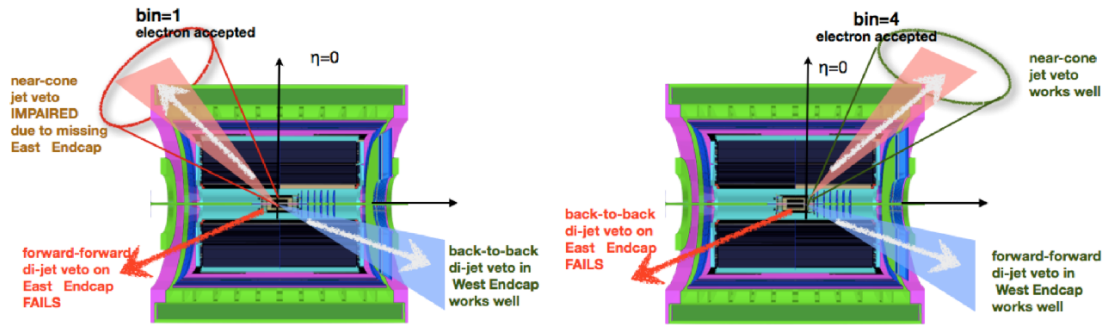


Figure 4.20: Estimate the second Endcap background for one  $\eta$  range from its mirror  $\eta$ -range, considering the forward-forward and forward-backward di-jet background events.

As has been mentioned in Section 4.4.1,  $Z \rightarrow e^+e^-$  events are also involved in second Endcap procedure. Instead of the di-jet,  $e^+e^-$  from  $Z$  decay have the same story in this procedure. To avoid the double counting of the contribution from  $Z \rightarrow e^+e^-$ , so, it is needed to exclude this part in either of  $Z \rightarrow e^+e^-$  background of the second Endcap background.  $Z$  contribution in second Endcap background

can be estimated via the same method, running the analysis twice on  $Z$  embedding sample with and without the EEMC.

Obviously, the second Endcap method is only suitable for background analysis for Barrel region. For analysis in Endcap region, this procedure is skipped.

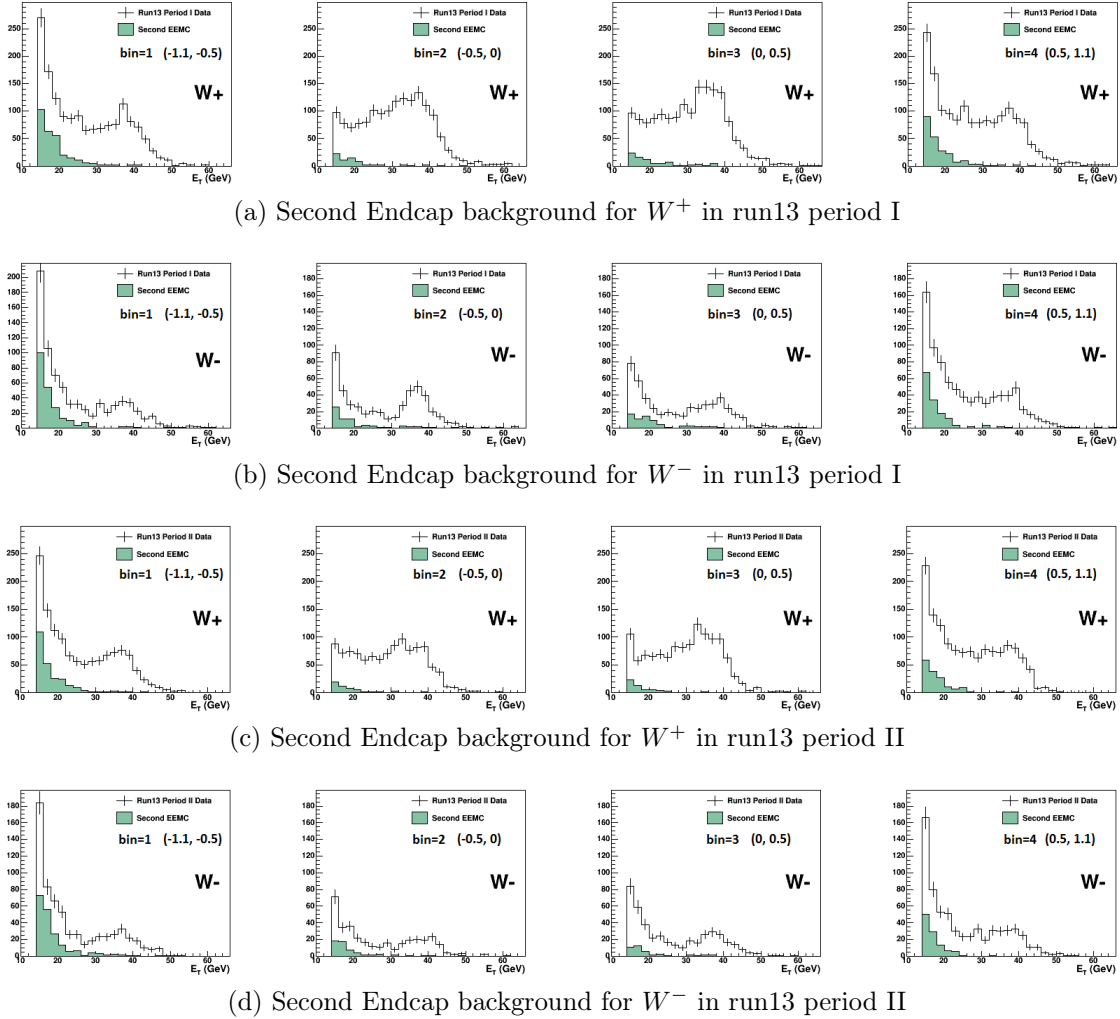


Figure 4.21: Second Endcap background contribution in  $W \rightarrow e\nu$  raw signal  $E_T$  spectrum for both charge signs and both periods of run13.

#### 4.4.3 Data-driven QCD Background for Barrel $W$

Other than the background contributions described above, another main contribution is from QCD di-jet events, which have one jet passing through the isolation cuts and the other is outside the range of all BEMC, EEMC and the fictitious second

EEMC. The  $E_T$  spectrum of this QCD background is estimated by using a data-driven procedure. It is expected to have exponential-like shape. The  $E_T$  shape used for data-driven is obtained from events which have passed all  $W$  selection cuts but failed the signed  $p_T$ -balance cut. Here, it is assumed that the  $E_T$  distribution behavior for QCD events with one jet is accepted as  $W$  decay electron (positron) should not depend on the signed  $p_T$ -balance value. In addition, there is definitely  $Z \rightarrow e^+e^-$  events among this QCD sample. Just similar with what is done in Second Endcap part, the  $Z$  contribution in the QCD sample used in data-driven is estimated from the embedding MC simulation.

Another cuts used here is removing the events like  $Z \rightarrow e^+e^-$  by pairing the candidate “electrons” with jets in back side in  $\phi$  which are required to contain an  $2 \times 2$  cluster with  $E_T^{2 \times 2}/E_T^{jet} > 0.5$ , and reconstructing an invariant mass of the candidate electron and the paired jet. If this invariant mass happens to be in range 70-100 GeV, this event will be tagged a  $Z$ -like event and cut off it. This is not mentioned in Section 4.1 because this cut doesn’t impacts the  $W$  selection. But, it does remove some events in the QCD sample which will be used for data-driven.

The prerequisite for the data-driven procedure is two  $E_T$  distributions: one is of the QCD sample just as described above, another one is the raw signal  $E_T$  spectrum with all the other backgrounds discussed in previous sections subtracted. With these two distributions, the normalization is done in  $E_T$  window [14,18] GeV, where is expected to be dominated by QCD events. But, for the backgrounds subtracted signal spectrum, there should be still some signal “contaminating” this background window. The embedding sample of  $W \rightarrow e\nu$  single is used to estimate this contamination. By considering all these factors, the QCD distribution is normalized to be consistent with the raw signal  $E_T$  distribution in the normalization window. This normalized QCD distribution is just referred to as the data-driven QCD background remains in the raw signal spectrum. Figure 4.22 shows the distributions in data-driven procedures. The ratio to scale the QCD distribution (blue histogram) is calculated from the bin counts of signal distribution (red histogram) in the window subtracting the MC-base estimated signal contamination over the bin counts of the QCD distribution. The blue dash histograms are the results of data-driven QCD.

Figure 4.23 and 4.24 show the  $E_T$  distributions of the raw signal in Barrel region respectively for 2011+2012 and 2013 and for both  $W^+$  and  $W^-$  with all

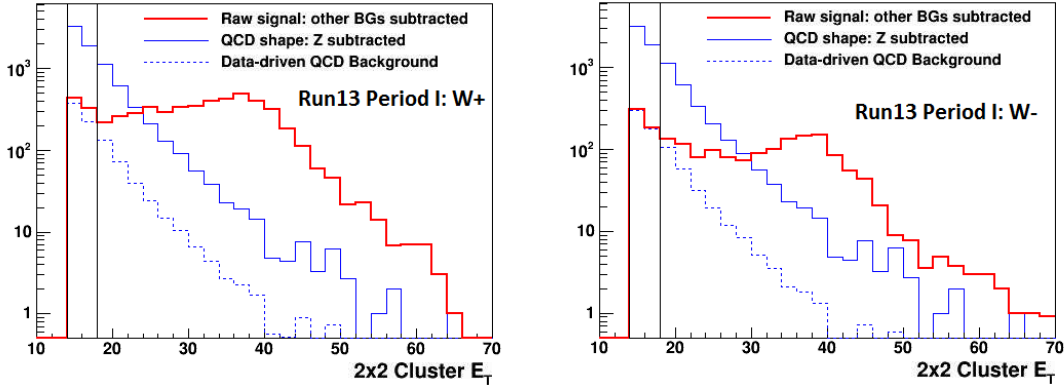
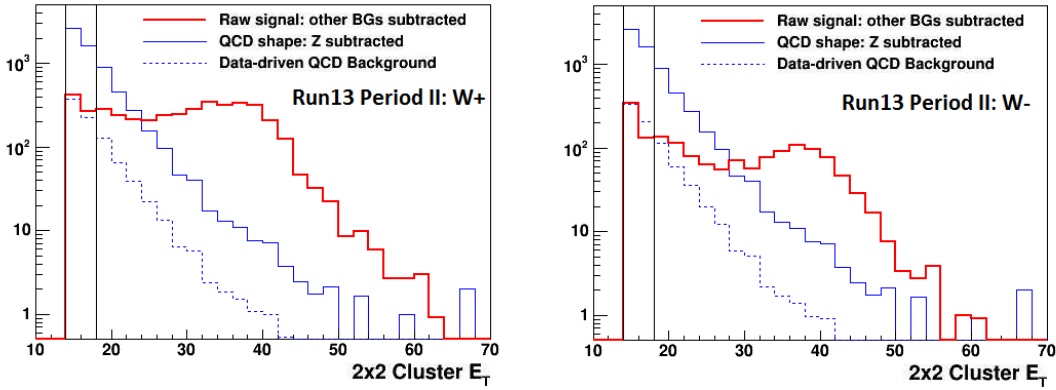
(a) Data-driven QCD background for  $W^+$  in 2013 period I(b) Data-driven QCD background for  $W^-$  in 2013 period I(c) Data-driven QCD background for  $W^+$  in 2013 period II(d) Data-driven QCD background for  $W^-$  in 2013 period II

Figure 4.22: Data-driven QCD background: Red histograms are the raw signal spectrum with all other backgrounds subtracted, blue solid histograms are the QCD spectrum for data-driven, blue dash histograms are normalized the data-driven QCD background results. The black boxes indicate the normalization window. Run periods and charge signs are put on the plots.

the background (color histograms in electronic version) and additionally including the embedding simulation of the signal  $W \rightarrow e\nu$  as comparison. For 2011+2012,  $\eta$ -bin 1 and 4, 2 and 3 have been merged together. Including all the background contributions, the MC curves (dashed line) are consistent with data  $E_T$  distributions for 2011+2012. For 2013 data, while the data and MC well agree with each other for forward bins, bin1 and bin4, the middle two bins, bin2 and bin3 show visible discrepancies where the  $W$  yields for data are lower than the MC curves around the Jacobian peak,  $30\sim 40$  GeV. This indicates an “ $\eta$ -dip” which appears in  $W$  reconstruction from data but isn’t reflected in the embedding procedure. The

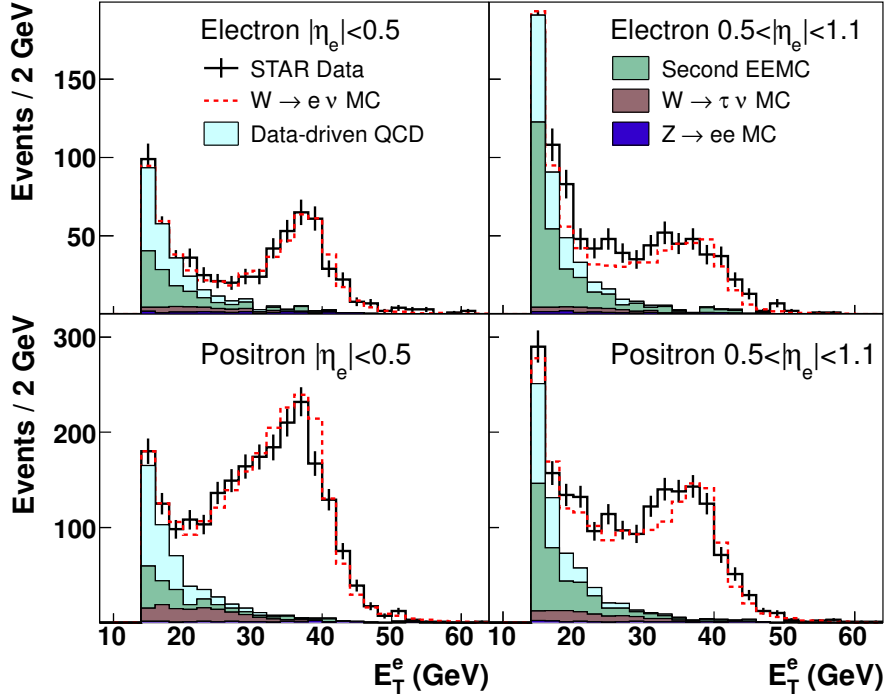
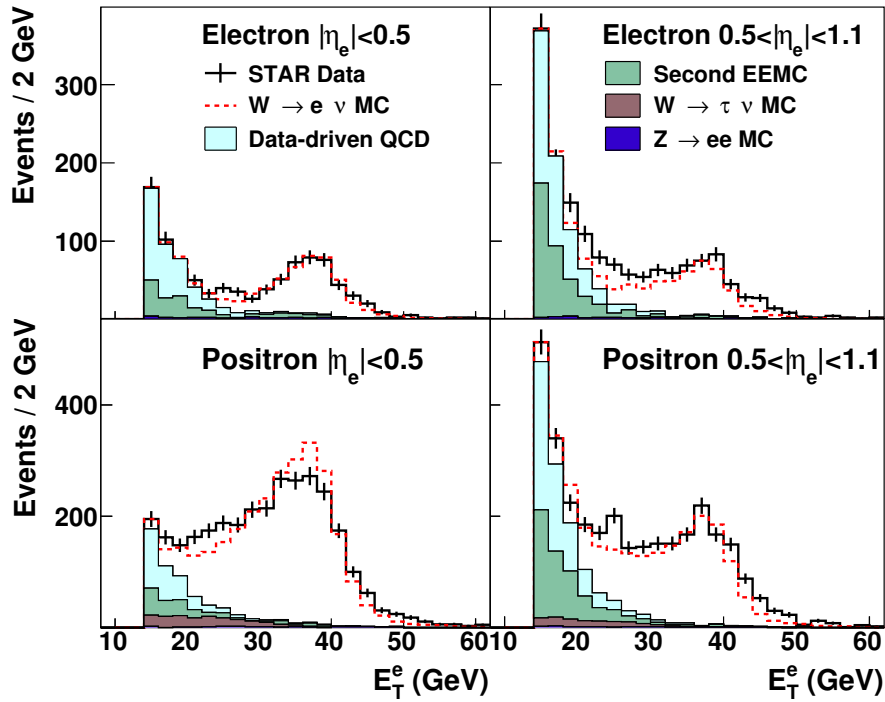
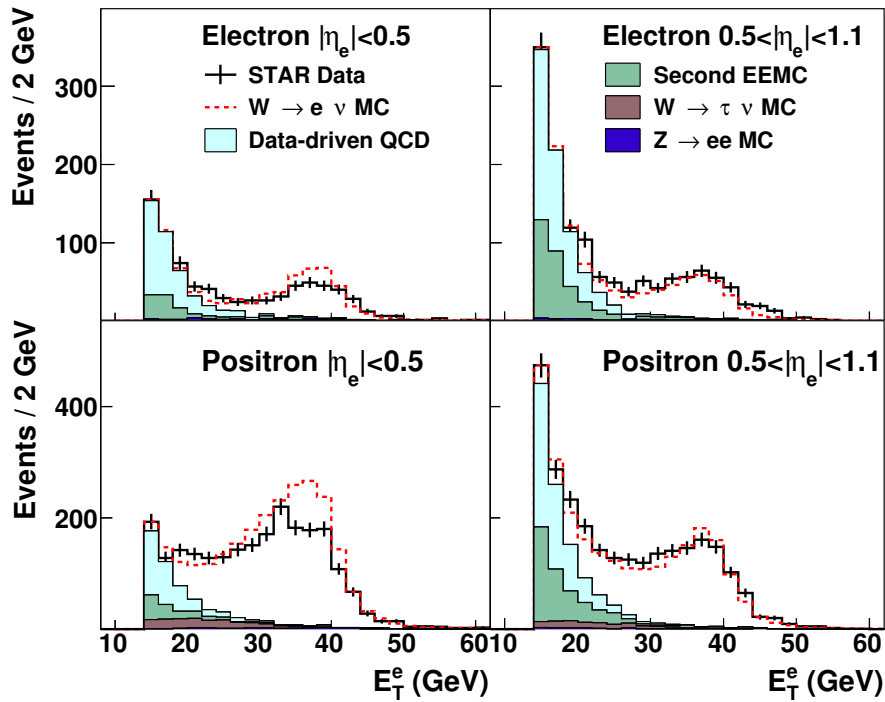


Figure 4.23: Electron  $E_T$  spectrum of Barrel  $W^+$  and  $W^-$  production with all background contributions in 2011+2012 data at STAR [73].

“ $\eta$ -dip” shows significant luminosity dependence. In 2013, the instantaneous luminosity increased from 2011 and 2012 and luminosity of period II were further higher than that of period I. It can be observed that the discrepancies of data and MC for middle bins pronounce more for period II than period I. At STAR, a new tracking algorithm is being developed and hopefully can improve the  $W$  reconstruction efficiency especially for high luminosity region. For this stage, the “ $\eta$ -dip” issue is thought to be spin-independent and should not impact the single-spin asymmetry result. In addition, the calibration of tower gains for the BEMC and EEMC also can impact the data and MC comparison since the embedding sample doesn’t depend on the calibration but the data sample does. Fortunately, the longitudinal single-spin asymmetry measurement in this analysis is insensitive to the calibration. A few percent difference from tower gain calibration can treat as a slight shift of  $\sim 1$  GeV for the lepton  $E_T$  cut which is negligible for the spin asymmetry extraction.



(a) Barrel backgrounds for run13 period I



(b) Barrel backgrounds for run13 period II

Figure 4.24: Electron  $E_T$  spectrum of Barrel  $W^+$  and  $W^-$  production with all background contributions in 2013 data at STAR.

#### 4.4.4 Background Study for Endcap $W$

The background study in Endcap region is very similar with that in Barrel region. The electroweak backgrounds are estimated via embedding MC simulation. It has been discussed above in Section 4.4.2 that the Second Endcap method used in Barrel background analysis is not suitable again for Endcap background analysis. Other than that, a similar data-driven procedure is implemented. The QCD background is estimated from the shape of the signed  $p_T$ -balance distribution for events with  $R_{ESMC} < 0.5$ . As discussed in Section 4.1.2,  $R_{ESMD}$  cut can effectively separate the QCD fragmentation from isolated electrons. Events which have passed all the isolation cuts but failed the  $R_{ESMD}$  cut is expected to be dominated by QCD background. The signed  $p_T$ -balance distribution should be a smoothly varying shape peaking around 0. On the other side, for the raw signal, the signed  $p_T$ -balance distribution is expected to contain real  $W$ s which mainly concentrated in large value range and a smooth background shape. The background shape is expected to peak around 0 in principle and extends to the signal range. With same logic, the data-driven estimation is done by normalizing the background distribution to the raw signal distribution in a QCD dominated window. In this analysis,  $[-8, 8]$  GeV is used. The normalization windows used in data-driven for both Endcap and Barrel are determined to be a “safe” interval. The effects by shifting the window are included in the systematic uncertainties. Figure 4.25 and Figure 4.26 show the signed  $p_T$ -balance distributions for  $W^+$  and  $W^-$  productions respectively for 2011+2012 and two periods of 2013 data with all the background contributions. Details can be found from the legends.

#### 4.4.5 Background Summary and Systematic Uncertainty

With the analysis discussed in this section, the residual backgrounds can be quantified into a dilution factor,  $\beta = \text{Signal}/(\text{Signal} + \text{Background})$ , to quantitatively deal with the background contamination in the following spin asymmetry extraction. There are five (four for Endcap) components among the raw signal, including the real  $W \rightarrow e\nu$  events and the various backgrounds. The fraction of each component is denoted as  $f_i$ , where  $i$  stands for different type, signal or background. They are calculated in the signal  $E_T^c$  window  $[25,50]$  GeV in this analysis. Details are listed in below:

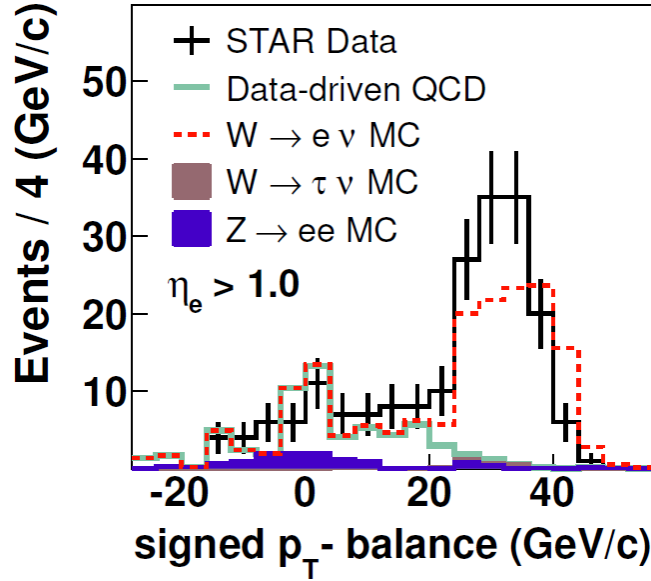


Figure 4.25: Signed  $p_T$ -balance distribution of Endcap  $W^\pm$  productions with all background contributions in 2011+2012 data at STAR [73].

- $f_W$ : fraction of  $W \rightarrow e\nu$  signal,
- $f_\tau$ : fraction of  $W \rightarrow \tau\nu$  ( $\tau \rightarrow e\nu\nu$ ) background,
- $f_Z$ : fraction of  $Z/\gamma^* \rightarrow e^+e^-$  backgrounds,
- $f_{EMC}$ : fraction of second Endcap background (only for Barrel region),
- $f_{QCD}$ : fraction of data-driven QCD background.

They satisfy  $\sum f_i = 1$  definitely.  $\beta$  can be reconstructed from these fractions:

$$\beta = 1 - f_Z - f_{EMC} - f_{QCD}. \quad (4.7)$$

It has been discussed in Section 4.4.1 that  $W \rightarrow \tau\nu$  would be treated as signal, so, it is not accounted into  $\beta$ . The statistical uncertainty of  $\beta$  is obtained from the propagation from those three components,  $\sqrt{\sum \sigma_{f_i}^2}$ , where  $\sigma_{f_i}$  is the statistical error of  $f_i$ .

$\beta$  is one of the key inputs to the single-spin asymmetry extraction. It is strongly related with the procedure of background suppression. Loosing or tightening cuts, the effects will finally go into  $\beta$ . The procedure of background estimation is one of

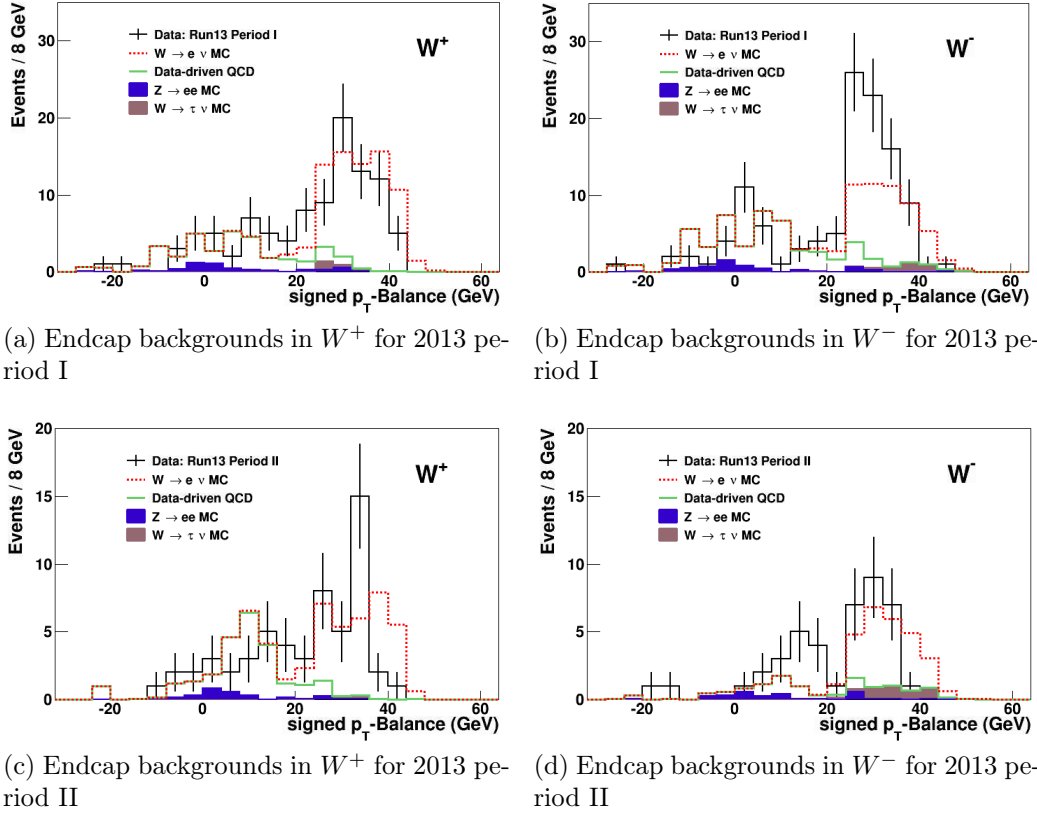


Figure 4.26: Signed  $p_T$ -balance distribution of Endcap  $W^\pm$  productions with all background contributions in 2013 data at STAR.

the main source of systematic uncertainty. In this section, the systematic uncertainty study will be discussed.

About the systematic uncertainty, there are two key points, the normalization window selection which is mentioned earlier and the QCD sample used for data-driven estimation. For the former one, the normalization is done in various windows with the lower bound being always 14 GeV where we cut off the low  $E_T$  particles in previous selection, and the upper bound varying from 16 GeV to 20 GeV in steps of 0.5 GeV. So, there will be 9 cases for normalization window selection. For the QCD sample selection, the “reversed” signed  $p_T$ -balance cut (“reversed” indicates the cut direction, just differing from signed  $p_T$ -balance cut in analysis) varies from 5 GeV to 25 GeV in step of 0.25 GeV. In this way there will be 81 different cases. Combining these two factors, 729 data-driven QCD shapes are obtained. As an example, Figure 4.27 shows the Barrel  $W^+$  candidates from run13 period I. There are 729 red data-driven QCD  $E_T$  distributions. It is clear to see how the QCD

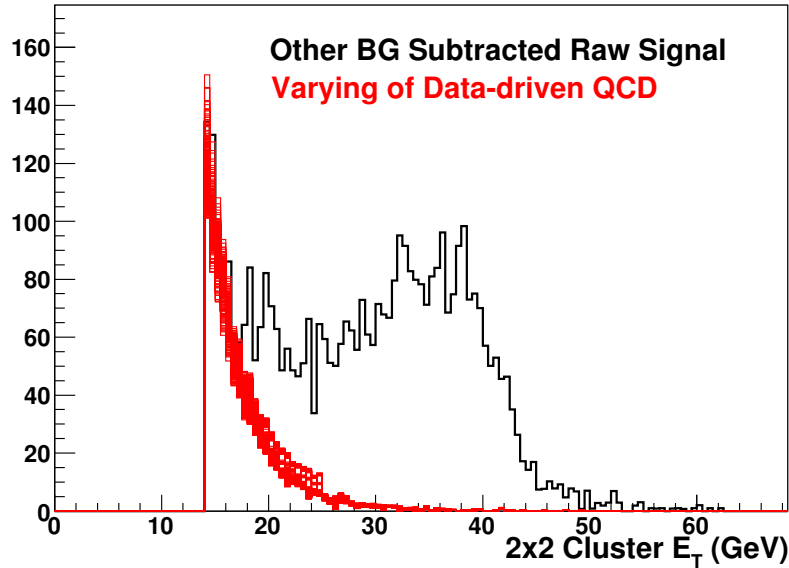


Figure 4.27: Data-driven QCD: 729 different shapes from 9 normalization windows and 81 QCD samples. This example shows for Barrel  $W^+$  candidates from run13 period I. The other parts are similar.

shapes vary for all these cases. It shows that the data-driven QCD is sensitive only in low  $E_T$  range, but fairly stable in high  $E_T$  range where the  $W$  signal is counted. The  $\beta$  distributions for all the cases for each Barrel eta bin for each charge and for each periods are listed in Figure 4.28.

The final values of  $\beta$  which will be used in asymmetry calculations are determined to be the mean values shown in Figures 4.28 and 4.29. The uncertainties are the quadratic sum of the systematic uncertainties,  $RMS$  from the  $\beta$  distributions and the statistical uncertainty described above,  $\sqrt{\sum \sigma_{f_i}^2}$ .

As mentioned in the beginning of this section, the background analysis described above are based on 2013 data sets. For 2011 and 2012, the same method was used. As a summary, Figure 4.30 shows the final results of  $\beta$  with errors for each eta bins for  $W^+$  and  $W^-$  and for run11, run12, and run13 period I, period II respectively. The corresponding numerical values are listed in Table 4.5. The background contamination factor  $\beta$  can be directly included in the asymmetry calculation in the following chapter.

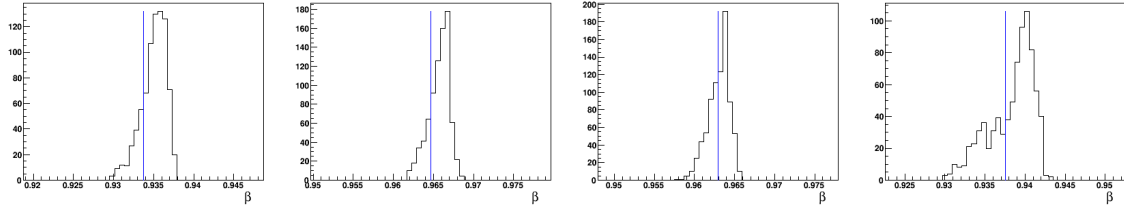
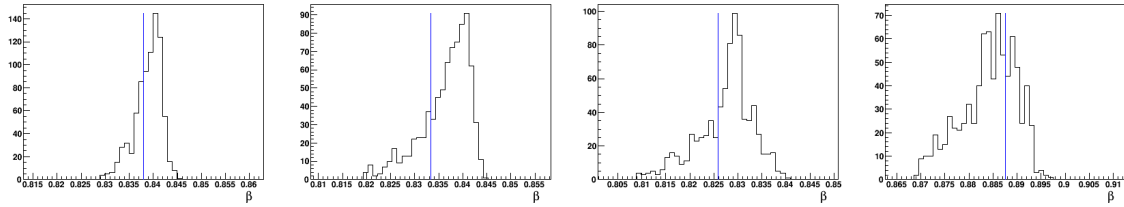
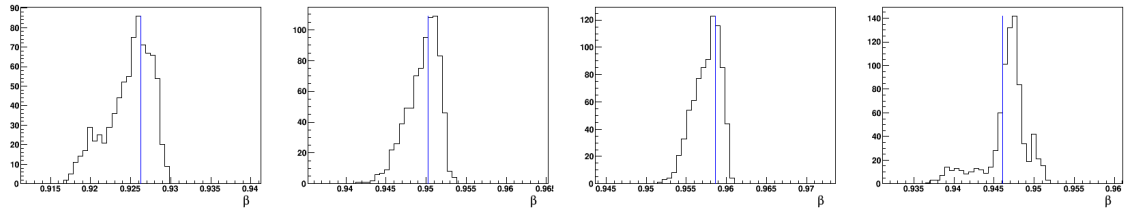
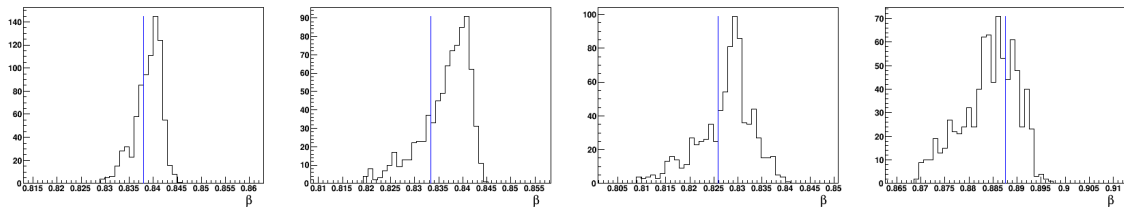
(a)  $\beta$  for  $W^+$  in run13 period I(b)  $\beta$  for  $W^-$  in run13 period I(c)  $\beta$  for  $W^+$  in run13 period II(d)  $\beta$  for  $W^-$  in run13 period II

Figure 4.28: Barrel:  $\beta$  distributions in systematic uncertainty study. In every rows, from left to right, they are for eta bin from 1 to 4. The blue line indicates the default  $\beta$  value used in Section 4.4.3.

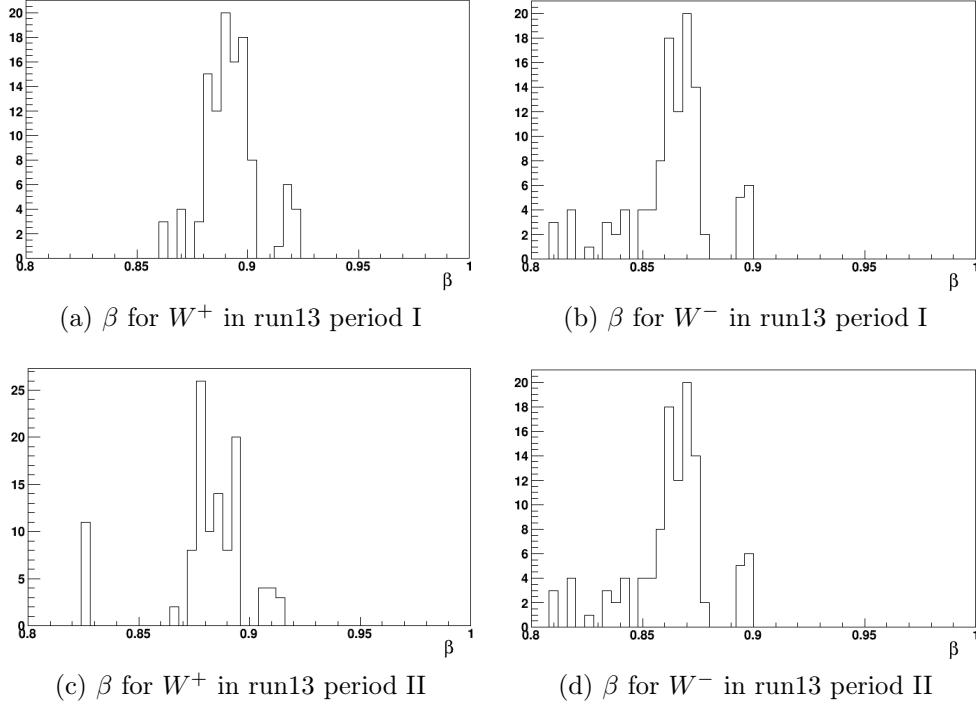
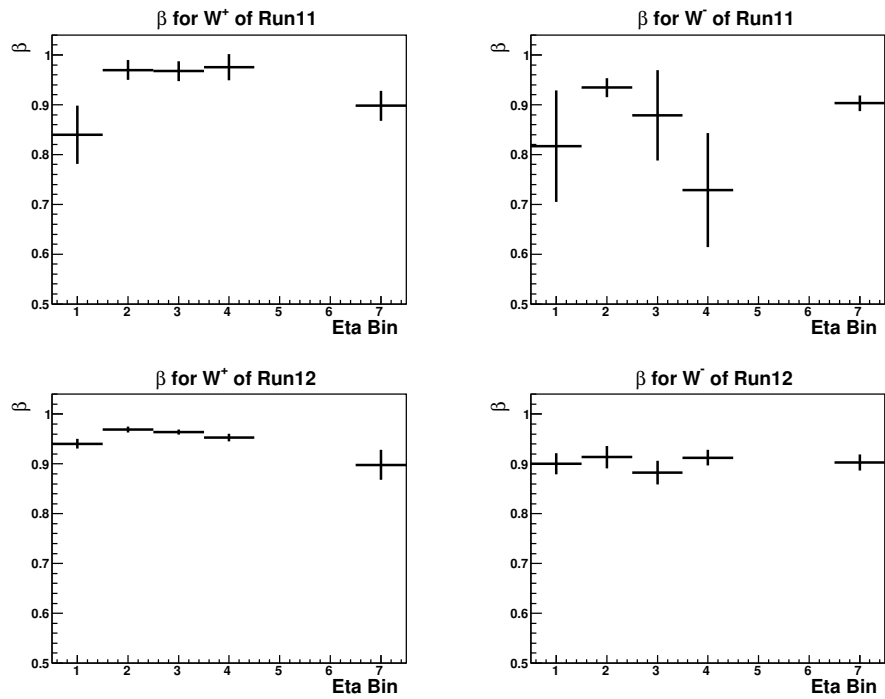


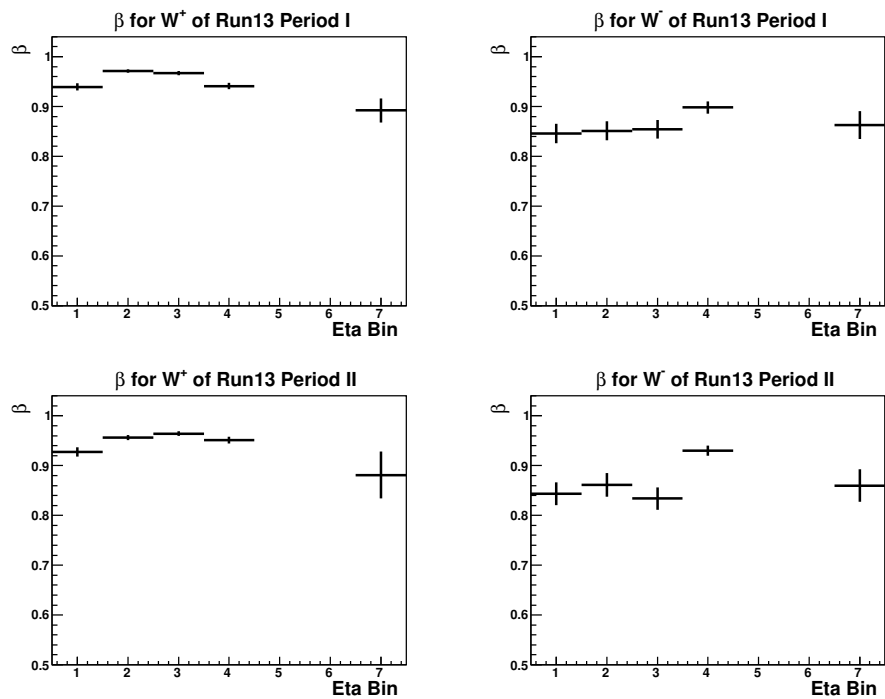
Figure 4.29: Endcap:  $\beta$  distributions in systematic uncertainty analysis. The blue line indicates the  $\beta$  value get in Section 4.4.3.

$\eta$ bin	1	2	3	4	7
2011 $W^+$	$0.84 \pm 0.06$	$0.97 \pm 0.02$	$0.97 \pm 0.02$	$0.98 \pm 0.03$	$0.90 \pm 0.03$
2011 $W^-$	$0.82 \pm 0.11$	$0.93 \pm 0.02$	$0.88 \pm 0.09$	$0.73 \pm 0.11$	$0.90 \pm 0.02$
2012 $W^+$	$0.94 \pm 0.01$	$0.97 \pm 0.01$	$0.96 \pm 0.01$	$0.95 \pm 0.01$	$0.90 \pm 0.03$
2012 $W^-$	$0.90 \pm 0.02$	$0.91 \pm 0.02$	$0.88 \pm 0.02$	$0.91 \pm 0.02$	$0.90 \pm 0.02$
2013 P. I $W^+$	$0.94 \pm 0.01$	$0.97 \pm 0.00$	$0.97 \pm 0.00$	$0.94 \pm 0.01$	$0.89 \pm 0.02$
2013 P. I $W^-$	$0.85 \pm 0.02$	$0.85 \pm 0.02$	$0.85 \pm 0.02$	$0.90 \pm 0.01$	$0.86 \pm 0.03$
2013 P. II $W^+$	$0.93 \pm 0.01$	$0.96 \pm 0.01$	$0.96 \pm 0.00$	$0.95 \pm 0.01$	$0.88 \pm 0.05$
2013 P. II $W^-$	$0.84 \pm 0.02$	$0.86 \pm 0.02$	$0.83 \pm 0.02$	$0.93 \pm 0.01$	$0.86 \pm 0.03$

Table 4.5:  $\beta$  values for all the eta bins, both  $W^+$  and  $W^-$ , corresponding to the data points in Figure 4.30.



(a) 2011+2012



(b) 2013

Figure 4.30:  $\beta$  with uncertainties, both statistical and systematic, for all the eta bins. Eta bin = 8 is for the full Barrel.



# Chapter 5

## Single-Spin Asymmetry Extraction

As discussed earlier, the measurement of parity-violating longitudinal single-spin asymmetry,  $A_L$ , for  $W$  production is one of the key parts of RHIC spin program. In this chapter, the  $A_L$  extraction and the results from 2011-2013 datasets will be given. The impact of STAR  $W$   $A_L$  measurements on the sea quark polarization will also be discussed.

### 5.1 Formulas of Single-Spin Asymmetry

The definition of  $A_L$  has been introduced in Section 1.2. In data analysis, Equation (1.13) can be written as

$$A_L = \frac{1}{P} \frac{N_+/l_+ - N_-/l_-}{N_+/l_+ + N_-/l_-}, \quad (5.1)$$

where  $P$  is the beam polarization,  $N_+$  ( $N_-$ ) is the  $W$  yield when the helicity of the polarized beam is positive (negative), and  $l_{\pm}$  are the relative luminosity correction factors to normalize the different luminosities of two helicity cases. At RHIC, both beams are polarized and 4 spin states of collisions ( $++$ ,  $+-$ ,  $-+$ , and  $--$ ) are provided (see Section 3.1.4). Single beam polarization can be obtained by summing up the other beam, e.g. summing  $++$  and  $+-$  gives one beam positively polarized and another beam unpolarized.

In longitudinally polarized  $pp$  collisions at STAR, the spin dependent yields detected in a given  $\eta$  range (e.g. eta bin 1 as described in Section 4.3) are expected to be impacted by the polarization of both beams  $P_1, P_2$  and the longitudinal single-

and double-spin asymmetries  $A_L, A_{LL}$  [74], as the formulas,

$$M_{++}^{\eta STAR} = N_{++}^{\eta STAR} / l_{++} = N_0 [1 + P_1 A_L(+\eta) + P_2 A_L(-\eta) + P_1 P_2 A_{LL}(|\eta|)] \quad (5.2)$$

$$M_{+-}^{\eta STAR} = N_{+-}^{\eta STAR} / l_{+-} = N_0 [1 + P_1 A_L(+\eta) - P_2 A_L(-\eta) - P_1 P_2 A_{LL}(|\eta|)] \quad (5.3)$$

$$M_{-+}^{\eta STAR} = N_{-+}^{\eta STAR} / l_{-+} = N_0 [1 - P_1 A_L(+\eta) + P_2 A_L(-\eta) - P_1 P_2 A_{LL}(|\eta|)] \quad (5.4)$$

$$M_{--}^{\eta STAR} = N_{--}^{\eta STAR} / l_{--} = N_0 [1 - P_1 A_L(+\eta) - P_2 A_L(-\eta) + P_1 P_2 A_{LL}(|\eta|)] \quad (5.5)$$

where  $N_i$  is the yield for each spin state,  $l_i$  is the relative luminosity correction factor mentioned above and will be discussed in detail later,  $M_i$  is the relative luminosity corrected yield,  $N_0$  is the expected yield of unpolarized collision,  $\eta^{STAR}$  denotes the pseudorapidity range referring to STAR detector, and  $\eta$  ( $-\eta$ ) denotes the pseudorapidity range referring to the blue (yellow) beam. The double-spin asymmetry  $A_{LL}$  is defined as

$$A_{LL} = \frac{(\sigma^{++} + \sigma^{--}) - (\sigma^{+-} + \sigma^{-+})}{(\sigma^{++} + \sigma^{--}) + (\sigma^{+-} + \sigma^{-+})}, \quad (5.6)$$

which is symmetric with  $\eta$  and  $-\eta$ . The background dilution effect is temporarily ignored here, and will be discussed in Section 5.2.

From Equation (5.2)-(5.5), the expressions of  $A_L(\eta)$ ,  $A_L(-\eta)$ , and  $A_{LL}$  can be derived as

$$A_L(\eta) = \frac{1}{P_1} \frac{M_{++}^{\eta STAR} + M_{+-}^{\eta STAR} - M_{-+}^{\eta STAR} - M_{--}^{\eta STAR}}{\sum_i M_i^{\eta STAR}}, \quad (5.7)$$

$$A_L(-\eta) = \frac{1}{P_2} \frac{M_{++}^{\eta STAR} - M_{+-}^{\eta STAR} + M_{-+}^{\eta STAR} - M_{--}^{\eta STAR}}{\sum_i M_i^{\eta STAR}}, \quad (5.8)$$

$$A_{LL}(|\eta|) = \frac{1}{P_1 P_2} \frac{M_{++}^{\eta STAR} - M_{+-}^{\eta STAR} - M_{-+}^{\eta STAR} + M_{--}^{\eta STAR}}{\sum_i M_i^{\eta STAR}}, \quad (5.9)$$

which are consistent with the definitions in Equation (5.1) and (5.6).

In Section 4.3, the Barrel and Endcap regions are divided into 5  $\eta$  bins, denoted as 1, 2, 3, 4, and 7 respectively. From the  $W$  yields in each bin,  $A_L$  for two different pseudorapidity values  $\eta$  and  $-\eta$  with respect to the blue or yellow beams respectively can be extracted. For bins in Barrel region, e.g.  $\eta$  bin 1 and  $\eta$  bin 4, they are symmetric with  $\eta = 0$ . In physical view,  $A_L(\eta)$  and  $A_L(-\eta)$  measured in  $\eta$  bin 1 are theoretically same with  $A_L(-\eta)$  and  $A_L(\eta)$  independently measured

in  $\eta$  bin 4. The  $A_L$  results can be calculated by combining these two independent measurements for same physical observable. It is similar for  $\eta$  bin 2 and  $\eta$  bin 3.

## 5.2 Background correction

The spin asymmetry formulas discussed in Section 5.1 are based on the assumption that the detected  $W$  yields are pure  $W \rightarrow e\nu$  signal. In practice, the correction of background contamination is needed to get the  $A_L^W$ . From the discussion in Section 4.4, it has been known that there are various residual backgrounds in the  $W$  raw signal spectrum, including electroweak and QCD backgrounds. Considering all these contributions, the  $A_L$  extracted from the spin sorted raw yields should be the linear combination of them:

$$A_L = f_W A_L^W + f_{W \rightarrow \tau} A_L^{W \rightarrow \tau} + f_{EEMC} A_L^{EEMC} + f_Z A_L^Z + f_{QCD} A_L^{QCD} \quad (5.10)$$

$$= (f_W + f_{W \rightarrow \tau}) A_L^W + f_{EEMC} A_L^{EEMC} + f_Z A_L^Z + f_{QCD} A_L^{QCD} \quad (5.11)$$

$$= (1 - f_{EEMC} - f_Z - f_{QCD}) A_L^W + f_{EEMC} A_L^{EEMC} + f_Z A_L^Z + f_{QCD} A_L^{QCD}, \quad (5.12)$$

where the  $f_i$  is the fraction of each component as introduced in Section 4.4.5, and the  $A_L^i$  is the corresponding single-spin asymmetry. From Equation (5.10)-(5.12),  $A_L^W$  can be extracted,

$$A_L^W = \frac{A_L - (f_{EEMC} A_L^{EEMC} + f_Z A_L^Z + f_{QCD} A_L^{QCD})}{1 - f_{EEMC} - f_Z - f_{QCD}} = \frac{A_L - \alpha}{\beta}, \quad (5.13)$$

where  $\beta$  is the background dilution factor described in Section 4.4.5,  $\alpha$  is the contribution from the polarized backgrounds. The QCD events (e.g. di-jet events) are expected to be parity conserved, so the  $A_L$  of QCD events should be zero. For the Second Endcap backgrounds (denoted as EEMC), it is expected to be same as QCD background with  $A_L^{EEMC} = 0$  since the double-counted  $Z$  component has been excluded. The  $A_L^Z$  can be estimated using the RHICBOS program [37] based on the DSSV polarized PDFs and found to be about -0.06 in barrel region. Combining with the fraction  $f_Z$  which is fairly small in order of 1%, the contribution from  $\alpha$ , the polarized background, is negligible comparing with the statistical uncertainty.

### 5.3 Relative Luminosity

In Equation (5.1)-(5.5), the relative luminosity corrections for each spin states are required. The relative luminosity correction factor is defined as  $l_i \equiv 4L_i/\Sigma_i L_i$ , where  $L_i$  is the integral luminosity for spin state  $i$  ( $i = ++, +-, -+, --$ ). They are determined from a QCD events sample which is expected to be parity-conserved and has no physical asymmetry. Since only the ratio of luminosities is needed, it is not necessary to know the absolute luminosity of each spin state. The QCD events sample with much larger statistics than  $W$  sample is expected to well reflect the relative luminosity. The  $l_i$  can be obtained from the spin sorted yields of the QCD events,  $l_i = 4N_i^{QCD}/\Sigma_i N_i^{QCD}$ .

The QCD events used for the relative luminosity monitoring are selected by the following cuts:

- fired the L2BW trigger,
- a high  $p_T$  track pointing to the BEMC,
- isolation ratio  $E_T^{2\times 2}/E_T^{4\times 4} < 0.95$ , very effectively exclude  $W$ ,
- $E_T^{2\times 2} < 20\text{GeV}$ , away from  $W$  Jacobian peak region.

Figure 5.1 shows the relative luminosity correction factors  $l_i$  for 2011, 2012, and 2013 period I and period II respectively. The corresponding numerical numbers are listed in Table 5.1.

Spin State	++	+-	-+	--
2011	$1.018\pm 0.007$	$0.989\pm 0.007$	$0.993\pm 0.007$	$1.000\pm 0.007$
2012	$0.994\pm 0.003$	$1.007\pm 0.003$	$0.992\pm 0.003$	$1.003\pm 0.003$
2013 Period I	$0.992\pm 0.002$	$0.998\pm 0.002$	$1.000\pm 0.002$	$1.010\pm 0.002$
2013 Period II	$1.007\pm 0.003$	$0.992\pm 0.003$	$0.997\pm 0.003$	$1.004\pm 0.003$

Table 5.1: Normalized relative luminosities for the four spin states corresponding to Figure 5.1.

In order to estimate the systematic uncertainty caused by the relative luminosity and also as a cross-check, an independent high- $p_T$  QCD background sample is selected using the reversed isolation and signed  $p_T$ -balance cuts (same as cuts for selecting the relative luminosity QCD events sample expect for the  $E_T$  cut), but

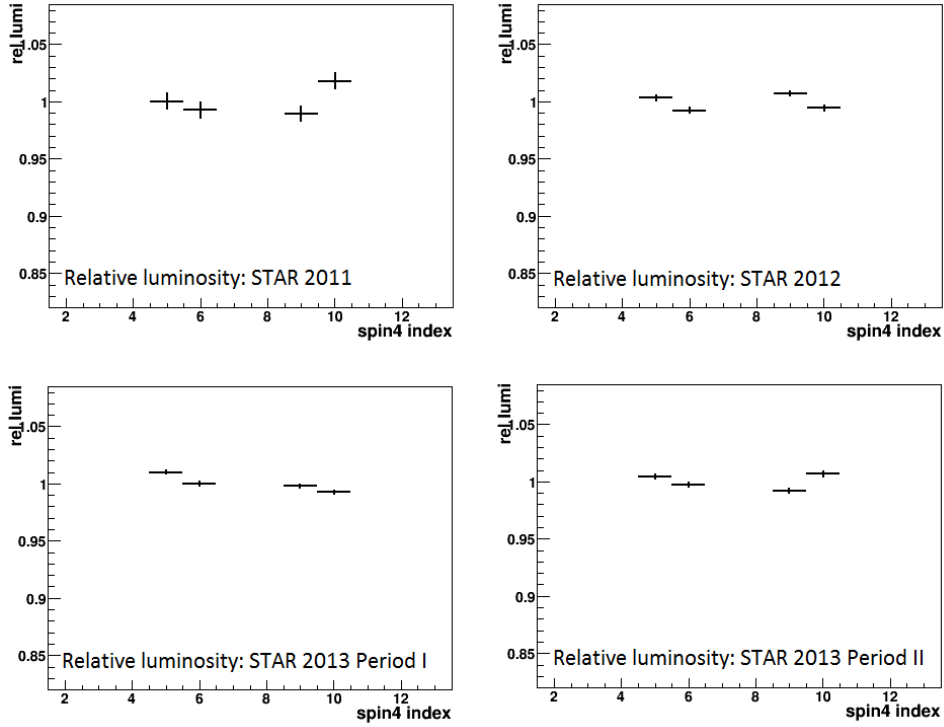


Figure 5.1: Normalized relative luminosity for the four spin states, for 2011, 2012, 2013 period I and period II.

same  $E_T$  range as  $W$  signal,  $25 < E_T < 50\text{GeV}$ . The  $A_L$  extracted from such a QCD sample provides a test that how well we know the events used in the relative luminosity correction are parity-conserved. The  $A_L^{QCD}$  results for 2011+2012 and 2013 are listed in Table 5.2, where can be seen that the  $A_L^{QCD}$  are consistent with zero as expected. The systematic uncertainties from relative luminosity are determined as half of the statistical errors of  $A_L^{QCD}$ , which are 0.007 and 0.004 for 2011+2012 and 2013 measurements respectively.

Year	2011 + 2012	2013
$A_L^{QCD+}$	$-0.003 \pm 0.011$	$0.003 \pm 0.007$
$A_L^{QCD-}$	$-0.009 \pm 0.013$	$0.004 \pm 0.008$

Table 5.2: Asymmetries measured for high  $p_T$  QCD background events (charge separated).

## 5.4 Spin Sorted $W$ Yields

After removing the candidates with ambiguous charge sign, the raw  $W$  yields are counted in the  $E_T$  range [25,50] GeV for  $W^+$  and  $W^-$  and for 4 spin states ( $++$ ,  $+-$ ,  $-+$ ,  $--$ ) respectively. The spin-sorted  $W^+$  and  $W^-$  yields in each  $\eta$  bin are listed in Table 5.3- 5.6.

As discussed in Section 3.1.2, the longitudinally polarized proton-proton collisions only lasted for only one week in 2011 due to the RHIC budget limitation. In Table 5.3, it can be found that  $W$  yields from 2011 are relatively small. Especially for  $W^-$  and Endcap region, there are only a few (even one) counts after being sorted in different spin states. By itself, 2011 statistic is not large enough to provide valuable  $\eta$  dependent  $A_L$  results since the uncertainties will be very large. In order to make good use of the data, a profile likelihood method has been developed to combine 2011 and 2012  $W$  sample. Details can be found in Section 5.5.

Charge	$W^+$					$W^-$				
Spin State	sum	++	+-	-+	--	sum	++	+-	-+	--
Eta bin 1	60	8	17	15	20	26	11	4	10	1
Eta bin 2	90	18	24	27	21	26	11	6	8	1
Eta bin 3	114	25	14	33	42	20	8	4	4	4
Eta bin 4	68	14	14	18	22	22	5	8	6	3
Eta bin 7	10	2	1	5	2	9	3	2	1	3

Table 5.3:  $W$  yields of STAR 2011 dataset.

Charge	$W^+$					$W^-$				
Spin State	sum	++	+-	-+	--	sum	++	+-	-+	--
Eta bin 1	487	75	132	104	176	185	67	41	41	36
Eta bin 2	663	87	186	160	230	152	47	44	36	25
Eta bin 3	746	103	188	184	271	171	44	46	47	34
Eta bin 4	464	82	94	125	163	169	54	46	38	31
Eta bin 7	57	10	10	17	20	57	16	15	16	10

Table 5.4:  $W$  yields of STAR 2012 dataset.

Charge	$W^+$					$W^-$				
Spin State	sum	++	+-	-+	--	sum	++	+-	-+	--
Eta bin 1	763	117	227	156	261	270	96	56	76	43
Eta bin 2	1054	161	266	265	360	265	84	62	66	53
Eta bin 3	1092	164	274	269	383	237	74	52	63	49
Eta bin 4	818	133	179	230	274	351	103	98	83	67
Eta bin 7	67	9	21	15	22	81	26	20	17	18

Table 5.5:  $W$  yields of STAR 2013 Period I dataset.

Charge	$W^+$					$W^-$				
Spin State	sum	++	+-	-+	--	sum	++	+-	-+	--
Eta bin 1	570	81	168	109	211	222	71	50	59	42
Eta bin 2	705	112	179	150	263	161	57	37	33	34
Eta bin 3	831	133	189	217	292	192	55	49	50	38
Eta bin 4	689	124	143	164	257	267	68	81	69	50
Eta bin 7	34	5	5	13	11	25	6	3	6	10

Table 5.6:  $W$  yields of STAR 2013 Period II dataset.

## 5.5 Profile Likelihood Method

As mentioned earlier, run 2011 at STAR is a relatively small dataset. It doesn't make sense to have a single measurement with 2011 dataset alone. A profile likelihood method has been developed and used to combine 2011 and 2012 datasets to treat the low statistics of the 2011 dataset [73]. More details about the profile likelihood method are given in Appendix A.

For a given data sample, a model for the expected, spin-sorted  $W^\pm$  yields in a given positive STAR detector  $\eta$  range, labeled as  $a$  can be defined for each spin state with similar format of Equation (5.2)-(5.5),

$$\mu_{++}^a = l_{++}N [1 + P_1\beta A_L(+\eta) + P_2\beta A_L(-\eta) + P_1P_2\beta A_{LL}], \quad (5.14)$$

$$\mu_{+-}^a = l_{+-}N [1 + P_1\beta A_L(+\eta) - P_2\beta A_L(-\eta) - P_1P_2\beta A_{LL}], \quad (5.15)$$

$$\mu_{-+}^a = l_{-+}N [1 - P_1\beta A_L(+\eta) + P_2\beta A_L(-\eta) - P_1P_2\beta A_{LL}], \quad (5.16)$$

$$\mu_{--}^a = l_{--}N [1 - P_1\beta A_L(+\eta) - P_2\beta A_L(-\eta) + P_1P_2\beta A_{LL}], \quad (5.17)$$

where the variables have the same meaning as in Equation (5.2)-(5.5) and the background dilution factor  $\beta$  is also included. A similar set of these four equations can be written for the symmetric negative pseudorapidity range of STAR detector, labeled as  $b$ , by interchange  $A_L(+\eta)$  with  $A_L(-\eta)$ . These eight spin-dependent yields for the pair of symmetric pseudorapidity regions in the STAR detector ( $a$  and  $b$ ) are used to define a likelihood function,

$$L = \prod_i^4 \mathcal{P}(M_i^a | \mu_i^a) \mathcal{P}(M_i^b | \mu_i^b) g(\beta^a) g(\beta^b), \quad (5.18)$$

which consists of a product of Poisson probabilities  $\mathcal{P}(M_i | \mu_i)$  for measuring  $M_i$  events in a helicity configuration  $i$  given the expected value  $u_i$  from Equation (5.14)-(5.17) and a Gaussian probability  $g(\beta)$  for the estimated background dilution. The spin asymmetries  $A_L(+\eta)$ ,  $A_L(-\eta)$ , and  $A_{LL}$  of this likelihood function are bounded to be within their physically allowed range of  $[-1,1]$ ,  $N^{a,b}$  and  $\beta^{a,b}$  are treated as nuisance parameters, and the remaining parameters ( $P$  and  $l_{\pm\pm}$ ) are known constants.

Separate likelihood functions are computed for the 2011 and 2012 datasets, and their product is used in a profile likelihood analysis to obtain the central values and confidence intervals for the asymmetries.

## 5.6 Results and Discussions

### 5.6.1 $A_L^{W^\pm}$ Results from 2011 and 2012 Data

From 2011 and 2012 datasets, the combined longitudinal single-spin asymmetry results,  $A_L^{W^\pm}$ , are extracted using the profile likelihood method described in Section 5.5. Figure 5.2 shows the  $A_L^{W^\pm}$  results as a function of the lepton pseudorapidity. The vertical black error bars show the 68% confidence intervals, which include the statistical uncertainty, as well as systematic uncertainty due to the unpolarized background dilution. The magnitude of the confidence intervals are dominated by the statistical precision of the data. The systematic uncertainty caused by relative luminosity is indicated by the gray band in Fig. 5.2, and the single-spin asymmetry has a common 3.4% normalization uncertainty due to the uncertainty in the measured beam polarization.

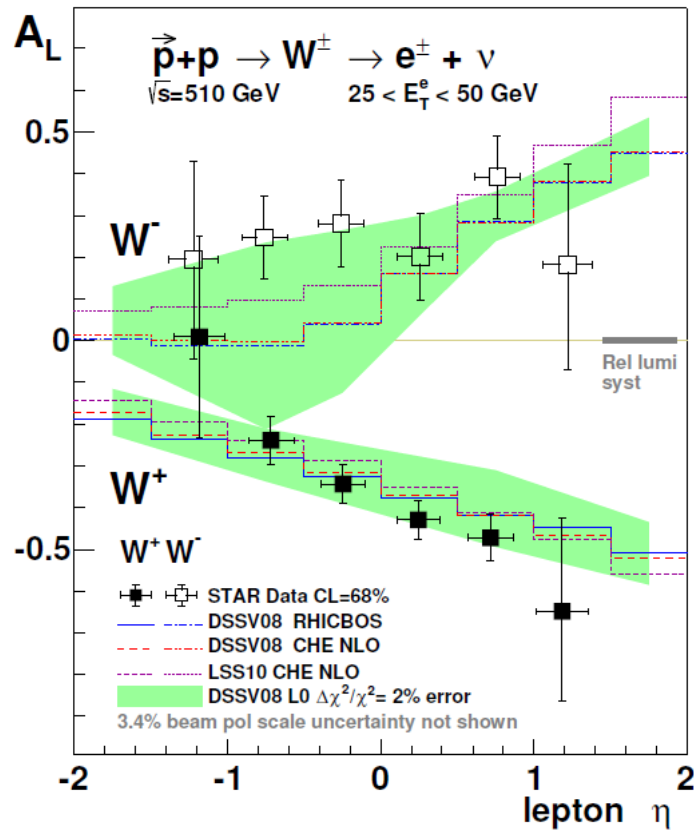


Figure 5.2: Longitudinal single-spin asymmetry  $A_L$  for  $W^\pm$  productions as a function of lepton pseudorapidity from STAR 2011+2012 data set in comparison to theoretical predictions [73].

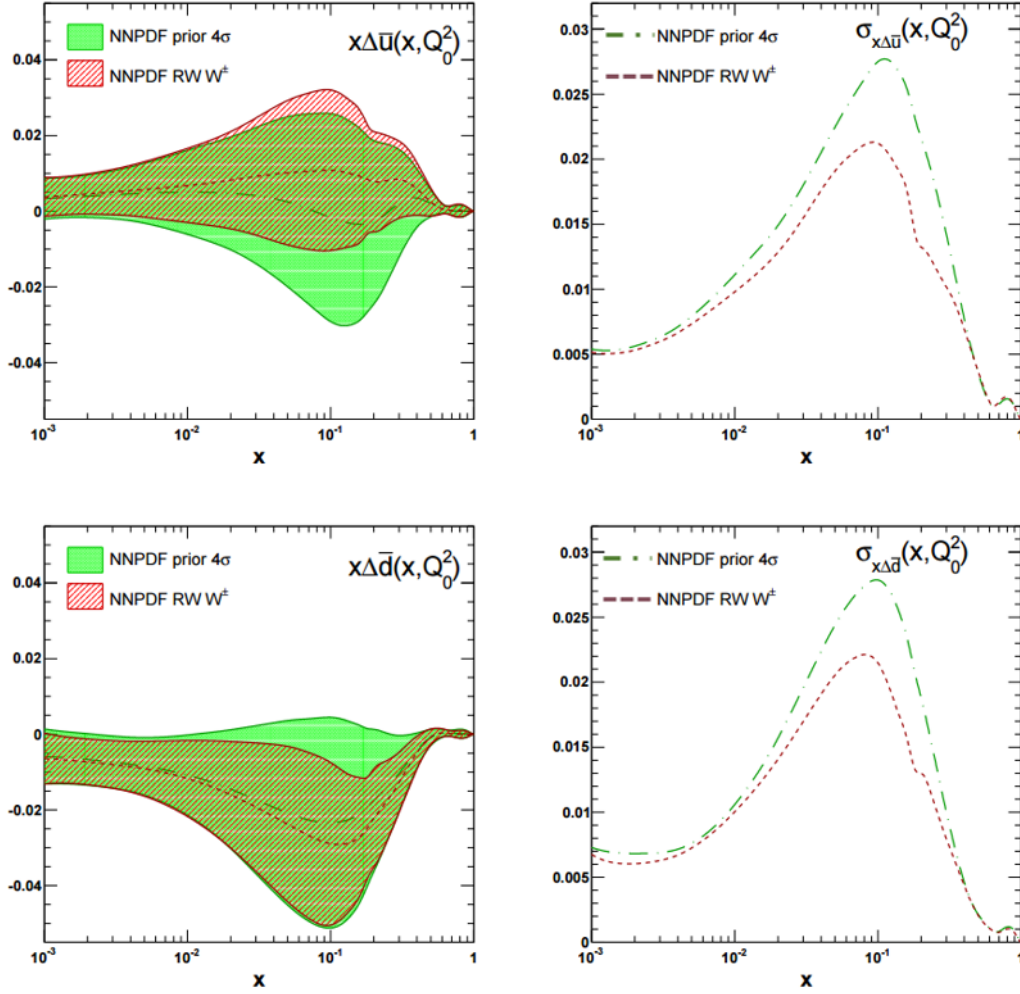
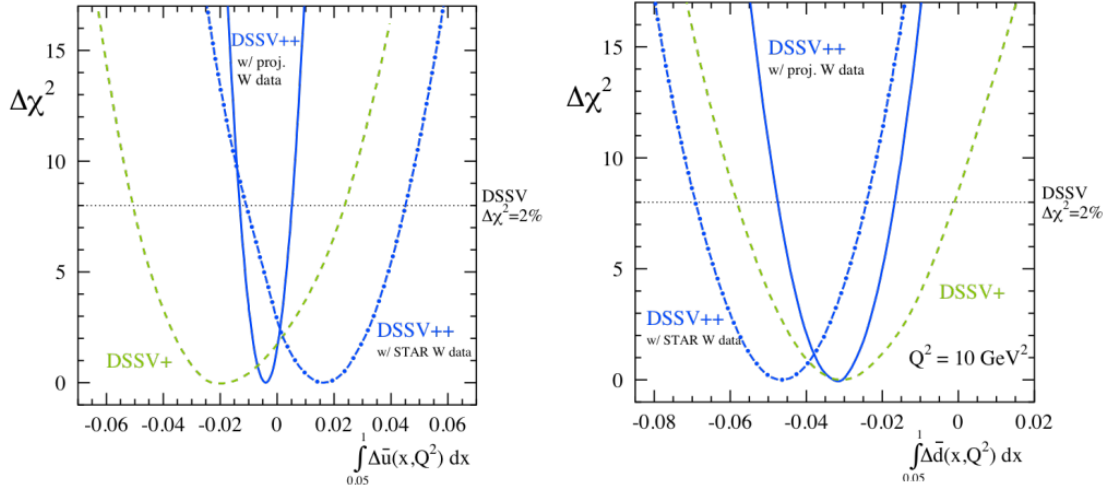


Figure 5.3: NNPDFpolz1.1 [32]: comparison between  $x$  dependent  $\Delta\bar{u}$  (upper) and  $\Delta\bar{d}$  (lower) before and after including the impact of STAR 2011+2012  $A_L^{W^\pm}$  results, at  $Q^2 = 1\text{GeV}^2$ . The absolute PDF uncertainty is also shown (right).

The measured  $A_L$  results are compared to the theoretical predictions described in Section 1.2, Figure 1.13. The  $A_L^{W^+}$  is negative, consistent with the theoretical predictions.  $A_L^{W^+}$  is sensitive to the polarization distributions of  $\bar{d}$  and  $u$  quark respectively at forward and backward lepton pseudorapidity regions. The agreement between  $A_L^{W^+}$  and the theoretical predictions indicates that polarized PDFs  $\Delta\bar{d}$  and  $\Delta u$  determined in polarized SIDIS and  $W$  production in polarized  $pp$  collisions give consistent results. For  $A_L^{W^-}$ , however, the measured asymmetries are in general larger than the theoretical predictions for negative pseudorapidity. This region is most sensitive to the  $\bar{u}$  quark polarization which is not currently well constrained

from SIDIS as can be seen from the large uncertainty band of the theoretical predictions. This is an indication of a sizable and positive  $\Delta\bar{u}$  in the range  $0.05 < x < 0.2$ , where current STAR  $W$  data provide sensitivity (see Equation (1.18)).  $A_L^{W^-}$  for positive pseudorapidity which is mostly sensitive to  $\Delta d$  well agree with the theoretical predictions which reflects the consistent results from  $W$  and from SIDIS.



(a)  $\chi^2$  profiles for  $\Delta\bar{u}$ (left) and  $\Delta\bar{d}$ (right) with the impact of the preliminary 2012 STAR  $A_L^{W^\pm}$  result (blue dashed-dotted curves) and the projection  $W$  data (blue curve)

Figure 5.4: DSSV++:  $\chi^2$  profiles for  $\Delta\bar{u}$ (left) and  $\Delta\bar{d}$ (right) with the impact of the preliminary 2012 STAR  $A_L^{W^\pm}$  result and the projected  $W$  data of run 2013 [75](down).

$A_L^{W^\pm}$  results from 2011 and 2012 data have been published [73] and included by NNPDF [32] and DSSV++ [75] (DSSV++ used STAR preliminary results) groups into their global analyses shown in Figure 5.3 and 5.4 respectively. NNPDF group implements a Bayesian reweighting method to include the contribution from STAR 2011 and 2012  $A_L^{W^\pm}$  results [32]. The NNPDF methodology consists of updating the representation of the probability distribution in the space of PDFs provided by an available PDF set by means of Bayes' theorem in such a way that the information contained in the new data sets is included. Based on the existing PDFs set, a set of experimental pseudo-observables with uncertainties inflating with a factor from the PDF uncertainties are sampled. In the left panel of Figure 5.3, the change in shapes of  $\Delta\bar{u}$  and  $\Delta\bar{d}$  compared with the prior (whose shape is determined by the shape of the DSSV08 best-fit PDFs and uncertainty is inflated from corresponding PDF uncertainty by a factor 4) is significant, especially for  $\Delta\bar{u}$ . It indicates that

the STAR 2011 and 2012  $A_L^{W^\pm}$  results pull in a different direction for  $\Delta\bar{u}$  than the polarized semi-inclusive DIS data used in DSSV08 PDFs. In the right panel of Figure 5.3, the respective absolute uncertainties are shown. The reduction in uncertainty is very visible,  $\sim 20\%$  in the peak region. STAR  $A_L^{W^\pm}$  results have provided significant constraints on both  $\Delta\bar{u}$  and  $\Delta\bar{d}$ . In Figure 5.4, the  $\chi^2$  profiles for  $\Delta\bar{u}$ (left) and  $\Delta\bar{d}$ (right) in DSSV global fitting are shown. The blue dashed-dotted curves are for global fits including STAR preliminary results of 2012  $A_L^{W^\pm}$  (2012 data dominates the 2011 and 2012 combination). Compared to the green dashed curves which are from global fit before including STAR  $A_L^{W^\pm}$  results (DSSV08), the best-fit values for  $\Delta\bar{u}$  and  $\Delta\bar{d}$  of blue dashed-dotted curves show remarkable shift. Especially for  $\Delta\bar{u}$ , the sign has changed from negative to positive. The widths are also significantly reduced with constraints provided by STAR data. Global fits from both groups give consistent results on STAR  $A_L^{W^\pm}$  impact. In Figure 5.4, DSSV group also provides the results with the projected RHIC 2013  $W$  data (blue curves), where the widths are further shrunked.

### 5.6.2 $A_L^{W^\pm}$ Results from 2013 Data

STAR 2013 data sample is about 3 times larger than previous years in luminosity (see Section 3.1.2). The  $A_L^{W^\pm}$  for each  $\eta$  bin is independently calculated for period I and period II using Equation (5.7)-(5.9). After combining two periods, Figure 5.5 shows the  $A_L^{W^\pm}$  results for STAR run 2013 as a function of the lepton pseudorapidity. They are compared to the theoretical predictions and STAR 2011 and 2012 results. The vertical error bars contain both the statistical uncertainty from  $W$  yields and the systematic uncertainty introduced by the background estimation procedure. In general,  $A_L^{W^\pm}$  measured from 2013 dataset are consistent with the published 2011 and 2012  $A_L^{W^\pm}$  results, and the uncertainties are significantly reduced by about 40% from 2011,2012. For  $A_L^{W^+}$ , 2013 result are consistent with the theoretical productions. For  $A_L^{W^-}$ , the measurements in  $\eta_e < 0$  region where is mostly sensitive to  $\bar{u}$  polarization are systematically larger than the theoretical predictions. Considering the impact of 2011, 2012  $A_L^{W^\pm}$  results, the  $\Delta\bar{u}$  distribution will be further constrained with a positive central value after including 2013 results. The quantitative impact will be manifested after being included in global analysis.

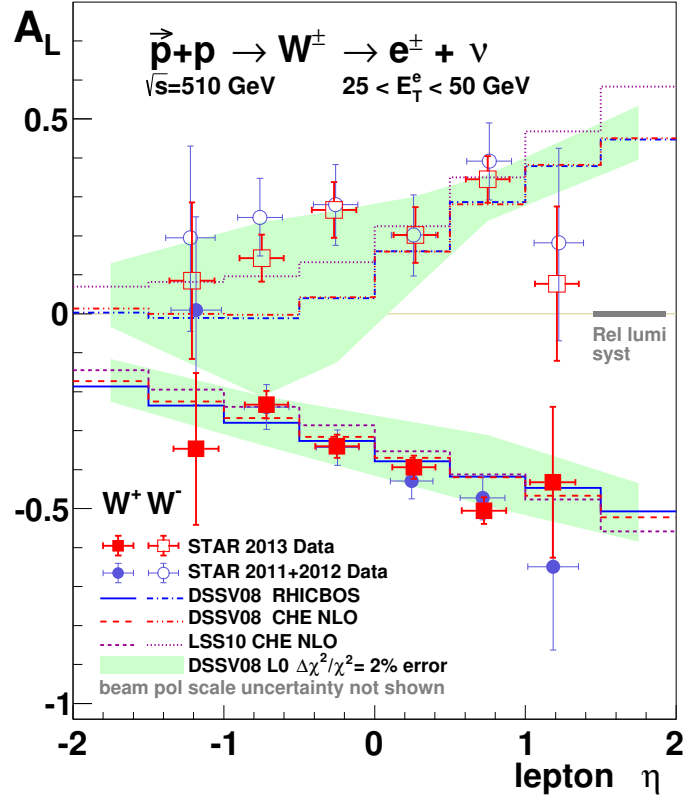


Figure 5.5: Longitudinal single-spin asymmetry  $A_L$  for  $W^\pm$  productions as a function of lepton pseudorapidity of STAR 2013 in comparison to 2011+2012 results and theory predictions.

### 5.6.3 $A_L^{Z/\gamma^*}$ and $A_{LL}^{W^\pm}$

As discussed in Section 4.2, the  $Z/\gamma^* \rightarrow e^+e^-$  events are also reconstructed from STAR 2011, 2012, and 2013 datasets along with  $W$  reconstruction. The  $Z/\gamma^*$  yields are counted within invariant mass window  $70 < m_{e^+e^-} < 110 \text{ GeV}/c^2$  where the  $e^\pm$  are within  $-1.1 < \eta < 1.1$  and  $E_T > 14 \text{ GeV}$ . The spin sorted yields of  $Z/\gamma^*$  are listed in Table 5.7 for 2011, 2012, and 2013. Due to the limited cross section at RHIC energies, the statistics of  $Z/\gamma^*$  production are relatively low.

There is a unique advantage that the  $e^+e^-$  final states can be fully reconstructed. Thus, the initial state kinematics can be determined,

$$x_{1(2)} = \frac{M_{e^+e^-}}{\sqrt{s}} e^{\pm y^Z}, \quad (5.19)$$

where  $y^Z$  is the rapidity of  $Z$ .

The longitudinal single-spin asymmetry of  $Z/\gamma^*$ ,  $A_L^{Z/\gamma^*}$  is sensitive to the combination of polarizations of up and down quarks and antiquarks. It is slightly complicated by the fact that both left- and right-handed quarks can couple to  $Z$  boson [74],

$$A_L^Z = \frac{\sum_f \mathcal{A}_f [\Delta \bar{q}_f(x_1) q_f(x_2) - \Delta q_f(x_1) \bar{q}_f(x_2)]}{\sum_f [\bar{q}_f(x_1) q_f(x_2) + q_f(x_1) \bar{q}_f(x_2)]}, \quad (5.20)$$

where  $f = u, d$ ,  $\mathcal{A}_f$  is a measure of vector coupling [74].

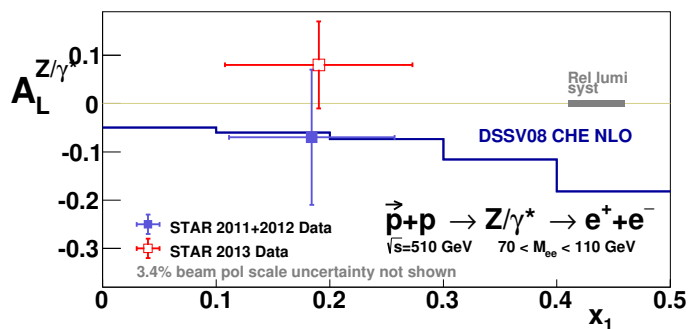


Figure 5.6: Longitudinal single-spin asymmetry  $A_L$  for  $Z/\gamma^*$  productions as a function of Bjorken scaling,  $x_1$ .

For 2011 and 2012 data sets, the  $A_L^{Z/\gamma^*}$  is extracted via the profile likelihood method, to be  $-0.07 \pm 0.14$ . This result has been reported together with 2011+2012  $W$  spin asymmetry results [73]. For 2013, the period I and period II combined  $A_L^{Z/\gamma^*}$  result is also measured,  $A_L^{Z/\gamma^*} = 0.08 \pm 0.09$ . The results of 2011+2012 and 2013 are shown in Figure 5.6 with comparison to theoretical predictions. Within uncertainties, the two results are consistent with each other and also with theoretical prediction.

Data sets	sum	++	+-	-+	--
2011	11	2	3	3	4
2012	77	20	16	19	22
2013 Period I	86	15	29	31	11
2013 Period II	72	19	18	19	16

Table 5.7: Spin sorted  $Z/\gamma^*$  yields for STAR 2011, 2012, and 2013.

The longitudinal double-spin asymmetry of  $W$  production,  $A_{LL}^{W^\pm}$ , which is defined as Equation (5.6) is also extracted along with  $A_L^{W^\pm}$  extraction from profile likelihood method for 2011 and 2012 data and from Equation (5.7)-(5.9) for 2013

data.  $A_{LL}^{W^\pm}$  is also sensitive to the flavor decomposition of polarized quark and antiquark distributions,

$$A_{LL}^{W^+} \sim \frac{\Delta u}{u} \frac{\Delta \bar{d}}{\bar{d}}, \quad A_{LL}^{W^-} \sim \frac{\Delta d}{d} \frac{\Delta \bar{u}}{\bar{u}}. \quad (5.21)$$

Also, it has been proposed by Kang [76] to test positivity constraints using a combination of  $A_L^{W^\pm}$  and  $A_{LL}^{W^\pm}$  [76].

$$1 \pm A_{LL}^{W^\pm(y_W)} > \left| A_L^{W^\pm}(y_W) \pm A_L^{W^\pm}(-y_W) \right|, \quad (5.22)$$

where  $y_W$  is the rapidity of  $W$  boson.

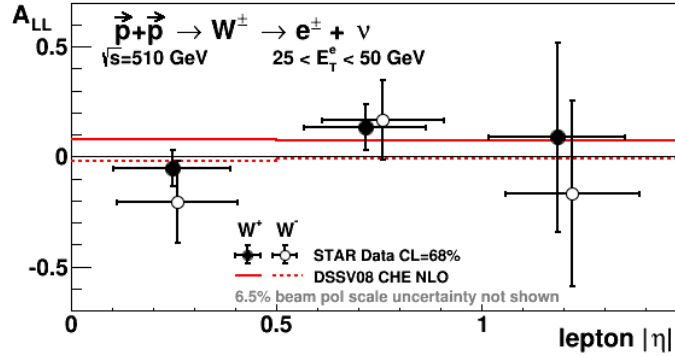


Figure 5.7: Longitudinal double spin asymmetry  $A_{LL}$  for  $W^\pm$  productions as a function of lepton pseudorapidity of STAR 2011+2012 in comparison to theory predictions [73].

Figure 5.7 [73] shows  $A_{LL}^{W^\pm}$  results extracted from 2011 and 2012 datasets using the profile likelihood method (see Section 5.5). There is a common 6.5% normalization uncertainty due to the uncertainty in the measured beam polarization. The results as a function of lepton  $\eta$  are consistent with the theoretical predictions and in conjunction with  $A_L^{W^\pm}$  satisfy the positivity bounds within the current uncertainties. In Figure 5.8, NNPDF [32] reported an examination of positivity bounds by combination of RHIC  $A_L^{W^\pm}$  and  $A_{LL}^{W^\pm}$  which are bounded to be non-negative.

Figure 5.9 shows the  $A_{LL}^{W^\pm}$  results calculated from STAR 2013 data. The comparison to 2011 and 2012 is also included. The 2013  $A_{LL}^{W^\pm}$  results are consistent with that of 2011 and 2012 with reduced uncertainty.

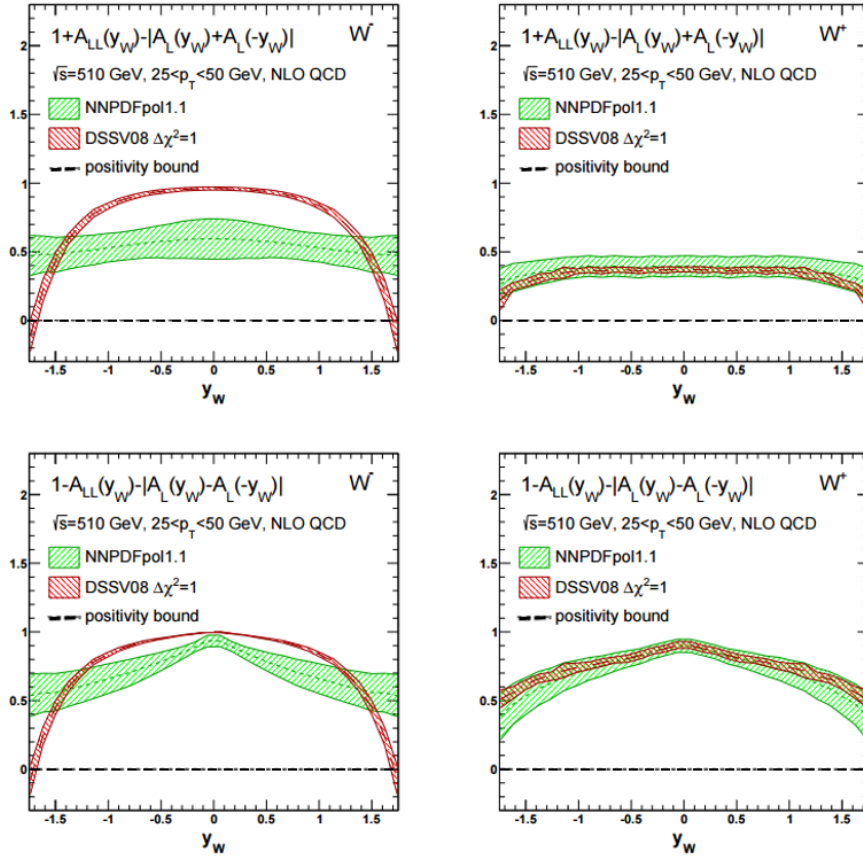


Figure 5.8: Positivity bounds  $A_{LL}^{W^\pm(y_W)} - \left| A_L^{W^\pm}(y_W) \pm A_L^{W^\pm}(-y_W) \right|$  as a function of  $W$  rapidity, from NNPDFpol1.1 and DSSV08 polarized PDFs. The positivity bounds are satisfied whenever the curves are positive [32].

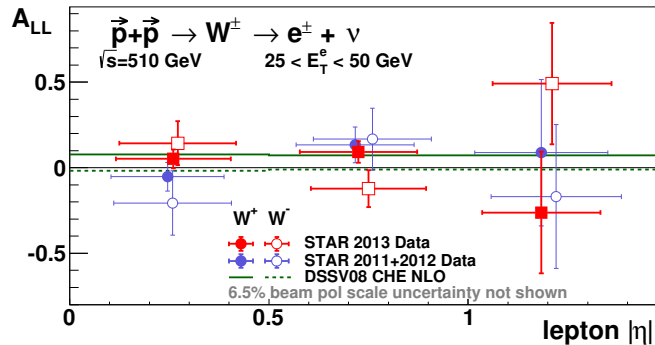


Figure 5.9: Longitudinal double spin asymmetry  $A_{LL}$  for  $W^\pm$  productions as a function of lepton pseudorapidity of STAR 2013 in comparison to 2011+2012 results and theory predictions.

## Chapter 6

# Conclusions and Outlook

As a fundamental challenge, understanding the nucleon spin structure has attracted many physicists in both experimental and theoretical aspects in the last few decades. For longitudinal spin structure, large amount of data have been accumulated by various experiments. Initiated by the EMC collaboration, the total contribution of quarks and antiquarks spin to the proton spin has been well constrained by the data obtained in polarized DIS experiments at CERN, DESY, SLAC, and JLab. The polarized semi-inclusive DIS experiments have provided flavor decomposition of the quark and antiquark polarization via identifying the hadrons in the final state relying on the understanding of parton fragmentation processes. Limited by the precision of the fragmentation functions, there are still large uncertainties on the flavor separated anti-quark polarized distributions. RHIC, taking advantage of the polarized proton-proton collisions, provides wonderful complementary information to the DIS experiments. Among RHIC spin program, the measurement of the parity-violating longitudinal single-spin asymmetry of  $W$  boson production provides an unique probe to the sea quark polarization. Due to  $V - A$  structure of weak interaction,  $W$  boson naturally selects the left-handed quarks and right-handed anti-quarks in its production in  $pp$  collisions. This provides an direct probe of the polarized PDFs and doesn't rely on fragmentation functions.

At RHIC, the  $W$  boson production is detected via its leptonic decay which has theoretically calculable kinematics. The candidate  $W$  events are selected out based on the kinematic and topological features that an isolated charged lepton and a large miss energy caused by the undetected neutrino. In this thesis, the measurements of longitudinal single-spin asymmetry of  $W$  boson at STAR are reported. The measurements are based on the data collected in 2011, 2012, and 2013 by STAR experiment at  $\sqrt{s}=500(510)$  GeV longitudinally polarized proton-proton

collisions at RHIC. From 2011 ( $9.4 \text{ pb}^{-1}$ ) and 2012 ( $77.4 \text{ pb}^{-1}$ ) data, the lepton  $\eta$  dependent  $W A_L$  is measured for the first time, which has provided the first valuable input from  $W$  to the global analysis of the polarized PDFs. The  $A_L^{W^+}$  results are consistent with the theoretical predictions which are based on the semi-inclusive DIS experiments. However, the  $A_L^{W^-}$  is larger than the theoretical predictions at negative lepton  $\eta$  region where the  $A_L^{W^-}$  is mostly sensitive to the  $\Delta\bar{u}$  distribution. This enhancement of  $A_L^{W^-}$  suggests a positive  $\bar{u}$  polarization. From 2013 ( $246.2 \text{ pb}^{-1}$ ) data, the precision of  $A_L^{W^\pm}$  measurement is significantly increased. With the uncertainty reduced,  $A_L^{W^-}$  is consistent with that of 2011 and 2012, and further enhances the positive preference of  $\Delta\bar{u}$  in the range  $0.05 < x < 0.2$ . According to an earlier estimation by DSSV group [77], the uncertainties for the  $\Delta\bar{u}$  and  $\Delta\bar{d}$  distributions for  $x$  above 0.05 are expected to reach 1% and 2% respectively with including all the statistics of RHIC  $A_L^{W^\pm}$  data in 2011, 2012, and 2013.

In the upcoming decade, the Electron Ion Collider [78] in planning is expected to play a key role in nuclear physics. It will be a new milestone for the investigation of the nuclear spin structure taking the advantage of the unprecedented luminosity. From the semi-inclusive scattering, the light-flavor helicity distributions of  $\Delta u$ ,  $\Delta d$  and their antiquark distributions can be probed in a wide kinematic range with a remarkably increased precision from current SIDIS measurements. With dedicated studies of kaon production, strange sea quark will also be accessible. The proton spin structure function  $g_1(x, Q^2)$  can be precisely measured including its scaling violation. With an EIC machine, the range of  $x$  and  $Q^2$  will be dramatically extended from the current spin related experiments of DIS and  $pp$  as shown in Figure 6.1. Definitely, it will provide very precise probe for gluon and sea quarks polarization when reaching much smaller  $x$  region. Among these rich opportunities, the flavor decomposition of the quark and antiquark spin can be accessed in the electroweak deep inelastic scattering by the exchange of  $Z$  and  $W^\pm$  bosons which will provide unique insights into the spin flavor structure of proton [79].

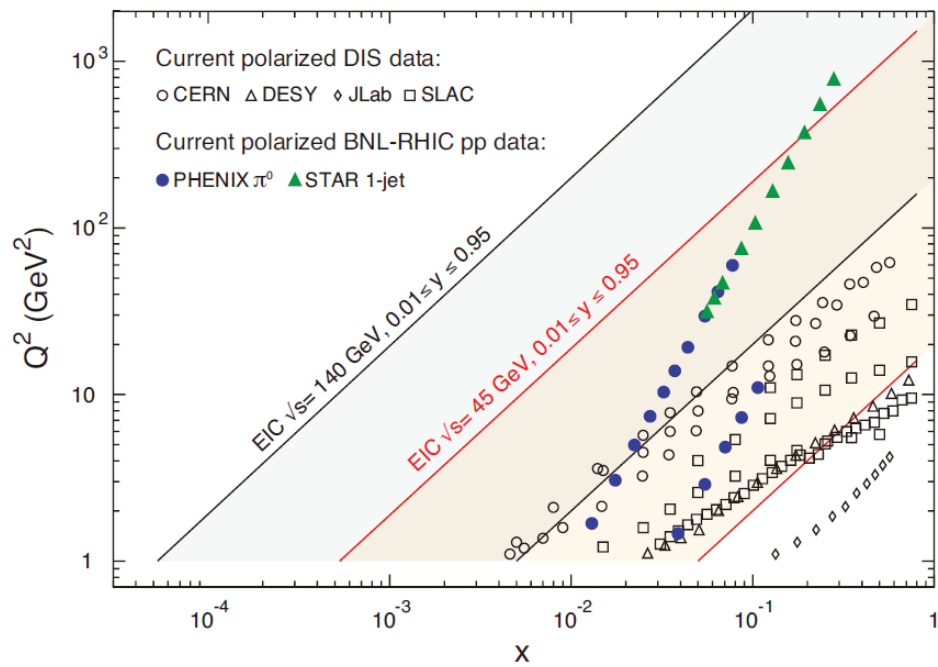


Figure 6.1: Regions in  $x$ ,  $Q^2$  covered by previous spin experiments and anticipated to be accessible at an EIC. [78]



# Appendix A

## Profile Likelihood Method

### A.1 Introduction

This work has been motivated by the desire to combine the 2011 and 2102 STAR data sets to extract the W-boson spin asymmetry  $A_L(\eta)$ . Due to the low statistics in the 2011 dataset we could not justify the use of Gaussian error propagation. Instead we have used a multi-dimensional likelihood, constructed from many Poisson distributions. For consistency, the same method will be used for extraction of the double spin asymmetry  $A_{LL}$ .

The essence of the problem which we need to address is finding the most probable value (MPV) and the confidence interval (CI) of an unknown parameter A, given a pair of measured yields  $N_+, N_-$  obeying a Poisson distribution, and knowing that the true relation between those quantities are

$$N_{\pm} = N^0(1 \pm A \cdot P) \quad (\text{A.1})$$

where  $N^0 > 0$  is a free parameter of no interest to us and P is a known constant,  $|P| < 1$ .

In the limit of large statistics the p.d.f. of measured yields  $N_{\pm}$  are well approximated by the Gaussian distribution. One can then solve Eqn. A.1 for A

$$A = \frac{1}{P} \frac{N_+ - N_-}{N_+ + N_-} \quad (\text{A.2})$$

and propagate the statistical errors of  $N_{\pm}$  into one standard deviation of A,  $\sigma(A)$

$$\sigma(A) = \frac{2}{P} \sqrt{\frac{N_+ N_-}{(N_+ + N_-)^3}} \quad (\text{A.3})$$

In such a case the CI  $[A - \sigma, A + \sigma]$  corresponds to CL=0.683.

Let's further assume we repeated the experiment K-times, measuring K pairs of yields  $N_{\pm,k}$ . However, each time the constant  $P_k$  was different. We want to again extract a single, common value of A based on the combined data from these K experiments.

In the limit of large statistics we can compute  $A_k, \sigma_k$  for each dataset k, then compute weighted average

$$\hat{A} = \sum_{k=1}^K A_k w_k, \quad (\text{A.4})$$

$$w_k = \sigma_k^{-2} / \sum_{k=1}^K \sigma_k^{-2} \quad (\text{A.5})$$

The procedure described above fails in the low statistic limit, say for  $N_{\pm}$  of few, when the Poisson p.d.f. is not symmetric around the central value any more. Consequently, the  $1-\sigma$  CI for  $A_k$  is not centered around the MPV. For a given CL we have CI  $[A_k^{lo}, A_k^{hi}]$  such that  $A_k - A_k^{lo} \neq A_k^{hi} - A_k$ . This means Eqn. A.5 can't be applied to compute the relative weights needed in Eqn. A.4.

**The alternative approach to finding the MPV of A from many, low statistics experiments is to apply the likelihood method (LM).** Knowing the p.d.f. for each measurement,  $N_{\pm,k}$ , obeys the Poisson distribution, we construct the likelihood of measuring each pair  $N_{\pm,k}$ , given A, assuming a physics justified model. Then, multiply the likelihoods from all experiments. Finally, find the global maximum and CI of A by marginalization of nuisance parameters.

Section A.2 describes the application of the profile likelihood method (PLM) for a simple 2-yield experiment. Section A.3 will expand the PLM for a more realistic case of a series 8-yield measurements and simultaneous extraction of multiple parameters of interest.

## A.2 PLM for 2 spin states and one-observable

Let's start with a very simple case of the **profile likelihood method** applied to extract the single-spin asymmetry (SSA) from an experiment using a polarized beam hitting an unpolarized target and involving one detector.

### A.2.1 Model

Let  $N_{\pm}$  be the measured yields of W-boson events in our experiment for two opposite polarizations of the beam ( $\pm$ ). Let  $\mu_{\pm}$  be the expected values of the yields from our model of the experiment, discussed below.

The W-boson reconstruction algorithm accepts a small fraction of non-W events (*i.e.* background) - this impacts the value of the measured SSA and needs to be corrected for. We have identified 3 dominant background sources indexed by the subscript  $i=Z,E,Q$ , and W:

'Z' labels  $Z \rightarrow e^+e^-$  events accepted if one of leptons misses the BEMC or EEMC, 'E' labels QCD  $\rightarrow$  jet-jet events for which one jet heads toward the non-existent East EMC endcap,

'Q' labels other subset of QCD events which sometimes hadronize in such a way that they pass the W reconstruction algorithm. For completeness, 'W' labels W-boson events of interest.

Let  $f_i$  denote the fraction of reconstructed event yield,  $n_i$ , of a given type :

$$f_i = \frac{n_i}{\sum_i n_i} ; \quad \sum_i f_i = 1 \quad (\text{A.6})$$

In general, the SSA for each background process,  $A_i$ , may be different and non-zero which leads to the following **model of spin dependent yields**,  $\mu_{\pm}$ , for all events accepted by the W algorithm:

$$N_{\pm} \rightarrow \mu_{\pm} = \mu_{W\pm} + \mu_{Z\pm} + \mu_{E\pm} + \mu_{Q\pm} \quad (\text{A.7})$$

$$N_{W\pm} \rightarrow \mu_{W\pm} = l_{\pm} N^0 f_W (1 \pm A^W P) \quad (\text{A.8})$$

$$N_{Z\pm} \rightarrow \mu_{Z\pm} = l_{\pm} N^0 f_Z (1 \pm A^Z P)$$

$$N_{E\pm} \rightarrow \mu_{E\pm} = l_{\pm} N^0 f_E (1 \pm A^E P)$$

$$N_{Q\pm} \rightarrow \mu_{Q\pm} = l_{\pm} N^0 f_Q (1 \pm A^Q P)$$

Eqn. A.7 implies the full model for the spin dependent yields,  $\mu_{\pm}$ , is the sum of all possible processes

$$\begin{aligned} \mu_{\pm} &= l_{\pm} N^0 [f_W + f_Z + f_E + f_Q \pm \\ &\quad P(f_W A^W + f_Z A^Z + f_E A^E + f_Q A^Q)] \end{aligned} \quad (\text{A.9})$$

$$= l_{\pm} N^0 [1 \pm P(\beta A^W + \alpha)] \quad (\text{A.10})$$

where

$$\beta = \frac{f_W}{f_W + f_Z + f_E + f_Q} \quad (\text{A.11})$$

$$\alpha = \frac{f_Z A^Z + f_E A^E + f_Q A^Q}{f_W + f_Z + f_E + f_Q} \quad (\text{A.12})$$

In practice the  $\alpha$ -term is much smaller than the statistical uncertainty of the experiment so we will ignore it in this paper. The final model of spin dependent yields is

$$\mu_{\pm} = l_{\pm} N^0 (1 \pm P\beta A^W) \quad (\text{A.13})$$

The beam polarization,  $P$ , is a **constant**. The relative luminosities  $l_{\pm}$  are also assumed to be **constants**.  $l_{\pm}$  depend on the (very large) number of events recorded by the luminosity monitor for both spin states  $N_{LUM\pm}$ .

$$l_{\pm} = \frac{2N_{LUM\pm}}{N_{LUM+} + N_{LUM-}}; \quad \frac{1}{2}(l_+ + l_-) = 1 \quad (\text{A.14})$$

$$\sigma_{l_{\pm}} = 1/\sqrt{N_{LUM+} + N_{LUM-}} \quad \text{are small} \quad (\text{A.15})$$

### A.2.2 Total likelihood function $L_{\Omega}$

The total likelihood  $L_{\Omega}(A^W, N^0, \beta)$  is constructed as the joint probability using all the information we gather from various sources:

$$L_{\Omega}(A^W, N^0, \beta) \equiv L_{PHY}(A^W) \cdot L_{SPIN}(A^W, N^0, \beta) \cdot L_{BCK}(\beta) \quad (\text{A.16})$$

where:

- $A^W$  is the SSA we want to extract from the experiment (*i.e.* the variable of

interest),

- $L_{PHY}(A^W) = H(1 - |A^W|)$  : restricts the range of the physically allowed values of SSA, where  $H(x)$  is the step function,
- $N_0$  and  $\beta$  are nuisance parameters describing the unpolarized expected yield and unpolarized background, respectively,
- $L_{SPIN}(A^W, N_0, \beta) = \prod_i^2 f(N_i | \mu_i(A^W, N^0, \beta))$  is product of Poisson distributions  $f(N|\mu)$ , describing the probability of measuring  $N$  events given the expected value was  $\mu$  from Eqn. A.13,
- $L_{BCK}(\beta) = g(\beta - \hat{\beta}, \sigma_\beta)$  is the probability distribution function for the unpolarized background magnitude, here parametrized as a Gaussian with a mean  $\hat{\beta}$  and standard deviation  $\sigma_\beta$ .

The following additional parameters:  $l_\pm, P$ , needed to compute the numerical values of  $\mu$  (see Eqn. A.13), are assumed to be constant.

Note: for the practical reasons the ranges of all nuisance parameters are bracketed to  $\pm 10\sigma$  around the respective central values.

### A.2.3 Extracting parameter of interest from $L_\Omega$

The following inputs are required to extract the asymmetry of interest  $A^W$

- $N_\pm$  : spin sorted yields from STAR experiment,
- $l_\pm$  : relative luminosities from STAR experiment,
- $\hat{\beta}, \sigma_\beta$  : description of background p.d.f., based on embedding, simulations, and theory,
- $P$  : beam polarization from RHIC.

With these inputs we can build the 3-dimensional total likelihood function  $L_\Omega(A^W, N^0, \beta)$ . To find the central value of the  $A^W$  we need to remove the nuisance parameters ( $N^0$  and  $\beta$ ) from the problem. One method to accomplish this is to marginalize  $L_\Omega$  (or

integrate over) the nuisance parameters to produce the 1-dimensional likelihood vs. the variable of interest,  $A^W$ :

$$L_{\text{marg}}(A^W) = \int dN^0 \int d\beta L_{\Omega}(A^W, N^0, \beta). \quad (\text{A.17})$$

Another method to treat the nuisance parameters, described in the PDG statistics review [3] (specifically Sec. 36.3.2.3) and a longer review from Cowan [80], is the profile likelihood method which we will use and should yield the same central value and confidence intervals as the marginalization method.

The profile likelihood method consists of two steps: (i) construction of the profile likelihood  $L_{\text{prof}}(A^W)$  and (ii) extraction of the central value and confidence interval for  $A^W$ .

### Profile likelihood

Let's group all nuisance parameters as a vector  $\nu \equiv (N^0, \beta)$ . For each value of  $A^W$ , there exist  $\hat{\nu}(A^W)$  which maximizes  $L_{\Omega}(A^W, \hat{\nu})$  defined by Eqn. A.16. The **profile likelihood**  $L_{\text{prof}}(A^W)$  is defined as

$$L_{\text{prof}}(A^W) = L_{\Omega}(A^W, \hat{\nu}) \quad (\text{A.18})$$

It is a 1-dimensional likelihood, depending only on  $A^W$ . Often one conveniently normalizes the profile likelihood by constructing the **profile likelihood ratio** defined as

$$\lambda_{\text{prof}}(A^W) \equiv \frac{L_{\text{prof}}(A^W)}{L_{\Omega 0}}, \quad (\text{A.19})$$

where  $L_{\Omega 0}$  is the global maximum of the 3D likelihood in the  $[A^W, N^0, \beta]$  parameter space.

The central value of  $A^W$  is the one which maximizes the profile likelihood  $L_{\text{prof}}(A^W)$ , or equivalently minimizes the negative log-likelihood,  $-\ln L_{\text{prof}}$ .

### Confidence interval

For a given confidence level (CL) the confidence interval of  $A^W$  is computed as the pair  $[A_{lo}^W, A_{hi}^W]$  satisfying the integral

$$\int_{A_{lo}^W}^{A_{hi}^W} L_{\text{prof}}(A) dA = CL \cdot \int_{\text{support}} L_{\text{prof}}(A) dA \quad (\text{A.20})$$

In the absence of constrain on A and for a non-symmetric p.d.f., as show in fig. A.1a), we need to impose additionally

$$L_{\text{prof}}(A_{lo}^W) = L_{\text{prof}}(A_{hi}^W) \quad (\text{A.21})$$

for unambiguous definition of CI.

The presence of the constrain on the support  $L_{PHY}(A^W)$ , see Fig. A.1b), complicates this picture slightly. For clarity, let's assume that the lower bound is closer to the maximum (as in the figure). In general two CI values divide the whole area on 3 parts, labeled x,y,z.

$$\int_x + \int_y + \int_z = \int_{-1}^{+1} L_{\text{prof}}(A) dA \quad (\text{A.22})$$

In particular,  $\int_x$  may be zero if chosen CL is too large. In such case we set  $A_{lo}^W = -1$  (*i.e.* the lower boundary of the constrain) and  $A_{hi}^W$  is defined by the modified relation

$$\int_{-1}^{A_{hi}^W} L_{\text{prof}}(A) dA = CL \cdot \int_{-1}^{+1} L_{\text{prof}}(A) dA \quad (\text{A.23})$$

### A.2.4 Numerical example

For numerical computation we will use the RooStats [81] (extension of CERN root). For educational purposes we have prepared several ready to use macros placed in the MIT disc at BNL.

The code used to produce Fig. A.1 is named `spin2Asy_constrain.C`. Since the original RooStast did not properly handle the constraint on the asymmetry to be within the physically allowed range, we developed

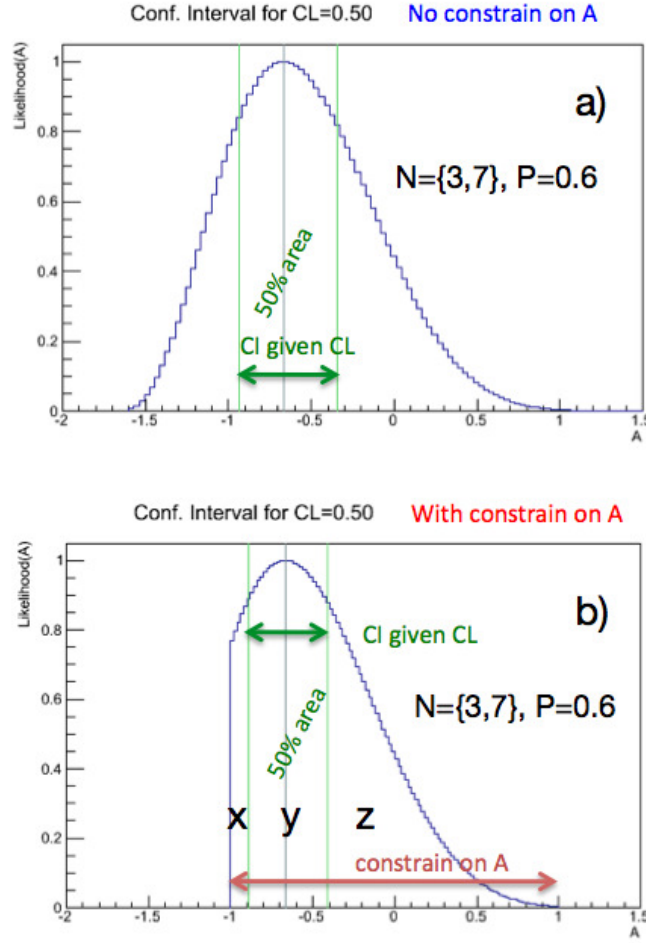


Figure A.1: Definition of confidence interval for the case w/o constrain on support (a) and with additional constrain (b).

our own after-burner macro

`getIntervGivenConstrSimple.C`, used in all sections of this paper.

### A.3 PLM for 4 spin states and two-observables

In section A.2 we have applied the profile likelihood method to a simplified case of extracting one parameter of interest ( $A^W$ ) out of a pair of measurements ( $N_+, N_-$ ), using a model (Eqn. A.13) with two additional nuisance parameters ( $N^0, \beta$ ) and 3 fixed parameters ( $l_{\pm}, P$ ). The complexity of the real world problem discussed in this section, extraction of  $A_L(\eta)$  for W-boson measured at STAR, is much larger.

### A.3.1 Model

In the following we will retain the naming convention of physical quantities, however we will add additional indexing. The indexes  $s, \eta, k$  denote the following:  
 $s$  spin state of colliding beams,  $s = [++, +-, -+, --]$ ,  
 $\eta$  pseudorapidity of 2 detector regions,  $\eta = [\eta_1, \eta_2]$ ,  
 $k$  labels the datasets,  $k=[1,2,\dots,K]$ .

Let's review the previously defined quantities with extended indexing:

$N_{s\eta k}$  are yields **measured** by STAR for spin state ( $s$ ), detector ( $\eta$ ), dataset ( $k$ ),

$\mu_{s\eta k}$  are yields **predicted** by the model defined below.

For clarity let's ignore, for the moment, the dataset index  $k$ . The generic formula for the model  $\mu_{s\eta}$  depends on similar parameters as Eqn. A.13:

$$\mu_{s\eta} = l_s N_\eta^0 [ 1 \oplus_s P_1 \beta_\eta A_{\eta'}^W \oplus_s P_2 \beta_\eta A_{\eta''}^W \oplus_s P_1 P_2 \beta_\eta A^{LL} ] \quad (\text{A.24})$$

where  $\oplus_s$  means the sign switch depending on the spin state 's'. The index of  $A^W$  depends on the angle between polarized beam and detector  $\eta$ -bin. The definitions of the parameters used in Eqn. A.24 are below:

$L_s$  are the relative luminosity corrections,

normalization:  $\sum_s l_s = 4$ , do not depend on the detector,

$N_\eta^0$  are the predicted spin-average yields, nuisance params, change with the detector

$P_1, P_2$  are the beam polarization magnitudes,

$A_{\eta'}^W, A_{\eta''}^W$  are the SSAs for a pair of symmetric  $\eta$ -bins with respect to the polarized beam; which are parameters of interest,

$\beta_\eta$  are the unpolarized corrections to  $A_\eta^W$ , depend on detector angle, nuisance parameter,

$A^{LL}$  is the DSA nuisance param, which has no  $\pm\eta$  detector dependence.

### Model for 8 yields

In total there are 8 different possibilities for the index  $s\eta$  defined in the full model (Eqn. A.24). Below we will write them explicitly

$$\begin{aligned}
 \mu_{++,1} &= l_{++} N_1^0 [ 1 + P_1 \beta_1 A_1^W + P_2 \beta_1 A_2^W + P_1 P_2 \beta_1 A^{LL} ] \\
 \mu_{+-,1} &= l_{+-} N_1^0 [ 1 + P_1 \beta_1 A_1^W - P_2 \beta_1 A_2^W - P_1 P_2 \beta_1 A^{LL} ] \\
 \mu_{-+,1} &= l_{+-} N_1^0 [ 1 - P_1 \beta_1 A_1^W + P_2 \beta_1 A_2^W - P_1 P_2 \beta_1 A^{LL} ] \\
 \mu_{--,1} &= l_{+-} N_1^0 [ 1 - P_1 \beta_1 A_1^W - P_2 \beta_1 A_2^W + P_1 P_2 \beta_1 A^{LL} ] \\
 \mu_{++,2} &= l_{++} N_1^0 [ 1 + P_1 \beta_2 A_2^W + P_2 \beta_2 A_1^W + P_1 P_2 \beta_2 A^{LL} ] \\
 \mu_{+-,2} &= l_{+-} N_1^0 [ 1 + P_1 \beta_2 A_2^W - P_2 \beta_2 A_1^W - P_1 P_2 \beta_2 A^{LL} ] \\
 \mu_{-+,2} &= l_{++} N_1^0 [ 1 - P_1 \beta_2 A_2^W + P_2 \beta_2 A_1^W - P_1 P_2 \beta_2 A^{LL} ] \\
 \mu_{--,2} &= l_{+-} N_1^0 [ 1 - P_1 \beta_2 A_2^W - P_2 \beta_2 A_1^W + P_1 P_2 \beta_2 A^{LL} ]
 \end{aligned} \tag{A.25}$$

From the mathematical perspective, the model of  $\mu_{s\eta}$  defined by Eqns. A.25 does not need any justification. However, if you are a curious physicist, Fig. A.2 defines directions of both beams and signs of the angles of the detector with respect to polarized beam.

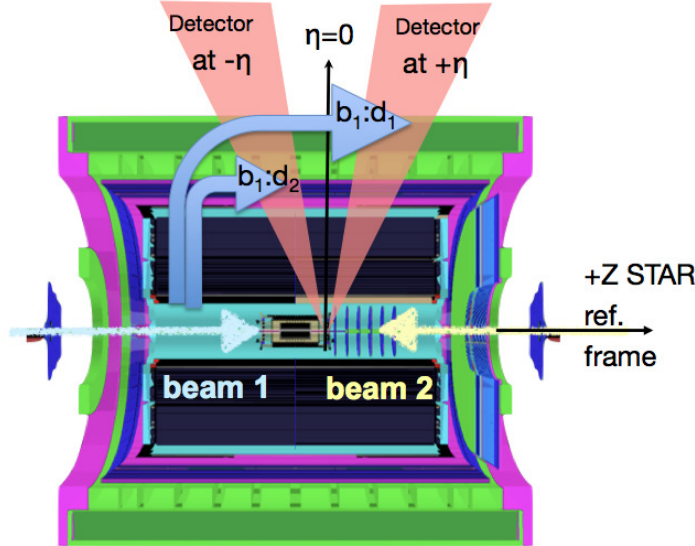


Figure A.2: Definition of beam direction and signs of the angles in the detector with respect to polarized beam needed to define dependence of polarized yields on SSA & DSA in eqs. A.25.

### Model for 4 yields

In certain cases we only have a single detector  $\eta$ . Then, we need only 4 equations for the model:

$$\mu_s = l_s N^0 [1 \oplus_s P_1 \beta A_{\eta'}^W \oplus_s P_2 \beta A_{\eta''}^W \oplus_s P_1 P_2 \beta A^{LL}] \quad (\text{A.26})$$

and,

$$\begin{aligned} \mu_{++} &= l_{++} N^0 [1 + P_1 \beta A_1^W + P_2 \beta A_2^W + P_1 P_2 \beta A^{LL}] \\ \mu_{+-} &= l_{+-} N^0 [1 + P_1 \beta A_1^W - P_2 \beta A_2^W - P_1 P_2 \beta A^{LL}] \\ \mu_{-+} &= l_{-+} N^0 [1 - P_1 \beta A_1^W + P_2 \beta A_2^W - P_1 P_2 \beta A^{LL}] \\ \mu_{--} &= l_{--} N^0 [1 - P_1 \beta A_1^W - P_2 \beta A_2^W + P_1 P_2 \beta A^{LL}] \end{aligned} \quad (\text{A.27})$$

### A.3.2 Total likelihood

The total likelihood for one dataset consisting of 8 measured yields  $N_{s\eta}$  is a product of all p.d.f.s, in analogy to Eqn. A.16,

$$\begin{aligned} L_{\Omega 8}(A_1^W, A_2^W, \nu_8) = \\ \prod_{s,\eta}^8 f(N_{s\eta} | \mu_{s\eta}) \prod_{\eta}^2 g(\beta_{\eta}) \prod_{\eta'}^2 H(1 - |A_{\eta'}^W|) H(1 - |A_{LL}|) \end{aligned} \quad (\text{A.28})$$

where  $\nu_8$  represent 5 nuisance parameters  $\nu_8 = [N_{\eta}^0, \beta_{\eta}, A^{LL}]$ . The functions  $f(\dots), g(\dots), H(\dots)$  were previously defined in the Sec. A.2.2. Fig. A.3 illustrates the impact of the constraints,  $H(x)$ , on the allowed parameter space of the total likelihood function.

Finally, lets allow for multiple datasets and restore the index 'k'. For 2 datasets,  $k=1,2$ , we measure a total of 16 yields  $N_{s\eta k}$  and need to almost double the number of nuisance parameters for the total likelihood. This is the final formula:

$$\begin{aligned} L_{\Omega 16}(A_1^W, A_2^W, \nu_{16}) = \\ \prod_{s,\eta,k}^{16} f(N_{s\eta k} | \mu_{s\eta k}) \prod_{\eta,k}^4 g(\beta_{\eta k}) \prod_{\eta'}^2 H(1 - |A_{\eta'}^W|) H(1 - |A_{LL}|) \end{aligned} \quad (\text{A.29})$$

where  $\nu_{16}$  represent 9 nuisance parameters  $[N_{\eta k}^0, \beta_{\eta k}, A^{LL}]$ .

Similarly, for the two dataset consisting of only 4 measured yields  $N_s$  for one pseudorapidity bin of the detector the total likelihood is:

$$L_{\Omega 8}(A_1^W, A_2^W, \nu_8) = \prod_{s,k}^8 f(N_{sk} | \mu_{sk}) \prod_k^2 g(\beta_k) \prod_k^2 H(1 - |A_{\eta'}^W|) H(1 - |A_{LL}|) \quad (\text{A.30})$$

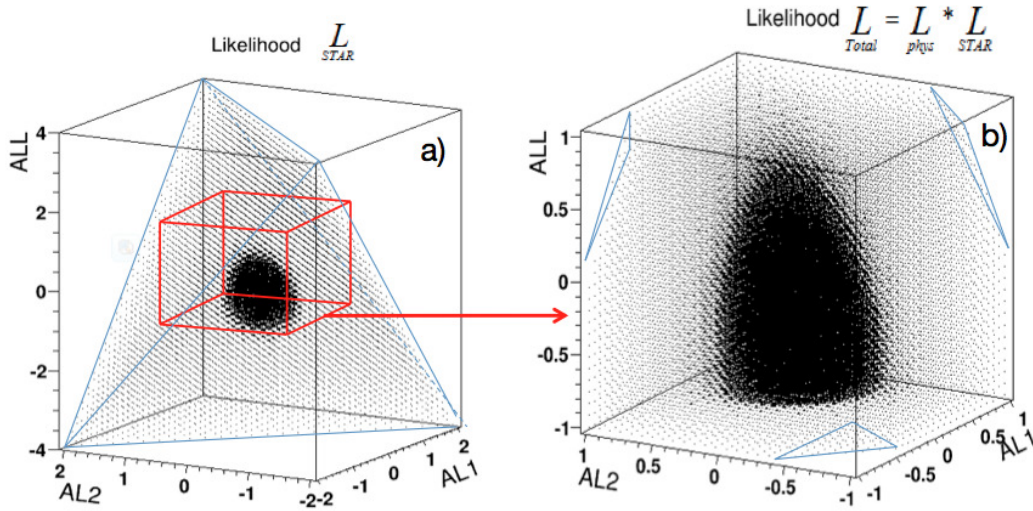


Figure A.3: Illustration of applying the physics constrain,  $L_{PHY}$ , on the support of the total likelihood for Eqn. A.16 . a) no constrains, b) after constrains are applied the support has been reduced.

### A.3.3 RooStats implementation

In section A.2.4 RooStats [81] was mentioned. It is a powerful tool to deal with the profile likelihood of multiple parameters, among many other things. If we define all the models and likelihood PDFs, RooStats will do all the rest of the work for us. To call the RooStats package, 5.28.00 or higher version of ROOT is required. An example of the solution to problem defined by Eqns. A.29 and A.30 is available at [82].

### RooWorkspace

The RooWorkspace is a persistent container for RooFit projects. A workspace can contain and own variables, p.d.f.s, functions and datasets. All objects that

live in the workspace are owned by the workspace. The `import()` method enforces consistency of objects upon insertion into the workspace (e.g. no duplicate object with the same name are allowed) and makes sure all objects in the workspace are connected to each other.

The code `creatPDF.C` is an example for how to define a `RooWorkspace` which contains all the variables, p.d.f.s and datasets that will be used in our analysis.

```
> root -l creatPDF.C
```

Executing this code will create the `RooWorkspace` and print it out.

### ProfileLikelihoodCalculator

In the calculation, all the relative variables should be initialized with the experimental parameters. The function `RooStats::ProfilelikelihoodCalculator` will do the main computation of the profile likelihood.

```
ProfileLikelihoodCalculator plC(*dataY,
    *modelConfig);
```

where the `dataY` is `RooDataSet` which contains all the observables (namely, the spin sorted yields for the  $W A_L$  analysis), and `modelConfig` is a `RooStats::ModelConfig` which contains the full likelihood function (e.g. Eqn. A.29 and Eqn. A.30) and the definition of parameters of interest ( $A^W$ ) for the model ( $\mu$ ).

### Confidence Interval

We can't use the output `ProfilelikelihoodCalculator` directly since it does not account correctly for the reduced support due to constraints. We instead call our "after-burner" code, discussed in section A.2.3. Taking out the profile likelihood ratio from the `ProfileLikelihoodCalculator`, we can get the central value and the confidence interval with given confidence level. The code `getIntervalGivenConstrain.C` is an example to get the result from a profile likelihood ratio that comes from `ProfilelikelihoodCalculator`.

### A.3.4 Numerical results

To allow a cross check by the reader we will report a few results for synthetic data.

#### $A^W$ for 2x8-yields

Lets assume the following 16 yields,  $N_{\eta d}$ , for the pair of 2 detectors, for 2 years:

$$N_{++,1,1}=18, \quad N_{+-,1,1}=24, \quad N_{-+,1,1}=27, \quad N_{--,1,1}=21$$

$$N_{++,2,1}=25, \quad N_{+-,2,1}=14, \quad N_{-+,2,1}=33, \quad N_{--,2,1}=43$$

$$N_{++,1,2}=87, \quad N_{+-,1,2}=184, \quad N_{-+,1,2}=161, \quad N_{--,1,2}=226$$

$$N_{++,2,2}=104, \quad N_{+-,2,2}=186, \quad N_{-+,2,2}=182, \quad N_{--,2,2}=269$$

Other parameters are:

$$L_{s,1} = \{ 1.0180, 0.9891, 0.9926, 1.0002 \}$$

$$L_{s,2} = \{ 0.9950, 1.0077, 0.9933, 1.0040 \}$$

$$P_{1,1}=0.49, P_{2,1}=0.49; P_{1,2}=0.55, P_{2,2}=0.57$$

$$\beta_{\eta,1} = \{ 0.976, 0.971 \}; \beta_{\eta,2} = \{ 0.967, 0.962 \}$$

$A^W$	Profile likelihood, CL=68.3%				Gaussian method*	
	mpv $A^W$	$A_{lo}^W$	$A_{hi}^W$	$\delta A^W$	$A^W$	$\sigma A^W$
$A_1^W$	-0.345	-0.391	-0.299	0.046	-0.345	0.046
$A_2^W$	-0.424	-0.470	-0.378	0.046	-0.425	0.045

Table A.1:  $A_1^W, A_2^W$  from RooStats and a comparison with the Gaussian method for 16-yields, input discussed in Sec. A.3.4.

\*Gaussian method: calculate  $A^W$  for each detector eta bin of each year dataset and then average them with error weight defined by Gaussian error propagation.

Implementation of the RooStats based code for the likelihood function of 16 yields (Eqn. A.29) was applied on this numerical example. The most probable values and confidence intervals for a 68% confidence level of  $A_1^W$  and  $A_2^W$  were obtained simultaneously.

$$A_1^W = -0.345, \text{ with confidence interval } [-0.391, -0.299]$$

$$A_2^W = -0.424, \text{ with confidence interval } [-0.469, -0.378]$$

Table A.1 lists results of  $A_1^W, A_2^W$  and a comparison with the Gaussian method. Results from both methods are consistent . To reproduce execute:

```
> root -l rdAprofF.C'(0,2,"AL")'
```

### $A^W$ for 2x4-yields

To test the case of one detector we assumed:

$$N_{++1}=3, \quad N_{+-1}=2, \quad N_{-+1}=1, \quad N_{--1}=3$$

$$N_{++2}=16, \quad N_{+-2}=15, \quad N_{-+2}=16, \quad N_{--2}=10$$

Other parameters as in section A.3.4, except

$$\beta_1 = 0.991, \quad \beta_2 = 0.962 .$$

For CL of 68% we got:

$$A_1^W = 0.167, \text{ with confidence interval } [-0.065, 0.399]$$

$$A_2^W = 0.181, \text{ with confidence interval } [-0.046, 0.403]$$

$A^W$	Profile likelihood , CL=68.3%				gauss method	
	mpv $A^W$	$A_{lo}^W$	$A_{hi}^W$	$\delta A^W$	$A^W$	$\sigma A^W$
$A_1^W$	0.167	-0.065	0.399	0.232	0.169	0.234
$A_2^W$	0.182	-0.046	0.403	0.224	0.179	0.224

Table A.2:  $A_1^W, A_2^W$  from RooStats and comparison with the Gaussian method for 8-yields, input discussed in Sec. A.3.4.

Table A.2 lists results of  $A_1^W, A_2^W$  and a comparison with the Gaussian method. As expected, the result also compare well for this case. Due to the low statistics, the difference between two methods is more significant. To reproduce execute:

```
> root -l rdAprofF.C'(1,7,"AL")'
```

### A.3.5 $A^W$ from single symmetry $\eta$ -bin

For the case of single symmetry  $\eta$ -bin, it is similar with the model for 4 yields discribed in Sec. A.3.1. The only difference is  $A_{\eta'}^W = A_{\eta''}^W$ , namely, the index  $\eta$  is skipped. So, the parameters of interest are reduced to only one,  $A^W$ . To test this case we assumed:

$$N_{++1}=64, \quad N_{+-1}=68, \quad N_{-+1}=89, \quad N_{--1}=105$$

$$N_{++2}=339, \quad N_{+-2}=586, \quad N_{-+2}=559, \quad N_{--2}=818$$

Other parameters as in section A.3.4, except  
 $\beta_1 = 0.950, \beta_2 = 0.990$  .

For CL of 68% we got:

$$A^W = -0.363, \text{ with confidence interval } [-0.398, 0.348]$$

We can reproduce the result by executing below line,

```
> root -l rdAprofF.C'(0,8,"AL")'
```

For the  $Z A^L$  calculation, we can also use this method by changing the input yields.

### A.3.6 $A^{LL}$ extraction

Previous subsections are focused on  $A^W$ , the single spin asymmetry. For  $A^{LL}$ , the double spin asymmetry, the case is similar. By setting  $A^W$ s as a nuisance parameters and setting  $A^{LL}$  as the parameter of interest, we can extract the most probable value and confidence interval of  $A^{LL}$ .

We used the sample yields from Sec. A.3.4 and A.3.4 to obtain the numerical results of  $A^{LL}$ . The most probable value and confidence interval with 68% confidence level for 2x8-yields and 2x4-yields respectively are shown below.

```
> root -l rdAprofF.C'(0,2,"ALL")'
```

$$A^{LL} = -0.050, \text{ with confidence interval } [-0.134, 0.035].$$

```
> root -l rdAprofF.C'(1,7,"ALL")'
```

$$A^{LL} = -0.155, \text{ with confidence interval } [-0.556, 0.251]$$

### A.3.7 Conclusion

Based on the knowledge from previous section, this method can be applied to extract  $W A_L$  from STAR data from multiple dataset. The Barrel part of STAR detector can be divided into pairs of symmetric pseudorapidity bins, where Eqn [A.29](#) applies. Since there is only one endcap at STAR the Eqn. [A.30](#) should be applied for this case. Applying the model and likelihood described in Sec. [A.3.1](#) and [A.3.2](#), we can obtain the  $W A_L$  pseudorapidity dependence in the full  $\eta$  range of the STAR detector. The  $W A_{LL}$  and  $Z A_L$  also can be extracted via this method.



## Appendix B

# Parameters in Jet Reconstruction

```
// Set analysis cuts for 12-point branch
StAnaPars* anapars12 = new StAnaPars;
anapars12->useTpc = true;
anapars12->useBemc = true;
anapars12->useEemc = true;
anapars12->setTowerEnergyCorrection(new\
  StjTowerEnergyCorrectionForTracksFraction(1.00));

// TPC cuts
anapars12->addTpcCut(new StjTrackCutFlag(0));
anapars12->addTpcCut(new StjTrackCutNHits(12));
anapars12->addTpcCut(new StjTrackCutPossibleHitRatio(0.51));
anapars12->addTpcCut(new StjTrackCutDca(3));
anapars12->addTpcCut(new StjTrackCutTdcaPtDependent);
anapars12->addTpcCut(new StjTrackCutPt(0.2,200));
anapars12->addTpcCut(new StjTrackCutEta(-2.5,2.5));
anapars12->addTpcCut(new StjTrackCutLastPoint(125));

// BEMC cuts
anapars12->addBemcCut(new StjTowerEnergyCutBemcStatus(1));
anapars12->addBemcCut(new StjTowerEnergyCutAdc(4,3));
anapars12->addBemcCut(new StjTowerEnergyCutEt(0.2));

// EEMC cuts
anapars12->addEemcCut(new StjTowerEnergyCutBemcStatus(1));
```

```
anapars12->addEemcCut(new StjTowerEnergyCutAdc(4,3));
anapars12->addEemcCut(new StjTowerEnergyCutEt(0.2));

// Jet cuts
anapars12->addJetCut(new StProtoJetCutPt(3.5,200));
anapars12->addJetCut(new StProtoJetCutEta(-100,100));

// Set anti-kt R=0.6 parameters
StFastJetPars* AntiKtR060Pars = new StFastJetPars;
AntiKtR060Pars->setJetAlgorithm(StFastJetPars::antikt_algorithm);
AntiKtR060Pars->setRparam(0.6);
AntiKtR060Pars->setRecombinationScheme(StFastJetPars::E_scheme);
AntiKtR060Pars->setStrategy(StFastJetPars::Best);
AntiKtR060Pars->setPtMin(3.5);

jetmaker->addBranch("AntiKtR060NHits12",anapars12,AntiKtR060Pars);
```

# Bibliography

- [1] M. Gell-Mann. “A schematic model of baryons and mesons ”. In: *Physics Letters* 8.3 (1964), pp. 214–215. ISSN: 0031-9163 (cit. on p. 2).
- [2] G. Zweig. “An SU(3) model for strong interaction symmetry and its breaking. Version 2”. In: *DEVELOPMENTS IN THE QUARK THEORY OF HADRONS. VOL. 1. 1964 - 1978*. Ed. by D.B. Lichtenberg and Simon Peter Rosen. 1964, pp. 22–101 (cit. on p. 2).
- [3] K. A. Olive et al. “Review of Particle Physics”. In: *Chin. Phys.* C38 (2014), p. 090001 (cit. on pp. 2, 5, 6, 60, 61, 102).
- [4] F. Halzen and Alan D. Martin. “QUARKS AND LEPTONS: AN INTRODUCTORY COURSE IN MODERN PARTICLE PHYSICS”. In: (1984). New York, Usa: Wiley ( 1984) 396p (cit. on p. 2).
- [5] Richard E. Taylor. “Deep inelastic scattering: The early years”. In: *Rev. Mod. Phys.* 63 (3 1991), pp. 573–595 (cit. on p. 2).
- [6] Henry W. Kendall. “Deep inelastic scattering: Experiments on the proton and the observation of scaling”. In: *Rev. Mod. Phys.* 63 (3 1991), pp. 597–614 (cit. on p. 2).
- [7] Jerome I. Friedman. “Deep inelastic scattering: Comparisons with the quark model”. In: *Rev. Mod. Phys.* 63 (3 1991), pp. 615–627 (cit. on p. 2).
- [8] J. D. Bjorken. “Asymptotic Sum Rules at Infinite Momentum”. In: *Phys. Rev.* 179 (1969), pp. 1547–1553 (cit. on p. 3).
- [9] E. D. Bloom, D. H. Coward, H. DeStaebler, et al. “High-Energy Inelastic  $e-p$  Scattering at  $6^\circ$  and  $10^\circ$ ”. In: *Phys. Rev. Lett.* 23 (16 1969), pp. 930–934 (cit. on p. 3).
- [10] M. Breidenbach, J. I. Friedman, H. W. Kendall, et al. “Observed Behavior of Highly Inelastic Electron-Proton Scattering”. In: *Phys. Rev. Lett.* 23 (16 1969), pp. 935–939 (cit. on p. 3).

- 
- [11] J. D. Bjorken and E. A. Paschos. “Inelastic Electron-Proton and  $\gamma$ -Proton Scattering and the Structure of the Nucleon”. In: *Phys. Rev.* 185 (5 1969), pp. 1975–1982 (cit. on p. 3).
- [12] Richard Phillips. Feynman. *Photon-hadron interactions*. W. A. Benjamin Reading, Mass, 1972, xvi, 282 p. ISBN: 0805325107 0805325115 (cit. on p. 3).
- [13] Julius Kuti and Victor F. Weisskopf. “Inelastic Lepton-Nucleon Scattering and Lepton Pair Production in the Relativistic Quark-Parton Model”. In: *Phys. Rev. D* 4 (11 1971), pp. 3418–3439 (cit. on p. 3).
- [14] C. G. Callan and David J. Gross. “High-Energy Electroproduction and the Constitution of the Electric Current”. In: *Phys. Rev. Lett.* 22 (4 1969), pp. 156–159 (cit. on p. 4).
- [15] Constantia Alexandrou. “Hadron structure in lattice QCD”. In: *Progress in Particle and Nuclear Physics* 67.2 (2012). From Quarks and Gluons to Hadrons and Nuclei International Workshop on Nuclear Physics, 33rd Course, pp. 101–116. ISSN: 0146-6410 (cit. on p. 4).
- [16] Pavel M. Nadolsky et al. “Implications of CTEQ global analysis for collider observables”. In: *Phys. Rev. D* 78 (1 2008), p. 013004 (cit. on p. 4).
- [17] A. D. Martin et al. “Parton distributions for the LHC”. In: *European Physical Journal C* 63 (2009), pp. 189–285. arXiv: [0901.0002 \[hep-ph\]](#) (cit. on p. 4).
- [18] Richard D. Ball et al. “Parton distributions with LHC data”. In: *Nuclear Physics B* 867.2 (2013), pp. 244–289. ISSN: 0550-3213 (cit. on p. 4).
- [19] Steven D. Bass. “The Proton spin puzzle: Where are we today?” In: *Mod. Phys. Lett.* A24 (2009), pp. 1087–1101. arXiv: [0905.4619 \[hep-ph\]](#) (cit. on p. 7).
- [20] Christine A. Aidala et al. “The spin structure of the nucleon”. In: *Rev. Mod. Phys.* 85 (2 2013), pp. 655–691 (cit. on p. 7).
- [21] J. Ashman et al. “A Measurement of the Spin Asymmetry and Determination of the Structure Function  $g(1)$  in Deep Inelastic Muon-Proton Scattering”. In: *Phys. Lett.* B206 (1988), p. 364 (cit. on p. 8).
- [22] J. Ashman et al. “An Investigation of the Spin Structure of the Proton in Deep Inelastic Scattering of Polarized Muons on Polarized Protons”. In: *Nucl. Phys.* B328 (1989), p. 1 (cit. on p. 8).

- 
- [23] R.L. Jaffe and Aneesh Manohar. “The g1 problem: Deep inelastic electron scattering and the spin of the proton”. In: *Nuclear Physics B* 337.3 (1990), pp. 509–546. ISSN: 0550-3213 (cit. on p. 8).
- [24] B. Adeva, T. Akdogan, E. Arik, et al. “Polarised quark distributions in the nucleon from semi-inclusive spin asymmetries”. In: *Physics Letters B* 420.1-2 (1998), pp. 180–190. ISSN: 0370-2693 (cit. on p. 8).
- [25] M. Hirai et al. “Determination of fragmentation functions and their uncertainties”. In: *Phys. Rev. D* 75 (9 2007), p. 094009 (cit. on p. 9).
- [26] Daniel de Florian, Rodolfo Sassot, and Marco Stratmann. “Global analysis of fragmentation functions for protons and charged hadrons”. In: *Phys. Rev. D* 76 (7 2007), p. 074033 (cit. on p. 9).
- [27] Daniel de Florian et al. “Extraction of spin-dependent parton densities and their uncertainties”. In: *Phys. Rev. D* 80 (3 2009), p. 034030 (cit. on p. 10).
- [28] D. de Florian et al. “Global Analysis of Helicity Parton Densities and their Uncertainties”. In: *Physical Review Letters* 101.7, 072001 (2008), p. 072001. arXiv: [0804.0422 \[hep-ph\]](#) (cit. on pp. 9, 15).
- [29] Daniel de Florian et al. “Evidence for Polarization of Gluons in the Proton”. In: *Phys. Rev. Lett.* 113 (1 2014), p. 012001 (cit. on pp. 9, 11).
- [30] Elliot Leader, Aleksander V. Sidorov, and Dimiter B. Stamenov. “Determination of polarized parton densities from a QCD analysis of inclusive and semi-inclusive deep inelastic scattering data”. In: *Phys. Rev. D* 82 (11 2010), p. 114018 (cit. on pp. 9, 15).
- [31] Richard D. Ball et al. “Unbiased determination of polarized parton distributions and their uncertainties NNPDF Collaboration”. In: *Nuclear Physics, Section B* 874.1 (2013), pp. 36–84. ISSN: 0550-3213 (cit. on p. 9).
- [32] Emanuele R. Nocera et al. “A first unbiased global determination of polarized PDFs and their uncertainties”. In: *Nucl. Phys.* B887 (2014), pp. 276–308. arXiv: [1406.5539 \[hep-ph\]](#) (cit. on pp. 9, 86, 87, 91, 92).
- [33] L. Adamczyk, J. K. Adkins, G. Agakishiev, et al. “Precision Measurement of the Longitudinal Double-Spin Asymmetry for Inclusive Jet Production in Polarized Proton Collisions at  $\sqrt{s} = 200\text{GeV}$ ”. In: *Phys. Rev. Lett.* 115 (9 2015), p. 092002 (cit. on pp. 10, 51).

- [34] Gerry Bunce et al. “PROSPECTS FOR SPIN PHYSICS AT RHIC”. In: *Annual Review of Nuclear and Particle Science* 50.1 (2000), pp. 525–575. eprint: <http://dx.doi.org/10.1146/annurev.nucl.50.1.525> (cit. on pp. 11, 12).
- [35] Daniel de Florian and Werner Vogelsang. “Helicity parton distributions from spin asymmetries in  $W$ -boson production at RHIC”. In: *Phys. Rev. D* 81 (9 2010), p. 094020 (cit. on pp. 14, 15).
- [36] Qinghua Xu. “Recent results on nucleon spin structure study at RHIC”. In: *Frontiers of Physics* 10.6, 4 (2015), p. 4 (cit. on p. 15).
- [37] P.M. Nadolsky and C.-P. Yuan. “Single-spin physics with weak bosons at RHIC ”. In: *Nuclear Physics B* 666.1-2 (2003), pp. 31 –55. ISSN: 0550-3213 (cit. on pp. 15, 79).
- [38] M. M. Aggarwal, Z. Ahammed, A. V. Alakhverdyants, et al. “Measurement of the Parity-Violating Longitudinal Single-Spin Asymmetry for  $W^\pm$  Boson Production in Polarized Proton-Proton Collisions at  $\sqrt{s}=500\text{GeV}$ ”. In: *Phys. Rev. Lett.* 106 (6 2011), p. 062002 (cit. on pp. 16, 33).
- [39] A. Adare et al. “Cross Section and Parity-Violating Spin Asymmetries of  $W^\pm$  Boson Production in Polarized  $p + p$  Collisions at  $\sqrt{s} = 500\text{GeV}$ ”. In: *Phys. Rev. Lett.* 106 (6 2011), p. 062001 (cit. on pp. 16, 33).
- [40] I. Alekseev et al. “Polarized proton collider at RHIC”. In: *Nuclear Instruments and Methods in Physics Research Section A: Accelerators, Spectrometers, Detectors and Associated Equipment* 499.2-3 (2003). The Relativistic Heavy Ion Collider Project: RHIC and its Detectors, pp. 392 –414. ISSN: 0168-9002 (cit. on p. 19).
- [41] *RHIC*. <https://www.bnl.gov/rhic/> (cit. on p. 19).
- [42] A. Zelenski, J. Alessi, B. Briscoe, et al. “Optically pumped polarized H-ion source for RHIC spin physics”. In: *Review of Scientific Instruments* 73.2 (2002), pp. 888–891 (cit. on p. 20).
- [43] V. Bargmann, Louis Michel, and V. L. Telegdi. “Precession of the Polarization of Particles Moving in a Homogeneous Electromagnetic Field”. In: *Phys. Rev. Lett.* 2 (10 1959), pp. 435–436 (cit. on p. 21).

- 
- [44] Ya. S. Derbenev, A. M. Kondratenko, S. I. Serednyakov, et al. “RADIATIVE POLARIZATION: OBTAINING, CONTROL, USING”. In: *Part. Accel.* 8 (1978), pp. 115–126 (cit. on p. 21).
- [45] W. W. MacKay et al. “Commissioning Spin Rotators in RHIC”. In: *Conf. Proc.* C030512 (2003), p. 1697 (cit. on p. 21).
- [46] I. Nakagawa et al. “Polarization Measurements of RHIC-pp RUN05 Using CNI pC-Polarimeter”. In: *AIP Conference Proceedings* 915.1 (2007), pp. 912–915 (cit. on p. 22).
- [47] I. G. Alekseev, A. Bravar, G. Bunce, et al. “Measurements of single and double spin asymmetry in  $pp$  elastic scattering in the CNI region with a polarized atomic hydrogen gas jet target”. In: *Phys. Rev. D* 79 (9 2009), p. 094014 (cit. on p. 22).
- [48] D. Smirnov and others. (RHIC Polarimetry Group). *Final Results for RHIC polarized pp data analysis*. <https://wiki.bnl.gov/rhicspin/Results> (cit. on pp. 23, 36).
- [49] K.H. Ackermann, N. Adams, C. Adler, et al. “STAR detector overview”. In: *Nuclear Instruments and Methods in Physics Research Section A: Accelerators, Spectrometers, Detectors and Associated Equipment* 499.2-3 (2003). The Relativistic Heavy Ion Collider Project: RHIC and its Detectors, pp. 624 – 632. ISSN: 0168-9002 (cit. on p. 23).
- [50] K. Adcox, S.S. Adler, M. Aizama, et al. “PHENIX detector overview”. In: *Nuclear Instruments and Methods in Physics Research Section A: Accelerators, Spectrometers, Detectors and Associated Equipment* 499.2-3 (2003). The Relativistic Heavy Ion Collider Project: RHIC and its Detectors, pp. 469 – 479. ISSN: 0168-9002 (cit. on p. 23).
- [51] M. Anderson, J. Berkovitz, W. Betts, et al. “The STAR time projection chamber: a unique tool for studying high multiplicity events at RHIC”. In: *Nuclear Instruments and Methods in Physics Research Section A: Accelerators, Spectrometers, Detectors and Associated Equipment* 499.2-3 (2003). The Relativistic Heavy Ion Collider Project: RHIC and its Detectors, pp. 659 –678. ISSN: 0168-9002 (cit. on pp. 25–27).

- 
- [52] M Anerella et al. “The RHIC magnet system”. In: *Nuclear Instruments and Methods in Physics Research Section A: Accelerators, Spectrometers, Detectors and Associated Equipment* 499.2-3 (2003). The Relativistic Heavy Ion Collider Project: RHIC and its Detectors, pp. 280 –315. ISSN: 0168-9002 (cit. on p. 25).
- [53] L. Kotchenda, S. Kozlov, P. Kravtsov, et al. “STAR TPC gas system ”. In: *Nuclear Instruments and Methods in Physics Research Section A: Accelerators, Spectrometers, Detectors and Associated Equipment* 499.2-3 (2003). The Relativistic Heavy Ion Collider Project: RHIC and its Detectors, pp. 703 –712. ISSN: 0168-9002 (cit. on p. 26).
- [54] M. Anderson, F. Bieser, R. Bossingham, et al. “A readout system for the STAR time projection chamber ”. In: *Nuclear Instruments and Methods in Physics Research Section A: Accelerators, Spectrometers, Detectors and Associated Equipment* 499.2-3 (2003). The Relativistic Heavy Ion Collider Project: RHIC and its Detectors, pp. 679 –691. ISSN: 0168-9002 (cit. on p. 26).
- [55] STAR Collaboration. “A Proposal for STAR Inner TPC Sector Upgrade (iTTPC) (STAR Note # 619)”. In: (2015) (cit. on p. 26).
- [56] J. Abele, J. Berkovitz, J. Boehm, et al. “The laser system for the STAR time projection chamber ”. In: *Nuclear Instruments and Methods in Physics Research Section A: Accelerators, Spectrometers, Detectors and Associated Equipment* 499.2-3 (2003). The Relativistic Heavy Ion Collider Project: RHIC and its Detectors, pp. 692 –702. ISSN: 0168-9002 (cit. on p. 26).
- [57] M. Beddo, E. Bielick, T. Fornek, et al. “The STAR Barrel Electromagnetic Calorimeter ”. In: *Nuclear Instruments and Methods in Physics Research Section A: Accelerators, Spectrometers, Detectors and Associated Equipment* 499.2-3 (2003). The Relativistic Heavy Ion Collider Project: RHIC and its Detectors, pp. 725 –739. ISSN: 0168-9002 (cit. on pp. 27, 29).
- [58] F.S. Bieser, H.J. Crawford, J. Engelage, et al. “The STAR trigger ”. In: *Nuclear Instruments and Methods in Physics Research Section A: Accelerators, Spectrometers, Detectors and Associated Equipment* 499.2-3 (2003). The Relativistic Heavy Ion Collider Project: RHIC and its Detectors, pp. 766–777. ISSN: 0168-9002 (cit. on pp. 29, 33).

- [59] C.E. Allgower, B.D. Anderson, A.R. Baldwin, et al. “The STAR Endcap Electromagnetic Calorimeter”. In: *Nuclear Instruments and Methods in Physics Research Section A: Accelerators, Spectrometers, Detectors and Associated Equipment* 499.2-3 (2003). The Relativistic Heavy Ion Collider Project: RHIC and its Detectors, pp. 740–750. ISSN: 0168-9002 (cit. on pp. [29–31](#), [49](#)).
- [60] L. Adamczyk, G. Agakishiev, M. M. Aggarwal, et al. “Measurement of the  $W \rightarrow e\nu$  and  $Z/\gamma^* \rightarrow e^+e^-$  production cross sections at mid-rapidity in proton-proton collisions at  $\sqrt{s}=500\text{GeV}$ ”. In: *Phys. Rev. D* 85 (9 2012), p. 092010 (cit. on p. [33](#)).
- [61] P. R. Cameron et al. “The RHIC wall current monitor system”. In: *18th IEEE Particle Accelerator Conference*. 1999, pp. 2146–2148 (cit. on p. [34](#)).
- [62] A. Drees et al. “Results from Vernier Scans at RHIC during the pp run 2001-2002”. In: *Particle Accelerator Conference, 2003. PAC 2003. Proceedings of the*. Vol. 3. 2003, 1688–1690 vol.3 (cit. on p. [35](#)).
- [63] S van der Meer. *Calibration of the effective beam height in the ISR*. Tech. rep. CERN-ISR-PO-68-31. ISR-PO-68-31. Geneva: CERN, 1968 (cit. on p. [35](#)).
- [64] Torbjörn Sjöstrand, Stephen Mrenna, and Peter Skands. “PYTHIA 6.4 physics and manual”. In: *Journal of High Energy Physics* 2006.05 (2006), p. 026 (cit. on pp. [39](#), [40](#)).
- [65] Peter Z. Skands. “Tuning Monte Carlo generators: The Perugia tunes”. In: *Phys. Rev. D* 82 (7 2010), p. 074018 (cit. on p. [40](#)).
- [66] P. Golonka, B. Kersevan, T. Pierzchala, et al. “The Tauola photos F environment for the TAUOLA and PHOTOS packages: Release. 2.” In: *Comput. Phys. Commun.* 174 (2006), pp. 818–835. arXiv: [hep-ph/0312240](#) [[hep-ph](#)] (cit. on p. [40](#)).
- [67] R. Brun et al. “Geant: Simulation Program for Particle Physics Experiments. User Guide and Reference Manual”. In: (1978) (cit. on p. [40](#)).
- [68] Rosi Reed. “Vertex finding in pile-up rich events for p+p and d+Au collisions at STAR, (Presented at CHEP). Available also as STAR note SN488”. In: (2008) (cit. on p. [44](#)).

- [69] M. Cacciari, G. P. Salam, and G. Soyez. “The anti- $k_t$  jet clustering algorithm”. In: *Journal of High Energy Physics* 4, 063 (2008), p. 063. arXiv: [0802.1189 \[hep-ph\]](#) (cit. on p. 51).
- [70] Pibero Djawotho, Carl Gagliardi, and Andrew Cudd. “Inclusive jet double-helicity asymmetry  $A_{LL}$  in polarized  $p+p$  collisions at  $\sqrt{s} = 200\text{GeV}$  (STAR Note # 573)”. In: (2013) (cit. on p. 51).
- [71] Felix Ringer and Werner Vogelsang. “Single-spin asymmetries in  $W$  boson production at next-to-leading order”. In: *Phys. Rev. D* 91 (9 2015), p. 094033 (cit. on p. 53).
- [72] Jan Balewski, Justin Stevens, and Jinlong Zhang. “Measurement of the parity-violating longitudinal single-spin asymmetry for weak boson production in polarized proton-proton collisions at  $\sqrt{s} = 510\text{GeV}$  (STAR Note # 597)”. In: (2014) (cit. on p. 60).
- [73] L. Adamczyk, J. K. Adkins, G. Agakishiev, et al. “Measurement of Longitudinal Spin Asymmetries for Weak Boson Production in Polarized Proton-Proton Collisions at RHIC”. In: *Phys. Rev. Lett.* 113 (7 2014), p. 072301 (cit. on pp. 67, 70, 84, 85, 87, 90, 91).
- [74] E. Leader. *Spin in Particle Physics*. 2001, p. 522 (cit. on pp. 78, 90).
- [75] E. Aschenauer, A. Bazilevsky, K. Boyle, et al. “The RHIC Spin Programs: Achievements and Future Opportunities”. In: (2013). arXiv: [1304.0079 \[nucl-ex\]](#) (cit. on p. 87).
- [76] Zhong-Bo Kang and Jacques Soffer. “General positivity bounds for spin observables in single particle inclusive production”. In: *Phys. Rev. D* 83 (11 2011), p. 114020 (cit. on p. 91).
- [77] E. Aschenauer, A. Bazilevsky, M. Diehl, et al. “The RHIC Spin Programs: Achievements and Future Opportunities”. In: (2015). arXiv: [1501.01220 \[nucl-ex\]](#) (cit. on p. 94).
- [78] A. Accardi, J. L. Albacete, M. Anselmino, et al. “Electron Ion Collider: The Next QCD Frontier - Understanding the glue that binds us all”. In: *ArXiv e-prints* (2012). arXiv: [1212.1701 \[nucl-ex\]](#) (cit. on pp. 94, 95).

- 
- [79] Elke C. Aschenauer, Thomas Burton, Marco Stratmann, et al. “Prospects for charged current deep-inelastic scattering off polarized nucleons at a future electron-ion collider”. In: *Phys. Rev. D* 88 (11 2013), p. 114025 (cit. on p. 94).
- [80] Glen Cowan. “Statistics for Searches at the LHC”. In: *Proceedings, 69th Scottish Universities Summer School in Physics : LHC Phenomenology (SUSSP69)*. 2013, pp. 321–355. arXiv: [1307.2487](https://arxiv.org/abs/1307.2487) [[hep-ex](#)] (cit. on p. 102).
- [81] *Statistical tool developed for LHC*. <https://twiki.cern.ch/twiki/bin/view/RooStats> (cit. on pp. 103, 108).
- [82] *Directory at MIT disc at BNL-RCF*. [/star/institutions/mit/balewski/freezer/2013-SN-590/](#) (cit. on p. 108).



# Acknowledgements

The accomplishment of this thesis indicates the end of my graduate student career. This will never happen without the support and consideration of many people. I would like to take this opportunity to express my gratitude to all of them listed or might not listed in the following.

First of all, to my supervisor, Professor Qinghua Xu, thank you for introducing me this amazing field, providing me opportunity to participate the STAR collaboration and study at BNL. From the very fundamental knowledge to the accomplishment of the thesis, from research to live, I deeply appreciate your continuous and patient guidance, encouragement and support.

To Professor Nu Xu and Zhangbu Xu, thank you for the support during the two and half years when I stayed at BNL and the opportunity to present on the international conference. To Jan Balewski and Justin Stevens, thank you for teaching me everything I know about the  $W$  analysis. I benefit so much from working with you at BNL and MIT. To Bernd Sorrow and Devika Gunarathne, thank you for the valuable discussions about the  $W$  analysis and BEMC calibration. To the remaining members of STAR spin group, especially Carl Gagliardi, Scott Wissink, Elke Aschenauer, Ernst Sichtermann, Renee Fatemi, Hal Spinka, Bill Christie, Will Jacobs, Anselm Vossen, and Jim Drachenberg, thank you for the nice scientific atmosphere, numerous ideas and valuable suggestions. I am also grateful to the STAR software and computing team, in particular Gene Van Buren, for all the technical support you provided and the helpful discussions.

I would like to thank the teaches in high energy group of Shandong University. They are Prof. Zuotang Liang, Prof. Xuexiao Zhang, Prof. Meng Wang, Prof. Cunfeng Feng, Prof. Chengguan Zhu, Prof. Xiangtao Huang, Prof. Yanshen Sun, Prof. Liang Xue, Prof. Qun Wu, Prof. Jiangbin Jiao, Prof. Jiang Deng, Prof. Hui Dong, Prof. Zongguo Si, Prof. Shiyuan Li, Prof. Lianliang Ma, Dr. Jiajin Zhou, Dr. Xiaolin Li, Mr. Changyu Li. Thank them, not only for the knowledge about the high energy physics they taught in the class, but also for the great research

community.

To my friends at high energy physics group of Shandong University, to Xin Xia, Xu Wang, Peng Ge, Tongye Xu, Weimin Ding, Teng Li, Bo Liu, Qingyuan Liu, Quanyou Cheng, Mengting Yan, Wenjing Zheng, Yanyan Du, , Ke Li, Zhangwen Zhu, Jincheng Mei, Fuwang Shen, Shuai Wang, Jie Cheng, Qiyun Li, Jiaojiao Song, Ningbo Chang, Shuyi Wei, Wei Zhu, Juntao Wang, Kaibao Chen, Ruiqing Wang, Weihua Yang, thank you for every help, every communication. When I recall Shandong University many years later, you will be the best part of it.

I spent half of my graduate career at Brookhaven Lab. I would like to thank my friends there. To Prof. Shusu Shi, Dr. Hongwei Ke, Dr. Bingchu Huang, Dr. Liang Zheng, Dr. Wangmei Zha, Dr. Chi Yang, Dr. Xuanli, Zilong Chang, Long Zhou, Long Ma, Zhengqiao Zheng, Qian Yang, Zhao Feng, Zaocheng Ye, Xiaozhi Bai, Xinjie Huang, Chensheng Zhou, and Xiaoxuan Chu, thank you for all the help and all the great time in such a place so far away from hometown. Specially to my roommates, Dr. Shuai Yang, Yifei Xu, thank you for making our apartment just like a home.

Last but not least, I would like to thank my family. To my parents, thank you for the warm home, for the ordinary but full of love family education, and for always giving me your best and being proud of me. To my sisters, thank you for the encouragement and accompanying our parents when I am away. To my wife Xiuqing, thank you for your constant love, support and understanding, for the sunshine you fill in my life. To my daughter, I never knew I could be so happy before your birth! You are the best gift!

# Publications and Presentations

## Papers (as Primary Author)

1. **Measurement of Longitudinal Spin Asymmetries for Weak Boson Production in Polarized Proton-Proton Collisions at RHIC**  
STAR collaboration, *Phys. Rev. Lett.* **113**, 072301(2014)

## Conference Proceedings

1. **Measurement of Longitudinal Spin Asymmetries for Weak Boson Production in Polarized Proton-Proton Collisions at STAR**  
Jinlong Zhang (for the STAR Collaboration), *Int. J. Mod. Phys. Conf. Ser.* **40**, 1660019(2014)

## Selected Presentations

1. Measurement of longitudinal spin asymmetries for  $W$  boson production in polarized proton-proton collisions at STAR, Twelfth Conference on the Intersections of Particle and Nuclear Physics, Vail, CO, MAY 2015
2. Measurement of longitudinal spin asymmetries for weak boson Production in polarized proton-proton collisions at STAR, The 21st International Symposium on Spin Physics, Beijing, China, OCTOBER 2014
3. Recent STAR results on  $W$  boson production in longitudinally polarized  $p+p$  collisions, APS Division of Nuclear Physics Fall Meeting, Newport News, VA, OCTOBER 2013



## Measurement of Longitudinal Spin Asymmetries for Weak Boson Production in Polarized Proton-Proton Collisions at RHIC

L. Adamczyk,<sup>1</sup> J. K. Adkins,<sup>23</sup> G. Agakishiev,<sup>21</sup> M. M. Aggarwal,<sup>35</sup> Z. Ahammed,<sup>53</sup> I. Alekseev,<sup>19</sup> J. Alford,<sup>22</sup> C. D. Anson,<sup>32</sup> A. Aparin,<sup>21</sup> D. Arkhipkin,<sup>4</sup> E. C. Aschenauer,<sup>4</sup> G. S. Averichev,<sup>21</sup> J. Balewski,<sup>27</sup> A. Banerjee,<sup>53</sup> D. R. Beavis,<sup>4</sup> R. Bellwied,<sup>49</sup> A. Bhasin,<sup>20</sup> A. K. Bhati,<sup>35</sup> P. Bhattarai,<sup>48</sup> H. Bichsel,<sup>55</sup> J. Bielcik,<sup>13</sup> J. Bielcikova,<sup>14</sup> L. C. Bland,<sup>4</sup> I. G. Bordyuzhin,<sup>19</sup> W. Borowski,<sup>45</sup> J. Bouchet,<sup>22</sup> A. V. Brandin,<sup>30</sup> S. G. Brovko,<sup>6</sup> S. Bültmann,<sup>33</sup> I. Bunzarov,<sup>21</sup> T. P. Burton,<sup>4</sup> J. Butterworth,<sup>41</sup> H. Caines,<sup>57</sup> M. Calderón de la Barca Sánchez,<sup>6</sup> J. M. Campbell,<sup>32</sup> D. Cebra,<sup>6</sup> R. Cendejas,<sup>36</sup> M. C. Cervantes,<sup>47</sup> P. Chaloupka,<sup>13</sup> Z. Chang,<sup>47</sup> S. Chattopadhyay,<sup>53</sup> H. F. Chen,<sup>42</sup> J. H. Chen,<sup>44</sup> L. Chen,<sup>9</sup> J. Cheng,<sup>50</sup> M. Cherney,<sup>12</sup> A. Chikanian,<sup>57</sup> W. Christie,<sup>4</sup> J. Chwastowski,<sup>11</sup> M. J. M. Codrington,<sup>48</sup> G. Contin,<sup>26</sup> J. G. Cramer,<sup>55</sup> H. J. Crawford,<sup>5</sup> X. Cui,<sup>42</sup> S. Das,<sup>16</sup> A. Davila Leyva,<sup>48</sup> L. C. De Silva,<sup>12</sup> R. R. Debbé,<sup>4</sup> T. G. Dedovich,<sup>21</sup> J. Deng,<sup>43</sup> A. A. Derevschikov,<sup>37</sup> R. Derradi de Souza,<sup>8</sup> S. Dhamija,<sup>18</sup> B. di Ruzza,<sup>4</sup> L. Didenko,<sup>4</sup> C. Dilks,<sup>36</sup> F. Ding,<sup>6</sup> P. Djawotho,<sup>47</sup> X. Dong,<sup>26</sup> J. L. Drachenberg,<sup>52</sup> J. E. Draper,<sup>6</sup> C. M. Du,<sup>25</sup> L. E. Dunkelberger,<sup>7</sup> J. C. Dunlop,<sup>4</sup> L. G. Efimov,<sup>21</sup> J. Engelage,<sup>5</sup> K. S. Engle,<sup>51</sup> G. Eppley,<sup>41</sup> L. Eun,<sup>26</sup> O. Evdokimov,<sup>10</sup> O. Eysler,<sup>4</sup> R. Fatemi,<sup>23</sup> S. Fazio,<sup>4</sup> J. Fedorisin,<sup>21</sup> P. Filip,<sup>21</sup> E. Finch,<sup>57</sup> Y. Fisyak,<sup>4</sup> C. E. Flores,<sup>6</sup> C. A. Gagliardi,<sup>47</sup> D. R. Gangadharan,<sup>32</sup> D. Garand,<sup>38</sup> F. Geurts,<sup>41</sup> A. Gibson,<sup>52</sup> M. Girard,<sup>54</sup> S. Gliske,<sup>2</sup> L. Greiner,<sup>26</sup> D. Grosnick,<sup>52</sup> D. S. Gunarathne,<sup>46</sup> Y. Guo,<sup>42</sup> A. Gupta,<sup>20</sup> S. Gupta,<sup>20</sup> W. Guryn,<sup>4</sup> B. Haag,<sup>6</sup> A. Hamed,<sup>47</sup> L.-X. Han,<sup>44</sup> R. Haque,<sup>31</sup> J. W. Harris,<sup>57</sup> S. Heppelmann,<sup>36</sup> A. Hirsch,<sup>38</sup> G. W. Hoffmann,<sup>48</sup> D. J. Hofman,<sup>10</sup> S. Horvat,<sup>57</sup> B. Huang,<sup>4</sup> H. Z. Huang,<sup>7</sup> X. Huang,<sup>50</sup> P. Huck,<sup>9</sup> T. J. Humanic,<sup>32</sup> G. Igo,<sup>7</sup> W. W. Jacobs,<sup>18</sup> H. Jang,<sup>24</sup> E. G. Judd,<sup>5</sup> S. Kabana,<sup>45</sup> D. Kalinkin,<sup>19</sup> K. Kang,<sup>50</sup> K. Kauder,<sup>10</sup> H. W. Ke,<sup>4</sup> D. Keane,<sup>22</sup> A. Kechechyan,<sup>21</sup> A. Kesich,<sup>6</sup> Z. H. Khan,<sup>10</sup> D. P. Kikola,<sup>54</sup> I. Kisel,<sup>15</sup> A. Kisiel,<sup>54</sup> D. D. Koetke,<sup>52</sup> T. Kollegger,<sup>15</sup> J. Konzer,<sup>38</sup> I. Koralt,<sup>33</sup> L. K. Kosarzewski,<sup>54</sup> L. Kotchenda,<sup>30</sup> A. F. Kraishan,<sup>46</sup> P. Kravtsov,<sup>30</sup> K. Krueger,<sup>2</sup> I. Kulakov,<sup>15</sup> L. Kumar,<sup>31</sup> R. A. Kycia,<sup>11</sup> M. A. C. Lamont,<sup>4</sup> J. M. Landgraf,<sup>4</sup> K. D. Landry,<sup>7</sup> J. Lauret,<sup>4</sup> A. Lebedev,<sup>4</sup> R. Lednický,<sup>21</sup> J. H. Lee,<sup>4</sup> M. J. LeVine,<sup>4</sup> C. Li,<sup>42</sup> W. Li,<sup>44</sup> X. Li,<sup>38</sup> X. Li,<sup>46</sup> Y. Li,<sup>50</sup> Z. M. Li,<sup>9</sup> M. A. Lisa,<sup>32</sup> F. Liu,<sup>9</sup> T. Ljubicic,<sup>4</sup> W. J. Llope,<sup>41</sup> M. Lomnitz,<sup>22</sup> R. S. Longacre,<sup>4</sup> X. Luo,<sup>9</sup> G. L. Ma,<sup>44</sup> Y. G. Ma,<sup>44</sup> D. M. M. D. Madagodagettige Don,<sup>12</sup> D. P. Mahapatra,<sup>16</sup> R. Majka,<sup>57</sup> S. Margetis,<sup>22</sup> C. Markert,<sup>48</sup> H. Masui,<sup>26</sup> H. S. Matis,<sup>26</sup> D. McDonald,<sup>49</sup> T. S. McShane,<sup>12</sup> N. G. Minaev,<sup>37</sup> S. Mioduszewski,<sup>47</sup> B. Mohanty,<sup>31</sup> M. M. Mondal,<sup>47</sup> D. A. Morozov,<sup>37</sup> M. K. Mustafa,<sup>26</sup> B. K. Nandi,<sup>17</sup> Md. Nasim,<sup>31</sup> T. K. Nayak,<sup>53</sup> J. M. Nelson,<sup>3</sup> G. Nigmatkulov,<sup>30</sup> L. V. Nogach,<sup>37</sup> S. Y. Noh,<sup>24</sup> J. Novak,<sup>29</sup> S. B. Nurushev,<sup>37</sup> G. Odyniec,<sup>26</sup> A. Ogawa,<sup>4</sup> K. Oh,<sup>39</sup> A. Ohlson,<sup>57</sup> V. Okorokov,<sup>30</sup> E. W. Oldag,<sup>48</sup> D. L. Olivitt, Jr.,<sup>46</sup> M. Pachr,<sup>13</sup> B. S. Page,<sup>18</sup> S. K. Pal,<sup>53</sup> Y. X. Pan,<sup>7</sup> Y. Pandit,<sup>10</sup> Y. Panebratsev,<sup>21</sup> T. Pawlak,<sup>54</sup> B. Pawlik,<sup>34</sup> H. Pei,<sup>9</sup> C. Perkins,<sup>5</sup> W. Peryt,<sup>54</sup> P. Pile,<sup>4</sup> M. Planinic,<sup>58</sup> J. Pluta,<sup>54</sup> N. Poljak,<sup>58</sup> K. Poniatowska,<sup>54</sup> J. Porter,<sup>26</sup> A. M. Poskanzer,<sup>26</sup> N. K. Pruthi,<sup>35</sup> M. Przybycien,<sup>1</sup> P. R. Pujahari,<sup>17</sup> J. Putschke,<sup>56</sup> H. Qiu,<sup>26</sup> A. Quintero,<sup>22</sup> S. Ramachandran,<sup>23</sup> R. Raniwala,<sup>40</sup> S. Raniwala,<sup>40</sup> R. L. Ray,<sup>48</sup> C. K. Riley,<sup>57</sup> H. G. Ritter,<sup>26</sup> J. B. Roberts,<sup>41</sup> O. V. Rogachevskiy,<sup>21</sup> J. L. Romero,<sup>6</sup> J. F. Ross,<sup>12</sup> A. Roy,<sup>53</sup> L. Ruan,<sup>4</sup> J. Rusnak,<sup>14</sup> O. Rusnakova,<sup>13</sup> N. R. Sahoo,<sup>47</sup> P. K. Sahu,<sup>16</sup> I. Sakrejda,<sup>26</sup> S. Salur,<sup>26</sup> J. Sandweiss,<sup>57</sup> E. Sangaline,<sup>6</sup> A. Sarkar,<sup>17</sup> J. Schambach,<sup>48</sup> R. P. Scharenberg,<sup>38</sup> A. M. Schmah,<sup>26</sup> W. B. Schmidke,<sup>4</sup> N. Schmitz,<sup>28</sup> J. Seger,<sup>12</sup> P. Seyboth,<sup>28</sup> N. Shah,<sup>7</sup> E. Shahaliev,<sup>21</sup> P. V. Shanmuganathan,<sup>22</sup> M. Shao,<sup>42</sup> B. Sharma,<sup>35</sup> W. Q. Shen,<sup>44</sup> S. S. Shi,<sup>26</sup> Q. Y. Shou,<sup>44</sup> E. P. Sichtermann,<sup>26</sup> R. N. Singaraju,<sup>53</sup> M. J. Skoby,<sup>18</sup> D. Smirnov,<sup>4</sup> N. Smirnov,<sup>57</sup> D. Solanki,<sup>40</sup> P. Sorensen,<sup>4</sup> H. M. Spinka,<sup>2</sup> B. Srivastava,<sup>38</sup> T. D. S. Stanislaus,<sup>52</sup> J. R. Stevens,<sup>27</sup> R. Stock,<sup>15</sup> M. Strikhanov,<sup>30</sup> B. Stringfellow,<sup>38</sup> M. Sumbera,<sup>14</sup> X. Sun,<sup>26</sup> X. M. Sun,<sup>26</sup> Y. Sun,<sup>42</sup> Z. Sun,<sup>25</sup> B. Surrøw,<sup>46</sup> D. N. Svirida,<sup>19</sup> T. J. M. Symons,<sup>26</sup> M. A. Szelezniak,<sup>26</sup> J. Takahashi,<sup>8</sup> A. H. Tang,<sup>4</sup> Z. Tang,<sup>42</sup> T. Tarnowsky,<sup>29</sup> J. H. Thomas,<sup>26</sup> A. R. Timmins,<sup>49</sup> D. Tlusty,<sup>14</sup> M. Tokarev,<sup>21</sup> S. Trentalange,<sup>7</sup> R. E. Tribble,<sup>47</sup> P. Tribedy,<sup>53</sup> B. A. Trzeciak,<sup>13</sup> O. D. Tsai,<sup>7</sup> J. Turnau,<sup>34</sup> T. Ullrich,<sup>4</sup> D. G. Underwood,<sup>2</sup> G. Van Buren,<sup>4</sup> G. van Nieuwenhuizen,<sup>27</sup> M. Vandenbroucke,<sup>46</sup> J. A. Vanfossen, Jr.,<sup>22</sup> R. Varma,<sup>17</sup> G. M. S. Vasconcelos,<sup>8</sup> A. N. Vasiliev,<sup>37</sup> R. Vertesi,<sup>14</sup> F. Videbæk,<sup>4</sup> Y. P. Vijoyi,<sup>53</sup> S. Vokal,<sup>21</sup> A. Vossen,<sup>18</sup> M. Wada,<sup>48</sup> F. Wang,<sup>38</sup> G. Wang,<sup>7</sup> H. Wang,<sup>4</sup> J. S. Wang,<sup>25</sup> X. L. Wang,<sup>42</sup> Y. Wang,<sup>50</sup> Y. Wang,<sup>10</sup> G. Webb,<sup>23</sup> J. C. Webb,<sup>4</sup> G. D. Westfall,<sup>29</sup> H. Wieman,<sup>26</sup> S. W. Wissink,<sup>18</sup> R. Witt,<sup>51</sup> Y. F. Wu,<sup>9</sup> Z. Xiao,<sup>50</sup> W. Xie,<sup>38</sup> K. Xin,<sup>41</sup> H. Xu,<sup>25</sup> J. Xu,<sup>9</sup> N. Xu,<sup>26</sup> Q. H. Xu,<sup>43</sup> Y. Xu,<sup>42</sup> Z. Xu,<sup>4</sup> W. Yan,<sup>50</sup> C. Yang,<sup>42</sup> Y. Yang,<sup>25</sup> Y. Yang,<sup>9</sup> Z. Ye,<sup>10</sup> P. Yepes,<sup>41</sup> L. Yi,<sup>38</sup> K. Yip,<sup>4</sup> I.-K. Yoo,<sup>39</sup> N. Yu,<sup>9</sup> Y. Zawisza,<sup>42</sup> H. Zbroszczyk,<sup>54</sup> W. Zha,<sup>42</sup> J. B. Zhang,<sup>9</sup> J. L. Zhang,<sup>43</sup> S. Zhang,<sup>44</sup> X. P. Zhang,<sup>50</sup> Y. Zhang,<sup>42</sup> Z. P. Zhang,<sup>42</sup> F. Zhao,<sup>7</sup> J. Zhao,<sup>9</sup> C. Zhong,<sup>44</sup> X. Zhu,<sup>50</sup> Y. H. Zhu,<sup>44</sup> Y. Zoukarneeva,<sup>21</sup> and M. Zyzak<sup>15</sup>

(STAR Collaboration)

<sup>1</sup>AGH University of Science and Technology, Cracow 30-059, Poland<sup>2</sup>Argonne National Laboratory, Argonne, Illinois 60439, USA

- <sup>3</sup>University of Birmingham, Birmingham B15 2TT, United Kingdom  
<sup>4</sup>Brookhaven National Laboratory, Upton, New York 11973, USA  
<sup>5</sup>University of California, Berkeley, California 94720, USA  
<sup>6</sup>University of California, Davis, California 95616, USA  
<sup>7</sup>University of California, Los Angeles, California 90095, USA  
<sup>8</sup>Universidade Estadual de Campinas, Sao Paulo 13131, Brazil  
<sup>9</sup>Central China Normal University (HZNU), Wuhan 430079, China  
<sup>10</sup>University of Illinois at Chicago, Chicago, Illinois 60607, USA  
<sup>11</sup>Cracow University of Technology, Cracow 31-155, Poland  
<sup>12</sup>Creighton University, Omaha, Nebraska 68178, USA  
<sup>13</sup>Czech Technical University in Prague, FNSPE, Prague 115 19, Czech Republic  
<sup>14</sup>Nuclear Physics Institute AS CR, 250 68 Řež/Prague, Czech Republic  
<sup>15</sup>Frankfurt Institute for Advanced Studies FIAS, Frankfurt 60438, Germany  
<sup>16</sup>Institute of Physics, Bhubaneswar 751005, India  
<sup>17</sup>Indian Institute of Technology, Mumbai 400076, India  
<sup>18</sup>Indiana University, Bloomington, Indiana 47408, USA  
<sup>19</sup>Alikhanov Institute for Theoretical and Experimental Physics, Moscow 117218, Russia  
<sup>20</sup>University of Jammu, Jammu 180001, India  
<sup>21</sup>Joint Institute for Nuclear Research, Dubna 141 980, Russia  
<sup>22</sup>Kent State University, Kent, Ohio 44242, USA  
<sup>23</sup>University of Kentucky, Lexington, Kentucky 40506-0055, USA  
<sup>24</sup>Korea Institute of Science and Technology Information, Daejeon 305-701, Korea  
<sup>25</sup>Institute of Modern Physics, Lanzhou 730000, China  
<sup>26</sup>Lawrence Berkeley National Laboratory, Berkeley, California 94720, USA  
<sup>27</sup>Massachusetts Institute of Technology, Cambridge, Massachusetts 02139-4307, USA  
<sup>28</sup>Max-Planck-Institut für Physik, Munich 80805, Germany  
<sup>29</sup>Michigan State University, East Lansing, Michigan 48824, USA  
<sup>30</sup>Moscow Engineering Physics Institute, Moscow 115409, Russia  
<sup>31</sup>National Institute of Science Education and Research, Bhubaneswar 751005, India  
<sup>32</sup>Ohio State University, Columbus, Ohio 43210, USA  
<sup>33</sup>Old Dominion University, Norfolk, Virginia 23529, USA  
<sup>34</sup>Institute of Nuclear Physics PAN, Cracow 31-342, Poland  
<sup>35</sup>Panjab University, Chandigarh 160014, India  
<sup>36</sup>Pennsylvania State University, University Park, Pennsylvania 16802, USA  
<sup>37</sup>Institute of High Energy Physics, Protvino 142281, Russia  
<sup>38</sup>Purdue University, West Lafayette, Indiana 47907, USA  
<sup>39</sup>Pusan National University, Pusan 609735, Republic of Korea  
<sup>40</sup>University of Rajasthan, Jaipur 302004, India  
<sup>41</sup>Rice University, Houston, Texas 77251, USA  
<sup>42</sup>University of Science and Technology of China, Hefei 230026, China  
<sup>43</sup>Shandong University, Jinan, Shandong 250100, China  
<sup>44</sup>Shanghai Institute of Applied Physics, Shanghai 201800, China  
<sup>45</sup>SUBATECH, Nantes 44307, France  
<sup>46</sup>Temple University, Philadelphia, Pennsylvania 19122, USA  
<sup>47</sup>Texas A&M University, College Station, Texas 77843, USA  
<sup>48</sup>University of Texas, Austin, Texas 78712, USA  
<sup>49</sup>University of Houston, Houston, Texas 77204, USA  
<sup>50</sup>Tsinghua University, Beijing 100084, China  
<sup>51</sup>United States Naval Academy, Annapolis, Maryland 21402, USA  
<sup>52</sup>Valparaiso University, Valparaiso, Indiana 46383, USA  
<sup>53</sup>Variable Energy Cyclotron Centre, Kolkata 700064, India  
<sup>54</sup>Warsaw University of Technology, Warsaw 00-661, Poland  
<sup>55</sup>University of Washington, Seattle, Washington 98195, USA  
<sup>56</sup>Wayne State University, Detroit, Michigan 48201, USA  
<sup>57</sup>Yale University, New Haven, Connecticut 06520, USA  
<sup>58</sup>University of Zagreb, Zagreb HR-10002, Croatia
- (Received 29 April 2014; published 13 August 2014)

We report measurements of single- and double-spin asymmetries for  $W^\pm$  and  $Z/\gamma^*$  boson production in longitudinally polarized  $p + p$  collisions at  $\sqrt{s} = 510$  GeV by the STAR experiment at RHIC. The asymmetries for  $W^\pm$  were measured as a function of the decay lepton pseudorapidity, which provides a

theoretically clean probe of the proton's polarized quark distributions at the scale of the  $W$  mass. The results are compared to theoretical predictions, constrained by polarized deep inelastic scattering measurements, and show a preference for a sizable, positive up antiquark polarization in the range  $0.05 < x < 0.2$ .

DOI: 10.1103/PhysRevLett.113.072301

PACS numbers: 24.85.+p, 13.38.Be, 13.38.Dg, 14.20.Dh

In high-energy proton-proton collisions, weak boson and Drell-Yan production are dominated by quark-antiquark annihilations. Because of the valence quark structure of the proton, these interactions primarily involve the lightest two quark flavors, up ( $u$ ) and down ( $d$ ). In unpolarized collisions, measurements of these processes are used to constrain the helicity-independent parton distribution functions (PDFs) of the quarks (e.g., Refs. [1,2]). In particular, Drell-Yan measurements [3,4] and earlier deep inelastic scattering (DIS) results [5,6] have reported a large enhancement in  $\bar{d}$  over  $\bar{u}$  quarks for a wide range of partonic momentum fractions  $x$ . Calculations have shown that perturbative QCD does not produce such a flavor asymmetry in the proton's light antiquark distributions, indicating another, likely nonperturbative, mechanism is needed [7,8]. This generated significant theoretical interest, with many nonperturbative models able to qualitatively describe the data [9–12].

In the case of longitudinally polarized proton collisions at RHIC, the coupling of  $W^\pm$  bosons to left-handed quarks and right-handed antiquarks ( $u_L \bar{d}_R \rightarrow W^+$  and  $d_L \bar{u}_R \rightarrow W^-$ ) determines the helicity of the incident quarks. This provides a direct probe of the helicity-dependent PDFs through a parity-violating longitudinal single-spin asymmetry, which is defined as  $A_L = (\sigma_+ - \sigma_-)/(\sigma_+ + \sigma_-)$ , where  $\sigma_{+(-)}$  is the cross section when the polarized proton beam has positive (negative) helicity. Analogous to the unpolarized case, measurements of this asymmetry can be used to constrain the helicity-dependent quark PDFs  $\Delta q = q^+ - q^-$ , where  $q^+$  ( $q^-$ ) is the distribution of quarks with spin parallel (antiparallel) to the proton spin. Of particular interest is a possible flavor asymmetry in the polarized case, given by  $\Delta \bar{u} - \Delta \bar{d}$ , which some nonperturbative models predict to be similar to, or even larger than, the unpolarized flavor asymmetry [11,12].

Semi-inclusive DIS measurements with polarized beams and targets also constrain the helicity-dependent PDFs, although they require the use of fragmentation functions to relate the measured final-state hadrons to the flavor-separated quark and antiquark distributions [13–15]. Both inclusive and semi-inclusive DIS measurements have been included in global QCD analyses to determine the helicity-dependent PDFs of the proton [16,17]. The extracted polarized flavor asymmetry  $\Delta \bar{u} - \Delta \bar{d}$  is positive within the sizable uncertainty afforded by the current measurements.

In this Letter, we report measurements of single- and double-spin asymmetries for weak boson production in longitudinally polarized  $p + p$  collisions from 2011 and 2012 by the STAR collaboration at RHIC for  $\sqrt{s} = 500$

and 510 GeV, respectively. The beam polarization and luminosity of this data set correspond to an order of magnitude reduction in the statistical variance for single-spin asymmetry measurements, in comparison to results reported previously by STAR [18] and PHENIX [19]. These measurements place new constraints on the helicity-dependent antiquark PDFs, and prefer a larger value for the up antiquark polarization  $\Delta \bar{u}$  than previously expected by global QCD analyses [16,17].

The polarizations of the two beams were each measured using Coulomb-nuclear interference proton-carbon polarimeters, which were calibrated with a polarized hydrogen gas-jet target [20]. The average luminosity-weighted beam polarization during 2011 (2012) was 0.49 (0.56), with a relative scale uncertainty of 3.4% for the single beam polarization and 6.5% for the product of the polarizations from two beams. The integrated luminosities of the data sets from 2011 and 2012 are 9 and 77 pb<sup>-1</sup>, respectively.

The subsystems of the STAR detector [21] used in this measurement are the Time Projection Chamber [22] (TPC), providing charged particle tracking for pseudorapidity  $|\eta| \lesssim 1.3$ , and the Barrel [23] and Endcap [24] Electromagnetic Calorimeters (BEMC, EEMC). These lead-sampling calorimeters cover the full azimuthal angle  $\phi$  for  $|\eta| < 1$  and  $1.1 < \eta < 2$ , respectively.

In this analysis,  $W^\pm$  bosons were detected via their  $W^\pm \rightarrow e^\pm \nu_e$  decay channels, and were recorded using a calorimeter trigger requirement of 12 (10) GeV of transverse energy  $E_T$  in a  $\Delta\eta \times \Delta\phi$  region of  $\sim 0.1 \times 0.1$  of the BEMC (EEMC). Primary vertices were reconstructed along the beam axis of the TPC within  $\pm 100$  cm of the center of the STAR interaction region. The vertex distribution was approximately Gaussian with an rms of 49 cm. The spread of the vertex distribution allows the detector  $\eta$  coverage to be extended by  $\sim 0.1$ .

The selection criteria for electrons and positrons detected in the BEMC, with  $e^\pm$  pseudorapidity  $|\eta_e| < 1.1$ , are described in previously reported measurements of the  $W^\pm$  and  $Z/\gamma^*$  cross sections [25], and will only be summarized here. At mid-rapidity,  $W^\pm \rightarrow e^\pm \nu_e$  events are characterized by an isolated  $e^\pm$  with a transverse energy  $E_T^e$  measured in the BEMC that peaks near half the  $W$  boson mass. Leptonic  $W^\pm$  decays also produce a neutrino, close to opposite in azimuth of the decay  $e^\pm$ . The neutrino is undetected and leads to a large missing transverse energy. As a result, there is a large imbalance in the vector transverse momentum ( $p_T$ ) sum of all reconstructed final-state objects for  $W^\pm$  events, in contrast to  $Z/\gamma^* \rightarrow e^+ e^-$  and QCD dijet events. We define a  $p_T$ -balance variable  $\vec{p}_T^{\text{bal}}$ , which is the vector

sum of the  $e^\pm$  candidate  $\vec{p}_T^e$  and the  $p_T$  vectors of all reconstructed jets outside an isolation cone around the  $e^\pm$  candidate track with a radius of  $\Delta R = \sqrt{\Delta\eta^2 + \Delta\phi^2} = 0.7$ . Jets were reconstructed from charged tracks in the TPC and energy deposits in the BEMC and EEMC using an anti- $k_T$  algorithm [26]. The scalar variable signed  $p_T$ -balance =  $(\vec{p}_T^{\text{bal}} \cdot \vec{p}_T^e) / |\vec{p}_T^e|$  is required to be larger than 14 GeV/c.

$W^\pm$  candidates were charge separated based on  $e^\pm$  track curvature measured in the TPC. The charge separated yields are shown in Fig. 1, along with the estimated contributions from electroweak processes and QCD backgrounds, as a function of  $E_T^e$ . The  $W^\pm \rightarrow \tau^\pm \nu_\tau$  and  $Z/\gamma^* \rightarrow e^+e^-$  electroweak contributions were determined from Monte Carlo (MC) samples simulated using PYTHIA 6.422 [27] with the Perugia 0 tune [28]. The generated events were passed through a GEANT [29] model of the STAR detector response, embedded in real STAR zero-bias triggered events [25], and reconstructed using the same selection criteria as the data. In the  $W^\pm \rightarrow \tau^\pm \nu_\tau$  sample the TAUOLA package was used for the polarized  $\tau^\pm$  decay [30]. Background yields from QCD processes were estimated independently for each  $\eta_e$  bin through two contributions described in Ref. [25], referred to as the second EEMC and data-driven QCD. These background contributions originate primarily from events that satisfy the  $W^\pm$  selection criteria but contain jets escaping detection due to the missing calorimeter coverage for  $\eta < -1$  and  $\eta > 2$ .

The EEMC was used to reconstruct the energy of the decay  $e^\pm$  candidates at forward rapidity ( $\eta_e > 1$ ). Charged track reconstruction was provided by the TPC, limiting the pseudorapidity acceptance to  $\eta_e \lesssim 1.3$ . Similar to the mid-rapidity event selection, isolation and signed  $p_T$ -balance requirements were used to select  $W^\pm \rightarrow e^\pm \nu_e$  candidates. Additionally, the EEMC Shower Maximum Detector

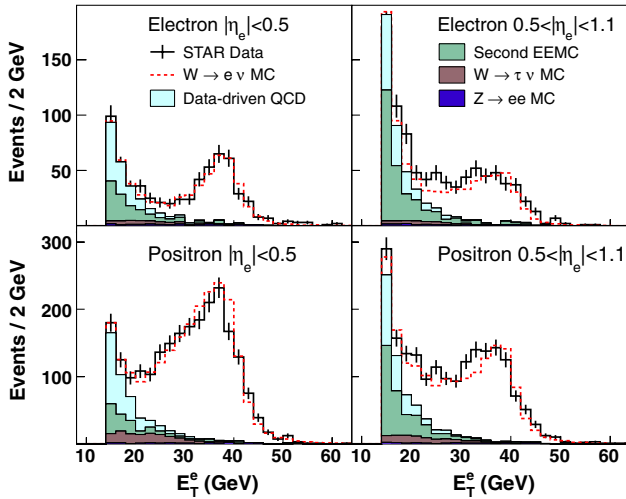


FIG. 1 (color online).  $E_T^e$  distribution of  $W^-$  (top) and  $W^+$  (bottom) candidate events (black), background contributions, and sum of backgrounds and  $W^\pm \rightarrow e^\pm \nu_e$  MC signal (red dashed).

(ESMD) [24], consisting of two orthogonal planes of scintillating strips at a depth of  $\sim 5$  radiation lengths, provided a measurement of the electromagnetic shower's profile transverse to its propagation direction. A single electromagnetic shower from a  $W^\pm \rightarrow e^\pm \nu_e$  decay should be isolated with a narrow transverse profile (Molière radius of  $\sim 1.5$  cm in lead [31]), while QCD background candidates typically contain a  $\pi^0$  or other additional energy deposits in proximity to the candidate track leading to a wider reconstructed shower. In addition, the location of the extrapolated TPC track and the shower reconstructed in the ESMD should be well correlated for  $W^\pm \rightarrow e^\pm \nu_e$  events. To further suppress QCD background events, a ratio of the energy deposited in the ESMD strips within  $\pm 1.5$  cm of the candidate TPC track to the energy deposited in the strips within  $\pm 10$  cm was computed. This ratio, denoted  $R_{\text{ESMD}}$ , was required to be greater than 0.6 to select isolated, narrow  $e^\pm$  showers.

The charge-summed candidate yield as a function of signed  $p_T$ -balance for forward rapidity  $e^\pm$  is shown in Fig. 2(a), where the electroweak contributions were estimated using the same MC samples described for the mid-rapidity case. The QCD background was estimated from the shape of the signed  $p_T$ -balance distribution for  $e^\pm$  candidates with  $R_{\text{ESMD}} < 0.5$ . This shape was determined for each charge sign independently and was normalized to the measured yield in the QCD background dominated region  $-8 < \text{signed } p_T\text{-balance} < 8$  GeV/c. Forward rapidity  $W^\pm$  candidates were selected by requiring signed  $p_T$ -balance  $> 20$  GeV/c. The difference between the data and  $W^\pm \rightarrow e^\pm \nu_e$  MC distributions for signed  $p_T$ -balance  $> 20$  GeV/c is within the MC normalization uncertainty, and this uncertainty provides a negligible contribution to the measured spin asymmetries.

Figure 2(b) shows the reconstructed charge sign multiplied by the ratio of  $E_T^e$  (measured by the EEMC) to  $p_T^e$  (measured by the TPC) for forward rapidity candidates. Because of their forward angle, these tracks have a reduced number of points along their trajectory measured by the TPC compared to the mid-rapidity case, which leads to a degraded  $p_T$  resolution. Despite that, a clear charge sign separation is observed. The data were fit to two

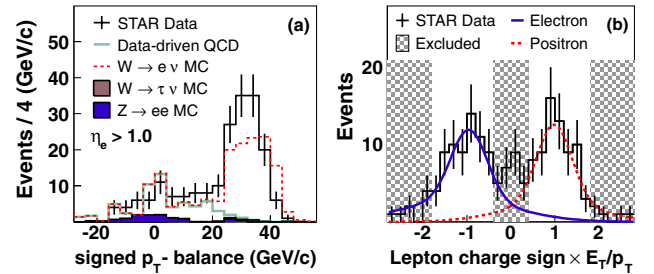


FIG. 2 (color online). (a) Signed  $p_T$ -balance distribution for  $e^\pm$  candidates reconstructed in the EEMC and (b) distribution of the product of the TPC reconstructed charge sign and  $E_T/p_T$ .

double-Gaussian template shapes generated from  $W^\pm$  MC samples to estimate the reconstructed charge sign purity. The shaded regions were excluded from the analysis to remove tracks with poorly reconstructed  $p_T$  and reduce the opposite charge sign contamination. The residual charge sign contamination is estimated to be 6.5%, which is small relative to the statistical uncertainties of the measured spin asymmetries.

Measurements of  $Z/\gamma^*$  production at RHIC energies are limited by a small production cross section. However, one unique advantage of this channel is the fully reconstructed  $e^+e^-$  final state, allowing the initial state kinematics to be determined event by event at leading order. A sample of 88  $Z/\gamma^* \rightarrow e^+e^-$  events was identified by selecting a pair of isolated, oppositely charged  $e^\pm$  candidates, as described in Ref. [25]. The resulting invariant mass distribution of  $e^+e^-$  pairs is shown in Fig. 3, superimposed with the MC expectation.

The measured spin asymmetries were obtained from the 2011 and 2012 data samples using a likelihood method to treat the low statistics of the 2011 sample. For a given data sample, a model for the expected, spin-dependent  $W^\pm$  event yield  $\mu$  in a given positive pseudorapidity range, labeled  $a$ , of the STAR detector can be defined for each of the four RHIC helicity states of the two polarized proton beams

$$\begin{aligned}\mu_{++}^a &= l_{++}N^a(1 + P_1\beta A_L^{+\eta_e} + P_2\beta A_L^{-\eta_e} + P_1P_2\beta A_{LL}), \\ \mu_{+-}^a &= l_{+-}N^a(1 + P_1\beta A_L^{+\eta_e} - P_2\beta A_L^{-\eta_e} - P_1P_2\beta A_{LL}), \\ \mu_{-+}^a &= l_{-+}N^a(1 - P_1\beta A_L^{+\eta_e} + P_2\beta A_L^{-\eta_e} - P_1P_2\beta A_{LL}), \\ \mu_{--}^a &= l_{--}N^a(1 - P_1\beta A_L^{+\eta_e} - P_2\beta A_L^{-\eta_e} + P_1P_2\beta A_{LL}),\end{aligned}\quad (1)$$

where  $P_1$  ( $P_2$ ) is the absolute value of the polarization of beam 1 (2),  $A_L^{+\eta_e}$  ( $A_L^{-\eta_e}$ ) is the single-spin asymmetry measured at positive (negative)  $\eta_e$  with respect to beam 1,  $A_{LL}$  is the parity-conserving double-spin asymmetry [32], which is symmetric with respect to  $\eta_e$ ,  $N^a$  is the spin averaged yield, and  $l_{\pm\pm}$  are the respective relative luminosities determined from an independent sample of QCD

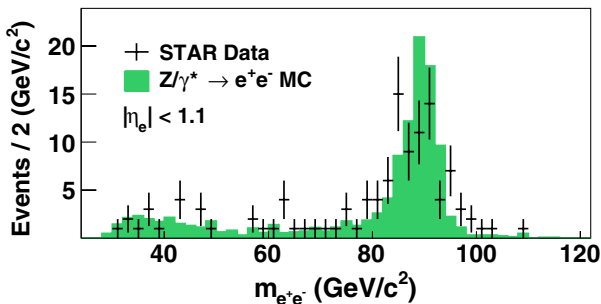


FIG. 3 (color online). Distributions of the invariant mass of  $Z/\gamma^* \rightarrow e^+e^-$  candidate events. The  $Z/\gamma^* \rightarrow e^+e^-$  MC distribution (filled histogram) is shown for comparison.

events, which required a nonisolated lepton candidate with  $E_T^e < 20$  GeV as described in Ref. [18].

A similar set of four equations can be written for the symmetric negative pseudorapidity range of the STAR detector, labeled  $b$ , by interchanging  $A_L^{+\eta_e}$  with  $A_L^{-\eta_e}$ . The dilution of the asymmetries due to unpolarized background contributions to the  $W^\pm$  candidate yield is represented by  $\beta = S/(S + B)$ , where  $S$  and  $B$  are the number of signal and background events as shown in Figs. 1 and 2, and were measured separately for regions  $a$  and  $b$ . The estimated  $W^\pm \rightarrow \tau^\pm\nu_\tau$  yield is not a background for the asymmetry measurement as it is produced in the same partonic processes as the primary signal,  $W^\pm \rightarrow e^\pm\nu_e$ .

The eight spin-dependent yields for the pair of symmetric pseudorapidity regions in the STAR detector ( $a$  and  $b$ ) are used to define a likelihood function

$$L = \prod_i^4 \mathcal{P}(M_i^a|\mu_i^a)\mathcal{P}(M_i^b|\mu_i^b)g(\beta^a)g(\beta^b)\quad (2)$$

consisting of a product of Poisson probabilities  $\mathcal{P}(M_i|\mu_i)$  for measuring  $M_i$  events in a helicity configuration  $i$  given the expected value  $\mu_i$  from Eq. (1) and a Gaussian probability  $g(\beta)$  for the estimated background dilution. The spin asymmetry parameters ( $A_L^{+\eta_e}$ ,  $A_L^{-\eta_e}$ , and  $A_{LL}$ ) of this likelihood function were bounded to be within their physically allowed range of  $[-1, 1]$ ,  $N^{a,b}$  and  $\beta^{a,b}$  were treated as nuisance parameters, and the remaining parameters ( $P$  and  $l_{\pm\pm}$ ) are known constants.

Separate likelihood functions were computed for the 2011 and 2012 data sets, consisting of 2759  $W^+$  and 837  $W^-$  candidates in total. The product of these two likelihood functions was used in a profile likelihood analysis [31] to obtain the central values and confidence intervals for the asymmetries. The  $W^\pm$  asymmetries were measured for  $e^\pm$  with  $25 < E_T^e < 50$  GeV and are shown in Figs. 4 and 5 as a function of  $e^\pm$  pseudorapidity for the single- and double-spin asymmetries, respectively. These results are consistent with our previous measurements of  $A_L$  [18]. The data points are located at the average  $\eta_e$  within each bin, and the horizontal error bars represent the rms of the  $\eta_e$  distribution within that bin. The vertical error bars show the 68% confidence intervals, which include the statistical uncertainty, as well as systematic uncertainties due to the unpolarized background dilutions. The magnitude of the confidence intervals is dominated by the statistical precision of the data. The relative luminosity systematic uncertainty is  $\pm 0.007$  as indicated by the gray band in Fig. 4. The single- (double-)spin asymmetries have a common 3.4% (6.5%) normalization uncertainty due to the uncertainty in the measured beam polarization.

The measured single-spin asymmetries are compared to theoretical predictions using both next-to-leading order (CHE) [33] and fully resummed (RHICBOS) [34] calculations in Fig. 4. The RHICBOS calculations are shown for the

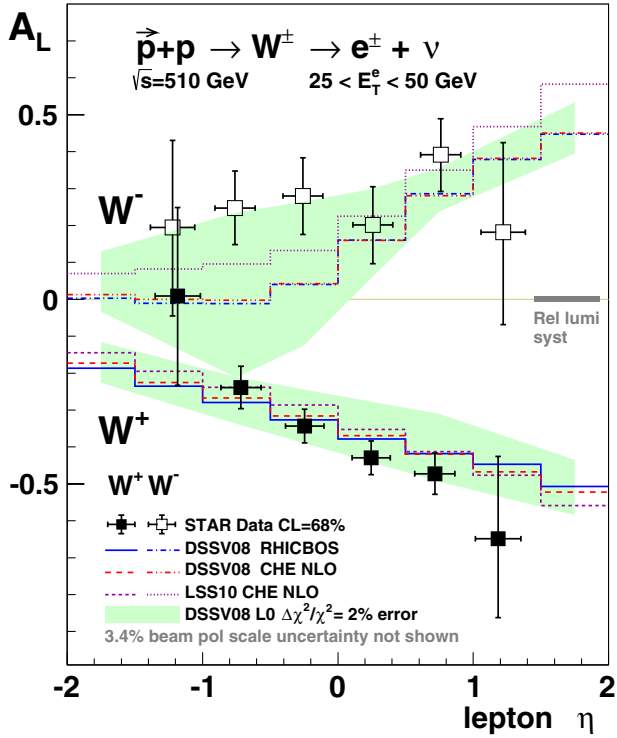


FIG. 4 (color online). Longitudinal single-spin asymmetry  $A_L$  for  $W^\pm$  production as a function of lepton pseudorapidity  $\eta_e$  in comparison to theory predictions (see text for details).

DSSV08 [16] helicity-dependent PDF set, and the CHE calculations are shown for DSSV08 [16] and LSS10 [17]. The DSSV08 uncertainties were determined using a Lagrange multiplier method to map out the  $\chi^2$  profile of the global fit [16], and the  $\Delta\chi^2/\chi^2 = 2\%$  error band in Fig. 4 represents the estimated PDF uncertainty for  $A_L^W$  [35].

The measured  $A_L^{W^+}$  is negative, consistent with the theoretical predictions. For  $A_L^{W^-}$ , however, the measured asymmetry is larger than the central value of the theoretical predictions for  $\eta_{e^-} < 0$ . This region is most sensitive to the

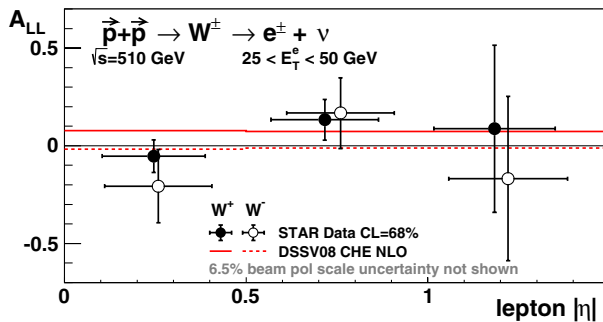


FIG. 5 (color online). Longitudinal double-spin asymmetry  $A_{LL}$  for  $W^\pm$  production as a function of lepton pseudorapidity  $|\eta_e|$  in comparison to theory predictions (see text for details).

up antiquark polarization  $\Delta\bar{u}$ , which is not currently well constrained [16,17] as can be seen by the large uncertainty in the theoretical prediction there. While consistent within the theoretical uncertainty, the large positive values for  $A_L^{W^-}$  indicate a preference for a sizable, positive  $\Delta\bar{u}$  in the range  $0.05 < x < 0.2$  relative to the central values of the DSSV08 and LSS10 fits. Global analyses from both DSSV++ [36] and neural network PDF [37] have extracted the antiquark polarizations, using our preliminary measurement from the 2012 data set. These analyses quantitatively confirm the enhancement of  $\Delta\bar{u}$  and the expected reduction in the uncertainties of the helicity-dependent PDFs compared to previous fits without our data.

The  $W^\pm$  double-spin asymmetry, shown in Fig. 5, is sensitive to the product of quark and antiquark polarizations, and has also been proposed to test positivity constraints using a combination of  $A_L$  and  $A_{LL}$  [38]. The measured double-spin asymmetries are consistent with the theoretical predictions and in conjunction with  $A_L^{W^\pm}$  satisfy the positivity bounds within the current uncertainties.

A similar profile likelihood procedure is used to determine the single-spin asymmetry  $A_L^{Z/\gamma^*}$  for  $Z/\gamma^*$  production with  $|\eta_e| < 1.1$ ,  $E_T^e > 14\text{ GeV}$ , and  $70 < m_{e^+e^-} < 110\text{ GeV}/c^2$ .  $A_L^{Z/\gamma^*}$  is sensitive to the combination of  $u$ ,  $\bar{u}$ ,  $d$ , and  $\bar{d}$  polarizations. The measured asymmetry  $A_L^{Z/\gamma^*} = -0.07^{+0.14}_{-0.14}$  is consistent, within the large uncertainty, with theoretical predictions using the different helicity-dependent PDFs  $A_L^{Z/\gamma^*}$  (DSSV08) =  $-0.07$  and  $A_L^{Z/\gamma^*}$  (LSS10) =  $-0.02$ .

In summary, we report new measurements of the parity-violating single-spin asymmetry  $A_L$  and parity-conserving double-spin asymmetry  $A_{LL}$  for  $W^\pm$  production as well as a first measurement of  $A_L$  for  $Z/\gamma^*$  production in longitudinally polarized proton collisions by the STAR experiment at RHIC. The dependence of  $A_L^{W^\pm}$  on the decay lepton pseudorapidity probes the flavor-separated quark and antiquark helicity-dependent PDFs at the  $W$  mass scale. A comparison to theoretical predictions based on different helicity-dependent PDFs suggests a positive up antiquark polarization in the range  $0.05 < x < 0.2$ . The inclusion of this measurement in global analyses of RHIC and DIS data should significantly improve the determination of the polarization of up and down antiquarks in the proton and provide new input on the flavor symmetry of the proton's antiquark distributions.

We thank the RHIC Operations Group and RCF at BNL, the NERSC Center at LBNL, the KISTI Center in Korea, and the Open Science Grid consortium for providing resources and support. We are grateful to M. Stratmann for useful discussions. This work was supported in part by the Offices of NP and HEP within the U.S. DOE Office of Science, the U.S. NSF, CNRS/IN2P3, FAPESP CNPq of Brazil, the Ministry of Education and Science of the Russian Federation, NNSFC, CAS, MoST and MoE of China, the Korean Research Foundation, GA and MSMT of

the Czech Republic, FIAS of Germany, DAE, DST, and CSIR of India, the National Science Centre of Poland, National Research Foundation (NRF-2012004024), the Ministry of Science, Education and Sports of the Republic of Croatia, and RosAtom of Russia.

- 
- [1] H.-L. Lai, M. Guzzi, J. Huston, Z. Li, P.M. Nadolsky, J. Pumplin, and C.-P. Yuan, *Phys. Rev. D* **82**, 074024 (2010).
- [2] A. D. Martin, W.J. Stirling, R. S. Thorne, and G. Watt, *Eur. Phys. J. C* **63**, 189 (2009).
- [3] A. Baldit *et al.* (NA51 Collaboration), *Phys. Lett. B* **332**, 244 (1994).
- [4] R. Towell *et al.* (E866/NuSea Collaboration), *Phys. Rev. D* **64**, 052002 (2001).
- [5] P. Amaudruz *et al.* (New Muon Collaboration), *Phys. Rev. Lett.* **66**, 2712 (1991).
- [6] See M. Arneodo *et al.* (New Muon Collaboration), *Phys. Rev. D* **50**, R1 (1994), which is a revised version of CERN-PPE-93-117.
- [7] D. Ross and C. T. Sachrajda, *Nucl. Phys.* **B149**, 497 (1979).
- [8] F.M. Steffens and A. W. Thomas, *Phys. Rev. C* **55**, 900 (1997).
- [9] G. T. Garvey and J.-C. Peng, *Prog. Part. Nucl. Phys.* **47**, 203 (2001).
- [10] S. Kumano and M. Miyama, *Phys. Rev. D* **65**, 034012 (2002).
- [11] B. Dressler, K. Goeke, M. V. Polyakov, P. Schweitzer, M. Strikman, and C. Weiss, *Eur. Phys. J. C* **18**, 719 (2001).
- [12] C. Bourrely, J. Soffer, and F. Buccella, *Eur. Phys. J. C* **23**, 487 (2002); *Phys. Lett. B* **726**, 296 (2013).
- [13] B. Adeva *et al.* (Spin Muon Collaboration), *Phys. Lett. B* **420**, 180 (1998).
- [14] A. Airapetian *et al.* (HERMES Collaboration), *Phys. Rev. D* **71**, 012003 (2005).
- [15] M. Alekseev *et al.* (COMPASS Collaboration), *Phys. Lett. B* **693**, 227 (2010).
- [16] D. de Florian, R. Sassot, M. Stratmann, and W. Vogelsang, *Phys. Rev. Lett.* **101**, 072001 (2008); *Phys. Rev. D* **80**, 034030 (2009).
- [17] E. Leader, A. V. Sidorov, and D. B. Stamenov, *Phys. Rev. D* **82**, 114018 (2010).
- [18] M. Aggarwal *et al.* (STAR Collaboration), *Phys. Rev. Lett.* **106**, 062002 (2011).
- [19] A. Adare *et al.* (PHENIX Collaboration), *Phys. Rev. Lett.* **106**, 062001 (2011).
- [20] RHIC Polarimetry Group, RHIC/CAD Accelerator Physics Note 490 (2013).
- [21] K. H. Ackermann *et al.* (STAR Collaboration), *Nucl. Instrum. Methods Phys. Res., Sect. A* **499**, 624 (2003).
- [22] M. Anderson *et al.* (STAR Collaboration), *Nucl. Instrum. Methods Phys. Res., Sect. A* **499**, 659 (2003).
- [23] M. Beddo *et al.* (STAR Collaboration), *Nucl. Instrum. Methods Phys. Res., Sect. A* **499**, 725 (2003).
- [24] C. Allgower *et al.* (STAR Collaboration), *Nucl. Instrum. Methods Phys. Res., Sect. A* **499**, 740 (2003).
- [25] L. Adamczyk *et al.* (STAR Collaboration), *Phys. Rev. D* **85**, 092010 (2012).
- [26] M. Cacciari, G. P. Salam, and G. Soyez, *J. High Energy Phys.* **04** (2008) 063.
- [27] T. Sjostrand, S. Mrenna, and P. Z. Skands, *J. High Energy Phys.* **05** (2006) 026.
- [28] P. Z. Skands, *Phys. Rev. D* **82**, 074018 (2010).
- [29] R. Brun *et al.*, CERN-DD-78-2-REV (1978).
- [30] P. Golonka, B. Kersevan, T. Pierzchała, E. Richter-Was, Z. Was, and M. Worek, *Comput. Phys. Commun.* **174**, 818 (2006).
- [31] J. Beringer *et al.* (Particle Data Group), *Phys. Rev. D* **86**, 010001 (2012).
- [32] The double-spin asymmetry is defined as
- $$A_{LL} = \frac{(\sigma_{++} + \sigma_{--}) - (\sigma_{+-} + \sigma_{-+})}{(\sigma_{++} + \sigma_{--}) + (\sigma_{+-} + \sigma_{-+})}, \quad (3)$$
- where  $\sigma_{+-}$  represents a cross section for beam protons with helicity (+) and (-).
- [33] D. de Florian and W. Vogelsang, *Phys. Rev. D* **81**, 094020 (2010).
- [34] P. M. Nadolsky and C. Yuan, *Nucl. Phys.* **B666**, 31 (2003).
- [35] DSSV Group (private communication).
- [36] E. Aschenauer *et al.*, [arXiv:1304.0079](https://arxiv.org/abs/1304.0079).
- [37] E. R. Nocera, *Proceedings of the XXI International Workshop on Deep-Inelastic Scattering and Related Subjects* (Proceedings of Science, Marseille, France, 2013).
- [38] Z.-B. Kang and J. Soffer, *Phys. Rev. D* **83**, 114020 (2011).



## Measurement of Longitudinal Spin Asymmetries for Weak Boson Production in Polarized Proton-Proton Collisions at STAR

Jinlong Zhang

for the STAR Collaboration

*School of Physics and Key Laboratory of Particle Physics  
and Particle Irradiation (MOE),  
Shandong University, Jinan, 250100, China  
jlzhang@rcf.rhic.bnl.gov*

Published 29 February 2016

The production of  $W^\pm$  bosons in longitudinally polarized  $p + p$  collisions is a powerful tool to study the spin-flavor structure of the proton. We report measurements of single- and double-spin asymmetries for  $W$  and  $Z/\gamma^*$  production in longitudinally polarized proton-proton collisions at  $\sqrt{s} = 510$  GeV at RHIC. The single-spin asymmetry results for  $W^\pm$  from data sets collected by STAR experiment in 2011 and 2012 provided new constraints on proton's polarized sea quark distributions and prefer a sizable value for  $\bar{u}$  polarization. The status for the analysis of a much larger data set collected by STAR in 2013 will also be given.

*Keywords:* Weak boson; quark polarization.

### 1. Introduction

Understanding the spin structure of proton is a fundamental and longstanding challenge in nuclear physics. The total quark contribution has been well measured from polarized inclusive deep-inelastic scattering (DIS) experiments, and was found to contribute only  $\sim 30\%$  of the proton spin.<sup>1</sup> The flavor separated contribution can be accessed through semi-inclusive DIS experiments, but they have to rely on the use of fragmentation functions to relate the measurements of the final state hadrons to the quark and anti-quark distributions. The extracted anti-quark helicity-dependent parton distribution functions (PDFs) have relatively large uncertainty<sup>2, 3</sup>

The production of  $W^\pm$  bosons in polarized proton-proton collisions at RHIC, the Relativistic Heavy-Ion Collider, is a powerful tool to study the spin-flavor structure of the proton. The coupling of  $W^\pm$  bosons to left-handed quarks and right-handed

This is an Open Access article published by World Scientific Publishing Company. It is distributed under the terms of the Creative Commons Attribution 3.0 (CC-BY) License. Further distribution of this work is permitted, provided the original work is properly cited.

anti-quarks determines the helicity of the incident quarks. This provides a theoretically clean probe of the helicity-dependent PDFs through a parity-violating longitudinal single-spin asymmetry, which is defined as  $A_L = (\sigma_+ - \sigma_-)/(\sigma_+ + \sigma_-)$ , where  $\sigma_{+(-)}$  is the cross section when the polarized beam has positive (negative) helicity. At leading order, the  $A_L$  of  $W^\pm$  can be directly sensitive to  $\Delta\bar{u}$  and  $\Delta\bar{d}$ , the helicity-dependent PDFs of  $\bar{u}$  and  $\bar{d}$  quarks, expressed by:

$$A_L^{W^+} \propto \frac{-\Delta u(x_1)\bar{d}(x_2) + \Delta\bar{d}(x_1)u(x_2)}{u(x_1)\bar{d}(x_2) + \bar{d}(x_1)u(x_2)}, \quad (1)$$

$$A_L^{W^-} \propto \frac{-\Delta d(x_1)\bar{u}(x_2) + \Delta\bar{u}(x_1)d(x_2)}{d(x_1)\bar{u}(x_2) + \bar{u}(x_1)d(x_2)}, \quad (2)$$

where  $x_1$  and  $x_2$  are the momentum fractions carried by the incident partons. We can directly measure the flavor separated quark and anti-quark polarizations, by identifying the rapidity of  $W$ ,  $y_W$ . The  $A_L^{W^+}$  ( $A_L^{W^-}$ ) approaches  $\Delta u/u$  ( $\Delta d/d$ ) in the very forward region ( $y_W \gg 0$ ), or  $-\Delta\bar{d}/\bar{d}$  ( $-\Delta\bar{u}/\bar{u}$ ) in the very backward region ( $y_W \ll 0$ ).<sup>4</sup>

First measurements of the single-spin asymmetry,  $A_L$ , for  $W$  production at RHIC were reported by the STAR<sup>5</sup> and PHENIX<sup>6</sup> collaborations from a data set collected in 2009, the successful commission run at  $\sqrt{s}=500\text{GeV}$ . In this contribution, we report the results for the single- and double-spin asymmetries for  $W^\pm$  and  $Z/\gamma^*$  production measured from data sets collected in 2011 and 2012 by STAR experiment, with integrated luminosity of 9 and 77  $\text{pb}^{-1}$ , and average beam polarization of 49% and 56%, respectively.

## 2. Analysis

At STAR,  $W^\pm$  bosons are detected via their  $W^\pm \rightarrow e^\pm\nu$  decay channels. The charge separation and  $p_T$  of the lepton tracks are measured by the Time Projection Chamber (TPC), and the lepton energy is measured by the Barrel and Endcap Electromagnetic Calorimeters (BEMC, EEMC). The candidate  $W^\pm \rightarrow e^\pm\nu$  events are characterized by an isolated  $e^\pm$  with a  $E_e^T$ , transverse energy, that peaks near half the  $W^\pm$  mass. Due to the large missing energy in the opposite azimuth of the  $e^\pm$  candidates caused by the undetected neutrinos decayed from  $W^\pm$ , there should be a large imbalance in the vector  $p_T$  sum of all reconstructed final-state objects for  $W^\pm$  events in contrast to  $Z/\gamma^* \rightarrow e^+e^-$  and QCD di-jet background events. The main  $W$  selection cuts used to suppress the background and enhance the  $W$  signals are based on the isolation and  $p_T$  imbalance requirements.

Firstly, we match reconstructed TPC tracks with  $p_T > 10$  GeV with the  $2 \times 2$  EMC tower clusters with  $E_T > 14$  GeV. The  $E_T$  fraction of the  $2 \times 2$  EMC cluster over the  $4 \times 4$  EMC cluster in which it is centered is required to be greater than 95%. Additionally, in the near-cone around the candidate lepton with a radius of

0.7 in  $\eta - \phi$  space, the excess  $E_T$  fraction is required to be less than 12%. To implement the  $p_T$  imbalance requirement, we reconstruct a  $p_T$ -balance variable  $\vec{p}_T^{bal}$  by summing the  $\vec{p}_T^e$  vector of candidate  $e^\pm$  and all jets, reconstructed using an anti- $k_T$  algorithm,<sup>8</sup> outside the near-cone mentioned above. Finally, we require the scaler variable signed  $p_T$ -balance,  $(\vec{p}_T^{bal} \cdot \vec{p}_T^e)/|\vec{p}_T^e|$ , to be larger than 14 GeV.

The charge separated  $W^\pm$  yields from 2011 and 2012 data sets as a function of  $E_e^T$  in different  $\eta$ -bins are shown at Fig. 1, along with the estimated residual background contributions from  $W^\pm \rightarrow \tau^\pm \nu_\tau$ ,  $Z/\gamma^* \rightarrow e^+e^-$  electroweak processes and QCD processes. The electroweak backgrounds were estimated from Monte-Carlo (MC) simulation, with PYTHIA events passing the STAR GEANT model and embedding into STAR zero-bias triggered events. The QCD backgrounds were estimated through two procedures, referred to ‘‘Second EEMC’’ and ‘‘Data-driven QCD’’, to account for QCD events which passed the W selection criteria due to missing detected jets in range  $-2 < \eta < -1.09$ , the mirror range of EEMC<sup>a</sup>, and range  $|\eta| > 2$ , respectively.

At forward rapidity ( $\eta_e > 1$ ), in addition to the isolation and signed  $p_T$ -balance requirement described above, the EEMC Shower Maximum Detector (ESMD) is used to suppress the backgrounds. More details are described in Ref. 9.

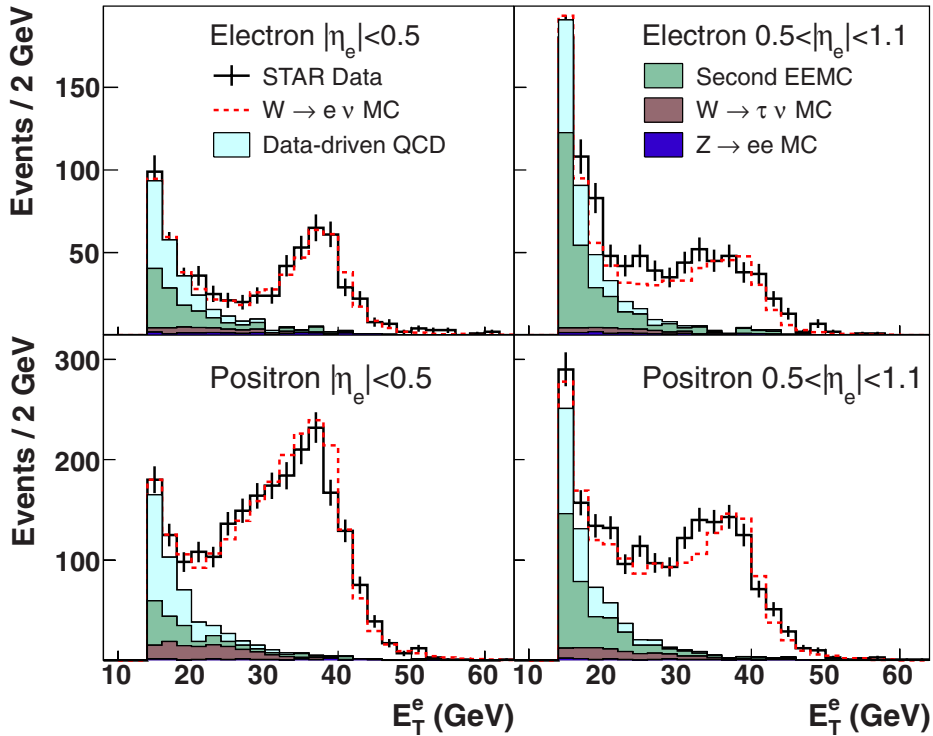


Fig. 1.  $E_T^e$  distribution of  $W^-$  (top) and  $W^+$  (bottom) candidate events (black), background contributions, and sum of backgrounds and  $W \rightarrow e\nu$  MC signal (red-dashed).<sup>9</sup>

<sup>a</sup>STAR detector has only one Endcap EMC in the west side, covering  $1.09 < \eta < 2$ .

### 3. Results

A likelihood method was used to extract the spin asymmetry results with 2011 and 2012 data sets, to treat the low statistics of 2011 sample. We defined the likelihood function  $L_{year}$  for 2011 and 2012 data sets independently,  $year=2011, 2012$ ,

$$L_{year} = \prod_i^4 \mathcal{P}(M_i^a | \mu_i^a) \mathcal{P}(M_i^b | \mu_i^b) g(\beta^a) g(\beta^b). \quad (3)$$

It is the product of two Poisson probabilities,  $\mathcal{P}(M_i | \mu_i)$ , for measuring  $M_i$  events in an expected value  $\mu_i$  and two Gaussian probabilities  $g(\beta)$  for the estimated background dilution. The superscripts  $a$  and  $b$  respectively stand for the positive side and negative side of a pair of symmetric detector  $\eta$  regions. The expected value  $\mu_i$  is the function of spin asymmetries, collision helicity configuration, beam polarization, and spin average yield.  $\beta$  is the unpolarized background dilution factor defined as  $\beta = S/(S+B)$ , where  $S$  and  $B$  are the numbers of signal and background events as shown in Fig. 1. The asymmetry results, central values and confidence intervals, are extracted from the product of likelihood functions,  $L_{2011} \times L_{2012}$ . The  $W^\pm$  single-spin asymmetry results measured for  $e^\pm$  with  $25 < E_T^e < 50$  GeV are shown in Fig. 2, as the function of decayed  $e^\pm$  pseudorapidity, with comparison to the theoretical predictions based on DSSV08<sup>2</sup> and LSS10<sup>3</sup> helicity-dependent PDF

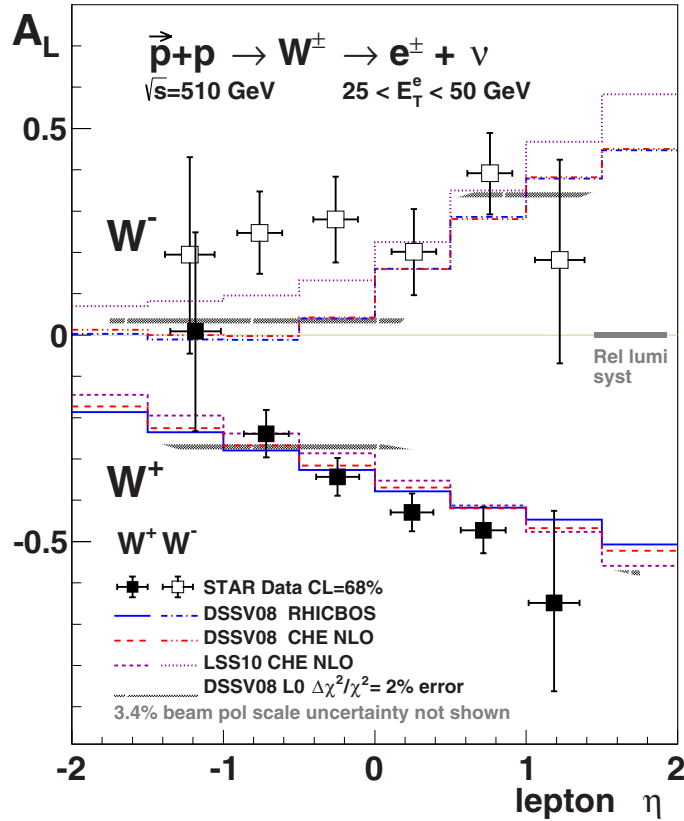


Fig. 2. Longitudinal single-spin asymmetries for  $W^\pm$  production as a function of lepton pseudorapidity magnitude,  $|\eta_e|$ , in comparison with theory predictions.<sup>9</sup>

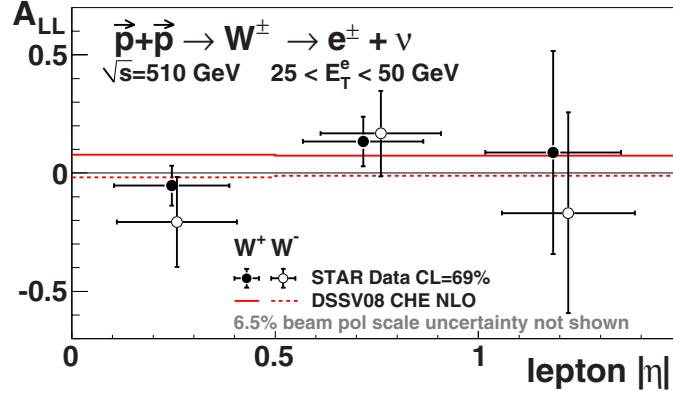


Fig. 3. Longitudinal double-spin asymmetries for  $W^\pm$  production as a function of lepton pseudorapidity magnitude,  $|\eta_e|$ , in comparison with theory predictions.<sup>9</sup>

sets, using both CHE<sup>10</sup> (next-to-leading order) and RHICBOS<sup>11</sup> (fully resummed), as indicated by the Legends.

In Fig. 2, the measured  $A_L^{W^+}$  is negative, consistent with the theoretical predictions. For  $A_L^{W^-}$  however, the measured asymmetry is larger than the central value of the theoretical predictions for  $\eta_{e^-} < 0$ . This region is most sensitive to the up antiquark polarization  $\Delta\bar{u}$ , which is not currently well constrained as can be seen by the large uncertainty in the theoretical prediction there. The large, positive values for  $A_L^{W^-}$  indicate a preference for a sizable, positive  $\Delta\bar{u}$  in the range  $x > 0.05$ .

The double-spin asymmetry,  $A_{LL}$  for  $W^\pm$  was also measured and is shown in Fig. 3, which is sensitive to the product of quark and antiquark polarizations, and has also been proposed to test positivity constraints using a combination of  $A_L$  and  $A_{LL}$ .<sup>12</sup> The measured double-spin asymmetries are consistent with the theoretical predictions and in conjunction with  $A_L^{W^\pm}$  satisfy the positivity bounds within the current uncertainties.

The sample of  $Z/\gamma^* \rightarrow e^+e^-$  was also reconstructed from a pair of isolated and oppositely charged  $e^\pm$  candidates from the 2011 and 2012 data sets. The single-spin asymmetry  $A_L^{Z/\gamma^*}$  for  $Z/\gamma^*$  production with  $|\eta| < 1.1$ ,  $E_T^e > 14$  GeV, and  $70 < m_{e^+e^-} < 110$  GeV/ $c^2$  was extracted through a similar likelihood method described above. The measured asymmetry is  $A_L^{Z/\gamma^*} = -0.07^{+0.14}_{-0.14}$ , which is consistent with theoretical predictions using the different helicity-dependent PDFs,  $A_L^{Z/\gamma^*}$  (DSSV08) = -0.07 and  $A_L^{Z/\gamma^*}$  (LSS10) = -0.02.

#### 4. Outlook

In 2013, the STAR experiment collected a much larger  $p + p$  data sample, with an integrated luminosity of  $\sim 300$  pb<sup>-1</sup> at  $\sqrt{s} = 510$  GeV with an average beam polarization of  $\sim 54\%$ , which is more than 3 times larger than the total integrated luminosity of previous years. And, with the Forward Gem Tracker (FGT) installed for 2013 running, the acceptance can be enlarged by a factor of 2 in pseudorapidity.

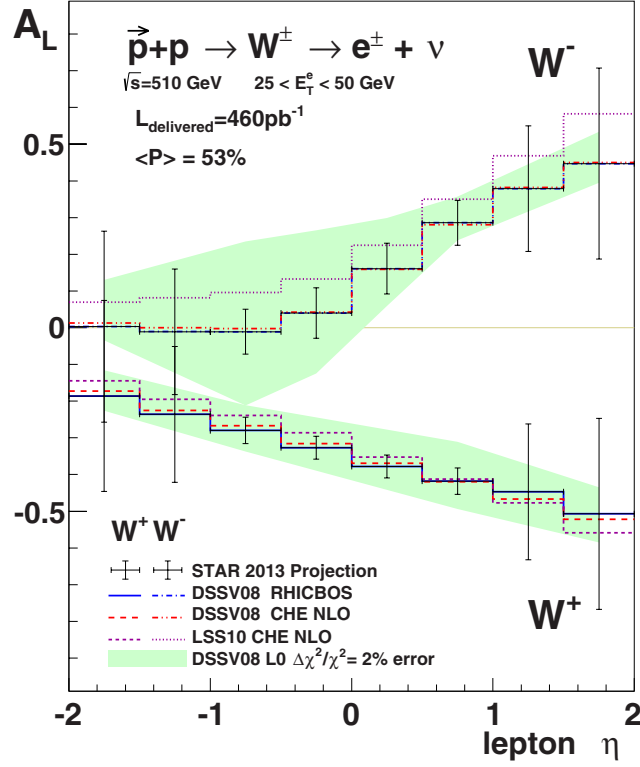


Fig. 4. Projected uncertainties for the longitudinal single-spin asymmetries as a function of lepton pseudorapidity for  $W^\pm$  production measurements from 2013 data set.

This will enhance the sensitivity to  $\bar{u}$  and  $\bar{d}$  quark polarization. Currently, the analysis on 2013 data set is ongoing and the expected precision for  $W^\pm A_L$  are shown in Fig. 4. The new measurements are expected to provide further important constraints on the sea quarks helicity-dependent PDFs.

The author is supported partially by the MoST of China (973 program No. 2014CB845400), and the NNSFC, China under Grant No. 11175106 and 11222551.

## References

1. B. W. Filipone and X. D. Ji, *Adv. Nucl. Phys.* **26**, 1 (2001).
2. D. de Florian, R. Sassor, M. Stratmann, and W. Vogelsang, *Phys. Rev. Lett.* **101**, 072001 (2008).
3. E. Leader, A. V. Sidorov, and D. B. Stamenov, *Phys. Rev. D* **82**, 114018 (2010).
4. G. Bunce, N. Saito, J. Soffer, and W. Vogelsang, *Ann. Rev. Nucl. Par. Sci.* **50** 525 (2000).
5. STAR Collab. (M. Aggarwal *et al.*), *Phys. Rev. Lett.* **106**, 062002 (2011).
6. PHENIX Collab. (A. Adare *et al.*), *Phys. Rev. Lett.* **106**, 062001 (2011).
7. STAR Collab. (L. Adamczyk *et al.*), *Phys. Rev. D* **85**, 092010 (2012).
8. M. Cacciari, G. P. Salam, and G. Soyez, *JHEP* **0804**, 063 (2008).
9. STAR Collab. (L. Adamczyk *et al.*), *Phys. Rev. Lett.* **113**, 072301 (2014).
10. D. de Florian and W. Vogelsang, *Phys. Rev. D* **81**, 094020 (2010).
11. P. M. Nadolsky and C. Yuan, *Nucl. Phys. B* **666**, 31 (2003)
12. Z.-B. Kang and J. Soffer, *Phys. Rev. D* **83**, 114020 (2011).

## 学位论文评阅及答辩情况表

论文评阅人	姓名	专业技术 职 务	是否博导 (硕导)	所 在 单 位		总体评价 ※	
答辩委员会成员	姓名		专业技术 职 务	是否博导 (硕导)	所 在 单 位		
	主席						
	委						
	员						
答辩委员会对论文的 总体评价※				答辩秘书		答辩日期	
备注							

※优秀为“A”；良好为“B”；合格为“C”；不合格为“D”。